

CENTER FOR COMPUTER RESEARCH IN MUSIC AND ACOUSTICS
MARCH 1997

DEPARTMENT OF MUSIC
REPORT NO. STAN-M-100

AN ACOUSTIC ANALYSIS OF SINGLE-REED WOODWIND
INSTRUMENTS WITH AN EMPHASIS ON DESIGN AND
PERFORMANCE ISSUES AND DIGITAL WAVEGUIDE MODELING
TECHNIQUES

GARY PAUL SCAVONE

CCRMA
DEPARTMENT OF MUSIC
STANFORD UNIVERSITY
STANFORD, CALIFORNIA 94305-8180

AN ACOUSTIC ANALYSIS OF SINGLE-REED WOODWIND
INSTRUMENTS WITH AN EMPHASIS ON DESIGN AND
PERFORMANCE ISSUES AND DIGITAL WAVEGUIDE
MODELING TECHNIQUES

A DISSERTATION
SUBMITTED TO THE DEPARTMENT OF MUSIC
AND THE COMMITTEE ON GRADUATE STUDIES
OF STANFORD UNIVERSITY
IN PARTIAL FULFILLMENT OF THE REQUIREMENTS
FOR THE DEGREE OF
DOCTOR OF PHILOSOPHY

Gary Paul Scavone

March 1997

© Copyright 1997 by Gary Paul Scavone
All Rights Reserved

AN ACOUSTIC ANALYSIS OF SINGLE-REED WOODWIND INSTRUMENTS WITH AN EMPHASIS ON DESIGN AND PERFORMANCE ISSUES AND DIGITAL WAVEGUIDE MODELING TECHNIQUES

Gary Paul Scavone
Stanford University, 1997

Current acoustic theory regarding single-reed woodwind instruments is reviewed and summarized, with special attention given to a complete analysis of conical air column issues. This theoretical acoustic foundation is combined with an empirical perspective gained through professional performance experience in a discussion of woodwind instrument design and performance issues. Early saxophone design specifications, as given by Adolphe Sax, are investigated to determine possible influences on instrument response and intonation. Issues regarding saxophone mouthpiece geometry are analyzed. Piecewise cylindrical and conical section approximations to narrow and wide mouthpiece chamber designs offer an acoustic basis to the largely subjective examinations of mouthpiece effects conducted in the past. The influence of vocal tract manipulations in the control and performance of woodwind instruments is investigated and compared with available theoretical analyses. Several extended performance techniques are discussed in terms of acoustic principles.

Discrete-time methods are presented for accurate time-domain implementation of single-reed woodwind instrument acoustic theory using digital waveguide techniques. Two methods for avoiding unstable digital waveguide scattering junction implementations, associated with taper rate discontinuities in conical air columns, are introduced. A digital waveguide woodwind tonehole model is presented which incorporates both shunt and series impedance parameters. Two-port and three-port scattering junction tonehole implementations are investigated and the results are compared with the acoustic literature. Several methods for modeling the single-reed excitation mechanism are discussed.

Expressive controls within the context of digital waveguide woodwind models are presented, as well as model extensions for the implementation of register holes and mouthpiece variations. Issues regarding the control and performance of real-time models are discussed. Techniques for verifying and calibrating the time-domain behavior of these models are investigated and a study is presented which seeks to identify an instrument's linear and nonlinear characteristics based on periodic prediction.

Acknowledgements

I am greatly indebted to the Department of Music and the Center for Computer Research in Music and Acoustics (CCRMA) for their financial support throughout my studies at Stanford University. CCRMA provided a wonderful interdisciplinary environment in which to pursue my interests. When I first sought out a means for combining my musical and technical interests, I had no clear vision of where this search would lead ... I'd like to thank John Chowning for encouraging me to apply to the Ph.D. program in Computer-Based Music Theory and Acoustics without a specific project in mind and the trust in my abilities he demonstrated by admitting me.

Along the way, Julius Smith and Perry Cook listened patiently to my questions and always had enlightened suggestions to make. Chris Chafe's enthusiasm, of course, was constant and greatly appreciated. Doug Keefe kindly allowed me to visit his laboratory in Seattle and graciously agreed to be a reader for this thesis, long before I even began writing it! The DSP group at CCRMA in general, and Tim Stilson, Bill Putnam, Scott Van Duyne, and Dave Berners in particular, provided much help during the course of this work. Fernando Lopez-Lezcano suffered through my seemingly endless computer glitches and troubles. My brother, John, did his part to help maintain my sanity through timely offers to visit his Lake Arrowhead cabin, as well as enticing ski trip proposals. Meanwhile, my family in Western New York just kept sending those packages of candy and encouraging cards. Despite the appearance that I would never finish this dissertation, their support never faltered ... many thanks to Jackie, Jerry, Sheri, Peter, Paul, Gail and Noni. My grandmother, Eleanor, has been and will always continue to serve as a source for encouragement in my life ... her picture sits prominently on top of my computer monitor. Finally, Melissa provided companionship, listened to my troubles, and helped take my mind off the work at hand, all of which played a large part in allowing me to enjoy this undertaking through to its completion. To all these people, I express my sincerest gratitude.

Preface

The study of musical instrument acoustic behavior is a relatively young science. Early work with direct application to woodwind instruments was conducted by Weber (1830), Helmholtz (1954), and Bouasse and Fouchée (1930). It is clear, however, that the instruments themselves “came first.” The art of instrument building was acquired principally through empirical means. Over the course of several centuries, knowledge was handed down from generation to generation and incremental gains were achieved. Most modern acoustic instruments reached their present form by the late nineteenth century and have undergone relatively little improvement since.

In the past, there was little association between the instrument builder and the physicist studying musical instrument acoustics. Several large instrument manufacturers, such as C. G. Conn Ltd., employed scientists for the purpose of improving their instrument designs, though their research was largely based on experimental measurements. Only in recent years has musical instrument *theoretical* acoustics reached an advanced enough level to offer potential rewards to the design process. One aim of this study is to demonstrate that these theoretical advances have necessitated close cooperation between scientists and professional instrument performers. That is, the theory has progressed to a point where subtle control issues incorporated by professional performers, but otherwise unknown to the physicist, can have great importance in confirming or refuting theoretical models. The insight of expert performers with reasonable grounding in acoustic fundamentals will play a significant role in refining current theory, as well as in further explorations into delicate issues of instrument behavior.

The primary objective of this study is to detail the implementation of the best available acoustic theory regarding single-reed woodwind instruments using digital waveguide techniques. Digital waveguide modeling is an efficient discrete-time method for time-domain simulation of one-dimensional wave propagation, which has gained increasing popularity in the field of musical acoustics research since the publication of McIntyre *et al.* (1983). Several studies have previously been conducted with regard to waveguide modeling of woodwind instruments (Hirschman, 1991; Välimäki, 1995). What distinguishes this work is its comprehensive scope, together with its foundation on the most current literature from the musical acoustics research community. Issues regarding conical air columns in general, and saxophones in particular, are analyzed in great detail. Instabilities associated with

discrete-time models of conical-section discontinuities are discussed and stable solutions are presented. A variety of extensions regarding toneholes, mouthpieces, and performance expression are introduced.

Chapter 1 of this study presents a detailed and comprehensive discussion of the acoustic behavior of single-reed woodwind instruments, as determined from available musical acoustics research literature. No new theory is presented in this chapter, though the discussion with regard to conical air columns is particularly comprehensive in comparison to most sources. Chapter 2 seeks to build on the material of the previous chapter and combine it with insights gained from professional performance expertise. Several issues relevant to instrument design and the performance community are analyzed in terms of acoustic principles. Chapter 3 shadows Chapter 1, detailing the implementation of the theory presented in the first chapter using digital waveguide techniques. A variety of improvements and/or extensions to current waveguide modeling theory are discussed. Chapter 4 offers further extensions to digital waveguide models of woodwind instruments which are inspired, in part, from the discussion of Chapter 2. Further, techniques for calibrating the models based on time-domain measurements are reviewed and an investigation of linear and nonlinear instrument behavior is presented.

Contents

Acknowledgements	iv
Preface	v
List of Figures	ix
List of Tables	xv
List of Symbols	xvi
1 Single-Reed Woodwind Acoustic Principles	1
1.1 Sound Propagation in Air	2
1.2 Lumped Acoustic Systems	5
1.3 Woodwind Instrument Bores	8
1.3.1 Cylindrical Bores	9
1.3.2 Conical Bores	15
1.3.3 Boundary Layer Effects	25
1.3.4 Time-Domain Descriptions	30
1.4 Sound Radiation	35
1.4.1 Non-Flaring Ends	36
1.4.2 Horns	38
1.4.3 Toneholes	40
1.5 The Nonlinear Excitation Mechanism	45
2 Acoustical Aspects of Woodwind Design & Performance	53
2.1 Woodwind Air Columns	54
2.1.1 Cylinders and Cones	55
2.1.2 Perturbations	63
2.1.3 The Saxophone's "Parabolic" Cone	68
2.2 Woodwind Toneholes	74
2.2.1 The Tonehole Lattice	75
2.2.2 The Single Tonehole	76
2.2.3 Register Holes	78
2.3 The Single-Reed Excitation Mechanism	80
2.3.1 Mouthpieces	80
2.3.2 Reeds	86
2.4 The Oral Cavity	88
2.5 Contemporary Performance Techniques	90
2.5.1 Multiphonics	91

2.5.2	The Saxophone's Altissimo Register	92
2.5.3	Additional Contemporary Techniques	93
3	Digital Waveguide Modeling of Single-Reed Woodwinds	95
3.1	Modeling Sound Propagation in One Dimension	96
3.2	Modeling Lumped Acoustic Systems	98
3.3	Modeling Woodwind Instrument Bores	101
3.3.1	Cylindrical Bores	102
3.3.2	Conical Bores	105
3.3.3	Diameter and Taper Discontinuities	111
3.3.4	Fractional Delay Lengths	124
3.3.5	Boundary-Layer Effects	128
3.4	Modeling Sound Radiation	131
3.4.1	Non-Flaring Ends	131
3.4.2	Horns	134
3.4.3	Toneholes	135
3.5	Modeling the Nonlinear Excitation Mechanism	147
3.5.1	The Pressure-Dependent Reflection Coefficient	149
3.5.2	The Reed-Reflection Polynomial	152
3.5.3	The Dynamic Woodwind Reed Model	153
3.5.4	Excitation Mechanisms Attached to Truncated Cones	157
4	Digital Waveguide Model Extensions and Calibration	159
4.1	Extensions to Digital Waveguide Models of Woodwinds	160
4.1.1	Register Holes	160
4.1.2	Mouthpiece Models	162
4.2	Performance Expression in Digital Waveguide Woodwind Models	166
4.2.1	Implementation Issues	166
4.2.2	Control Issues	170
4.2.3	Summary	172
4.3	Calibrating Digital Waveguide Woodwind Models	172
4.3.1	Measuring Woodwind Instrument Responses in the Time Domain	172
4.3.2	Periodic Prediction for the Determination of Linear and Nonlinear Instrument Behavior	173
5	Conclusions and Future Research	197
5.1	Summary and Conclusions	197
5.2	Suggestions for Future Research	198
A	The Surface Area of a Spherical Wave Front in a Cone	201
B	Saxophone Air Column Measurements	203
C	Experimental Equipment	204
D	MATLAB Code	205
D.1	openpipe.m	205
D.2	boundary.m	207
D.3	openhole.m	209
D.4	closhole.m	212
D.5	branch.m	215
D.6	clarinet.m	217

List of Figures

1.1	Wave-induced pressure variations on a cubic section of air.	3
1.2	Linear acoustic system block diagrams.	6
1.3	The Helmholtz resonator and its mechanical analog.	8
1.4	A cylindrical pipe in cylindrical polar coordinates.	9
1.5	A non-uniform bore (a) and its approximation in terms of cylindrical sections (b). . .	14
1.6	Theoretical input impedance magnitude, relative to Z_0 at $x = 0$, of the cylindrical section structure shown in Fig. 1.5(b).	16
1.7	A conical section in spherical coordinates.	16
1.8	A divergent conical section and its associated dimensional parameters.	20
1.9	A convergent conical section and its associated dimensional parameters.	21
1.10	Partial frequency ratios, relative to f_0 , for a closed-open conic frustum.	23
1.11	A non-uniform bore (a) and its approximation in terms of cylindrical and conical sections (b).	24
1.12	Theoretical input impedance magnitude, relative to $Z_0 = \rho c/S$ at $x = 0$, of the cylindrical and conic section structure shown in Fig. 1.11(b).	25
1.13	Phase velocity (v_p) normalized by c vs. frequency (top); Attenuation coefficient (α) vs. frequency (bottom).	28
1.14	Input impedance magnitude of an ideally terminated cylindrical bore with viscous and thermal losses (bore length = 0.3 meters, bore radius = 0.008 meters).	28
1.15	A general wind instrument represented by linear and nonlinear elements in a feedback loop.	30
1.16	Theoretical input impedance magnitude (top) and impulse response (bottom) of a cylindrical bore, normalized by the bore characteristic impedance.	31
1.17	Theoretical input impedance magnitude (top) and impulse response (bottom) of a conical bore, relative to $R_0 = \rho c/S(0)$ at the small end of the bore.	33
1.18	A conical frustum.	33
1.19	Reflectance magnitude and length correction (l/a) versus the frequency parameter ka for a flanged and unflanged circular pipe.	37
1.20	Cross-section of a horn and the displacement of a volume element within it.	39
1.21	Basic tonehole geometry.	41
1.22	T section transmission-line element representing the tonehole.	44
1.23	L section transmission-line element representing the tonehole.	44
1.24	Input impedance magnitude (top), relative to the main bore wave impedance Z_0 , and reflectance (bottom) for the written note G_4 on a simple six-hole flute, as described in Keefe (1990).	45
1.25	A single-reed woodwind mouthpiece.	46
1.26	The single-reed as a mechanical oscillator blown closed.	46

1.27	The volume flow and pressure relationships for a single-reed oral cavity/mouthpiece geometry.	47
1.28	Steady flow (u_{ro}) through a pressure controlled valve blown closed.	49
1.29	Dynamic flow through a pressure controlled valve blown closed for $p_{oc}/p_C = 0.4$. . .	50
2.1	Open-end radiation characteristics for an unflanged cylindrical pipe: (top) Load impedance magnitude relative to the wave impedance Z_0 ; (bottom) Tuning deviation in cents.	57
2.2	Thermoviscous effects for wave travel over two lengths of a cylindrical pipe of length 0.5 meters and radius 0.008 meters: (top) Attenuation characteristic; (bottom) Tuning deviation in cents.	57
2.3	Partial frequency ratios for a closed-open conic section versus β , the ratio of closed-to open-end radii. The frequencies are normalized by f_0 , the fundamental resonance for an open-open pipe of the same length as the frustum.	59
2.4	Partial frequency ratios for a closed-open conic section versus β , the ratio of closed-to open-end radii. The frequencies are normalized by f_c , the fundamental resonance for the same conic section complete to its apex.	60
2.5	Partial frequency ratios for a closed-open conic section versus frustum length, for a cone of half angle 2° and small-end radius of 0.005 meters. The partial frequencies are normalized by f_0 , the fundamental resonance for an open-open pipe of the same length as the frustum.	61
2.6	The input impedance magnitude, relative to $R_0 = \rho c/S$ at its input end, of a conical frustum of length 0.5 meters, small-end radius 0.005 meters, and half angle of 2° . . .	62
2.7	Exponential horn profiles for flare parameters of $m = 2$ (—) and $m = 3$ (---).	65
2.8	Partial frequency ratios, relative to the fundamental resonance, for exponential horns defined by flare parameters of $m = 2$ (—) and $m = 3$ (---).	65
2.9	Partial frequency ratios, relative to the fundamental resonance of an open-open conic frustum of the same length, for exponential horns defined by the flare parameters $m = 2$ (—) and $m = 3$ (---).	66
2.10	The profile of an alto saxophone built by Adolphe Sax, in exaggerated proportions [after (Kool, 1987)].	69
2.11	Quadratic surfaces: (a) Circular cone; (b) Elliptic cone; (c) Hyperboloid of one sheet; (d) Elliptic paraboloid.	70
2.12	Various views of a "Parabolic cone."	71
2.13	Profile of an alto saxophone bore, up to its lower bow. The bore section between the neckpipe and lower bow is represented by a conical frustum (—) and an exponential horn (---).	73
2.14	Partial frequency ratios, relative to the fundamental resonance of an open-open conic section of the same length, of a combined cone/exponential horn structure (—) and a closed-open conical frustum (---). The dotted lines indicate exact integer multiple relationships to the first closed-open conical frustum resonance.	73
2.15	An early saxophone mouthpiece design.	83
2.16	Approximate saxophone mouthpiece structures: (top) Wide chamber design; (bottom) Narrow chamber design.	84
2.17	Theoretical mouthpiece and air column structure input impedances, relative to $R_0 = \rho c/S$ at the input of the structure: (top) Wide chamber design; (bottom) Narrow chamber design.	85
2.18	Normalized partial frequency ratios for the theoretical mouthpiece and air column structures vs. air column length: (—) Wide chamber design; (---) Narrow chamber design.	85
2.19	A <i>Bb</i> clarinet multiphonics fingering and the corresponding written notes it produces. . .	91

3.1	Digital waveguide implementation of ideal, lossless plane-wave propagation in air [after (Smith, 1996a)]. The z^{-1} units represent one-sample delays.	97
3.2	Lumped impedance block diagrams [after (Smith, 1996a)]: (a) Impedance representation; (b) Digital waveguide representation.	98
3.3	Digital waveguide implementation of ideal, lossless plane-wave propagation in a cylindrical tube. The z^{-1} units represent one-sample delays.	102
3.4	Digital waveguide implementation of plane-wave propagation in a cylindrical tube, neglecting viscothermal losses.	103
3.5	Simplified digital waveguide implementation of plane-wave propagation in a cylindrical tube using a single delay line and neglecting viscothermal losses. The pressure observation point is constrained to the entryway of the bore.	104
3.6	Digital waveguide model of a closed-open cylindrical bore.	104
3.7	Digital waveguide implementation of ideal, lossless spherical-wave propagation in a conical tube [after (Smith, 1996a)].	106
3.8	Divergent conical section rigidly terminated by a spherical cap at x_0	107
3.9	The conical truncation reflectance: (top) Continuous-time and discrete-time filter phase responses; (bottom) Digital allpass filter coefficient value versus x_0	108
3.10	Digital waveguide implementation of a closed-open truncated conical section excited at $x = x_0$	109
3.11	Impulse response of conical bore closed at $x = x_0$ and open at $x = L$. Open-end radiation is approximated by a 2nd-order discrete-time filter and viscothermal losses are ignored.	110
3.12	Equivalent circuit of a conical waveguide [after Benade (1988)].	110
3.13	Junction of two cylindrical tube sections.	111
3.14	(a) The Kelly-Lochbaum scattering junction for diameter discontinuities in cylindrical bores; (b) The one-multiply scattering junction [after (Markel and Gray, 1976)].	113
3.15	The digital waveguide model of two discontinuous cylindrical sections.	113
3.16	(a) A non-uniform bore and (b) its approximation in terms of cylindrical sections.	114
3.17	Input impedance magnitude, normalized by Z_0 at $x = 0$, calculated using a digital waveguide model of the cylindrical section structure shown in Fig. 3.16(b).	114
3.18	Junction of two conical tube sections.	115
3.19	(a) The scattering junction for diameter and taper discontinuities in conical bores; (b) The one-multiply scattering junction for a taper discontinuity only [after (Välimäki, 1995)].	116
3.20	(a) Cylinder-diverging cone junction; (b) Cylinder-converging cone junction. All lengths are in millimeters.	118
3.21	(top) Discrete-time reflection function $r(n)$ and (bottom) discrete-time impulse response, normalized by Z_0 of the cylinder, calculated using a digital waveguide model of the cylinder-diverging cone structure shown in Fig. 3.20(a).	118
3.22	Discrete-time reflection function $r(n)$ calculated using a digital waveguide model of the cylinder-converging cone structure shown in Fig. 3.20(b).	119
3.23	(a) A non-uniform bore and (b) its approximation in terms of conical and cylindrical sections.	120
3.24	Input impedance magnitude, normalized by Z_0 at $x = 0$, calculated using a digital waveguide model of the conical and cylindrical section structure shown in Fig. 3.23(b).	121
3.25	(a) A bore profile which results in an unstable digital waveguide filter implementation and (b) a lumped-section model which allows a stable digital waveguide filter implementation.	121
3.26	Input impedance magnitude, normalized by $R_0 = \rho c/S(x)$ at the bore input, calculated using (top) transmission matrices and (bottom) a lumped section digital waveguide model as illustrated in Fig. 3.25(b).	123

3.27	Impulse response, normalized by $R_0 = \rho c/S(x)$ at the bore input, calculated using (top) transmission matrices and (bottom) a lumped section digital waveguide model as illustrated in Fig. 3.25(b).	124
3.28	The digital waveguide lumped section scattering junction with extracted linear phase terms and modified reflectance and transmittance filters.	124
3.29	Frequency response and phase delay of first-order, Lagrange interpolation filters for 11 delay values in the range $0 \leq D \leq 1$ [after (Jaffe and Smith, 1983)].	125
3.30	Frequency response and phase delay of third-order, Lagrange interpolation filters for 11 delay values in the range $1 \leq D \leq 2$ [after (Jaffe and Smith, 1983)].	126
3.31	Phase delay of first-order, allpass interpolation filters [after (Jaffe and Smith, 1983)].	127
3.32	Impulse response of digital waveguide system using (top) first-order Lagrange interpolation and (bottom) first-order allpass interpolation.	128
3.33	Frequency response of the filter $H(z)$: Magnitude (top); Phase delay (bottom).	129
3.34	Digital waveguide implementation of lossy plane-wave propagation in air [after (Smith, 1996a)]. The unit delays have been incorporated into $H(z)$	130
3.35	Commutated thermoviscous losses in a digital waveguide cylindrical air column implementation.	130
3.36	Continuous-time filter $H_b^{76}(s)$ and 5th-order discrete-time filter $H_b^{76}(z)$ responses.	131
3.37	Continuous-time and digital filter magnitude and phase characteristics for the Levine and Schwinger reflectance in a cylindrical duct of radius 0.008 meters.	132
3.38	Sound radiation filter implementations in a digital waveguide cylindrical duct model: (top) Complementary transmittance filter [after (Smith, 1986)]; (bottom) Residual sound output.	133
3.39	Levine and Schwinger unflanged open end reflectance magnitude and length correction extensions.	134
3.40	T section transmission line element representing the tonehole.	135
3.41	Tonehole two-port scattering junction.	137
3.42	Two-port tonehole junction closed-hole reflectance, derived from Keefe (1981) shunt and series impedance parameters [(—) continuous-time response; (—) discrete-time filter response]. (top) Reflectance magnitude; (bottom) Reflectance phase.	138
3.43	Two-port tonehole junction open-hole reflectance, derived from Keefe (1981) shunt and series impedance parameters [(—) continuous-time response; (—) discrete-time filter response]. (top) Reflectance magnitude; (bottom) Reflectance phase.	138
3.44	Reflection functions for note B (all six finger holes open) on a simple flute [see (Keefe, 1990)]. (top) Transmission-line calculation; (bottom) Digital waveguide implementation.	139
3.45	Reflection functions for note G (three finger holes closed, three finger holes open) on a simple flute [see (Keefe, 1990)]. (top) Transmission-line calculation; (bottom) Digital waveguide implementation.	140
3.46	Reflection functions for note D (all six finger holes closed) on a simple flute [see (Keefe, 1990)]. (top) Transmission-line calculation; (bottom) Digital waveguide implementation.	140
3.47	The three-port tonehole junction where a side branch is connected to a uniform cylindrical tube [after (Välimäki, 1995)].	141
3.48	Tonehole three-port scattering junction implementation in one-multiply form.	143
3.49	Reflection functions for notes B (top) and G (bottom) on a six-hole flute, determined using a digital waveguide three-port tonehole junction implementation and an inertance approximation for the tonehole driving-point impedance.	144
3.50	Continuous-time magnitude responses for two open-tonehole reflectance models.	145

3.51	Reflection functions for notes <i>B</i> (top) and <i>G</i> (bottom) on a six-hole flute, determined using a digital waveguide three-port tonehole junction implementation and an explicit open cylinder approximation for the tonehole driving-point impedance.	145
3.52	The volume flow and pressure relationships for a single-reed oral cavity/mouthpiece geometry.	147
3.53	Dynamic flow through a pressure controlled valve blown closed for $p_{oc}/p_C = 0.4$. . .	148
3.54	Pressure-dependent reflection coefficient curves versus reed stiffness (top) [reed resonances of 2500 Hz (—), 3000 Hz (---), 3500 Hz (··)] and equilibrium reed tip opening (bottom) [$y_0 = 1.5$ mm (—), 1.0 mm (---), 0.5 mm (··)].	150
3.55	An example reflection coefficient table $\hat{r}(p_\Delta^+)$ (top), and the corresponding reed volume flow $\hat{u}_r(p_\Delta^+)$ (bottom).	152
3.56	The reed/bore scattering junction.	152
3.57	(a) The pressure-dependent reflection coefficient digital waveguide implementation; (b) The reed-reflection polynomial digital waveguide implementation.	153
3.58	The single-reed as a mechanical oscillator blown closed.	153
3.59	Second-order reed filter $H_r(z)$	155
3.60	Oscillation onsets for digital waveguide clarinet implementations: (top) Pressure-dependent reflection coefficient; (middle) Reed-reflection polynomial; (bottom) Dynamic reed model.	157
4.1	A cylindrical and conical section approximation to a narrow chamber saxophone mouthpiece structure.	162
4.2	(a) A saxophone mouthpiece and air column profile approximated by cylindrical and conical sections and (b) a lumped-section model which allows a stable digital waveguide filter implementation.	163
4.3	Continuous- and discrete-time frequency responses for the forward reflectance \mathcal{R}^+ determined by lumping the three left-most sections of the mouthpiece shape of Fig. 4.1.	164
4.4	Forward reflectance $\mathcal{R}^+(z)$ discrete-time filter approximation zero and pole locations in the z -plane.	165
4.5	Impulse response, normalized by $Z_0 = \rho c/S$ at the bore input, calculated using (top) transmission matrices and (bottom) a lumped section digital waveguide model as illustrated in Fig. 4.2(b).	165
4.6	A digital waveguide system for implementing tonguing variation.	167
4.7	A digital waveguide system for implementing breath pressure modulation.	168
4.8	An efficient digital waveguide system for implementing multiphonic tones.	169
4.9	The experimental setup of Agulló <i>et al.</i> (1995).	173
4.10	A general wind instrument represented by linear and nonlinear elements in a feedback loop.	173
4.11	A general wind instrument represented by linear, nonlinear, and delay elements in a feedback loop.	174
4.12	An experimental “pseudo-clarinet” instrument.	175
4.13	Steady-state waveform measured inside the “pseudo-clarinet” instrument.	175
4.14	A general wind instrument air column represented by delay and lumped linear elements in a feedback loop.	176
4.15	An adaptive linear periodic forward predictor.	177
4.16	The assumed wind instrument model used for the nonlinear prediction experiment.	177
4.17	An adaptive nonlinear periodic forward predictor.	178
4.18	An example piecewise reflection coefficient table and its polynomial approximation (top), and the corresponding general nonlinear function responses (bottom).	183
4.19	Linear element experiment setup.	184
4.20	Recorded response of the PVC tube.	185

4.21	Single pulse response in the PVC tube.	186
4.22	Pulse response in the PVC tube via a palm-strike.	186
4.23	Measured input signal: (top) Time domain; (bottom) Frequency domain.	187
4.24	Frequency Response Magnitude of Linear Weights.	188
4.25	Direct palm strike signal: (top) Time domain; (bottom) Frequency domain.	188
4.26	Frequency response magnitude of the predicted linear weights using the palm strike excitation.	189
4.27	Nonlinear element experiment setup.	190
4.28	Internal pressure signal in PVC tube under normal blowing conditions.	190
4.29	Nonlinear polynomial function extracted from a synthesized sound.	191
4.30	Nonlinear reflection coefficient, as determined using nonlinear predictor weights which were extracted from a synthesized sound.	191
4.31	Nonlinear polynomial functions extracted from the internal pressure signal measured in the experimental instrument.	192
4.32	Nonlinear reflection coefficient, as determined using nonlinear predictor weights which were extracted from the internal pressure signal measured in the experimental instru- ment.	193
4.33	Histograms of the transient (top) and steady-state (bottom) portions of the recorded signal.	194
4.34	A revised wind instrument model that might better correspond to the experimental instrument.	195
A.1	A conical section in spherical coordinates.	202

List of Tables

1.1	Hypothetical dimensions (in meters) of the bore shape shown in Fig. 1.5(a) and its approximation by cylindrical sections in Fig. 1.5(b).	15
2.1	The first four partial frequency ratios, relative to the first resonance frequency, for conical frusta defined by β equal to 0.15 and 0.24.	61
B.1	Air column measurements and estimated truncation ratios (β) for Selmer and Schenke-laars alto saxophones.	203

List of Symbols

These symbols are used consistently throughout this study for the following representations:

ρ	density of air
c	speed of sound in air
s	Laplace transform frequency variable
Ω	continuous-time frequency variable
ω	discrete-time frequency variable ($-\pi \leq \omega \leq \pi$)
f	frequency variable
f_s	discrete-time sampling frequency
j	imaginary unit ($j = \sqrt{-1}$)
k	wavenumber ($k = \Omega/c$)
t	continuous time variable
n	discrete time index
z	z -transform variable
S	surface area
Z_0	characteristic or wave impedance
Y_0	characteristic or wave admittance
u or U	volume velocity within an acoustic structure
p or P	sound pressure
\mathcal{R}	frequency-dependent reflection coefficient or reflectance
\mathcal{T}	frequency-dependent transmission coefficient or transmittance

Chapter 1

Single-Reed Woodwind Acoustic Principles

All musical instruments are united by the fact that each produces vibrations of air pressure or sounds. In each case, a resonator is forced to oscillate by a particular means of excitation and the resulting vibrations are transferred to the surrounding air in a suitable manner. Instruments which produce periodic sounds can be grouped by the particular medium in which the vibrations occur. Only uniform tubes of air and stretched strings have been found to adequately maintain one-dimensional oscillations in a quasi-periodic manner. In general, instruments which incorporate stretched strings are excited by impulsive and “stick-slip” mechanisms, while those using uniform tubes are excited by “blowing” mechanisms. This study is primarily concerned with single-reed woodwind instruments such as clarinets and saxophones, as well as less common folk instruments such as the tarogato and tenora. All common woodwind instruments have a series of finger holes along the length of their air columns through which sound radiation and pitch variation are achieved. The single-reed excitation mechanism is particular to a limited subset of woodwind instruments, though its operation is similar in many ways to that of lip-driven brass instruments and to a lesser extent, the human voice. In the case of the human voice, however, the presence of the vocal tract is not necessary for the production of periodic vibrations of the vocal folds.

Because of their similarities, the operation of all musical instruments can be analyzed in terms of three principal components: an excitation mechanism, a resonator, and a radiating element. For single-reed woodwind instruments, the performer, reed, and mouthpiece combination produces the excitation, the air column is the resonator, and sound radiation is accomplished via the tonehole lattice and air-column open end. Adolphe Sax’s invention of the saxophone around 1840 can be viewed as a combination of the clarinet’s excitation mechanism and the oboe’s resonator and radiating components. In this way, Sax was experimenting with acoustical building blocks, though

considerable craft was necessary to make them function properly as a whole.

This chapter reviews the current understanding of woodwind instrument acoustic principles. Most of the information presented here has previously been covered in acoustic texts or journal publications. Issues relating to the conical bore are discussed in this study with as much detail as the more common cylindrical bore and to a greater extent than in most sources currently available. The material of this chapter is presented as a foundation for the analyses of the subsequent chapters. This chapter deals exclusively with continuous-time representations, for which the frequency variable Ω is used. Discrete-time frequency will be indicated with the variable ω . Frequency-dependent variables are represented throughout by upper-case symbols, while time-domain expressions are represented by the corresponding lower-case symbols.

1.1 Sound Propagation in Air

Many musical instruments, such as those of the string and percussion families, produce sounds via the coupling of mechanical vibrations to the surrounding air. In wind instruments, however, sound generation is directly initiated and maintained in the air medium. The propagation of sound in air thus plays a fundamental role in the study of woodwind acoustics. Air has both mass and elasticity and these properties allow it to store kinetic and potential energy, respectively. The propagation of air pressure variations, or sound waves, is possible through the alternating transfer of energy between its kinetic and potential states. Such motion is primarily longitudinal because gases, such as air, do not support shear forces to first approximation.[†]

Figure 1.1 illustrates a cubic section of air exposed to wave-induced pressure variations on all six sides. These forces produce a volume change dQ in the gas with respect to its unperturbed volume Q , called *dilation* or *volume strain*, which is given in Cartesian coordinates by

$$\epsilon = \frac{dQ}{Q} = \frac{\partial \xi}{\partial x} + \frac{\partial \eta}{\partial y} + \frac{\partial \zeta}{\partial z} = \nabla \cdot \boldsymbol{\varrho}, \quad (1.1)$$

where $\boldsymbol{\varrho}(\mathbf{r}, t)$ is a vector function of air displacement. The dilation, in turn, produces an elastic restoring force due to the compressibility of the gas. The relationship between applied pressure and dilation may be estimated using Hooke's law for fluids. For $\epsilon \ll 1$, the dilation and associated incremental pressure are linearly related through the elastic bulk modulus B as

$$p = -B\epsilon = -B\nabla \cdot \boldsymbol{\varrho}. \quad (1.2)$$

This relationship is the acoustic counterpart to Hooke's law for mechanical springs. The negative sign in Eq. (1.2) results from the fact that positive pressure produces a negative dilation.

[†]Air can support shear forces via viscosity, but in the frequency range of interest to this study, the most significant influences of this viscosity can be localized within a boundary layer between the air and the walls of a wind-instrument air column.

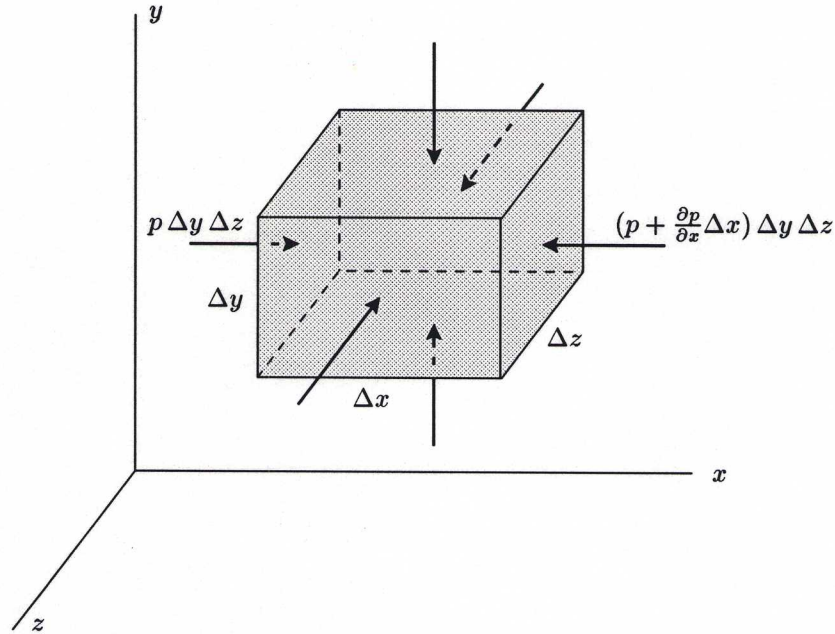


Fig. 1.1. Wave-induced pressure variations on a cubic section of air.

The kinetic energy component of air is manifest in the motion of the gas in Fig. 1.1 and its associated inertia. The net force in the positive x direction is given by $-(\partial p / \partial x) \Delta x \Delta y \Delta z$. Summing the forces along each of the coordinate axes, the net vector force on the cubical element is

$$\Delta \mathbf{F} = -\nabla p \Delta x \Delta y \Delta z, \quad (1.3)$$

where

$$\nabla p \equiv \mathbf{i} \frac{\partial p}{\partial x} + \mathbf{j} \frac{\partial p}{\partial y} + \mathbf{k} \frac{\partial p}{\partial z} \quad (1.4)$$

is the *pressure gradient*. The mass of the fluid is $\rho \Delta x \Delta y \Delta z$, where ρ is the fluid density, and its vector acceleration is $\partial^2 \mathbf{g} / \partial t^2$. Newton's second law, normalized by the cubic volume $\Delta x \Delta y \Delta z$, results in the relationship

$$-\nabla p = \rho \frac{\partial^2 \mathbf{g}}{\partial t^2}. \quad (1.5)$$

Equations (1.2) and (1.5) can be combined to produce the three-dimensional scalar wave equation

$$\nabla^2 p = \frac{1}{c^2} \frac{\partial^2 p}{\partial t^2}, \quad (1.6)$$

where $c = (B/\rho)^{1/2}$ is the wave velocity. The left side of Eq. (1.6) is the *Laplacian* of the pressure p , which can subsequently be expanded in the desired coordinate system for any given problem. Assuming sinusoidal wave components with time dependence $e^{j\Omega t}$, Eq. (1.6) simplifies to the time-independent wave equation (or scalar *Helmholtz equation*)

$$\nabla^2 P + k^2 P = 0, \quad (1.7)$$

where P is the spatial part of the sinusoidal pressure wave and $k = \Omega/c^\dagger$ is the wave number (Elmore and Heald, 1985, p. 138). In deriving the linear wave equation, any variation in the fluid density ρ with respect to position has been ignored. For sound propagation in air, this approximation is normally valid. The use of Hooke's law assumes small particle displacement, which is accurate for most applications in musical acoustics. However, there are instances in which this approximation may break down, such as in brass instruments at *forte* dynamic levels.

Sound waves are often adequately represented by plane wave fronts normal to their direction of travel. For plane-wave propagation along the x -axis only, Eq. (1.6) reduces to

$$\frac{\partial^2 p}{\partial x^2} = \frac{1}{c^2} \frac{\partial^2 p}{\partial t^2}. \quad (1.8)$$

Solutions to this equation describe the pressure evolution of one-dimensional plane waves of sound propagating in air. By assuming sinusoidal time dependence, a general frequency-domain solution to Eq. (1.8) is

$$P(x, t) = [Ae^{-jkx} + Be^{jkx}] e^{j\Omega t}, \quad (1.9)$$

where A and B are complex amplitudes for wave components traveling to the right and left, respectively. For this solution, the particle velocity can be found with the aid of Eq. (1.5) as

$$V(x, t) = \frac{\partial \varrho}{\partial t} = \frac{1}{\rho c} [Ae^{-jkx} - Be^{jkx}] e^{j\Omega t}. \quad (1.10)$$

The ratio of sinusoidal pressure to sinusoidal particle velocity for wave components traveling to the right only ($B = 0$),

$$Z = \frac{P(x, t)}{V(x, t)} = \rho c, \quad (1.11)$$

is called the *wave impedance* or *characteristic impedance*. The wave impedance is defined in terms of frequency-domain quantities, namely the ratio of pressure to particle velocity at a particular frequency. For plane-wave propagation in open air, the wave impedance is purely real and frequency independent. Further, the wave impedance for plane waves is independent of direction.

Sound waves generated by a point source spread out in all directions in a nearly spherical manner. For one-dimensional spherical-wave propagation, Eq. (1.6) reduces to

$$\frac{1}{x^2} \frac{\partial}{\partial x} \left(x^2 \frac{\partial p}{\partial x} \right) = \frac{1}{c^2} \frac{\partial^2 p}{\partial t^2}, \quad (1.12)$$

where x measures the radial distance from the point source. A general frequency-domain solution to Eq. (1.12) which assumes sinusoidal time dependence is given by

$$P(x, t) = \left[\frac{A}{x} e^{-jkx} + \frac{B}{x} e^{jkx} \right] e^{j\Omega t}, \quad (1.13)$$

[†]The symbol Ω will be used throughout this study to represent continuous-time frequency. Discrete-time frequency will be represented by the symbol ω .

where A and B are complex amplitudes for outgoing and incoming wave components, respectively. For this solution, the particle velocity can be found with the aid of Eq. (1.5) as

$$V(x, t) = \frac{\partial g}{\partial t} = \frac{1}{\rho c} \left[\frac{A}{x} \left(1 + \frac{1}{jkx} \right) e^{-jkx} - \frac{B}{x} \left(1 - \frac{1}{jkx} \right) e^{jkx} \right] e^{j\Omega t}. \quad (1.14)$$

The wave impedance for spherical waves is dependent on both frequency and direction and varies with position x . For outgoing wave components ($B = 0$),

$$Z(x) = \frac{P(x, t)}{V(x, t)} = \rho c \left(\frac{jkx}{1 + jkx} \right), \quad (1.15)$$

while the incoming wave impedance is given by $Z^*(x)$ or the complex conjugate of the outgoing wave impedance. For $kx \gg 1$ or when x is much greater than one wavelength, these impedances reduce to ρc , which is the wave impedance of plane waves of sound. In effect, one-dimensional spherical wave components far from their source can be approximated by plane waves of sound. Near the source, however, $kx \ll 1$ and pressure and particle velocity wave components grow increasingly out of phase.

1.2 Lumped Acoustic Systems

An acoustic system in which sound wave propagation is determined by solutions to the wave equation is referred to as a *distributed* system. In such a structure, system parameters, such as air mass and elasticity, are considered evenly distributed throughout its volume and wave variables are given by functions of both space and time. It is often convenient or necessary to determine a lumped input-output response of sound wave propagation through an acoustic system without knowing the exact behavior everywhere within it. This is the case when wave propagation within an acoustic structure is extremely complex and inadequately represented by solutions to the one-dimensional wave equation. A *lumped acoustic response* may be experimentally measured which describes the total system output for a known input but which provides no information regarding wave propagation at points within the system. A lumped system description is also convenient when analyzing the behavior of large wavelength (or low-frequency) sound waves within small structures. In the *low-frequency limit*, an acoustic system can be characterized in terms of fundamental acoustic components analogous to masses, springs, and dampers in mechanical system analysis or inductors, capacitors, and resistors in electrical circuit analysis. The remainder of this section explores lumped acoustic systems in the low-frequency limit. The determination of lumped system responses by experimental measurement will not be considered in this study.

Assuming an acoustic system is well approximated by linear theory, its frequency-domain response can be given by an *admittance* Γ , or the velocity response of the system to an applied pressure input, as represented in Fig. 1.2a. Velocity can take the form of either *particle velocity* V (in meters per second) for systems in open air or *volume velocity* U (in meters cubed per second) for enclosed

structures. Inversely, a system can be characterized by its pressure response to an applied velocity input, or its *impedance*, as represented in Fig. 1.2b. The impedance or admittance of a system is a frequency-domain description, indicating the relationship between pressure and velocity at a particular frequency.

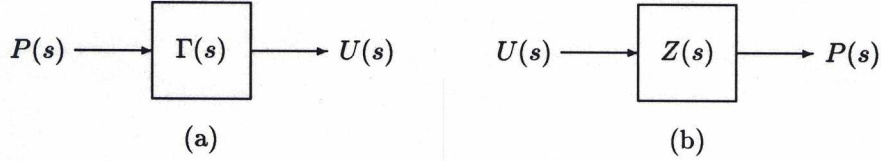


Fig. 1.2. Linear acoustic system block diagrams.

The fundamental wavelength of sound produced by a musical instrument is generally much larger than the dimensions of certain of its component parts, such as toneholes and mouthpieces. The behavior of large wavelength sound waves within small structures is generally well approximated by assuming uniform pressure throughout the volume of interest (Fletcher and Rossing, 1991). In the low-frequency limit, the air within a short, open tube will be displaced by equal amounts at both its ends when subjected to an external pressure at one end only. If the length and cross section of the tube are given by L and S , respectively, then the enclosed air has a mass of ρLS , where ρ is the density of air. The frequency-domain response of this system is analyzed by assuming an applied sinusoidal pressure P of frequency Ω . Using Newton's second law (force = mass \times acceleration),

$$PS = \rho LS \frac{dV}{dt} = \rho L \frac{dU}{dt}, \quad (1.16)$$

where $U = SV$ is the acoustic volume velocity of the air mass. The volume velocity response to the applied pressure will also vary sinusoidally with frequency Ω , so that Eq. (1.16) reduces to

$$P(\Omega) = \frac{j\Omega\rho L}{S}U(\Omega). \quad (1.17)$$

The acoustic impedance of the tube, expressed in terms of the Laplace transform with frequency variable $s = \sigma + j\Omega$, is completely reactive ($\sigma = 0$) and is given by

$$Z(s) = \frac{P(s)}{U(s)} = \left(\frac{\rho L}{S} \right) s \quad (1.18)$$

for zero initial volume velocity. In the low-frequency limit, the open tube is called an acoustic inductance or an *inertance* and it has a direct analogy to the inductance in electrical circuit analysis or the mass in mechanical system analysis. The impedance of a mechanical mass is equal to ms , and thus the open tube has an equivalent acoustic "mass" equal to $\rho L/S$. An inertance is also sometimes referred to as a *constriction* (Morse, 1981, p. 234).

The acoustic analog of the electrical capacitor or the mechanical spring is a cavity, or a *tank* (Morse, 1981, p. 234). In the low-frequency limit, an applied external pressure will compress the

enclosed air, which then acts like a spring because of its elasticity. Assuming a cavity volume Q , an increase in applied pressure P will decrease this volume by an amount $-dQ$. As discussed in the previous section, the ratio of change in volume to original volume is called volume strain or dilation and is given by $\epsilon = -dQ/Q$. For small dilation, Hooke's law for fluids provides an accurate approximation to the relationship between the increase in applied pressure, the resulting strain, and the bulk modulus B ,

$$P = -B \frac{dQ}{Q} = -B\epsilon. \quad (1.19)$$

The bulk modulus for sound waves is nearly *adiabatic*[†] and is expressed in terms of the density of air ρ and the speed of sound c as $B_{ad} = \rho c^2$. Using Eq. (1.19) and writing the change in cavity volume, $-dQ$, in terms of the sinusoidal volume velocity U as

$$-dQ = \int U dt = \frac{U}{j\Omega}, \quad (1.20)$$

the acoustic impedance of the cavity is given in terms of the Laplace transform by

$$Z(s) = \left(\frac{\rho c^2}{Q} \right) \frac{1}{s}. \quad (1.21)$$

The impedance of a mechanical spring is equal to k/s , so by analogy the acoustic cavity has an equivalent "spring constant" equal to $\rho c^2/Q$.

There are instances when losses within an acoustic system can be approximated by a real-valued, frequency-independent resistive component with impedance

$$Z(s) = R. \quad (1.22)$$

The volume velocity and applied pressure are in phase, analogous to an electrical resistor or a mechanical dashpot. Viscous and thermal losses in short acoustic tubes may be characterized in this way, though such losses in larger structures are most accurately represented by complex, frequency-dependent parameters.

The *Helmholtz resonator* can be easily analyzed in the low-frequency limit in terms of an acoustic inertance and cavity. The enclosed volume of air, or cavity, is coupled to the outside air via the short tube. If excited at the open end of the short tube, this structure is acoustically equivalent to the mechanical mass-spring system shown in Fig. 1.3. A volume velocity impulse initiated by an external pressure source will flow through the short tube and the cavity in series, so that the resulting lumped impedance of the resonator is given by the sum of the short tube and cavity impedances,

$$Z = \left(\frac{\rho L}{S} \right) s + \left(\frac{\rho c^2}{Q} \right) \frac{1}{s}. \quad (1.23)$$

[†]An adiabatic process is one in which no heat flows into or out of the system. Under normal circumstances, a gas which is compressed will incur a temperature increase unless heat can flow out of it. In sound waves, the thermal conductivity of air is low and the distance between adjacent compressions and expansions is relatively large. Further, the rate or frequency of these alternating compressions and expansions is high. Therefore, this process is nearly adiabatic.

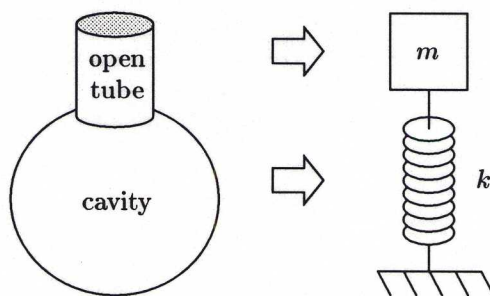


Fig. 1.3. The Helmholtz resonator and its mechanical analog.

The resonance frequency of this system occurs at the impedance minimum and is easily found to be $\Omega_0 = c(S/LQ)$. A musical instrument which operates under the same principles as the Helmholtz resonator is the ocarina.

1.3 Woodwind Instrument Bores

The resonator of a musical instrument serves to emphasize certain desirable frequencies of sound, corresponding to its normal modes. A wind instrument bore is a subclass of general resonators and functions to encourage the production of sustained, quasi-periodic oscillations of sound within a feedback system. In order that the bore be musically useful, it is necessary that it support sound production over a wide range of frequencies. This is accomplished by allowing the tube length to be variable while also encouraging sound production based on higher normal modes. Acoustically speaking, two principle requirements need be met for a wind instrument resonator to be musically useful. It is first necessary that the ratio between the first and successively higher normal modes be independent of horn length. In this way, the perceived *timbre* or spectral content of sounds will remain similar over the full range of the bore. Further, this permits the production of sounds based on second and third resonances, or *overblowing*, over the full length of the tube. Secondly, a stable regenerative process associated with the nonlinear excitation mechanism in wind instruments is favored when the successive partial frequencies, particularly the first few, are related to the fundamental frequency by integer multiple ratios (Benade, 1959, 1977).

In woodwind instrument bores, the primary mode of wave propagation is along the central axis of the tube. Equations describing this wave motion are possible if a coordinate system can be found in which one coordinate surface coincides with the walls of the given pipe and in which the Helmholtz equation, Eq. (1.7), is separable (Fletcher and Rossing, 1991, p. 187). There are 11 coordinate systems in which the Helmholtz equation is separable. One-parameter waves, however, are possible only in rectangular, circular cylindrical, and spherical coordinates, which correspond to pipes of uniform cross-section and conical horns, respectively (Putland, 1993). Wave propagation in the other separable coordinate systems must be comprised of an admixture of orthogonal modes

and be a function of more than one coordinate. In order to perfectly meet the requirements of a musically useful wind instrument bore as discussed above, one-parameter wave propagation is necessary. Thus, cylindrical pipes and conical horns are the two obvious choices for wind instrument bores. All woodwind air columns are based on shapes roughly corresponding to cylinders or cones. Further, accurate representations of wave propagation in actual, imperfectly shaped bores can be well approximated in terms of cylindrical and conic sections.

The three-dimensional wave equation derived in Section 1.1 applies to the propagation of sound waves in any homogeneous, isotropic fluid and in any coordinate system. In this section, propagation within cylindrical and conical bores is explored by solving the associated Helmholtz equation in circular cylindrical and spherical coordinates and applying the boundary conditions appropriate for each of these structures. The presence of a rigid tube implies the fundamental limitation that the acoustic volume flow normal to the walls be zero at the boundary. This condition is usually expressed in terms of the pressure wave component p as $\mathbf{n} \cdot \nabla p = 0$ on the boundaries, where \mathbf{n} is the unit vector normal to the boundary.

1.3.1 Cylindrical Bores

In the woodwind family, clarinets and flutes are the most prominent members built with cylindrical bores. Plane waves of sound can theoretically propagate without reflection or loss along the principal axis of an infinite cylindrical pipe, assuming the walls are rigid, perfectly smooth, and thermally insulating. Longitudinal wave motion is also possible in planes orthogonal to the principal axis, though it will be seen that these transverse modes are only weakly excited in musical instrument bores of small diameter. This section presents the basic properties of cylindrical tubes, without accounting for radiation at open ends, the effects of toneholes, or viscothermal losses.

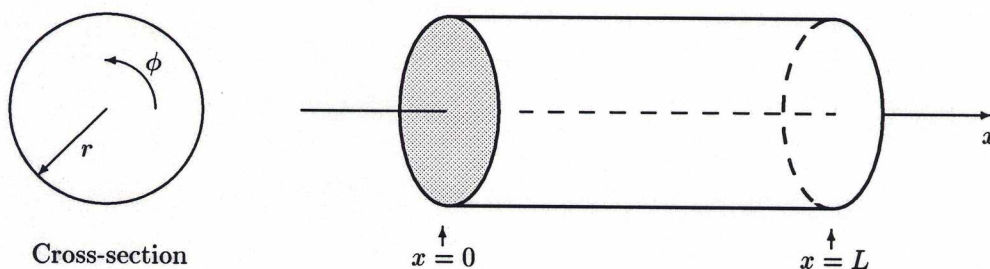


Fig. 1.4. A cylindrical pipe in cylindrical polar coordinates.

A short section of cylindrical pipe in cylindrical polar coordinates (r, ϕ, x) is depicted in Fig. 1.4. The wave equation in this geometric coordinate system is

$$\frac{1}{r} \frac{\partial}{\partial r} \left(r \frac{\partial p}{\partial r} \right) + \frac{1}{r^2} \frac{\partial^2 p}{\partial \phi^2} + \frac{\partial^2 p}{\partial x^2} = \frac{1}{c^2} \frac{\partial^2 p}{\partial t^2}. \quad (1.24)$$

The Helmholtz equation is separable in circular cylindrical coordinates, resulting in the following differential equations

$$\frac{\partial^2 \Phi}{\partial \phi^2} + m^2 \Phi = 0, \quad (1.25a)$$

$$r \frac{d}{dr} \left(r \frac{dR}{dr} \right) + (\beta^2 r^2 - m^2) R = 0, \quad (1.25b)$$

$$\frac{d^2 X}{dx^2} + (k^2 - \beta^2) X = 0, \quad (1.25c)$$

where m and β are separation constants. Equation (1.25a) governs motion along transverse concentric circles in the pipe. The solution $\Phi(\phi)$ must be periodic with period 2π , so that $m = 0, 1, \dots$ and $\Phi_m = \cos(m\phi)$, $\Phi_m^* = \sin(m\phi)$. Solutions to Eq. (1.25b) describe transverse radial motion within the pipe. The boundary condition at the tube walls is $\partial p / \partial r = 0$, which allows a solution for the radially dependent variable of the form (Benade and Jansson, 1974a; Fletcher and Rossing, 1991)

$$R_{mn}(r) = J_m \left(\frac{\alpha_{mn} r}{a} \right), \quad (1.26)$$

where J_m is a Bessel function, a is the radius of the cylinder, and α_{mn} denotes the positive zeros of the derivative $J'_m(\alpha_{mn})$. Pressure wave motion of this form results in transverse circular nodal lines. Axial motion in the cylinder is described by solutions to Eq. (1.25c), which have the form

$$X(x) = C e^{-jk_{mn}x}, \quad (1.27)$$

where C is a constant,

$$k_{mn}^2 = k^2 - \beta^2 = k^2 - (\alpha_{mn}/a)^2, \quad (1.28)$$

and k is the wave number for propagation in free space. Boundary conditions in x determine exact solutions to Eq. (1.27). A complete general solution to the Helmholtz equation in circular polar coordinates is then given by

$$P_{mn}(r, \phi, x) = \Phi(\phi) R(r) X(x) = P_0 \cos(m\phi) J_m \left(\frac{\alpha_{mn} r}{a} \right) e^{-jk_{mn}x}. \quad (1.29)$$

The wavenumber for a sinusoidal disturbance propagating axially along the tube, k_{mn} , varies with mode (m, n) . One-dimensional plane-wave propagation corresponds to mode $(0, 0)$, for which $k_{00} = k = \Omega/c$. Higher modes, however, will propagate only if k_{mn} is positive, so that the frequency must exceed a cutoff value given by

$$\Omega_c = \frac{\alpha_{mn} c}{a}. \quad (1.30)$$

For frequencies less than Ω_c , the mode is evanescent and decays exponentially with distance. The plane-wave mode has a cut-off frequency of zero and no transverse wave motion. The next two propagating modes are the $(1, 0)$ and $(2, 0)$ nodal plane modes, which have cutoff frequencies $\Omega_c = 1.84c/a$ and $\Omega_c = 3.05c/a$, respectively. A typical clarinet has a radius of about 7.5 millimeters for a majority of its length, while that of a flute is about 8.5 millimeters. With the speed of sound

approximated by $c = 347.23$ meters per second for a temperature of 26.85°C , these cutoff frequencies are 13.56 kHz and 22.5 kHz for the clarinet and 11.96 kHz and 19.8 kHz for the flute. The first propagating transverse mode is well within the range of human hearing. However, excitation of this mode requires transverse circular motion, which will not occur with any significance in musical instruments. Evanescent mode losses may be possible in a woodwind instrument mouthpiece and near toneholes, though such losses will be minimal for the purposes of this study.

Given the previous analysis, wave motion in cylindrical woodwind bores is primarily planar and along the principal axis of the tube. The equation of motion for a pressure wave propagating in this way along the x -axis with sinusoidal time dependence has the form

$$P(x, t) = C e^{j(\Omega t - kx)}, \quad (1.31)$$

as found by substitution in Eq. (1.29) for the (0,0) mode. In order to determine the associated volume velocity within the tube, the three-dimensional expression for Newton's second law found in Section 1.1 [Eq. (1.5)] can be rewritten for one-dimensional plane waves as

$$\frac{\partial p}{\partial x} = -\rho \frac{\partial^2 \xi}{\partial t^2}. \quad (1.32)$$

This same expression in terms of volume velocity is

$$\frac{\partial p}{\partial x} = -\frac{\rho}{S} \frac{\partial U}{\partial t}, \quad (1.33)$$

where S is the cross-sectional area of the pipe. For pressure waves given by Eq. (1.31), the associated volume flow is found from Eq. (1.33) as

$$U(x, t) = \left(\frac{S}{\rho c} \right) C e^{j(\Omega t - kx)} \quad (1.34)$$

and the characteristic or wave impedance is

$$Z_0(x) = \frac{P(x)}{U(x)} = \frac{\rho c}{S}. \quad (1.35)$$

Similar relationships were previously found in Section 1.1 for plane waves of sound in free space, though in terms of particle velocity instead of volume velocity. These *traveling-wave* components of pressure and velocity are in-phase and the wave impedance is purely resistive.

The discussion thus far has been concerned only with bores of infinite length. In a pipe of finite length, propagating wave components will experience discontinuities at both ends. A longitudinal wave component which encounters a discontinuous and finite load impedance Z_L at one end of the tube will be partly reflected back into the tube and partly transmitted into the discontinuous medium. Wave variables in a finite length tube are then composed of superposed right- and left-going traveling waves. In this way, sinusoidal pressure in the pipe at position x is given by

$$P(x, t) = [A e^{-jkx} + B e^{jkx}] e^{j\Omega t}, \quad (1.36)$$

where A and B are complex amplitudes. From Eq. (1.33), the corresponding volume velocity is found to be

$$\begin{aligned} U(x, t) &= \left(\frac{S}{\rho c} \right) [Ae^{-jkx} - Be^{jkx}] e^{j\Omega t} \\ &= \frac{1}{Z_0} [Ae^{-jkx} - Be^{jkx}] e^{j\Omega t} \end{aligned} \quad (1.37)$$

At any particular position x and time t , the pressure and volume velocity traveling-wave components are related by

$$P^+ = Z_0 U^+ \quad P^- = -Z_0 U^- \quad (1.38)$$

with

$$P = P^+ + P^- \quad U = U^+ + U^- \quad (1.39)$$

The plus (+) superscripts indicate wave components traveling in the positive x -direction or to the right, while negative (−) superscripts indicate travel in the negative x -direction or to the left. The characteristic wave impedance Z_0 is a frequency-domain parameter, though for plane waves of sound it is purely real and independent of position. Therefore, these relationships are equally valid for both frequency- and time-domain analyses of pressure and volume velocity traveling-wave components.

Traveling waves of sound are typically reflected at an acoustic discontinuity in a frequency-dependent manner. A frequency-dependent reflection coefficient, or *reflectance*, characterizes this behavior and indicates the ratio of incident to reflected complex amplitudes at a particular frequency. Similarly, the ratio of incident to transmitted complex amplitudes at a particular frequency is characterized by a frequency-dependent transmission coefficient, or *transmittance*. For a pipe which extends from $x = 0$ to $x = L$ and is terminated at $x = L$ by the load impedance Z_L , the pressure wave reflectance is

$$\frac{B}{A} = e^{-2jkL} \left[\frac{Z_L - Z_0}{Z_L + Z_0} \right] \quad (1.40)$$

and the transmittance is

$$\frac{P(L, t)}{A} = e^{-jkL} \left[\frac{2Z_L}{Z_L + Z_0} \right]. \quad (1.41)$$

The phase shift term e^{-2jkL} in Eq. (1.40) appears as a result of wave propagation from $x = 0$ to $x = L$ and back and has unity magnitude. Sound radiation at the open end of a tube and the corresponding characteristics of the load impedance Z_L will be covered in Section 1.4. However, for low-frequency sound waves, the open end of a tube can be approximated by $Z_L = 0$. In this limit, the bracketed term of the reflectance becomes negative one, indicating that pressure traveling-wave components are reflected from the open end of a cylindrical tube with an inversion (or a 180° phase shift). There is no transmission of incident pressure into the new medium when $Z_L = 0$. If the pipe is rigidly terminated at $x = L$, an appropriate load impedance approximation is $Z_L = \infty$, corresponding to $U(L, t) = 0$ for all time. The bracketed term in Eq. (1.40) is then equal to one, which implies that pressure traveling waves reflect from a rigid barrier with no phase shift and no

attenuation. At the same time, the pressure transmittance magnitude is equal to two for the rigid barrier approximation. Though physically unintuitive, this value reflects the assumed continuity of pressure at $x = L$, which has a magnitude of $2A$.

The impedance at $x = 0$, or the *input impedance* of the cylindrical tube, is given by

$$Z_{IN} = \frac{P(0,t)}{U(0,t)} = Z_0 \left[\frac{A+B}{A-B} \right] \quad (1.42)$$

$$= Z_0 \left[\frac{Z_L \cos(kL) + jZ_0 \sin(kL)}{jZ_L \sin(kL) + Z_0 \cos(kL)} \right]. \quad (1.43)$$

The input impedance of finite length bores can be estimated using the low-frequency approximation $Z_L = 0$ for an open end and $Z_L = \infty$ for a closed end. Equation (1.43) reduces to

$$Z_{IN} = -jZ_0 \cot(kL) \quad (1.44)$$

for the rigidly terminated pipe and

$$Z_{IN} = jZ_0 \tan(kL) \quad (1.45)$$

for the ideally open pipe. In the low-frequency limit, $\tan(kL)$ is approximated by kL and the input impedance of the open pipe reduces to $j\Omega\rho L/S$. This is the same expression found in Section 1.2 for the impedance of a short open tube, or an acoustic inductance. Making a similar approximation for $\cot(kL)$, the input impedance of the rigidly terminated pipe reduces to $-(j/\Omega)(\rho c^2/LS)$, which is equivalent to the impedance of a cavity in the low-frequency limit. By equating an open pipe end at $x = 0$ with a value of $Z_{IN} = 0$ in the previous expressions, the resonance frequencies of the open-closed (o-c) pipe and the open-open (o-o) pipe are given for $n = 1, 2, \dots$ by

$$f^{(o-c)} = \frac{(2n-1)c}{4L} \quad (1.46)$$

$$f^{(o-o)} = \frac{nc}{2L}, \quad (1.47)$$

respectively. The open-closed pipe is seen to have a fundamental wavelength equal to four times its length and higher resonances which occur at odd integer multiples of the fundamental frequency. The open-open pipe has a fundamental wavelength equal to two times its length and higher resonances which occur at all integer multiples of the fundamental frequency.

The input impedance of an acoustic structure provides valuable information regarding its natural modes of vibration. Various methods for measuring and/or calculating the input impedance of musical instrument bores have been reported (Benade, 1959; Backus, 1974; Plitnik and Strong, 1979; Caussé *et al.*, 1984). No wind instrument is constructed of a perfectly uniform cylindrical pipe. However, it is possible to approximate non-uniform bore shapes with cylindrical sections, as illustrated in Fig. 1.5. The input impedance of such a structure can then be estimated in terms of the individual cylindrical section impedances. The calculation procedure is initiated at the last of a sequence of cylindrical sections by applying Eq. (1.43) with an appropriate approximation for the load impedance Z_L at the output of the structure. The input impedance Z_{IN} determined for

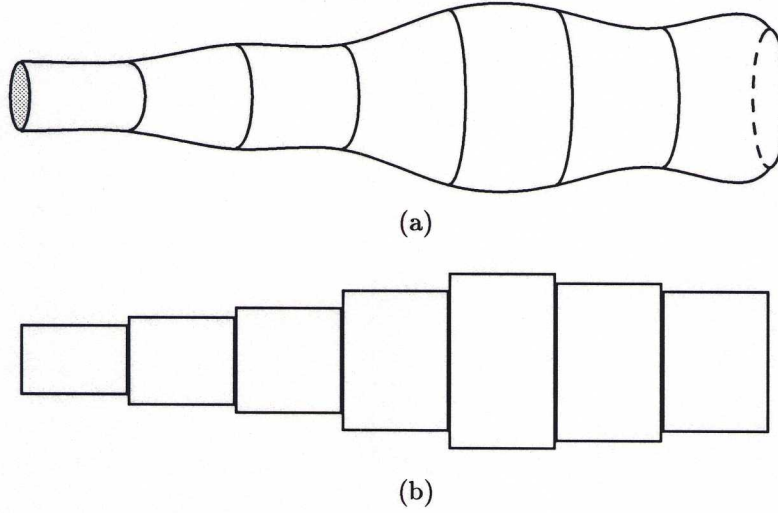


Fig. 1.5. A non-uniform bore (a) and its approximation in terms of cylindrical sections (b).

this section then becomes the load impedance for the adjacent section. Working back from the output end of the bore, the input impedance is calculated for the entire acoustic structure. These calculations can be formulated in terms of *transmission matrices* (Keefe, 1981) which relate pressure and volume velocity at the input and output of a single cylindrical section of length L as

$$\begin{bmatrix} P_0 \\ U_0 \end{bmatrix} = \begin{bmatrix} a & b \\ c & d \end{bmatrix} \begin{bmatrix} P_L \\ U_L \end{bmatrix} \quad (1.48)$$

and where the lossless transmission-matrix coefficients are given by

$$\begin{aligned} a &= \cos(kL) \\ b &= jZ_0 \sin(kL) \\ c &= \frac{j}{Z_0} \sin(kL) \\ d &= \cos(kL). \end{aligned}$$

In this way, each cylindrical section is represented by a separate transmission matrix, according to its particular length and radius. By comparison with Eq. (1.43), the input impedance of the section can be calculated from the transmission-matrix coefficients as

$$Z_{IN} = \frac{b + aZ_L}{d + cZ_L}. \quad (1.49)$$

For a sequence of n cylindrical sections, the input variables for each section become the output variables for the previous section. The transmission matrices can then be cascaded as

$$\begin{bmatrix} P_0 \\ U_0 \end{bmatrix} = \begin{bmatrix} a_1 & b_1 \\ c_1 & d_1 \end{bmatrix} \begin{bmatrix} a_2 & b_2 \\ c_2 & d_2 \end{bmatrix} \cdots \begin{bmatrix} a_n & b_n \\ c_n & d_n \end{bmatrix} \begin{bmatrix} P_L \\ U_L \end{bmatrix}$$

$$= \begin{bmatrix} A & B \\ C & D \end{bmatrix} \begin{bmatrix} P_L \\ U_L \end{bmatrix} \quad (1.50)$$

where

$$\begin{bmatrix} A & B \\ C & D \end{bmatrix} = \prod_{i=1}^n \begin{bmatrix} a_i & b_i \\ c_i & d_i \end{bmatrix}, \quad (1.51)$$

and the input impedance found for the entire acoustic structure as

$$Z_{IN} = \frac{B + AZ_L}{D + CZ_L}. \quad (1.52)$$

As an example of this procedure, the input impedance of the cylindrical section structure shown in Fig. 1.5(b) is calculated and assumed to approximate the input impedance of the non-uniform bore shape of Fig. 1.5(a). Table 1.1 provides hypothetical dimensions for these structures which are used in the calculations. Boundary layer effects are ignored, though a theoretically accurate representation of Z_L at the open end of the bore is incorporated. Figure 1.6 is a plot of the

Bore Position (x)	Bore Diameter at x	Cylindrical Section Diameter
0.0	0.016	0.016
0.1	0.016	0.020
0.2	0.024	0.024
0.3	0.024	0.032
0.4	0.040	0.040
0.5	0.040	0.036
0.6	0.032	0.032

Table 1.1. Hypothetical dimensions (in meters) of the bore shape shown in Fig. 1.5(a) and its approximation by cylindrical sections in Fig. 1.5(b).

calculated input impedance of the structure in Fig. 1.5(b). Frequency values have been indicated over the first six impedance peaks in order to clearly point out the inharmonicity of this structure's normal modes. The accuracy of the approximation is, of course, dependent on the size and number of cylindrical sections used to approximate the actual bore shape.

1.3.2 Conical Bores

Woodwind instruments constructed with bores which are primarily conical in shape include oboes, bassoons, and saxophones. Spherical waves of sound can theoretically propagate without reflection or loss away from the apex and along the principal axis of an infinite conical bore, assuming the walls are rigid, perfectly smooth, and thermally insulating. Longitudinal wave motion in conical bores is also possible along orthogonal trajectories to the principal axis. While these transverse modes are only weakly excited in most musical instruments, they can become significant, for example, in the

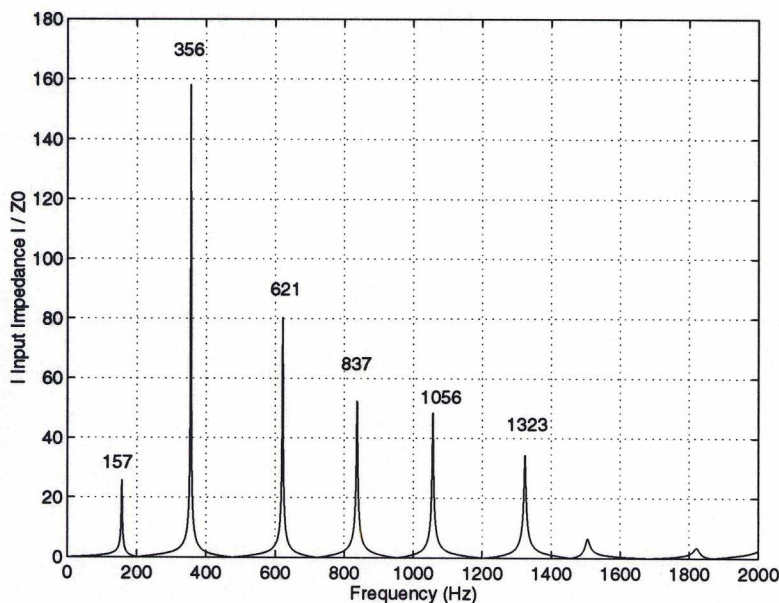


Fig. 1.6. Theoretical input impedance magnitude, relative to Z_0 at $x = 0$, of the cylindrical section structure shown in Fig. 1.5(b).

vicinity of a strongly flaring bell. This section presents the basic properties of conical bores, without accounting for radiation at open ends, the effects of toneholes, or viscothermal losses.

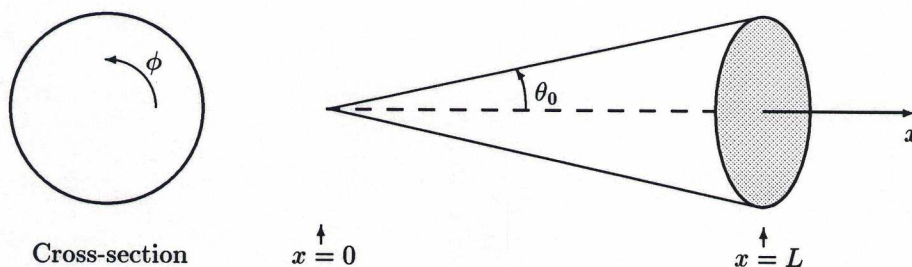


Fig. 1.7. A conical section in spherical coordinates.

A conical bore section in spherical coordinates (x, ϕ, θ) is depicted in Fig. 1.7. The wave equation in this geometric coordinate system is

$$\frac{1}{x^2} \frac{\partial}{\partial x} \left(x^2 \frac{\partial p}{\partial x} \right) + \frac{1}{x^2 \sin \theta} \frac{\partial}{\partial \theta} \left(\sin \theta \frac{\partial p}{\partial \theta} \right) + \frac{1}{x^2 \sin^2 \theta} \frac{\partial^2 p}{\partial \phi^2} = \frac{1}{c^2} \frac{\partial^2 p}{\partial t^2}. \quad (1.53)$$

The Helmholtz equation is separable in spherical coordinates, and the resulting differential equations describe sinusoidal wave motion, or standing-wave distributions, along each of the spherical

coordinate axes,

$$\frac{\partial^2 \Phi}{\partial \phi^2} + m^2 \Phi = 0, \quad (1.54a)$$

$$\left(\frac{1}{\sin \theta} \right) \frac{d}{d\theta} \left(\sin \theta \frac{d\Theta}{d\theta} \right) + \left(\beta^2 - \frac{m^2}{\sin^2 \theta} \right) \Theta = 0, \quad (1.54b)$$

$$\frac{d^2(xX)}{dx^2} + \left(k^2 - \frac{\beta^2}{x^2} \right) (xX) = 0, \quad (1.54c)$$

where m and β are separation constants. Equation (1.54a) governs sinusoidal motion along transverse concentric circles in the cone. The solution $\Phi(\phi)$ must be periodic with period 2π , so that $m = 0, 1, \dots$ and $\Phi_m = \cos(m\phi)$, $\Phi_m^* = \sin(m\phi)$. Solutions to Eq. (1.54b) describe transverse radial motion within the cone and are given by *associated Legendre functions*

$$\Theta_n^m(y) = (1 - y^2)^{m/2} \frac{d^m \Theta_n}{dy^m}, \quad (1.55)$$

where $y = \cos(\theta)$ and $\beta = n(n+1)$. In order that the Legendre functions remain finite over the range $0 \leq \theta \leq \pi$, n must be an integer equal to m or larger (Morse and Feshbach, 1953, p. 1462). However, for cones of central angle $2\theta_0$, n will in general be nonintegral because of the limited domain of θ (Benade and Jansson, 1974a). Pressure wave motion of this form results in transverse circular nodal lines which vary in diameter with distance from the cone apex. Axial motion in the cone is described by solutions to Eq. (1.54c), which have the form

$$X(x) = (kx)^{-\frac{1}{2}} J_{n+\frac{1}{2}}(kx), \quad (1.56)$$

where $J_{n+\frac{1}{2}}(kx)$ is a Bessel function. A complete general solution of the Helmholtz equation in spherical coordinates is then given by

$$P_{mn}(x, \phi, \theta) = \Phi(\phi) \Theta(\theta) X(x) = \frac{P_0}{(kx)^{\frac{1}{2}}} \cos(m\phi) \Theta_n^m(\cos \theta) J_{n+\frac{1}{2}}(kx). \quad (1.57)$$

One-dimensional spherical-wave propagation along the central axis of the cone is possible for $m = 0$ and $\beta = 0$, in which case Eq. (1.57) reduces to a general solution of the form

$$P(x) = \frac{C}{x} e^{-jkx}, \quad (1.58)$$

where C is a constant and k is the wave number in open air. Waves of this type will propagate at all frequencies.

The boundary condition at the tube wall, or at $\theta = \theta_0$, is $\partial p / \partial \theta = 0$, which can be met by adjusting the values of m and n so that an extremum of $\Theta_n^m(\cos \theta)$ occurs at the wall. Calculation of the Legendre functions for nonintegral n is nontrivial, and an accurate determination of cutoff frequencies for these modes is beyond the scope of this study. For axial symmetric waves ($m = 0$), Hoersch (1925) has presented a method for determining values of n which satisfy the boundary condition in conical horns of various angles. Typical values of θ_0 for saxophones, oboes, and bassoons

are 2° , 1.5° , and 0.5° , respectively (Nederveen, 1969). Using this procedure, the lowest values of n calculated for these angles are 109.27, 145.86, and 438.58, respectively. Computer calculations using *MATLAB*[®] of the associated Legendre functions for integer values of n support these values and further indicate that solutions with $m = 1$ and n approximately equal to 53, 70, and 213, respectively are possible. These are nodal plane modes which correspond to the (1,0) mode in cylinders. Cutoff frequencies for these values of n are determined where the expression $k^2 - \beta^2/x^2$ in Eq. (1.54c) becomes positive. These cutoff frequencies are dependent on x , so that waves of sinusoidal type having $\beta \neq 0$ are only possible in the outer or wider portions of a cone (Benade and Jansson, 1974a). Near the cone tip, any higher order modes that are excited will be evanescent. For the $m = 1$ mode solutions given above, the corresponding cutoff frequencies are approximately $f_c = 2.94/x$ kHz for saxophones, $f_c = 3.87/x$ kHz for oboes, and $f_c = 11.72/x$ kHz for bassoons, where x is given in meters. Alto saxophones, oboes, and bassoons have approximate lengths of 1 meter, 0.64 meters, and 2.5 meters, and thus transverse modes can propagate well within the audio spectrum at certain locations in these instruments. In comparison to cylindrical tubes, these higher modes propagate at much lower frequencies. However, excitation of the $m = 1$ mode requires transverse circular motion, which will not occur with any regularity in musical instruments. As mentioned with regard to cylindrical bores, evanescent mode losses may occur in a woodwind instrument mouthpiece and near toneholes. It is expected, however, that such losses will generally be insignificant for the analyses of this study.

For musical purposes, the principal mode of wave propagation in conical tubes is spherical and along the central axis of the tube. During a steady-state excitation, sinusoidal pressure at position x in a finite length conic section is composed of superposed spherical traveling-wave components of the form

$$P(x, t) = \left[\frac{A}{x} e^{-jkx} + \frac{B}{x} e^{jkx} \right] e^{j\Omega t}, \quad (1.59)$$

where A and B are complex amplitudes and sinusoidal time dependence is assumed. The associated volume velocity in the cone is found by rewriting the three-dimensional expression for Newton's second law [Eq. (1.5)] for one-dimensional spherical waves as

$$\frac{\partial p}{\partial x} = -\frac{\rho}{S(x)} \frac{\partial U}{\partial t}, \quad (1.60)$$

where $S(x)$ is the surface area of a spherical cap which intersects the principal axis of the pipe at position x^\dagger . For pressure waves of the form of Eq. (1.59), the corresponding volume flow is found using Eq. (1.60) as

$$\begin{aligned} U(x, t) &= \frac{S(x)}{x\rho c} \left[A \left(1 + \frac{1}{jkx} \right) e^{-jkx} - B \left(1 - \frac{1}{jkx} \right) e^{jkx} \right] e^{j\Omega t}, \\ &= \frac{1}{x} \left[\frac{A}{Z_0(x)} e^{-jkx} - \frac{B}{Z_0^*(x)} e^{jkx} \right] e^{j\Omega t}. \end{aligned} \quad (1.61)$$

[†]A derivation of the spherical wave front surface area is provided in Appendix A.

The wave impedance for spherical traveling-wave components propagating away from the cone apex is

$$Z_0(x) = \frac{P(x)}{U(x)} = \frac{\rho c}{S(x)} \left(\frac{jkx}{1 + jkx} \right) = \frac{\rho c}{S(x)} \left(\frac{1}{1 + \frac{1}{jkx}} \right), \quad (1.62)$$

which depends both on position x and frequency Ω . The characteristic impedance for spherical traveling-wave components propagating in a cone toward its apex is given by $Z_0^*(x)$, or the complex conjugate of $Z_0(x)$. For $kx \gg 1$, the spherical wave fronts become more planar in shape and $Z_0(x)$ approaches $\rho c/S(x)$, the wave impedance for plane waves in a duct of cross section S . Near the apex of the cone, however, the imaginary part of $Z_0(x)$ becomes increasingly dominant and in the limit as $x \rightarrow 0$, the pressure and velocity traveling-wave components become 90° out of phase at the cone tip. It is intuitively helpful to rewrite the characteristic impedance in the form

$$Z_0(x) = \frac{1}{\frac{S(x)}{\rho c} + \frac{S(x)}{j\Omega \rho x}}, \quad (1.63)$$

which is equivalent to the resistive wave impedance of a cylindrical bore in parallel with a lumped inertance of *acoustic* mass $\rho x/S(x)^\dagger$. At low frequencies and near the conical apex, the inertance effectively shunts out the resistive element.

At any particular position x and frequency Ω , sinusoidal pressure and volume velocity traveling-wave components are related by

$$P^+(x, \Omega) = Z_0(x, \Omega) U^+(x, \Omega) \quad P^-(x, \Omega) = -Z_0^*(x, \Omega) U^-(x, \Omega) \quad (1.64)$$

with

$$P(x, \Omega) = P^+(x, \Omega) + P^-(x, \Omega) \quad U(x, \Omega) = U^+(x, \Omega) + U^-(x, \Omega) \quad (1.65)$$

The plus (+) superscripts indicate wave components traveling in the positive x -direction or away from the cone apex, while negative (−) superscripts indicate travel in the negative x -direction or toward the apex. These relationships are similar to those for the cylindrical bore, with the important difference that the characteristic impedance for waves traveling toward the cone tip is the complex conjugate of that for waves traveling away from the apex. In other words, wave propagation toward the apex is different from propagation away from the apex because a conical waveguide is nonsymmetric about its midpoint (Keefe, 1981, p. 70). This point has an important consequence in the time-domain analysis of wave propagation in conical tubes, to be discussed later in this study. Also, because the wave impedance for spherical-wave components is frequency dependent, these relationships are valid only for frequency-domain analyses.

Figure 1.8 illustrates a divergent conical frusta for which the apical section is truncated at $x = x_0$. The frequency-domain pressure wave reflectance and transmittance for such a section, assuming a

[†]While mechanical impedance is measured in units of kilograms/second, acoustic impedance is given in units of kilograms/(meters⁴· second). Thus, acoustic mass is not equivalent to mechanical mass.

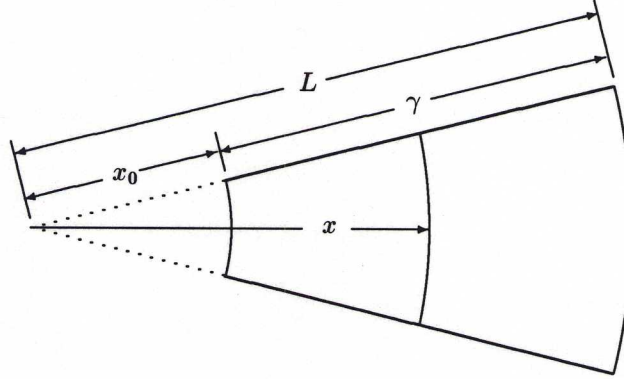


Fig. 1.8. A divergent conical section and its associated dimensional parameters.

load impedance Z_L at $x = L$, are given by

$$\frac{B}{A} = e^{-2jkL} \left[\frac{Z_L Z_0^*(L) - Z_0(L) Z_0^*(L)}{Z_L Z_0(L) + Z_0(L) Z_0^*(L)} \right], \quad (1.66)$$

and

$$\frac{p(L, t)}{A} = \frac{e^{-jkL}}{L} \left[\frac{Z_L Z_0(L) + Z_L Z_0^*(L)}{Z_L Z_0(L) + Z_0(L) Z_0^*(L)} \right], \quad (1.67)$$

respectively. The phase shift term e^{-2jkL} in Eq. (1.66) represents wave propagation to $x = L$ and back and has unity magnitude. The length parameter in this term is $2L$ because the cone apex is defined at $x = 0$. In this context, it would be more intuitive to set the input or small end of the cone at $x = 0$, so that the length parameter is equal to two times the length of the conic section. In order to maintain a consistent approach throughout this section, however, the conventions established in Fig. 1.8 will continue to be followed. The $1/L$ factor in the transmittance is characteristic of conical waveguides and results from the spreading of pressure across an increasing surface area as the traveling-wave component of pressure propagates away from the cone apex (Benade, 1988). The load impedance at the apex is given by $Z_L = \infty$ and in the limit as $x \rightarrow 0$, the term in brackets reduces to negative one. Thus, while the apex of a cone is a pressure antinode, pressure traveling-wave components reflect from the apex with an inversion, a behavior which at first appears paradoxical. It should be remembered that the boundary condition at the tip must be met by the sum of the two traveling-wave components and their corresponding $1/x$ factors. The inversion of reflected pressure is necessary to maintain a finite pressure at $x = 0$, which can then be determined by l'Hôpital's rule (Ayers *et al.*, 1985). This behavior can also be explained in terms of pressure wave reflection at a rigid termination, as discussed above. It was seen that pressure wave components reflect from a rigid conical bore boundary with unity magnitude and a phase shift equal to $2 \angle Z_0$. Since the angle of $Z_0(0)$ is 90° , pressure is reflected from the tip with a 180° phase shift or with an inversion.

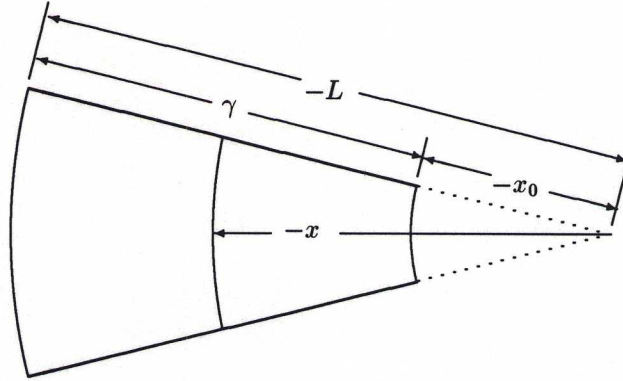


Fig. 1.9. A convergent conical section and its associated dimensional parameters.

The *input admittance* $Y(x)$ of a conical bore is more simply stated than its input impedance. For a conic section truncated at $x = x_0$, the input admittance is

$$Y_{IN}(x_0) = \frac{1}{Z(x_0)} = \frac{U(x_0, t)}{P(x_0, t)} = \frac{S(x_0)}{\rho c} \left\{ \left[\frac{e^{-jkx_0} - \frac{B}{A}e^{jkx_0}}{e^{-jkx_0} + \frac{B}{A}e^{jkx_0}} \right] + \frac{1}{jkx_0} \right\}, \quad (1.68)$$

where the pressure wave reflectance B/A is determined by the length of the bore and the boundary conditions at the opposite end, as discussed above. Equation (1.68) applies equally well to bores of increasing and decreasing diameter by using either positive or negative values of x as indicated in Figs. 1.8 and 1.9, respectively. Equation (1.68) may be interpreted as a parallel combination of an acoustic inertance and a term reminiscent of the impedance of a cylindrical waveguide (Benade, 1988). The impedance of the acoustic inertance, which has an equivalent acoustic mass $\rho x_0/S(x_0)$, approaches infinity as $x_0 \rightarrow 0$. The input admittance seen from the open end (at $x = -L$) of a complete cone reduces to

$$\begin{aligned} Y_{IN}(-L) &= \frac{S(L)}{\rho c} \left\{ \left[\frac{e^{j k L} - \frac{B}{A}e^{-j k L}}{e^{j k L} + \frac{B}{A}e^{-j k L}} \right] - \frac{1}{j k L} \right\} \\ &= \frac{S(L)}{\rho c} \left\{ \left[\frac{e^{j k L} + e^{-j k L}}{e^{j k L} - e^{-j k L}} \right] - \frac{1}{j k L} \right\} \\ &= \frac{S(L)}{j \rho c} \left[\cot(kL) - \frac{1}{kL} \right], \end{aligned} \quad (1.69)$$

where the pressure reflectance at the cone apex ($x = 0$) is negative one. An open end at $x = -L$ can be approximated by the low-frequency estimate $Y_{IN} = \infty$. The resonance frequencies of a complete cone ideally open at its large end are thus found at the infinities of Eq. (1.69), which are given for $n = 1, 2, \dots$ by

$$f = \frac{nc}{2L}. \quad (1.70)$$

The complete cone with open mouth has a fundamental wavelength equal to two times its length and higher resonances which occur at all integer multiples of the fundamental frequency, as was

observed for open-open cylindrical pipes. The anti-resonances of the complete cone, however, do not fall exactly midway between its resonances, but are influenced by the inertance term in Eq. (1.69).

The complete cone, of course, is musically useless. Conical bores are always truncated to some extent, to allow excitation at their small end. Assuming the mouth of the cone at $x = L$ is ideally open, so that $Z_L = 0$, the reflectance B/A becomes $-e^{-2jkL}$ and the input admittance of a truncated cone reduces to

$$Y_{IN}(x_0) = \frac{S(L)}{j\rho c} \left[\cot(k\gamma) - \frac{1}{kx_0} \right], \quad (1.71)$$

where $\gamma = L - x_0$. If the small end of the cone, at $x = x_0$, is assumed ideally open, the resonance frequencies of the open-open (o-o) conic frustum are at the infinities of Eq. (1.71), which are given for $n = 1, 2, \dots$ by

$$f^{(o-o)} = \frac{nc}{2(L - x_0)} = \frac{nc}{2\gamma}. \quad (1.72)$$

Thus, the higher natural frequencies of the open-open conic frustum are also related to the fundamental by integer multiple ratios. If the input end of the cone at $x = x_0$ is assumed ideally closed, which is nearly the case for reed-driven conical woodwind instruments, the resonance frequencies are found at the zeros of the input admittance. In this case, the partials of the closed-open conic frustum do not occur at exact integer multiples of the fundamental frequency, but are generally more widely spread apart depending on the magnitude of x_0 . The natural frequencies of the truncated cone closed at its small end are found by solving the transcendental equation

$$\tan(k\gamma) = -kx_0. \quad (1.73)$$

Equation (1.73) can be rewritten in the form

$$\tan\left(\pi \frac{f}{f_0}\right) = -\frac{\beta}{1 - \beta} \left(\pi \frac{f}{f_0}\right), \quad (1.74)$$

where $\beta = x_0/L$ and $f_0 = c/(2\gamma)$ is the fundamental frequency for the open-open conic frustum of length γ (Ayers *et al.*, 1985). Figure 1.10 illustrates the partial frequency ratios for a closed-open conic frustum, relative to the fundamental frequency of an open-open conic frustum of the same length, for $\beta = 0$ (complete cone) to $\beta = 1$ (closed-open cylinder). The dotted lines indicate exact integer relationships above the first partial and serve only to make more apparent the stretching of the partial ratios. The perfect harmonicity of the partials of an open-open conic frustum are distorted when a single-reed excitation mechanism is placed at one end. The fundamental frequency of the conic section is most affected by truncation and closure, as the inertance term in the admittance is largest for low frequencies. In terms of the fundamental wavelength of an open-open conic frustum of the same length, the inertance contributes a positive length correction which increases with truncation x_0 but decreases with frequency. Viewed in terms of the normal modes of a closed-open cylinder, however, the inertance contributes a negative length correction which is inversely proportional to truncation x_0 and frequency.

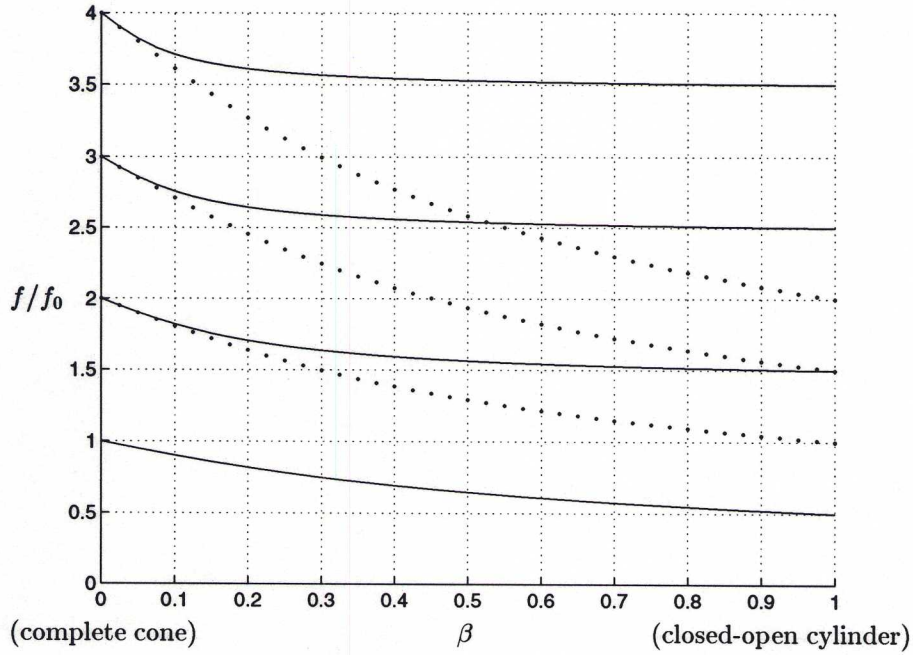


Fig. 1.10. Partial frequency ratios, relative to f_0 , for a closed-open conic frustum.

The approximation of real wind instrument bore shapes and the calculation of their associated input impedances using cylindrical sections was described in Section 1.3.1. A similar procedure is also possible with conical sections, and usually results in more accurate approximations. Figure 1.11 illustrates the use of both cylindrical and conical sections to approximate the non-uniform bore shape originally shown in Fig. 1.5. This approximation is clearly better compared with that using cylindrical sections.

For a diverging conical section as shown in Fig. 1.8, the input and output pressure and volume velocity are related through the transmission matrix

$$\begin{bmatrix} P_{x0} \\ U_{x0} \end{bmatrix} = \begin{bmatrix} a & b \\ c & d \end{bmatrix} \begin{bmatrix} P_L \\ U_L \end{bmatrix}, \quad (1.75)$$

where the lossless conical waveguide transmission-matrix coefficients are given by (Keefe, 1981; Caussé *et al.*, 1984; Mapes-Riordan, 1993; van Walstijn and de Bruin, 1995)

$$\begin{aligned} a &= \left(\frac{L}{x_0} \right) \cos(k\gamma) - \left(\frac{1}{kx_0} \right) \sin(k\gamma), \\ b &= \left(\frac{x_0}{L} \right) jR_{x_0} \sin(k\gamma), \\ c &= \left(\frac{j}{R_{x_0}} \right) \left\{ \left[\left(\frac{L}{x_0} \right) + \left(\frac{1}{kx_0} \right)^2 \right] \sin(k\gamma) - \left(\frac{\gamma}{x_0} \right) \left(\frac{1}{kx_0} \right) \cos(k\gamma) \right\}, \\ d &= \left(\frac{x_0}{L} \right) \left[\cos(k\gamma) + \left(\frac{1}{kx_0} \right) \sin(k\gamma) \right], \end{aligned}$$

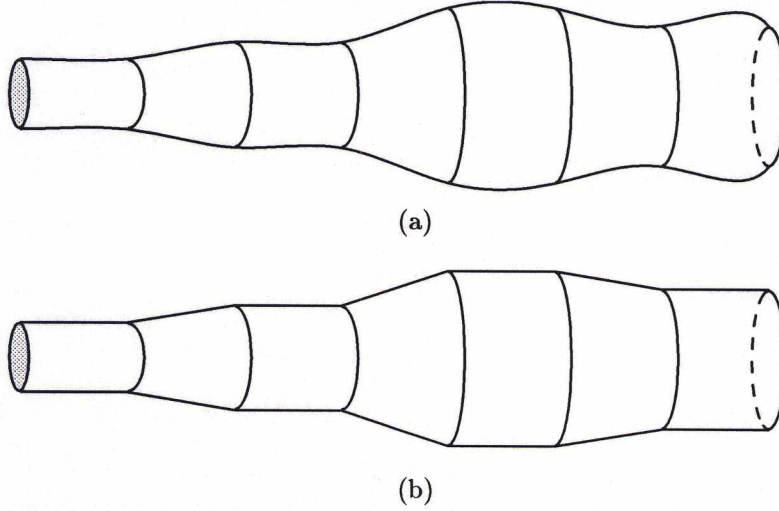


Fig. 1.11. A non-uniform bore (a) and its approximation in terms of cylindrical and conical sections (b).

$R_{x_0} = \rho c / \pi a_{x_0}^2$, and a_{x_0} is the radius at $x = x_0$. These coefficients have been simplified by assuming that spherical wave fronts at the beginning and end of each section are reasonably well approximated by plane wave fronts. Without such an assumption, the transmission-matrix coefficients are given by

$$\begin{aligned}
 a &= \frac{R_{x_0}}{R_L} \left[\left(\frac{x_0}{L} \right) \cos(k\gamma) - \left(\frac{x_0}{kL^2} \right) \sin(k\gamma) \right], \\
 b &= \left(\frac{x_0}{L} \right) j Z_0 \sin(k\gamma), \\
 c &= \left(\frac{j}{R_L} \right) \left\{ \left[\left(\frac{x_0}{L} \right) + \left(\frac{1}{kL} \right)^2 \right] \sin(k\gamma) - \left(\frac{\gamma}{kL^2} \right) \cos(k\gamma) \right\}, \\
 d &= \left(\frac{x_0}{L} \right) \left[\cos(k\gamma) + \left(\frac{1}{kx_0} \right) \sin(k\gamma) \right],
 \end{aligned}$$

where $R_{x_0} = \rho c / S(x_0)$ and the surface area of the spherical wave front which intersects the principle axis of the cone at $x = x_0$ with half angle θ is $S(x_0) = 2\pi x_0^2 (1 - \cos \theta)^\dagger$. A converging conical section, as shown in Fig. 1.9 and also found at the sixth segment of Fig. 1.11b, is represented by the inverse conjugate matrix of Eq. (1.75) or

$$\begin{bmatrix} P_{-L} \\ U_{-L} \end{bmatrix} = \begin{bmatrix} d & b \\ c & a \end{bmatrix} \begin{bmatrix} P_{-x_0} \\ U_{-x_0} \end{bmatrix}, \quad (1.76)$$

where all length parameters in the transmission-matrix coefficients are given by positive values. The input impedance of the cylindrical and conical section structure of Fig. 1.11b is calculated and plotted in Figure 1.12. Boundary layer effects are ignored in the calculations, though a theoretically

[†]A derivation of the spherical wave front surface area is provided in Appendix A.

accurate approximation to Z_L at the open end of the bore is employed. The impedance peak frequencies and amplitudes are close to those found using cylindrical sections only [Fig. 1.6] and most likely represent a better approximation to the resonances of the non-uniform bore shown in Fig. 1.11a. The accuracy of the approximation is again dependent on the number and size of the sections used.

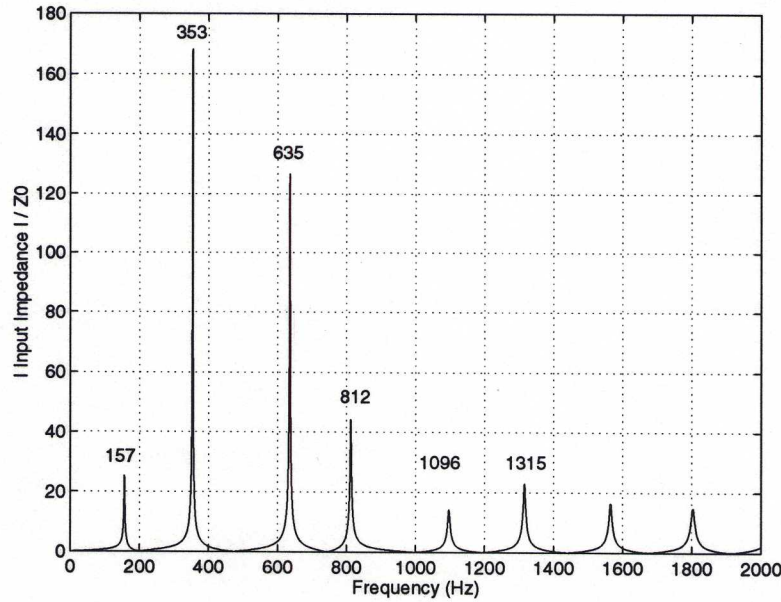


Fig. 1.12. Theoretical input impedance magnitude, relative to $Z_0 = \rho c/S$ at $x = 0$, of the cylindrical and conic section structure shown in Fig. 1.11(b).

1.3.3 Boundary Layer Effects

The preceding analysis of woodwind bores assumed lossless wave propagation. In practice, however, viscous drag and thermal conduction occur along the tube walls and cause deviations from ideal behavior[†]. Friction along the walls acts to resist the acceleration of air in a pipe and decreases the storage of kinetic energy. Thermal energy exchange between the air and tube surface violates the assumed adiabatic character of sound waves and reduces the potential energy component of wave motion in the pipe (Benade, 1968). These effects take place within a thin boundary layer along the bore walls. The thicknesses of the viscous and thermal layers are dependent on the angular frequency Ω and are given respectively by (Benade, 1968)

$$\delta_v = \left(\frac{\eta}{\Omega \rho} \right)^{1/2} \approx 1.6 \times 10^{-3} f^{-1/2}, \quad (1.77)$$

[†]Molecular viscosity and heat conduction cause internal losses for wave propagation in free space as well, though to a lesser degree than in narrow ducts (Morse and Ingard, 1968). Further losses, such as hysteresis in internal heat absorption and nonlinear effects, will not be considered here.

$$\delta_t = \left(\frac{\kappa}{\Omega \rho C_p} \right)^{1/2} \approx 1.9 \times 10^{-3} f^{-1/2}, \quad (1.78)$$

where δ_v and δ_t are given in meters, f is the frequency in hertz, ρ is the density, η the viscosity, κ the thermal conductivity, and C_p the specific heat of air per unit volume. The frictional effects are characterized by the parameter r_v , given as the ratio of the tube radius a to the viscous boundary layer thickness δ_v ,

$$r_v = \left(\frac{\Omega \rho}{\eta} \right)^{1/2} a. \quad (1.79)$$

Similarly, the thermal effects are characterized by the parameter r_t , which is proportional to the ratio of the tube radius to the thermal boundary layer thickness δ_t . This parameter is given by

$$r_t = \left(\frac{\Omega \rho C_p}{\kappa} \right)^{1/2} a. \quad (1.80)$$

Near 300 K (26.85°C), Benade (1968) provides the numerical values

$$r_v \approx 632.8 a f^{1/2} (1 - 0.0029 \Delta T), \quad (1.81)$$

and

$$r_t \approx 532.2 a f^{1/2} (1 - 0.0031 \Delta T), \quad (1.82)$$

where the tube radius a is in meters, the frequency f is in hertz, and ΔT is the temperature deviation from 300 K. Within the main bore of typical clarinets and flutes, $r_v \approx 67.1$ and 76.1 , and $r_t \approx 56.4$ and 64 , respectively, at 200 Hz and 300 K.

The effects of these losses are incorporated into the wave propagation expressions by rewriting the wave vector k as the complex number $\Omega/v_p - j\alpha$, where v_p is the phase velocity and α is an attenuation coefficient per unit length. The wave amplitude then decays as $e^{-\alpha x}$ for plane waves or $e^{-\alpha x}/x$ for spherical waves. The phase velocity and attenuation coefficient are approximated for large r by (Keefe, 1984)

$$v_p^{-1} = c^{-1} \left\{ 1 + \left(\frac{r_v^{-1}}{\sqrt{2}} \right) \left(1 + \frac{\gamma-1}{\nu} \right) - \left(\frac{r_v^{-3}}{\sqrt{2}} \right) \left[\frac{7}{8} + \frac{\gamma-1}{\nu} - \frac{1}{2} \left(\frac{\gamma-1}{\nu^2} \right) - \frac{1}{8} \left(\frac{\gamma-1}{\nu^3} \right) - \frac{1}{2} \left(\frac{\gamma-1}{\nu} \right)^2 + \frac{1}{2} \frac{(\gamma-1)^2}{\nu^3} + \frac{1}{2} \left(\frac{\gamma-1}{\nu} \right)^3 \right] \right\}, \quad (1.83)$$

and

$$\alpha = \left(\frac{\Omega}{c} \right) \left\{ \left(\frac{r_v^{-1}}{\sqrt{2}} \right) \left(1 + \frac{\gamma-1}{\nu} \right) + r_v^{-2} \left[1 + \frac{\gamma-1}{\nu} - \frac{1}{2} \left(\frac{\gamma-1}{\nu^2} \right) - \frac{1}{2} \left(\frac{\gamma-1}{\nu} \right)^2 \right] + \left(\frac{r_v^{-3}}{\sqrt{2}} \right) \left[\frac{7}{8} + \frac{\gamma-1}{\nu} - \frac{1}{2} \left(\frac{\gamma-1}{\nu^2} \right) - \frac{1}{8} \left(\frac{\gamma-1}{\nu^3} \right) - \frac{1}{2} \left(\frac{\gamma-1}{\nu} \right)^2 + \frac{1}{2} \frac{(\gamma-1)^2}{\nu^3} + \frac{1}{2} \left(\frac{\gamma-1}{\nu} \right)^3 \right] \right\}, \quad (1.84)$$

where ν is the square root of the Prandtl number

$$\nu = \left(\frac{\eta C_p}{\kappa} \right)^2. \quad (1.85)$$

For the special case of air at 300 K and $r_v > 2$, these values can be simplified to (Keefe, 1984)

$$v_p^{-1} = c^{-1} (1 + 1.045r_v^{-1}), \quad (1.86)$$

and

$$\alpha = \left(\frac{\Omega}{c}\right) (1.045r_v^{-1} + 1.080r_v^{-2} + 0.750r_v^{-3}). \quad (1.87)$$

The characteristic impedance of cylindrical ducts is also affected by viscous and thermal losses. The ideal, real valued characteristic impedance becomes frequency dependent and is given by (Keefe, 1984)

$$\Re(Z_c) = Z_0 \left\{ 1 + \left(\frac{r_v^{-1}}{\sqrt{2}}\right) \left(1 - \frac{\gamma-1}{\nu}\right) - \left(\frac{r_v^{-3}}{\sqrt{2}}\right) \left[\frac{7}{8} - \frac{\gamma-1}{\nu} + \frac{1}{2} \left(\frac{\gamma-1}{\nu^2}\right) + \frac{1}{8} \left(\frac{\gamma-1}{\nu^3}\right) + \frac{3}{2} \left(\frac{\gamma-1}{\nu}\right)^2 - \frac{3}{2} \frac{(\gamma-1)^2}{\nu^3} - \frac{5}{2} \left(\frac{\gamma-1}{\nu}\right)^3 \right] \right\}, \quad (1.88)$$

$$-\Im(Z_c) = Z_0 \left\{ \left(\frac{r_v^{-1}}{\sqrt{2}}\right) \left(1 - \frac{\gamma-1}{\nu}\right) + r_v^{-2} \left[1 - \frac{\gamma-1}{\nu} + \frac{1}{2} \left(\frac{\gamma-1}{\nu^2}\right) + \frac{3}{2} \left(\frac{\gamma-1}{\nu}\right)^2 \right] + \left(\frac{r_v^{-3}}{\sqrt{2}}\right) \left[\frac{7}{8} - \frac{\gamma-1}{\nu} + \frac{1}{2} \left(\frac{\gamma-1}{\nu^2}\right) + \frac{1}{8} \left(\frac{\gamma-1}{\nu^3}\right) + \frac{3}{2} \left(\frac{\gamma-1}{\nu}\right)^2 - \frac{3}{2} \frac{(\gamma-1)^2}{\nu^3} - \frac{5}{2} \left(\frac{\gamma-1}{\nu}\right)^3 \right] \right\}, \quad (1.89)$$

where Z_0 is the real-valued wave impedance of the pipe in the absence of losses. For air at 300 K and $r_v > 2$, the characteristic impedance reduces to (Keefe, 1984)

$$Z_c = Z_0 \{ (1 + 0.369r_v^{-1}) - j (0.369r_v^{-1} + 1.149r_v^{-2} + 0.303r_v^{-3}) \}. \quad (1.90)$$

Figure 1.13 illustrates the frequency dependence of the phase velocity and attenuation coefficient for a bore radius of 0.008 meters. The attenuation coefficient is proportional to \sqrt{f} , so that high frequency sound components are damped more than low ones. All resonance frequencies in the bore will be lowered to some extent because the phase velocity is always less than c . Inharmonicity of the bore resonances, particularly at low frequencies, will also occur due to the variation of v_p with frequency. The input impedance magnitude of an ideally terminated ($Z_L = 0$) cylindrical bore with viscous and thermal losses is shown in Fig. 1.14. The resonance peaks decrease in magnitude with frequency, as expected from the characteristic of the attenuation coefficient. A small frequency shift of the resonance peaks is measurable but too slight to be observed in the plot. For low- and mid-frequency sounds, thermal and viscous losses in the main air column of a musical instrument are generally more significant than radiation losses via open ends and/or toneholes. These effects may also be important when considering wave behavior within the smaller tubes of woodwind toneholes.

Thermoviscous losses can be incorporated into the cylindrical and conical transmission matrices presented in the previous sections by defining a complex propagation wavenumber $\Gamma = \alpha + j\Omega/v_p$ and

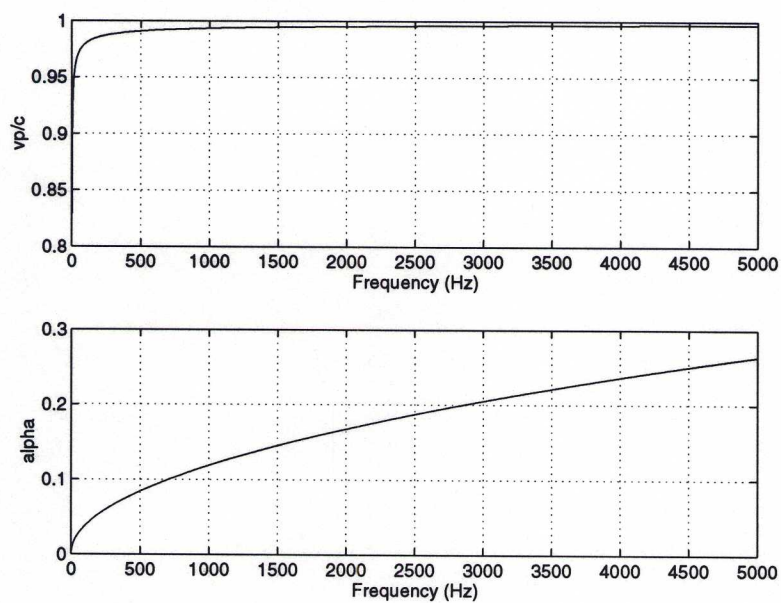


Fig. 1.13. Phase velocity (v_p) normalized by c vs. frequency (top); Attenuation coefficient (α) vs. frequency (bottom).

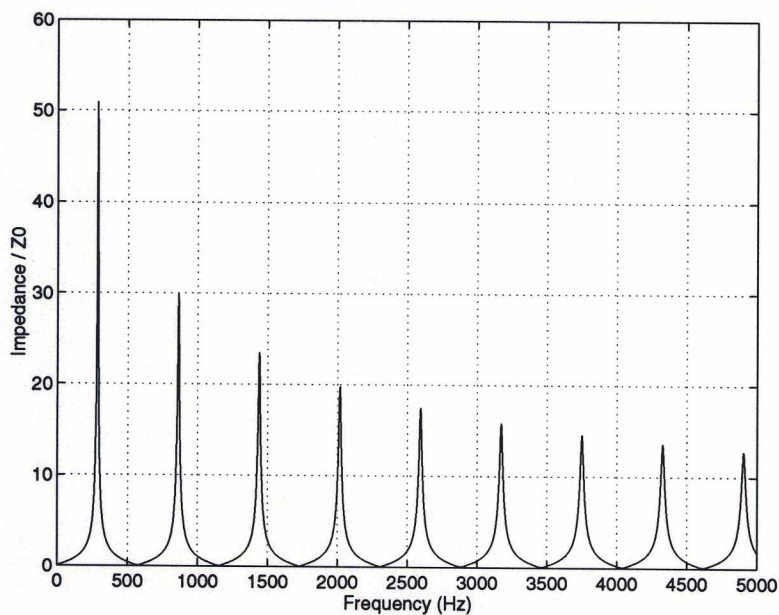


Fig. 1.14. Input impedance magnitude of an ideally terminated cylindrical bore with viscous and thermal losses (bore length = 0.3 meters, bore radius = 0.008 meters).

using the complex characteristic impedance Z_c as defined above. The lossy cylindrical transmission-matrix coefficients are then given by

$$\begin{aligned} a &= \cosh(\Gamma L) \\ b &= Z_c \sinh(\Gamma L) \\ c &= \frac{1}{Z_c} \sinh(\Gamma L) \\ d &= \cosh(\Gamma L), \end{aligned}$$

while the lossy conical transmission-matrix coefficients are (Keefe, 1981; Caussé *et al.*, 1984; Mapes-Riordan, 1993; van Walstijn and de Bruin, 1995)

$$\begin{aligned} a &= \left(\frac{L}{x_0}\right) \left[\cosh(\Gamma \gamma) - \left(\frac{1}{\Gamma L}\right) \sinh(\Gamma \gamma) \right], \\ b &= \left(\frac{x_0}{L}\right) Z_c \sinh(\Gamma \gamma), \\ c &= \left(\frac{1}{Z_c}\right) \left\{ \left[\left(\frac{L}{x_0}\right) - \left(\frac{1}{\Gamma x_0}\right)^2 \right] \sinh(\Gamma \gamma) + \left(\frac{\gamma}{\Gamma x_0^2}\right) \cosh(\Gamma \gamma) \right\}, \\ d &= \left(\frac{x_0}{L}\right) \left[\cosh(\Gamma \gamma) + \left(\frac{1}{\Gamma x_0}\right) \sinh(\Gamma \gamma) \right]. \end{aligned}$$

The length parameters in these expressions remain as originally defined for cylindrical and conical sections. The conical coefficients have been simplified by assuming that spherical wave fronts at the beginning and end of each section are reasonably well approximated by plane wave fronts. Thermoviscous losses are defined above for cylindrical waveguides. In order to calculate appropriate values of Γ for the conical coefficients, it is common to determine a “mean” conical section radius which is used to define r_v . The conical section characteristic impedance is calculated using $Z_0 = \rho c/S$, where S is the cross-sectional area at the input to the section.

The results provided above for thermal and viscous losses in a rigid pipe were derived under the assumption that the inner walls remain isothermal during the oscillatory cycle. However, an exchange of thermal energy at the walls inherently contradicts an isothermal condition and thus, the heat losses discussed above are overestimated to some extent. Franken *et al.* (1981) have provided an analysis of non-isothermal heat exchange in a cylindrical tube when the outside walls are assumed isothermal. Keefe (1984) has shown that these results can be incorporated in the previous expressions [Eqs. (1.83, 1.84, 1.88, 1.89)] by substituting γ_e for γ , where

$$\gamma_e = \frac{\gamma - 1}{1 + \epsilon_w} + 1 \quad (1.91)$$

The dimensionless parameter ϵ_w , which governs the oscillatory heat transfer characteristics of a solid-gas interface (Keefe, 1984), is given by

$$\epsilon_w = \left(\frac{\rho C_p \kappa}{\rho_w C_w \kappa_w} \right)^{1/2}, \quad (1.92)$$

where ρ_w is the mass density, C_w is the specific heat, and κ_w is the thermal conductivity of the tube wall material. The effects of non-isothermal inner tube walls will not be further accounted for in this study.

1.3.4 Time-Domain Descriptions

Because wave propagation in isolated wind instrument bores is well approximated by linear theory, the acoustic behavior of these structures can be described using frequency-domain analysis techniques. The operation of a complete wind instrument, however, is dependent on the interaction of the air column and a nonlinear, time-varying excitation mechanism, represented by the block diagram of Fig. 1.15. The nonlinear element, or reed mechanism in woodwind instruments, excites a passive linear element, such as a cylindrical or conical tube. Feedback from the bore subsequently influences the operation of the nonlinear element. In the study or simulation of such coupled systems, it is most appropriate to use time-domain representations for both the linear and nonlinear elements. The frequency-domain descriptions previously derived in this section for woodwind instrument bores have time-domain counterparts which are briefly explored here. This discussion is intended only as an introduction to time-domain analysis of acoustic systems. A more detailed investigation of time-domain acoustic modeling will be conducted in Chapter 3.

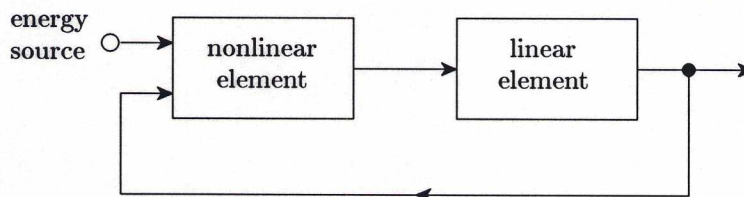


Fig. 1.15. A general wind instrument represented by linear and nonlinear elements in a feedback loop.

The time-domain description of linear acoustic systems is traditionally given by the inverse Fourier transform of the input impedance, called the *impulse response* $h(t)$ or the Green's function of the system. The impulse response describes the pressure evolution at the input of an acoustic structure originated by the introduction of a volume velocity unit impulse at this same point. Pressure and flow at the input are then related by means of the convolution product

$$p(t) = \int_0^t h(t-t')u(t')dt' = h(t) * u(t). \quad (1.93)$$

The theoretical input impedance and impulse response for a cylindrical bore with thermoviscous losses and open-end radiation are shown in Fig. 1.16. Because radiation and internal damping are typically low in musical air columns, the impulse response is a slowly decaying function, as expected from the sharply peaked nature of the input impedance. In the time-domain simulation of a musical

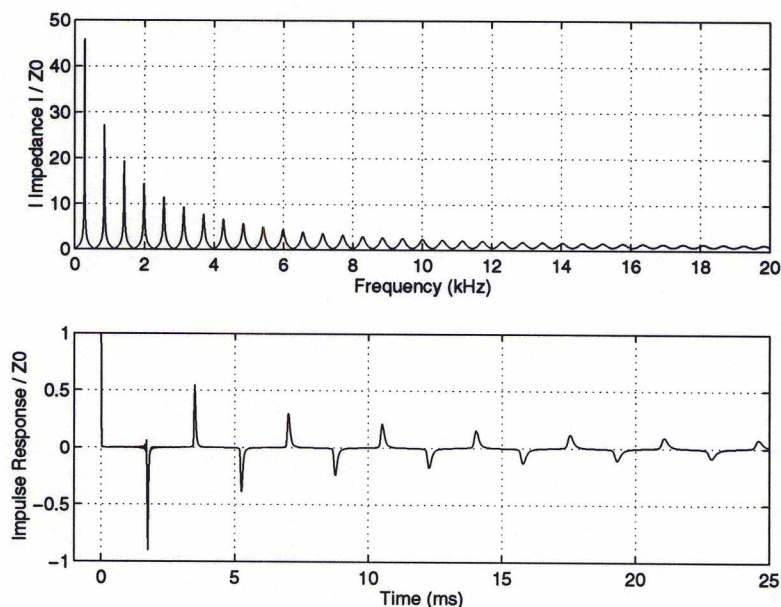


Fig. 1.16. Theoretical input impedance magnitude (top) and impulse response (bottom) of a cylindrical bore, normalized by the bore characteristic impedance.

instrument feedback system, the calculation of $p(t)$ using Eq. (1.93) is therefore extremely inefficient. Inspection of the theoretical impulse response of a cylindrical bore in Fig. 1.16 reveals a series of reflected pulses which are successively distorted by viscous and thermal losses at the tube walls and by radiation at the open end of the tube. The physical characteristics of the tube are completely defined, however, in the first $2L/c$ seconds, or the time necessary for the original impulse to travel to the opposite end of the tube (at $x = L$) and back with speed c . Subsequent reflections are given by the reapplication of this tube characteristic to the result of the previous roundtrip. In this sense, the instrument air column has an effective “memory” of only the past $t = 2L/c$ seconds. The phase delay and attenuation characteristics associated with pressure traveling-wave propagation to the end of the bore and back are specified by the plane-wave pressure reflection function $r_p(t)$. The plane-wave reflection function is defined as the inverse Fourier transform of the plane-wave reflectance, previously derived for cylindrical pipes in Eq. (1.40) as

$$\begin{aligned} \mathcal{R}_p(\Omega) &= e^{-2jkL} \left[\frac{Z_L(\Omega) - Z_0}{Z_L(\Omega) + Z_0} \right], \\ &= \frac{Z(\Omega) - Z_0}{Z(\Omega) + Z_0}, \end{aligned} \quad (1.94)$$

where L is the length of the pipe, Z_0 is the real characteristic wave impedance of the cylindrical pipe, $Z_L(\Omega)$ is the load impedance at $x = L$, and $Z(\Omega)$ is the input impedance of the pipe given by Eq. (1.42). The successive reflections typical in the impulse response do not occur in the reflection function because it essentially characterizes traveling-wave propagation to the end of the pipe and back only. However, it is common to interpret the plane-wave reflection function in terms of the

response of a cylindrical bore fitted with an anechoic termination at its input end. The reflection function then represents the pressure evolution at the input of an anechoically terminated cylindrical section caused by the introduction of a pressure unit impulse at this point. In this sense, traveling-wave components reflected from the open end of the pipe experience no discontinuity at the input end and propagate without reflection into the anechoic termination. Neglecting viscous and thermal losses along the bore walls, the phase term in Eq. (1.94) represents a time delay of $2L/c$ seconds in $r_p(t)$, so that the reflection function is given by a time shifted representation of the reflectance property of the load at the end of the pipe. The input impedance can be written in terms of the reflectance as

$$Z(\Omega) = Z_0 \left(\frac{1 + \mathcal{R}_p(\Omega)}{1 - \mathcal{R}_p(\Omega)} \right), \quad (1.95)$$

verifying the suggestion above that $Z(\Omega)$ is completely defined by $\mathcal{R}_p(\Omega)$ (or $h(t)$ is defined by $r_p(t)$). Equation (1.95) may be rewritten as (Ayers, 1996)

$$Z(\Omega) = Z_0 + Z_0 \mathcal{R}_p(\Omega) + \mathcal{R}_p(\Omega) Z(\Omega), \quad (1.96)$$

which has an inverse Fourier transform given by

$$h(t) = Z_0 \delta(t) + Z_0 r_p(t) + r_p(t) * h(t). \quad (1.97)$$

By convolving both sides of Eq. (1.97) with an injected flow $u(t)$ and using Eq. (1.93), the pressure at the junction of a nonlinear excitation mechanism and a cylindrical air column can be written as

$$p(t) = Z_0 u(t) + r_p(t) * [p(t) + Z_0 u(t)], \quad (1.98)$$

an expression generally attributed to McIntyre and Woodhouse (1979) and Schumacher (1981). Because the nonzero length of $r_p(t)$ is generally several orders of magnitude shorter than $h(t)$, Eq. (1.98) offers an efficient means for the calculation of pressure in a musical instrument feedback system. The volume velocity terms $u(t)$ in Eq. (1.98) represent flow entering the junction via the nonlinear excitation, while the term $[p(t) + Z_0 u(t)]$ represents the past components of pressure and injected flow feeding back from the bore. Given the nature of $r_p(t)$ discussed above, only $2L/c$ seconds of past history need be retained for the calculation of present values. For an isolated air column without an excitation mechanism, $u(t) = 0$ and Eq. (1.98) reduces to $p(t) = r_p(t) * p(t)$. This is equivalent to rewriting Eq. (1.93) in terms of the reflection function and indicates that the current pressure is simply the past pressure convolved with the reflection function.

The theoretical input impedance and impulse response of a conical divergent bore with thermoviscous losses and open-end radiation are shown in Fig. 1.17. The essential characteristics are similar to those of the cylindrical air column, though exponential wakes are evident which arise from the complex wave impedance of conical bores. The phase delay and attenuation characteristics associated with pressure traveling-wave propagation to the end of the conical bore and back are specified by the spherical-wave pressure reflection function $r_s(t)$. The spherical-wave reflectance $\mathcal{R}_s(\Omega)$ for a

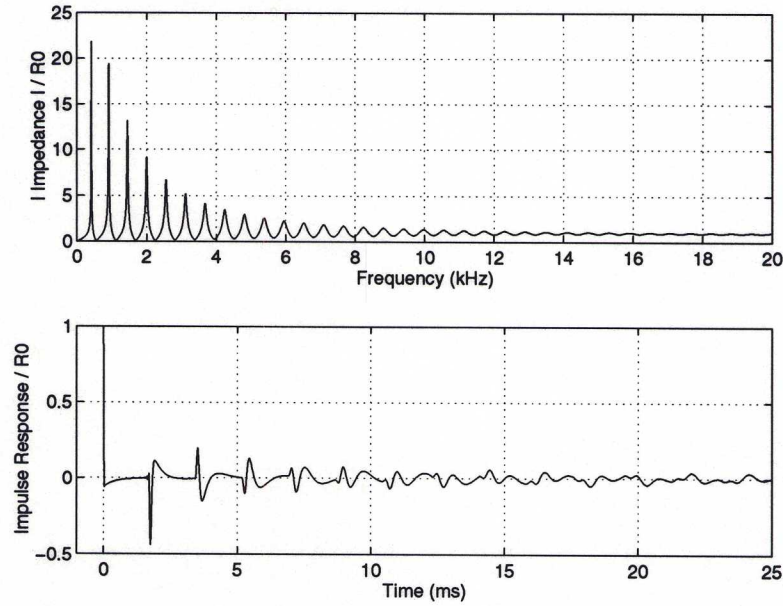


Fig. 1.17. Theoretical input impedance magnitude (top) and impulse response (bottom) of a conical bore, relative to $R_0 = \rho c / S(0)$ at the small end of the bore.

divergent conical section was derived in Section 1.3.2 and given by Eq. (1.66). For the conic section depicted in Fig. 1.18, $\mathcal{R}_s(\Omega)$ is

$$\mathcal{R}_s(\Omega) = e^{-2jkL} \left[\frac{Z_L(\Omega)Z_0^*(L, \Omega) - Z_0(L, \Omega)Z_0^*(L, \Omega)}{Z_L(\Omega)Z_0(L, \Omega) + Z_0(L, \Omega)Z_0^*(L, \Omega)} \right], \quad (1.99)$$

where L is the length of the segment, $Z_L(\Omega)$ is the load impedance at $x = L$, and $Z_0(L, \Omega)$ is the spherical-wave characteristic impedance evaluated at $x = L$. The input impedance of a divergent conical bore can be expressed in terms of the spherical-wave pressure reflectance as

$$Z(\Omega) = \frac{Z_0(\Omega)Z_0^*(\Omega)[1 + \mathcal{R}_s(\Omega)]}{Z_0^*(\Omega) - Z_0(\Omega)\mathcal{R}_s(\Omega)}. \quad (1.100)$$

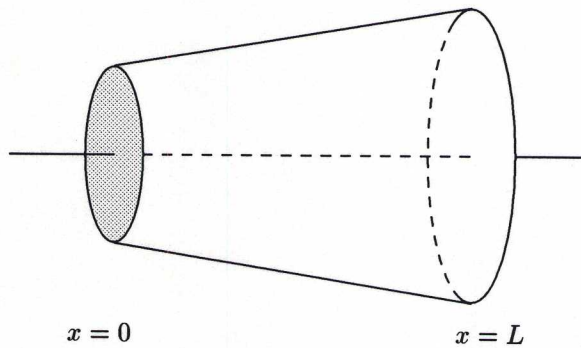


Fig. 1.18. A conical frustum.

Due to the frequency-dependent nature of its characteristic impedance, the divergent conical bore has an impulse response which is more complex than its plane-wave counterpart. Expressed in terms of $r_s(t)$, the impulse response is given by

$$h(t) = \frac{\rho c}{S(0)} [\delta(t) + r_s(t)] + r_s(t) * \left[h(t) - \frac{c}{x_0} \int_0^t h(\lambda) d\lambda \right] - \frac{c}{x_0} \int_0^t h(\lambda) d\lambda, \quad (1.101)$$

where $S(0)$ is the surface area of the spherical wave front at the input end ($x = 0$) and x_0 is the distance from the imaginary cone apex to the input of the conic section. Pressure at the junction of a nonlinear excitation mechanism and a conical air column is then determined from Eq. (1.101) by convolution with the input volume velocity $u(t)$ as (Agulló *et al.*, 1988)

$$p(t) = \frac{\rho c}{S(0)} u(t) + r_s(t) * \left(p(t) + \frac{\rho c}{S(0)} u - \frac{c}{x_0} \int_0^t p(\lambda) d\lambda \right) - \frac{c}{x_0} \int_0^t p(\lambda) d\lambda. \quad (1.102)$$

The spherical-wave pressure reflection function is similar in shape to $r_p(t)$ for open-end discontinuities and decays much faster than the conical bore impulse response. Equation (1.102) thus offers a significantly more efficient means for the time-domain calculation of pressure at the input of a conical section.

The origin of the exponential wake in the impulse response of conical bores is found by considering the impedance relationship between spherical traveling-wave components of pressure and velocity. The frequency-domain expressions are given by

$$P^+(x, \Omega) = Z_0(x, \Omega) U^+(x, \Omega) \quad P^-(x, \Omega) = -Z_0^*(x, \Omega) U^-(x, \Omega) \quad (1.103)$$

where

$$Z_0(x, \Omega) = \frac{\rho c}{S(x)} \left(\frac{1}{1 + \frac{c}{j\Omega x}} \right) \quad Z_0^*(x, \Omega) = \frac{\rho c}{S(x)} \left(\frac{1}{1 - \frac{c}{j\Omega x}} \right) \quad (1.104)$$

The inverse Fourier transform of $Z_0(x, \Omega)$ results in the time-domain impulse response of an anechoic divergent conical bore,

$$h^+(x, t) = \frac{\rho c}{S(x)} \left[\delta(t) - \frac{c}{x} e^{-(c/x)t} \epsilon(t) \right], \quad (1.105)$$

where $\epsilon(t)$ is the Heaviside unit step function. Equation (1.105) represents the pressure response at x produced by the introduction of a volume velocity impulse at x and $t = 0$. The decaying exponential term is a byproduct of the dispersive character of velocity waves in a cone. The impulse response of an anechoic convergent conical bore cannot be determined from $Z_0^*(x, \Omega)$ because it has no causal inverse Fourier transform. However, by analytic continuation, the z -transform $Z_0^*(x, z)$ can be constructed and inverted to obtain (Gilbert *et al.*, 1990a)

$$h^-(x, t) = -\frac{\rho c}{S(x)} \left[\delta(t) + \frac{c}{x} e^{(c/x)t} \epsilon(t) \right]. \quad (1.106)$$

Agulló *et al.* (1992) also derived this expression using time-domain techniques. The growing pressure exponential term appears to violate the assumed passivity of the conical bore, though a corresponding decreasing volume velocity exponential guarantees conservation of power in the overall system.

Also, a traveling wave cannot propagate indefinitely toward the apex of a physically realizable cone. Whether the cone is complete or truncated, reflected traveling waves will combine to cancel the growing exponential and ensure the complete system is passive. This point is underscored by the previous analysis of input admittances in conical sections. It was found in Eq. (1.69), for example, that the input admittance seen looking into a complete convergent cone is proportional to $[-j \cot(kL) - 1/(jkL)]$, which when transformed to the time-domain, represents an infinite series of impulses and their associated exponential wakes separated by $2L/c$. For an initial volume velocity impulse excitation at the wide end of the cone, the increasing exponential term associated with the traveling-wave component of pressure propagating toward the cone tip and the inverted, negatively increasing exponential term associated with the reflected pressure traveling-wave component propagating away from the cone tip must therefore almost completely cancel out to produce the sequence of impulses. Growing exponential wakes occur between the impulses because of the delay L/c which occurs before the first reflection from the apex. The principal problem posed by the expressions which contain growing exponentials does not affect the analysis of conical sections, but rather time-domain procedures used to calculate the evolution of traveling wave components within a bore composed of many conical sections. In particular, the discretization of variables for calculations using computers introduces potential round-off and limit cycle errors which make exact cancellation of exponential terms impossible. Further, the representation of growing exponentials through the use of digital filters produces inherently unstable systems which cannot be realized in finite precision.

Any discontinuity or nonzero curvature within a wind instrument bore, such as toneholes or variations from perfect cylindrical or conical shape, causes traveling-wave scattering to some extent. Each discontinuity can be characterized by a reflection function, so that the complete bore is described by a series of cascaded reflection functions. This is similar to the cascading of transmission matrices in the frequency-domain, with the important distinction that transmission matrices relate observable wave variables while reflection functions are applied to individual traveling-wave components. Time-domain reflection functions in series are convolved together in a process referred to as *multiconvolution* (Martínez *et al.*, 1988). Digital waveguide techniques for discrete-time modeling of acoustic systems, which are the focus of Chapter 3, closely parallel multiconvolution. For this reason, further discussion of time-domain acoustic modeling issues will be deferred to the analysis of Chapter 3.

1.4 Sound Radiation

The discussion thus far has been principally concerned with the propagation of sound waves within musical instrument bores. When considering finite length ducts, the load impedance at the end of the bore has generally been given by ideal, low-frequency approximations. In order that sound

waves be heard, however, it is necessary that they escape from the bore and propagate into the surrounding environment. The fact that sounds can be heard emanating from a perfect cylindrical bore with an abrupt open end demonstrates the inadequacy of the ideal, $Z_L = 0$, approximation. All wind-blown musical instruments are dependent on a significant amount of sound wave reflection at the end of their air columns, both for the establishment of bore resonances and for proper operation of their self-sustaining excitation mechanisms. This is particularly important for low-frequency or fundamental components. Thus, the wind instrument designer must seek a balance between sound reflection to encourage stable regimes of oscillation and sound transmission for the distribution of instrument sounds into the surrounding environment. Adjustment of bell and tonehole parameters provides the principal means for controlling the sound radiation properties of a wind instrument. The flare of a bell produces a specific impedance mismatch between the bore and the surrounding air, and gives rise to a particular reflection and transmission characteristic. Toneholes not only provide a means for bore length variation but also control sound radiation behavior according to their radius, height, and if present, keypad location. The effect of a bell at the end of a tonehole lattice is significant only at those times when all or most of the toneholes are closed. This section first addresses the behavior of sound waves at the end of an open tube and within bells, followed by an analysis of the sound radiating characteristics of woodwind instrument toneholes.

1.4.1 Non-Flaring Ends

Musical instruments which have no flare at the open end of their air column include organ pipes and flutes. For such cases, it is necessary to determine the sound radiation characteristics at the open end of a cylindrical pipe. The first theoretical results were obtained for a circular piston set in an infinite wall (Lord Rayleigh, 1896; Morse, 1981; Olson, 1957). Assuming the wave front at the open end of the pipe is planar, the load impedance of a cylinder fitted with an infinite flange at its end is given by

$$Z = A + jB, \quad (1.107)$$

where

$$A = Z_0 \left[\frac{(ka)^2}{2} - \frac{(ka)^4}{2^2 \cdot 3} + \frac{(ka)^6}{2^2 \cdot 3^2 \cdot 4} - \dots \right], \quad (1.108)$$

$$B = \frac{Z_0}{\pi k^2 a^2} \left[\frac{(2ka)^3}{3} - \frac{(2ka)^5}{3^2 \cdot 5} + \frac{(2ka)^7}{3^2 \cdot 5^2 \cdot 7} - \dots \right], \quad (1.109)$$

a is the radius of the pipe, k is the propagation wave number, and Z_0 is the characteristic wave impedance of the cylinder (Fletcher and Rossing, 1991). Levine and Schwinger (1948) obtained a rigorous and explicit solution for the radiation of sound from an unflanged circular pipe. For $ka \ll 1$, they found that the cylindrical pipe acts as if lengthened by a fraction of the radius. The end correction in this limit for a cylindrical pipe with no flange is $0.6133a$, compared to $0.85a$ for the flanged pipe. Figure 1.19 shows the magnitudes and end corrections for the flanged and unflanged

approximations, where the reflectance is given by

$$\mathcal{R} = -|\mathcal{R}|e^{-2jkl}. \quad (1.110)$$

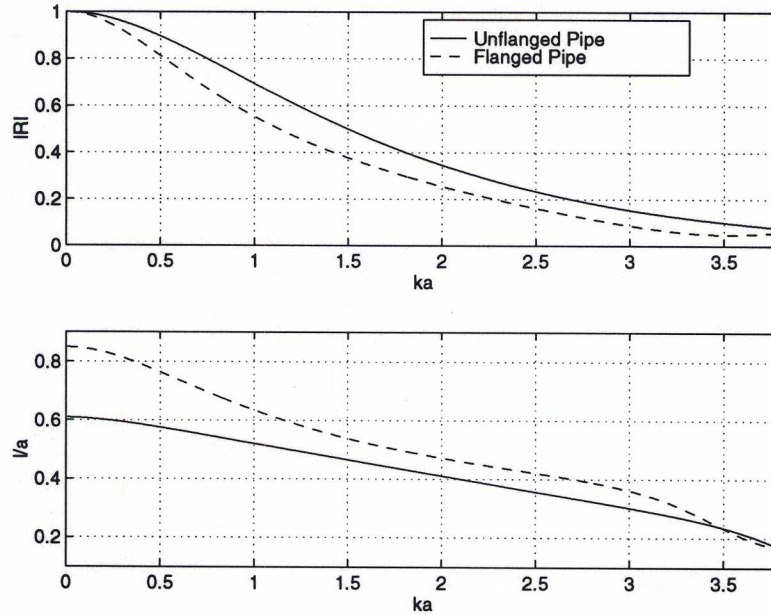


Fig. 1.19. Reflectance magnitude and length correction (l/a) versus the frequency parameter ka for a flanged and unflanged circular pipe.

Because the end correction is frequency dependent, high-frequency wave components experience a longer effective tube length than low-frequency components. This effect causes a slight flattening of higher normal mode frequencies and results in a rolloff of high frequency sound content during steady-state excitation. Despite the frequency dependence of the end correction, however, it is common to approximate the behavior of a cylindrical tube in the low-frequency limit by simply adding the constant end correction term given above to the physical length of the pipe. The reflectance specifies the reflective properties at the end of the bore. The corresponding transmission characteristics for each case are given by a transmittance, which has the complementary relationship $\mathcal{T} = 1 + \mathcal{R}$. Both reflectance magnitudes are seen to approach one as $ka \rightarrow 0$. The results of Levine and Schwinger are generally accepted as representing a better approximation to open-end radiation in musical instruments. Due to the complexity of their solution, approximations are generally made by curve fitting procedures for use in numerical calculations.

No explicit theoretical solution for sound radiation at the open end of a cone exists. For this reason, the impedance at the open end of a cone is usually approximated by

$$Z_{R'} = \frac{S_p}{S_s} Z_R, \quad (1.111)$$

where S_p is the cross-sectional surface area at the end of the cone, S_s is the spherical-wave surface area at the end of the cone, and Z_R is the radiation impedance given by Levine and Schwinger for a cylindrical pipe of cross-section S_p (Caussé *et al.*, 1984).

1.4.2 Horns

The bell at the end of a musical instrument attempts to form a smooth impedance transition from the interior of the bore to the surrounding air. Whereas a stereo speaker cone is designed for maximum sound transmission, a wind instrument bell needs to balance its sound reflection and transmission properties. The bell is a significant component of brass instruments because all sound must radiate through it. However, it is much less important in most woodwind instruments, where sound radiation is principally achieved via the tonehole lattice. Nevertheless, two related methods of analysis have been developed in conjunction with horns that can be used to approximate the slight flare near the end of some woodwind instruments, as well as explore the effects of bore shape perturbations.

One method of analysis involves an approximate solution to the wave equation in an infinite horn of general shape. It is assumed that one-parameter waves can exist and propagate within the horn, that the wave fronts are normal to the horn walls, and that the area of such wave fronts is known. In reality, one-parameter waves are possible only in rectangular, circular cylindrical, and spherical coordinates, which correspond to pipes of uniform cross-section and conical horns, respectively (Putland, 1993). However, wave propagation in horns for which the flare is not too great can be approximated by a one-parameter solution with reasonable accuracy. Referring to Fig. 1.20, the thin shell of air $ABCD$ is considered to have an average surface area $S(x)$, defined by its intersection with the central axis of the horn, and a volume of $S(x) dx$. If this shell is displaced a distance ξ , the volume of the new element $A'B'C'D'$ is given by

$$S(x) dx + dx \frac{\partial}{\partial x} (S\xi). \quad (1.112)$$

Using Newton's and Hooke's laws, the wave equation becomes

$$\frac{1}{S} \frac{\partial}{\partial x} \left(S \frac{\partial p}{\partial x} \right) = \frac{1}{c^2} \frac{\partial^2 p}{\partial t^2}, \quad (1.113)$$

which is known as *Webster's equation* (Webster, 1919). One-parameter waves represent iso-phase surfaces propagating within a horn. Because the pressure is constant across these surfaces, a transformation of the form $p = \psi S^{-1/2}$ can be made so that ψ is constant in magnitude throughout the horn. By writing S in terms of a local equivalent radius a , such that $S = \pi a^2$, Eq. (1.113) becomes

$$\frac{\partial^2 \psi}{\partial x^2} + (k^2 - U) \psi = 0, \quad (1.114)$$

where a sinusoidal time dependence of frequency Ω has been assumed. This form of Webster's equation was given by Salmon (1946a,b) for plane wave fronts and Benade and Jansson (1974a)

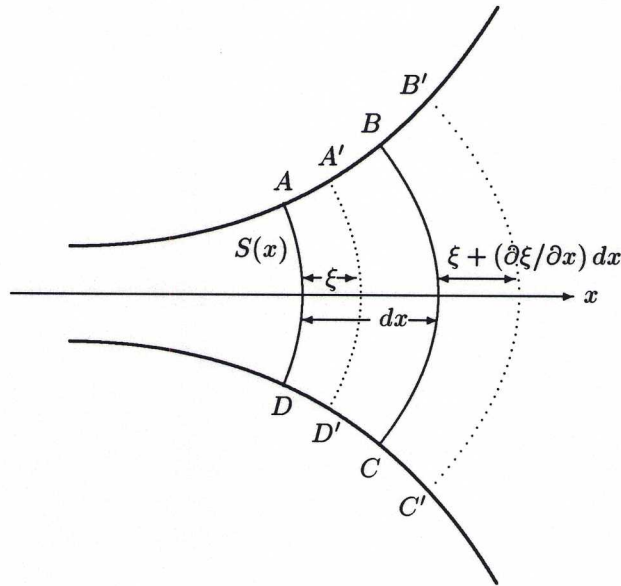


Fig. 1.20. Cross-section of a horn and the displacement of a volume element within it.

subsequently recast it for spherical wave fronts. The horn function U is given by

$$U \equiv \frac{1}{a} \frac{\partial^2 a}{\partial x^2}, \quad (1.115)$$

and determines whether the wave is propagating or nonpropagating at any particular location x . Benade and Jansson point out that Eq. (1.114) is equivalent to the one-dimensional Schroedinger equation of quantum physics, and that U plays the same role in horn theory as does the potential energy function in quantum theory. It is typical to use plane-wave approximations in conjunction with Webster's equation, as this allows analytic solutions for a variety of horn shapes. For horns which flare rapidly, however, this approximation is clearly insufficient. Benade and Jansson (1974*a,b*) show that the use of spherical-wave approximations produce more accurate results and more closely resemble the wave fronts in flaring horns. Plane and spherical waves propagate only in cylinders and cones, respectively, and thus the use of this equation remains an approximation. The determination of horn radiation characteristics using Webster's equation is not of principal concern in this study. This subject, however, will be re-examined in Chapter 2, in conjunction with the effects of bore shape perturbations.

In Section 1.3, a method was discussed for estimating and calculating the acoustical properties of an air column of non-uniform shape using a series of cylindrical or conical sections. This technique represents a discretization of the Webster equation approach. Results obtained using transmission matrices will converge on any analytic solution of the Webster equation in the limit as the length of each acoustic section approaches zero. While analytic solutions are possible for the so-called *Bessel horns* and *exponential horns* using a plane-wave approximation, such solutions are more difficult to

achieve using the spherical-wave approach. Without a closed-form solution, the differential equations must be solved using numerical methods. An alternative horn equation is derived by Keefe *et al.* (1993) which addresses some of these issues.

1.4.3 Toneholes

The influence of open and closed toneholes on wave propagation within a musical instrument bore greatly complicates the ideal behavior discussed for pure cylindrical and conical tubes in Section 1.3. The easiest (and most incorrect) approximation that can be made is to assume that *closed* toneholes have no affect on wave propagation and that the bore is simply truncated at its first open tonehole. Thus, all reflection and transmission of sound waves occurs at the first open tonehole and the radiation properties of an unflanged end found in Section 1.4.1 can be directly applied to the shortened tube. Unfortunately, the actual behavior is far from this simple. Benade (1960) presents an analysis based on the assumption that the tonehole lattice (THL) of woodwind instruments can be approximated by a sequence of uniformly spaced holes of equal size. This approximation begins with the characteristic impedance and propagation wave number relationships for a cylindrical pipe pierced by an infinite sequence of side branches of equal input impedance Z_b and spacing $2s$ (Stewart and Lindsay, 1930, p. 337)

$$Z_c = Z_0 \left(\frac{1 + j (Z_0/2Z_b) \tan(ks)}{1 - j (Z_0/2Z_b) \cot(ks)} \right)^{1/2}, \quad (1.116)$$

$$\cosh(2\Gamma s) = \cos(2ks) [1 + j (Z_0/2Z_b) \tan(2ks)], \quad (1.117)$$

where Z_0 is the wave impedance of the main air column. These equations are derived by assuming continuity of volume flow and conservation of mass at the junctions of the main bore and side branches, and are applicable to plane-wave propagation only. The side branch impedance for a closed tonehole of length t is approximated by that of an open-closed cylindrical section, $-jZ_{b0} \cot(kt)$, where Z_{b0} is the real characteristic impedance of the tonehole, while the impedance for an open tonehole of effective length t_e is approximated by that of an open-open cylindrical section, $jZ_{b0} \tan(kt_e)$, as derived in Section 1.3.1. For a lattice of closed toneholes, Benade shows that Eqs. (1.116) and (1.117) can be written in the low-frequency limit as

$$Z_c^{(c)} = Z_0 \left(1 + D^{(c)} \right)^{1/2}, \quad (1.118)$$

and

$$v_p^{(c)} = \frac{c}{(1 + D^{(c)})^{1/2}}, \quad (1.119)$$

where $D^{(c)} = (1/2)(b/a)^2(t/s)$, $v_p^{(c)}$ is the closed-THL phase velocity, a is the radius of the main bore, and b is the radius of the toneholes. These equations imply that the closed THL has a larger “effective” cross section and a lower phase velocity than that of a simple, unpierced cylindrical pipe

of the same radius. The effect of the phase velocity variation can be viewed in terms of an equivalent length correction. Similarly, the open-THL characteristic impedance and wave number are given in the low-frequency limit by (Keefe, 1990)

$$Z_c^{(o)} = jZ_0 k C^{(o)}, \quad (1.120)$$

and

$$2\Gamma^{(o)} s = 2\sqrt{D^{(o)}} \left[1 - (a/b)^2 (2ks)(kt_e) \left(1 + \frac{2}{3} D^{(o)} \right) \right]^{1/2}, \quad (1.121)$$

where $D^{(o)} = (1/2)(b/a)^2(s/t_e)$ and

$$C^{(o)} = s \left(\frac{1 + D^{(o)}}{D^{(o)}} \right)^{1/2} \quad (1.122)$$

is the open-hole lattice length correction. The characteristic impedance of Eq. (1.120) has the form of an inductance, so that the open THL forms a “masslike” termination to a cylindrical bore. The propagation wave number given by Eq. (1.121) is purely real in the low-frequency limit, so that there is no wavelike propagation in the open-hole section of the bore. Rather, the pressure variations along this portion of the air column are in phase and damped exponentially with distance from the first open hole. The open THL behaves like a highpass transmittance filter and reflects low-frequency sound waves back into the closed-hole portion of the bore. Benade (1960) offers a variety of interesting observations regarding tonehole lattices, though his results are generally limited to low-frequency characteristics.

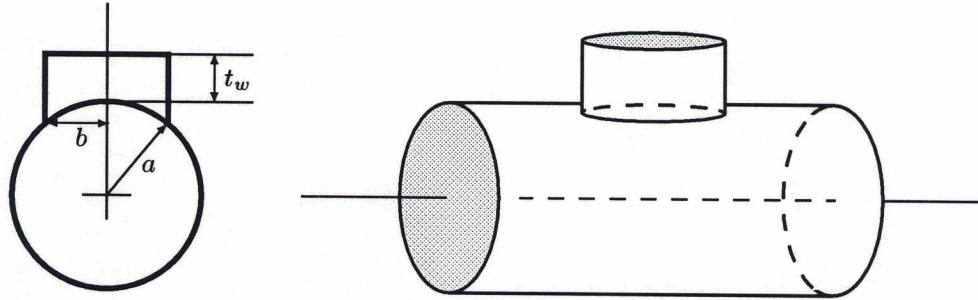


Fig. 1.21. Basic tonehole geometry.

The largest single contribution to the theory of toneholes was made by Keefe (1981). His analysis is principally concerned with a single tonehole, which can then be extended to a series of toneholes by linear superposition. By separating the acoustic disturbance at the discontinuity into two parts, corresponding to even and odd symmetry of the fundamental mode about the center of the tonehole, a lumped circuit representation for a single tonehole discontinuity is shown to be

$$\begin{bmatrix} P_0 \\ U_0 \end{bmatrix} = \begin{bmatrix} 1 & Z_a \\ Z_s^{-1} & 1 \end{bmatrix} \begin{bmatrix} P_1 \\ U_1 \end{bmatrix} \quad (1.123)$$

in the limit $|Z_a/Z_s| \ll 1$. The elements Z_s and Z_a are referred to as the shunt and series impedances, respectively, of the T section transmission-line model and their values depend on whether the tonehole is open (o) or closed (c) as follows

$$Z_s^{(o)} = Z_0(a/b)^2 (jkt_e + \xi_e), \quad (1.124a)$$

$$Z_s^{(c)} = -jZ_0(a/b)^2 \cot(kt), \quad (1.124b)$$

$$Z_a^{(o)} = -jZ_0(a/b)^2 kt_a^{(o)}, \quad (1.124c)$$

$$Z_a^{(c)} = -jZ_0(a/b)^2 kt_a^{(c)}. \quad (1.124d)$$

The tonehole height t is defined such that its product with the cross-sectional area of the tonehole is exactly equal to the geometric volume V_h of the tonehole (Keefe, 1990). For a typical tonehole structure, such as shown in Fig. 1.21, t is well approximated by

$$t = t_w + \frac{1}{8}b(b/a) [1 + 0.172(b/a)^2], \quad (1.125)$$

where a is the radius of the main bore of the instrument, b is the radius of the tonehole, and t_w is the shortest distance from the top of the tonehole to the main bore. The open-tonehole effective length t_e depends on the presence or absence of a pad above the hole. If no pad is present,

$$t_e = \frac{k^{-1} \tan(kt) + b [1.40 - 0.58(b/a)^2]}{1 - 0.61kb \tan(kt)}, \quad (1.126)$$

and if a pad of diameter $2R$ is placed an average height h above the tonehole, then

$$t_e = \frac{k^{-1} \tan(kt) + b \{0.61(R/b)^{0.18}(b/h)^{0.39} + (\pi/4) [1 - 0.74(b/a)^2]\}}{1 - 0.61(R/b)^{0.18}(b/h)^{0.39}kb \tan(kt)}. \quad (1.127)$$

The specific resistance ξ_e of the open tonehole is given by

$$\xi_e = 0.25(kb)^2 + \alpha t + (1/4)kd_v \ln(2b/r_c), \quad (1.128)$$

where r_c is an effective radius of curvature of the external end of the tonehole wall, $d_v = \sqrt{2\eta/(\rho\omega)}$ is the viscous boundary layer thickness in terms of the shear viscosity of air η , and α is the real part of the propagation wavenumber within the tonehole, as discussed in Section 1.3.3. The specific resistance accounts for viscothermal losses along the tonehole walls and radiation at the open end. The open and closed tonehole series equivalent lengths are

$$t_a^{(o)} = \frac{0.47b(b/a)^4}{\tanh(1.84t/b) + 0.62(b/a)^2 + 0.64(b/a)}, \quad (1.129)$$

$$t_a^{(c)} = \frac{0.47b(b/a)^4}{\coth(1.84t/b) + 0.62(b/a)^2 + 0.64(b/a)}. \quad (1.130)$$

While these equations present a substantial increase in analytic complexity compared with that of Benade, there are similarities between the two analyses. The closed tonehole shunt impedance is just that of a cylindrical tube of length t and radius b , and plays the same role as Z_b in Eq. (1.116).

In the low-frequency limit, this reduces to a cavity impedance with volume V_h . The open tonehole shunt impedance is likewise similar to that used by Benade, though the $\tan(kt)$ factor is found in the definition of t_e . The other terms in t_e express the acoustical inertance localized at the intersection of the tonehole with the main bore and the radiation inertance localized just outside the tonehole. In the low-frequency limit, this impedance term reduces to that of an acoustic inertance. The series impedance terms are additions to the theory of Benade and represent negative length corrections to the main bore length due to the presence of the tonehole. The tonehole is theoretically represented by a lumped impedance located at the midpoint of the tonehole. The negative length correction terms thus serve to offset the overestimated bore length parameters on both sides of the tonehole. The predicted closed- and open-hole series length correction terms are of similar order.

The pressure and flow at the two ends of the combined main bore and tonehole system, shown in Fig. 1.21, are related by

$$\begin{bmatrix} P_0 \\ U_0 \end{bmatrix} = \begin{bmatrix} \cosh(\Gamma L) & Z_c \sinh(\Gamma L) \\ Z_c^{-1} \sinh(\Gamma L) & \cosh(\Gamma L) \end{bmatrix} \begin{bmatrix} 1 & Z_a \\ Z_s^{-1} & 1 \end{bmatrix} \begin{bmatrix} \cosh(\Gamma L) & Z_c \sinh(\Gamma L) \\ Z_c^{-1} \sinh(\Gamma L) & \cosh(\Gamma L) \end{bmatrix} \begin{bmatrix} P_{2L} \\ U_{2L} \end{bmatrix}, \quad (1.131)$$

where the tonehole is exactly centered on the main cylindrical air column of total length $2L$ and the lossy, complex propagation wave number Γ and characteristic impedance Z_c are determined as discussed in Section 1.3.3. The analysis of an entire tonehole lattice using cascaded transmission matrices can be carried out assuming that there are no interactions between the toneholes. The tonehole discontinuity, however, results in the conversion of acoustical energy from the propagating one-dimensional wave front to higher order evanescent modes. The evanescent modes decay over a length approximately equal to a duct diameter for low frequencies (Keefe, 1983). Thus, if consecutive tonehole edges are separated by less than two times the duct diameter, there will be an overlap of tonehole disturbances, and the tonehole lattice can no longer be analyzed as a set of independent tonehole units. Further, there is also the possibility of external interactions between open holes. Keefe (1983) estimated the effects of such internal and external tonehole interactions and found that they are most significant in woodwinds with large diameter holes and short tonehole chimneys, such as found on saxophones and Boehm style flutes. An improved theory of external interactions is given by Kergomard (1989). In general, the external interactions are much less significant than those inside the bore and do not significantly change the effective length of the tonehole at low frequencies.

Keefe's derivation of the tonehole parameters is based on a symmetric T section, as shown in Fig. 1.22. The resulting transmission matrix for this system is

$$\begin{bmatrix} P_1 \\ U_1 \end{bmatrix} = \begin{bmatrix} 1 & Z_a/2 \\ 0 & 1 \end{bmatrix} \begin{bmatrix} 1 & 0 \\ Z_s^{-1} & 1 \end{bmatrix} \begin{bmatrix} 1 & Z_a/2 \\ 0 & 1 \end{bmatrix} \begin{bmatrix} P_2 \\ U_2 \end{bmatrix} \quad (1.132)$$

$$= \begin{bmatrix} 1 + \frac{Z_a}{2Z_s} & Z_a \left(1 + \frac{Z_a}{4Z_s}\right) \\ Z_s^{-1} & 1 + \frac{Z_a}{2Z_s} \end{bmatrix} \begin{bmatrix} P_2 \\ U_2 \end{bmatrix}. \quad (1.133)$$

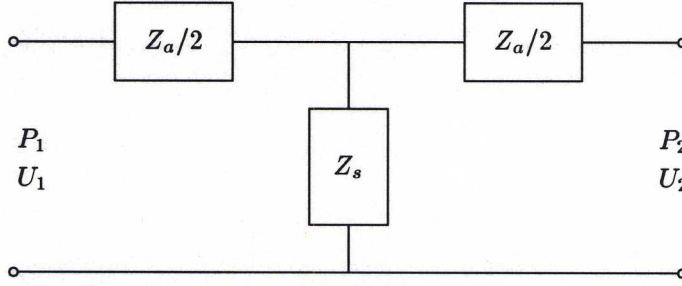


Fig. 1.22. *T* section transmission-line element representing the tonehole.

The transmission matrix given by Eq. (1.123) results for the assumption that $|Z_a/Z_s| \ll 1$. In (Keefe, 1990), an *L* section, such as shown in Fig. 1.23, is used to simplify the calculation process. This

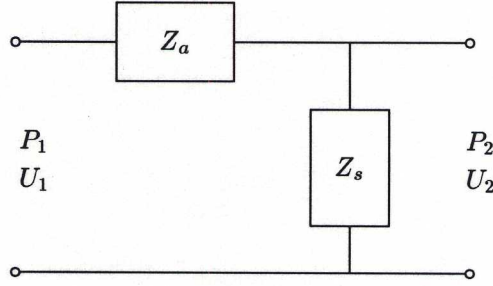


Fig. 1.23. *L* section transmission-line element representing the tonehole.

structure is represented by

$$\begin{bmatrix} P_1 \\ U_1 \end{bmatrix} = \begin{bmatrix} 1 & Z_a \\ 0 & 1 \end{bmatrix} \begin{bmatrix} 1 & 0 \\ Z_s^{-1} & 1 \end{bmatrix} \begin{bmatrix} P_2 \\ U_2 \end{bmatrix} \quad (1.134)$$

$$= \begin{bmatrix} 1 + \frac{Z_a}{Z_s} & Z_a \\ Z_s^{-1} & 1 \end{bmatrix} \begin{bmatrix} P_2 \\ U_2 \end{bmatrix}, \quad (1.135)$$

which still reduces to Eq. (1.123) for $|Z_a/Z_s| \ll 1$.

Figure 1.24 plots the input impedance magnitude and reflectance for the written note G_4 on a simple six-hole flute, calculated using *L* section tonehole transmission matrices. The dimensions of the instrument are described in (Keefe, 1990). Both plots show significant departure from ideal cylindrical bore behavior and offer some insight into the effects of both open and closed toneholes. In particular, the sharp dip in the reflectance around 1200 Hz indicates the open-THL cutoff frequency. Experimental measurements to verify the tonehole theory were conducted by Keefe for frequencies below about 5 kHz, so that results above this limit are purely theoretical. Nonetheless, this formulation contributes immensely to the determination of tonehole behavior in woodwind instruments. Tonehole lattice approximations which incorporate the effects of the tonehole series impedance can be obtained in terms of the single unit *T* section matrix coefficients of Eq. (1.131) (Keefe, 1981,

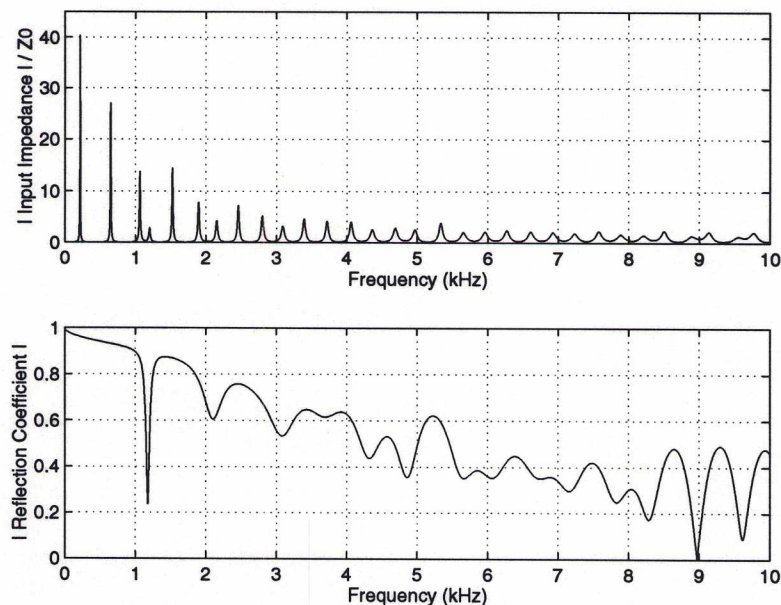


Fig. 1.24. Input impedance magnitude (top), relative to the main bore wave impedance Z_0 , and reflectance (bottom) for the written note G_4 on a simple six-hole flute, as described in Keefe (1990).

1990). Such an analysis, however, offers little insight into tonehole lattice behavior beyond the results of Benade (1960). The tonehole theory described in this section has recently been improved upon in the dissertation of Veronique Dubois (1996), Le Mans, France (Keefe, 1997).

1.5 The Nonlinear Excitation Mechanism

The single-reed and mouthpiece arrangement of clarinets and saxophones, as shown in Fig. 1.25, acts as a pressure-controlled valve which allows energy into the instrument for the initialization and maintenance of oscillations in the acoustic resonator. It plays the same role as the human lips to brass instruments or the bow to stringed instruments. There are several nonlinear aspects of this mechanism, one of which is demonstrated by the fact that DC pressure applied by a player is converted into acoustic energy at a number of harmonically related frequencies. Single-reed mechanisms are the primary focus in this section, though reference will be made when appropriate to other excitation processes. Double-reeds have been scarcely studied to date and thus little is understood about the complexities of their behavior (Hirschberg *et al.*, 1995).

In the simplest terms, the reed movement is controlled by the pressure difference between the player's oral cavity and the pressure in the reed channel or inside the mouthpiece, $p_\Delta = p_{oc} - p_r$. The oral cavity pressure is typically assumed constant and tends to force the reed toward the mouthpiece lay. Negative pressure in the mouthpiece tends to reinforce this action, pulling the reed toward the lay, while positive pressure in the mouthpiece, if acting alone, tends to push the reed away from the

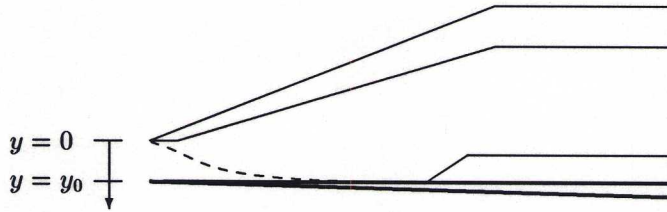


Fig. 1.25. A single-reed woodwind mouthpiece.

mouthpiece lay. The reed itself is a damped mechanical oscillator, with a substantial portion of its damping coming from the player's lower lip. The single-reed valve is initially open but can be blown shut against the mouthpiece lay by an appropriate pressure p_Δ , as depicted in Fig. 1.26. This model was first expressed by Worman (1971).

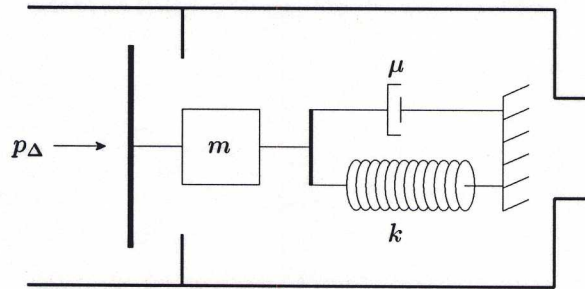


Fig. 1.26. The single-reed as a mechanical oscillator blown closed.

Some of the earliest research on musical instrument reeds was conducted by Helmholtz, who concluded that pipes excited by inwardly striking reeds “of light material which offers but little resistance” produce tones at frequencies corresponding to the resonant frequencies of the pipe, which are much lower than the natural frequency of the reed itself (Helmholtz, 1954, p. 390). The lowest resonance frequency of a typical clarinet reed falls approximately in the range 2-3 kHz, while normal playing frequencies for clarinets are below 1 kHz. A mass-spring system driven at a frequency well below resonance is said to be stiffness dominated and its displacement amplitude will approach f/k , where k is the spring constant and f is the applied force. Thus, a common simplification for woodwind instruments has been to neglect the effect of the mass altogether and to simply model the reed system as a memory-less nonlinearity (Backus, 1963; Nederveen, 1969; McIntyre *et al.*, 1983). This is equivalent to assuming an infinite reed resonance frequency. Assuming the force on the reed is equal to $S_r \cdot p_\Delta$, where S_r is the effective surface area of the reed exposed to p_Δ , the displacement of the reed from its equilibrium position y_0 is given by Hooke's law as

$$y = y_0 - \frac{S_r \cdot p_\Delta}{k}. \quad (1.136)$$

The movement of the reed controls the volume flow through the reed channel and into the

mouthpiece, which is typically determined from the Bernoulli equation for steady flow (Backus, 1963; Worman, 1971; Wilson and Beavers, 1974; Thompson, 1979; Saneyoshi *et al.*, 1987; Fletcher and Rossing, 1991). The oral cavity is viewed as a large tank with essentially constant pressure p_{oc}

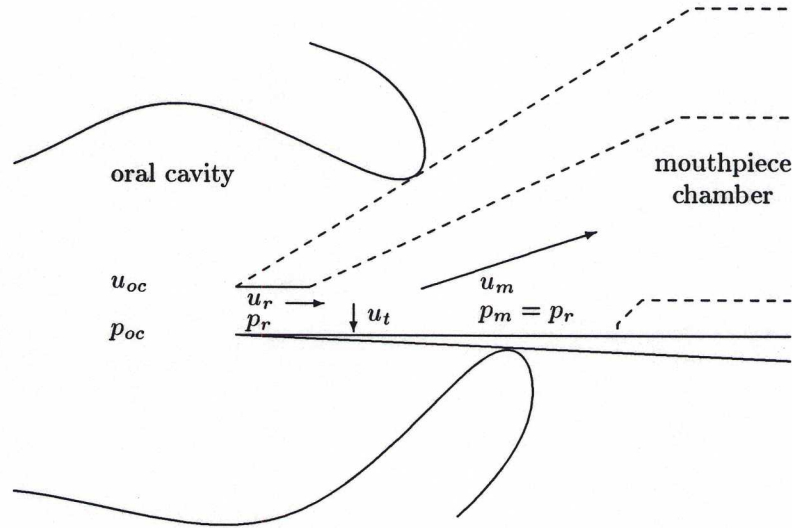


Fig. 1.27. The volume flow and pressure relationships for a single-reed oral cavity/mouthpiece geometry.

and zero volume flow u_{oc} . By conservation of energy, Bernoulli's equation gives

$$u_r = w y \left(\frac{2p_\Delta}{\rho} \right)^{1/2} \text{sgn}(p_\Delta), \quad (1.137)$$

where y and w are the height and width of the reed channel, respectively, and ρ is the density of air. Backus (1963) measured the volume flow through a reed aperture for known blowing pressures, and proposed a modified version of Eq. (1.137) of the form

$$u_r = \gamma y^{4/3} p_\Delta^{2/3}, \quad (1.138)$$

where γ is a constant dependent on the reed channel width and the density of air. He attributed the differences in his results from Eq. (1.137) to the curvature of the lay and the flexibility of the reed tip. Backus (1963) also determined expressions for the threshold blowing pressure necessary to set the reed in motion and fractional frequency shifts due to reed channel height adjustments by a performer. Hirschberg *et al.* (1990, 1994) point out that Eq. (1.137) is derived by assuming flow separation from the wall at the end of the reed channel and formation of a free jet into the mouthpiece. The reed channel itself is considered of uniform cross-section and pressure throughout its length. The free jet is a region of high velocity bounded by shear layers. Rotational motion along these layers causes the free jet to be inherently unstable, breaking down into vortical structures which are eventually

dissipated by turbulence (Hirschberg *et al.*, 1995, p. 314). In a turbulent region, viscous dissipation of kinetic energy is dominant and the Bernoulli equation is not valid. Thus, it is reasonable to expect that pressure will not be recovered in the mouthpiece region beyond the reed channel, as might be presumed from the Bernoulli equation. Instead, the mouthpiece and reed channel pressures are assumed equivalent and conservation of volume flow to hold in the mouthpiece chamber.

Much research has been conducted during the past decade on the aero-acoustics[†] of musical instruments. In the study of reeded organ pipes, Hirschberg *et al.* (1990) have shown the need to account for friction due to flow reattachment in the reed channel. However, the present understanding with regard to clarinet and saxophone geometries indicates that such friction is not significant in these systems due to the shortness of the reed channel. Thus, Eq. (1.137) is a good first approximation. It appears that experimental measurements in the presence of *unsteady* flow are needed to gain further understanding of the complex aero-acoustic relationships in these instruments (Hirschberg *et al.*, 1994).

Equations (1.136) and (1.137) may be combined to find the reed channel volume velocity in the presence of a mass-less reed valve

$$\begin{aligned} u_r &= w \left(y_0 - \frac{S_r \cdot p_\Delta}{k} \right) \left(\frac{2p_\Delta}{\rho} \right)^{1/2} \text{sgn}(p_\Delta) \\ &= w y_0 \left(1 - \frac{p_\Delta}{p_C} \right) \left(\frac{2p_\Delta}{\rho} \right)^{1/2} \text{sgn}(p_\Delta), \end{aligned} \quad (1.139)$$

where $p_C = ky_0/S_r$ is the pressure necessary to push the reed against the mouthpiece facing and completely close the reed channel. Under normal playing conditions, steady-state pressure and flow in the reed channel and mouthpiece will be made up of oscillating and non-oscillating components. For the static or non-oscillating regime, p_Δ can be approximated by p_{oc} because the reed channel pressure will be nearly zero. This is substantiated by the fact that the input impedance at zero frequency in the bore, which results from thermoviscous losses only, is very small (Hirschberg *et al.*, 1995, p. 236). Under this approximation, the reed channel volume velocity for static flow is given by

$$u_{ro} = w y_0 \left(1 - \frac{p_{oc}}{p_C} \right) \left(\frac{2p_{oc}}{\rho} \right)^{1/2}. \quad (1.140)$$

Equation (1.139) can then be expressed in terms of its static and dynamic pressure components as (Hirschberg *et al.*, 1995, p. 237)

$$u_r = u_{ro} \left(1 + \frac{p_r}{p_C - p_{oc}} \right) \left(1 - \frac{p_r}{p_{oc}} \right)^{1/2} \quad \text{if } p_{oc} > p_r > p_{oc} - p_C, \quad (1.141a)$$

$$u_r = 0 \quad \text{if } p_r \leq p_{oc} - p_C, \quad (1.141b)$$

[†]Aero-acoustics is the study of the coupling between a region in space where linear wave propagation prevails and flow regions where nonlinear phenomena are essential and responsible for the transfer of energy to the acoustical flow (Hirschberg *et al.*, 1994).

$$u_r = -u_{ro} \left(1 + \frac{p_r}{p_C - p_{oc}} \right) \left(\frac{p_r}{p_{oc}} - 1 \right)^{1/2} \quad \text{if } p_r > p_{oc}. \quad (1.141c)$$

Figure 1.28 illustrates the nonlinear *steady* volume flow characteristic given by Eq. (1.140) for $0 \leq p_{oc} \leq p_C$. An initial increase in the oral cavity pressure results in a rapid increase in u_{ro} . However, a continued increase in p_{oc} begins to force the reed toward the mouthpiece lay, resulting in a decrease of volume flow. When $p_{oc} = p_C$, the reed valve is completely closed. Figure 1.29 displays the nonlinear *dynamic* volume flow characteristic given by Eqs. (1.141a)–(1.141c) for a constant oral cavity pressure $p_{oc}/p_C = 0.4$. In this context, the oral cavity pressure can be understood to push the reed some constant distance toward the mouthpiece lay. The dynamic flow then results from the varying reed channel pressure p_r inside the mouthpiece. For values of $p_r/p_C \leq -0.6$ in Fig. 1.29, the volume flow is zero because $p_r \leq p_{oc} - p_C$. In this range, the reed channel pressure is negative, which in conjunction with the positive oral cavity pressure, serves to pull the reed against the mouthpiece lay and stop all volume flow. As p_r increases in the range $p_{oc} > p_r > p_{oc} - p_C$, the reed channel volume flow increases rapidly, but then decreases as p_r approaches p_{oc} and a resultant $p_\Delta = 0$. When the reed channel pressure exceeds the oral cavity pressure, negative flow into the mouth occurs.

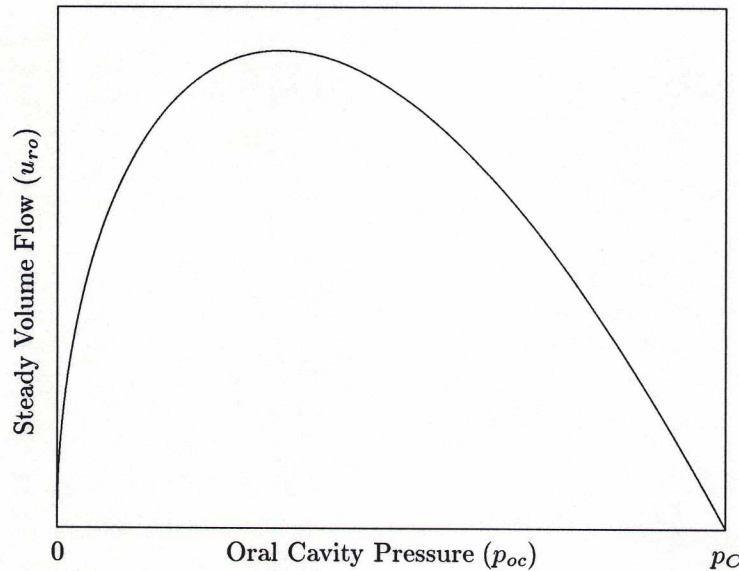


Fig. 1.28. Steady flow (u_{ro}) through a pressure controlled valve blown closed.

For dynamic regimes of flow, u_r leaving the reed channel is divided into two parts, as shown in Fig. 1.27. The flow u_m enters the mouthpiece chamber, while the motion of the reed surface results in a flow $u_t = S_r(dy/dt)$. As mentioned above, the mouthpiece chamber pressure p_m is assumed equal to the reed channel pressure p_r . An additional Bernoulli flow-induced force on the reed was proposed by Worman (1971), though Hirschberg *et al.* (1990) have pointed out that the existence

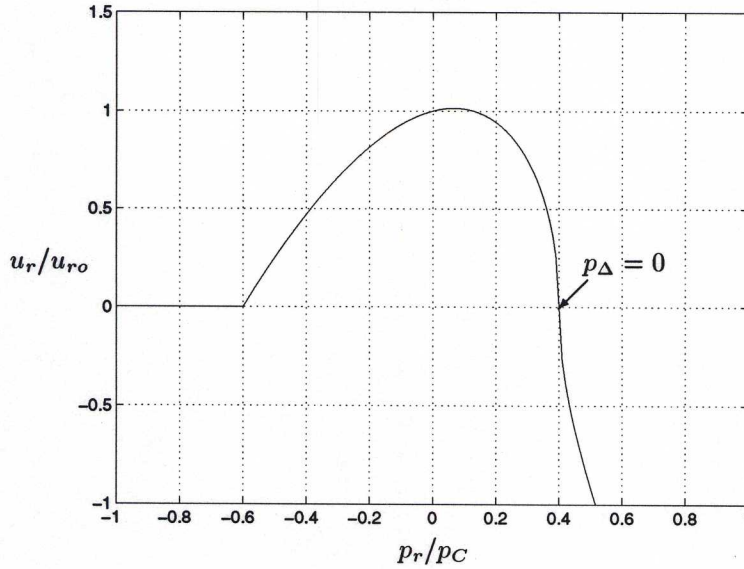


Fig. 1.29. Dynamic flow through a pressure controlled valve blown closed for $p_{oc}/p_C = 0.4$.

of such a force would violate the assumptions used to derive Eq. (1.137). Another modification to the flow control equations involving nonlinearity of the reed stiffness has been discussed by Gilbert *et al.* (1990b). Behavior of this sort seems reasonable because of the asymmetrical shape of the reed and the magnitude of the reed displacement. However, experiments to determine the extent of this possible effect have not been conducted.

The normal playing range of clarinets and saxophones is typically well below the first resonance frequency of the reed, thus justifying the use of Eq. (1.136). However, extended range playing has become increasingly common on these instruments, so that reed mass need be accounted for to properly model reed motion at these high frequencies. Stewart and Strong (1980) and Sommerfeldt and Strong (1988) modeled the reed as a damped, driven, nonuniform bar using a fourth-order differential equation. In this way, changes in effective mass and stiffness with bending along the curvature of the lay are automatically incorporated. For the purposes of this study, however, such added complexity is unnecessary. Instead, the reed can be modeled as a simple damped harmonic oscillator, and if desired, the reed parameters can be made functions of reed displacement to simulate nonlinear effects due to the mouthpiece geometry and reed shape. The motion of a second-order mass-spring system is given by

$$m \frac{d^2 y}{dt^2} + \mu \frac{dy}{dt} + k(y - y_0) = -S_r p_\Delta(t). \quad (1.142)$$

where m is the equivalent reed mass, μ is the damping factor, and k is the reed spring constant. The natural frequency of the mass-spring system in the absence of damping and for constant reed parameters is $\Omega_o = \sqrt{k/m}$. A closed-form solution to the volume flow relationships in the reed

channel, such as given by Eq. (1.141a), is impossible when the reed motion is described as in Eq. (1.142). However, modeling techniques can easily handle these equations as well as incorporate time- and space-varying parameters, as will be discussed in Chapter 3.

Linear approximations to the operation of the reed have been made by assuming steady-state, low amplitude oscillations, so that p, y , and u vary sinusoidally about equilibrium values. In this situation, an approximate expression for the acoustic admittance can be derived that sheds some intuitive light on the operation of the reed (Fletcher, 1979). If the reed generator admittance defined from the mouthpiece is given by Y_r and the instrument bore admittance is Y_b , then the conditions for steady-state excitation are

$$\Re(Y_r + Y_b) = 0, \quad (1.143a)$$

$$\Im(Y_r + Y_b) = 0. \quad (1.143b)$$

The condition of Eq. (1.143a) corresponds to the equalization of radiation and thermoviscous losses in the bore and energy input via the reed mechanism. The imaginary component of Y_r is positive for reeds blown closed, so that by Eq. (1.143b), $\Im(Y_b)$ must be negative. This will occur at frequencies just below bore resonances, so that reed woodwind instruments should sound slightly flat compared to their natural stopped-pipe normal modes.

Chapter 2

Acoustical Aspects of Woodwind Design & Performance



"Posterity will never forgive you, Adolphe Sax!" (Shafer, 1950)

Despite the fairly detailed mathematical analysis of woodwind instrument acoustic principles presented in Chapter 1, the design and manufacture of musical instruments remains largely an empirical art to this day. This is due in part to the lack of a thorough acoustic theory regarding composite musical instrument systems. That is, while the isolated behavior of individual components may be well understood, the interaction of these components within the complete instrument is not. In this chapter, the design and performance of single-reed woodwind instruments is studied in a semi-empirical, semi-theoretical manner. Much of the acoustic behavior analyzed in Chapter 1 is reconsidered here in

a more intuitive fashion. This discussion will provide insight into common instrument shortcomings and possibly suggest means for their correction. This author has extensive professional performance experience, particularly with regard to contemporary saxophone techniques, and is acutely aware of the more subtle aspects of instrument performance. The insights gained from this experience, combined with a solid foundation in acoustic principles, provide a unique perspective throughout this study.

Both the designer and performer have control over the response and intonation of a musical instrument. As will be seen, a variety of adjustments can be made during the design and manufacturing processes to a woodwind's air column shape and tonehole parameters which have direct consequences on the instrument's resonance structure. The choice of a mouthpiece, particularly for conical bored instruments, also is important in determining the overall tone quality. While playing, the performer uses lip pressure and position adjustments, together with oral cavity manipulations, to influence the behavior of the instrument.

The analysis of this chapter will be particularly oriented toward the frequency-domain characteristics of a musical instrument. The position and magnitude of an instrument's resonances provide an accurate means for determining its response and intonation. The nature of the single-reed excitation mechanism is such that if several of the air column resonances are aligned in integer multiple relationships, a stable *regime of oscillation* will result (Benade, 1976, p. 395). Conventional steady-state sounds produced by wind instruments are quasi-periodic, which means that their spectral components are related to the fundamental frequency by integer multiples. The nonlinear action of the reed promotes the distribution of oscillatory energy among the higher harmonics of the fundamental mode of vibration. Thus, it is desired that the normal modes of an instrument be properly aligned over its complete range. When investigating the influences of various design perturbations or performer controls, such considerations will form the basis of the analysis.

2.1 Woodwind Air Columns

The air column of a woodwind plays a crucial role in determining the overall quality of the instrument. From the musician's point of view, the instrument should "speak" easily at all dynamic levels and be "in tune" with itself over its complete range. In addition to supporting sound production at a particular fundamental frequency, the wind instrument bore can facilitate stable regimes of oscillation by emphasizing frequencies which are aligned in integral multiples to the fundamental. The better aligned the air column resonances are for a particular note, the easier that note will "speak." It is also necessary that the partial structure of the air column be independent of its length. In this way, the bore length can be varied to produce a continuum of pitches without affecting the timbre or tone quality of the instrument. As discussed in Chapter 1, the only useful bore shapes which meet the above requirements are cylinders and cones.

In evaluating the acoustical quality of a musical instrument bore, it is common to measure and/or calculate the structure's input impedance. For instruments which have pressure-controlled excitation mechanisms, the impedance peak positions correspond to air column resonance frequencies. The magnitudes of these peaks indicate the relative strength of such resonances. Because wind instrument excitation mechanisms are dependent on feedback from their attached air columns for proper operation, sound production is particularly favored at input impedance peaks. In the case of single-reed woodwinds, the air column resonances essentially control the reed vibrations. For small-amplitude vibrations, or at a *piano* (*p*) dynamic level, the reed will typically begin to oscillate at the strongest air column resonance frequency. At louder playing levels, this regime will be further supported by harmonically related higher air column modes. If the lower resonances are misaligned in some way, response will be negatively influenced and/or the reed may find a more stable regime based on a different fundamental frequency. Misalignment of high air column resonances will have less affect on the stability of the sound, but will alter the resulting sound quality or timbre.

2.1.1 Cylinders and Cones

The axial normal modes of cylindrical and conical air columns are typically estimated by applying ideal boundary conditions at each end of the tube and neglecting viscothermal losses along the walls. In this sense, a closed end is assumed perfectly rigid and represented by an infinite impedance, while an open end is approximated in the low-frequency limit by an impedance of zero. Such an approach was taken in Section 1.3.1 and the resonance frequencies of a closed-open cylindrical pipe were found for $n = 1, 2, \dots$ to be

$$f^{(c-o)} = \frac{(2n-1)c}{4L}, \quad (2.1)$$

where c is the speed of sound in air and L is the length of the tube. Similarly, the resonance frequencies of a *complete* cone are given for $n = 1, 2, \dots$ by

$$f = \frac{nc}{2L}, \quad (2.2)$$

as determined in Section 1.3.2. The fundamental resonance frequency of a closed-open cylindrical pipe has a corresponding wavelength equal to four times the pipe length and higher resonances occurring exactly at odd integer multiples of the fundamental. The partials of a complete cone occur at all integer multiples of the fundamental frequency, which has a corresponding wavelength equal to two times the cone length. The resonances of an air column indicate frequencies at which excitation is constructively supported, while excitation at an anti-resonance is destructively influenced. Thus, single-reed musical instruments formed from a cylindrical bore produce steady-state sounds principally comprised of odd harmonics. Further, the 1:3 ratio of the first two resonances in such instruments indicate that they overblow at the twelfth. Instruments with conical bores produce steady-state sounds having a complete harmonic spectrum and overblow at the octave, as implied by the 1:2 ratio of their first two resonances.

When cylindrical and conical air columns are analyzed in terms of more *physically realistic* boundary conditions, however, variations from the above ideal behavior are found. Two theoretical solutions for sound reflection/radiation at the open end of a cylindrical pipe were discussed in Section 1.4.1. In both cases, the open end is represented by a frequency-dependent load impedance. Figure 2.1 shows the open-end impedance magnitude, normalized by the wave impedance $Z_0 = \rho c/S$, as determined by Levine and Schwinger (1948) for an unflanged cylindrical pipe of radius 0.0075 meters (similar to that of a typical clarinet). Sound waves traveling from within the bore experience an impedance change at the open end of the pipe which is greatest for low-frequency components, as given in the figure by small ratios of radiation impedance to wave impedance. On the other hand, high-frequency sound components are least affected by the open end, as indicated in Fig. 2.1 by near-unity impedance ratios. The magnitude of the impedance change indicates the relative strength of sound-wave reflection at the open end. In this way, low-frequency sound components are more completely reflected back into the bore while high-frequency components are largely transmitted out the open end of the tube. Seen from within the bore, this corresponds to a reduction in the strength of high-frequency resonances because of radiation from the open end. Also associated with the open end is a frequency-dependent length correction which causes high-frequency wave components to “see” a longer effective bore than low-frequency components. Alternately, high-frequency wave components can be considered to propagate farther out the open end before reflection than their low-frequency counterparts. The bottom plot of Fig. 2.1 illustrates this frequency deviation in cents versus frequency. As a result, open-end radiation/reflection causes the axial normal modes of a cylindrical pipe to be slightly compressed from their ideal, harmonic frequency values.

Another source for both resonance damping and tuning deviation is thermoviscous losses along the inner walls of the instrument bore, as discussed in Section 1.3.3. For common cylindrical bored instruments, such as clarinets and flutes, such effects are more significant than those associated with open-end radiation. However, radiation losses are greater than thermoviscous losses in air columns with a large open-end radius. The attenuation of high-frequency sound components via boundary-layer effects is dependent on the length of the bore. Thus, the resonances of shorter tubes will be less effected than those of longer tubes. Thermoviscous effects also produce a frequency-dependent phase velocity which is independent of tube length. Figure 2.2 plots the attenuation and tuning deviation effects that result from thermoviscous losses as a sound wave travels over two lengths of a cylindrical pipe of length 0.5 meters and radius 0.008 meters. As a result of viscous drag along the tube walls, all air column resonances are “flattened” to some extent, though most significantly at lower frequencies.

Air temperature fluctuations will affect the speed with which sound waves propagate. In general, the speed of sound c increases with air temperature and is given for the range $290 \text{ K} \leq T \leq 310 \text{ K}$ as (Benade, 1968)

$$c = 347.23 (1 + 0.00166\Delta T) \text{ m}\cdot\text{sec}^{-1}, \quad (2.3)$$

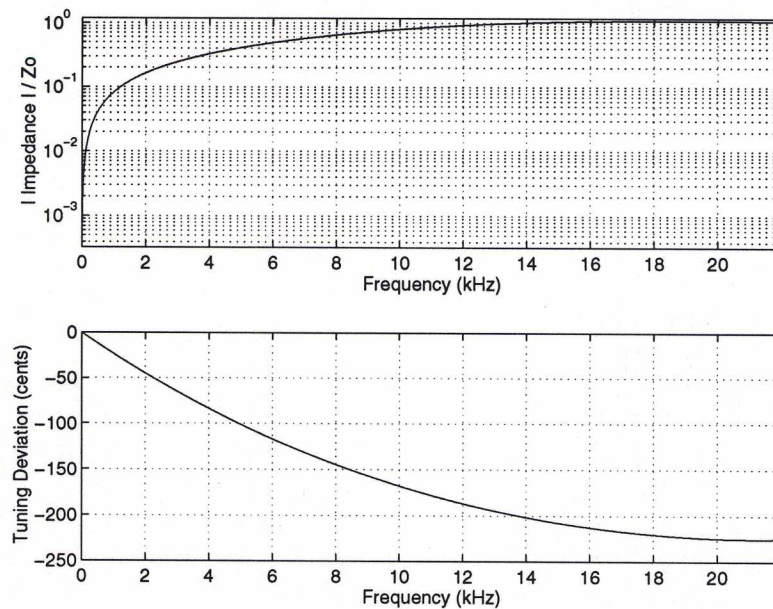


Fig. 2.1. Open-end radiation characteristics for an unflanged cylindrical pipe: (top) Load impedance magnitude relative to the wave impedance Z_0 ; (bottom) Tuning deviation in cents.

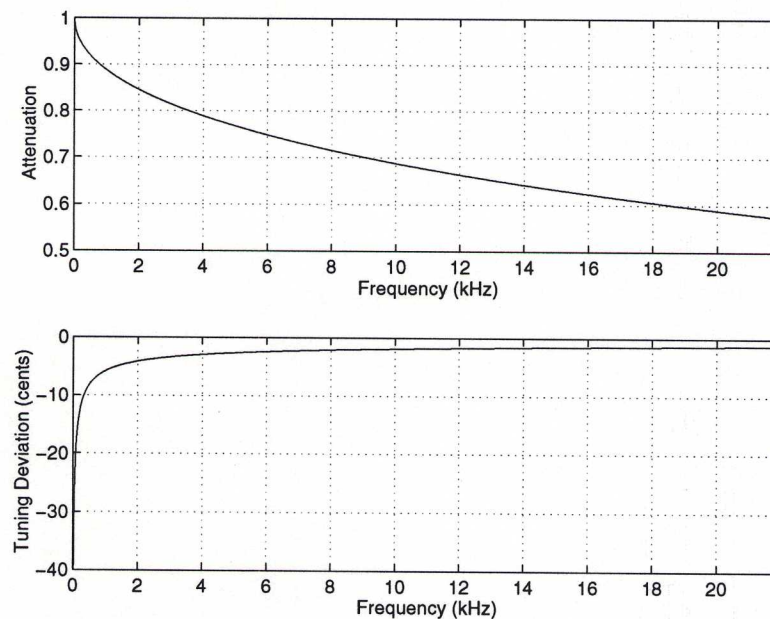


Fig. 2.2. Thermoviscous effects for wave travel over two lengths of a cylindrical pipe of length 0.5 meters and radius 0.008 meters: (top) Attenuation characteristic; (bottom) Tuning deviation in cents.

where $\Delta T = T - 300 \text{ K}$ (26.85°C). Changes in humidity and gas content will cause further variations in the speed of sound. Homogeneous changes in c will affect the resonance frequencies of a wind instrument but will not detune the partial relationships. In other words, a lower speed of sound will cause all of the resonance frequencies of an air column to be lowered in equal proportions. However, it is reasonable to expect that air entering the instrument is somewhat near 37°C , or the body temperature of the player, and that it quickly cools as it travels down the bore (Nederveen, 1969). Temperature differences of 13°C between the top and bottom of woodwind bores are reported by Benade (1963). As a result, the fundamental resonance of a clarinet can be flattened by up to 9 cents, whereas the second partial can be stretched by 8 cents. Temperature gradients in musical instruments are difficult to estimate because of environmental dependencies. Throughout this study, a mean homogeneous temperature of 26.85°C is assumed throughout the instrument, a value which was measured by Coltman (1966) in flutes.

Several members of the woodwind family are constructed with bent tubes, including saxophones, bassoons, and bass clarinets. While these bends permit compact key mechanisms and manageable instrument proportions, they cause disturbances to propagating sound waves which may produce noticeable frequency shifts in steady-state tones (Benade, 1976, p. 409). Measurements have shown that the effective length of the bent tube is dependent on the standing-wave patterns within the air column (Brindley, 1973). In general, a bent tube behaves as if slightly oversized, so that two straight cylindrical tubes of equal diameter should be joined by a half-torus of slightly smaller diameter.

All of the effects discussed thus far in this section are equally applicable to conical bores as well as cylindrical bores. While a theoretical analysis of open-end radiation from a conical bore has not been determined to date, it is reasonable to assume that the effects are similar to those in a cylinder. As discussed in Section 1.4.1, the impedance at the open end of a cone is typically approximated by

$$Z_{R'} = \frac{S_p}{S_s} Z_R, \quad (2.4)$$

where Z_R is the radiation impedance of a cylinder of equal open-end radius, S_p is the cross-sectional surface area at the end of the cone, and S_s is the spherical-wave surface area at the end of the cone (Caussé *et al.*, 1984). The ratio S_p/S_s is typically just slightly less than one, so that the impedance mismatch at the open end is slightly greater in conical bores.

The analysis of air column resonances in conical bores is considerably more complicated than that associated with cylindrical bores because of effects related to the truncation of the cone tip. The perfectly harmonic alignment of partials in a conical bore mentioned at the opening of this section applies only to a complete cone with ideal boundary conditions and rigid walls. In order to make such a structure useful as a musical instrument, it is necessary to truncate the cone and apply an excitation mechanism near its apex. The single-reed excitation mechanism effectively forms a rigid termination at the truncation point. As discussed in Section 1.3.2, the partials of a conic frustum closed at its small end are not related by integral multiples to its fundamental resonance. Rather, the partials are stretched away from perfect harmonicity to an extent which is dependent on

tube length and the size of the missing, truncated section. Figure 2.3 is repeated from Section 1.3.2 to illustrate the variation of partial alignment in closed-open conic frusta. The partial frequencies

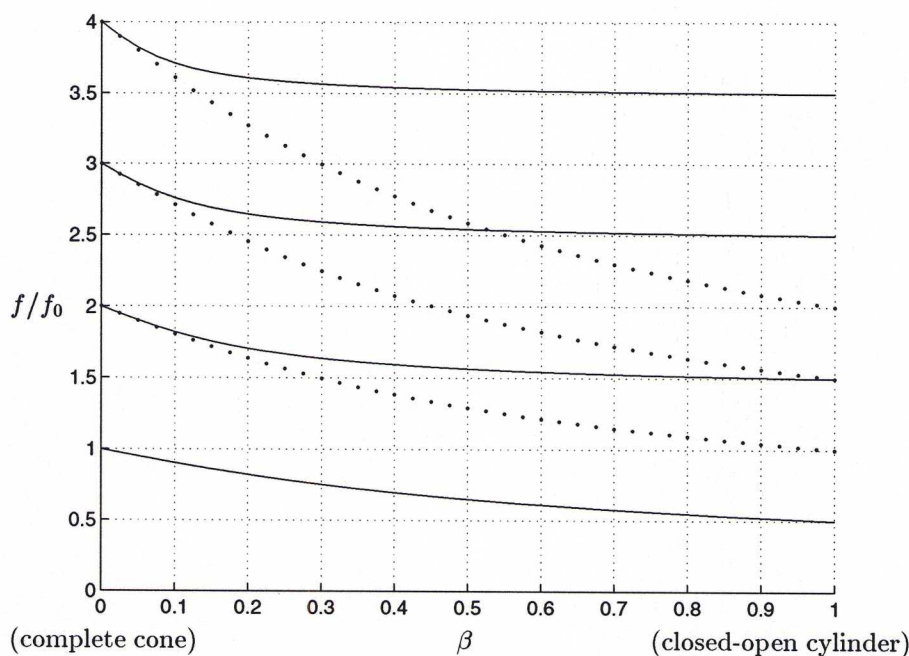


Fig. 2.3. Partial frequency ratios for a closed-open conic section versus β , the ratio of closed- to open-end radii. The frequencies are normalized by f_0 , the fundamental resonance for an open-open pipe of the same length as the frustum.

are plotted against β , the ratio of closed- to open-end radii (or equivalently, the ratio of x_0 to L , as defined in Fig 1.8). A complete cone is represented by $\beta = 0$ (left edge of plot) and has modal frequencies aligned at exact integer multiples of the fundamental. A closed-open cylinder is given by $\beta = 1$ (right edge of plot) and has axial normal modes aligned at odd integer multiples of the fundamental. Between these extremes, the partial frequencies are non-harmonically aligned to various extents. The modal frequencies in Fig. 2.3 are normalized by f_0 , the fundamental resonance for an open-open pipe of the same length as the frustum. The dotted lines indicate exact integer relationships above the first partial and serve only to make more apparent the stretching of the partial ratios. The fundamental frequency of the conic frustum is most affected by truncation and closure, as this resonance descends quickly toward the fundamental of the closed-open cylindrical pipe. Figure 2.4 offers another perspective on the partial alignment in closed-open conic frusta. In this plot, the partial frequencies are normalized by f_c , the fundamental resonance for the same conic section complete to its apex. From this figure, it is evident that in the range $0 \leq \beta \leq 0.2$, the fundamental normal mode of a closed-open conic frustum behaves as though it were complete to its apex. This point will become important in subsequent discussions in this chapter.

For woodwind instruments constructed with conical air columns, the size of the truncated section

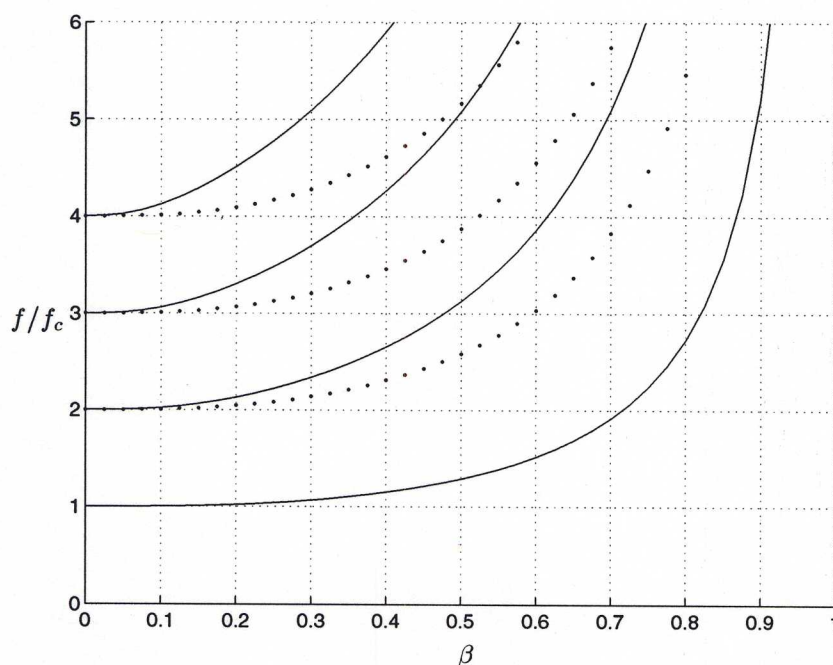


Fig. 2.4. Partial frequency ratios for a closed-open conic section versus β , the ratio of closed- to open-end radii. The frequencies are normalized by f_c , the fundamental resonance for the same conic section complete to its apex.

is constant, while the length of the bore itself is typically varied through the use of toneholes. Similarly, the bore radius at the point of truncation is constant, while the effective open-end radius changes according to the opening and closing of toneholes. Thus, the parameter β fluctuates over the range of the instrument, indicating a variation of the partial structure. Shorter tube lengths will have an associated value of β which is greater than that for longer bore lengths, so that the extent of the stretching of their partial structure away from integer multiples of the fundamental is larger for shorter tube lengths. This point is illustrated in Fig. 2.5, which plots the partial frequency ratios for a conic frustum of fixed angle and small-end radius versus length. Measurements were made on a modern Selmer Paris® Super Action 80, Series II, *E♭* alto saxophone to estimate the β values of various pitches produced on the instrument. The measured lengths are provided in Appendix B, together with measurements given by Nederveen (1969) for comparison. Averaging these two sets of data, estimated values of β for the written pitches *D4* and *B4*[†] are 0.15 and 0.24, respectively. Corresponding partial values, normalized by the first resonance frequency, for these β parameters are listed in Table 2.1, indicating the extent of partial stretching for these particular tube lengths.

It is common that the fundamental resonance of long truncated cones be of weaker magnitude than the second resonance. Such a feature is evident in Fig. 2.6, which plots the input impedance of

[†]The written pitches *D4* and *B4* on an *E♭* alto saxophone correspond to the concert pitches *F3* and *D4*, respectively. For reference, the concert pitch *A4* is given by a frequency of 440 Hz.

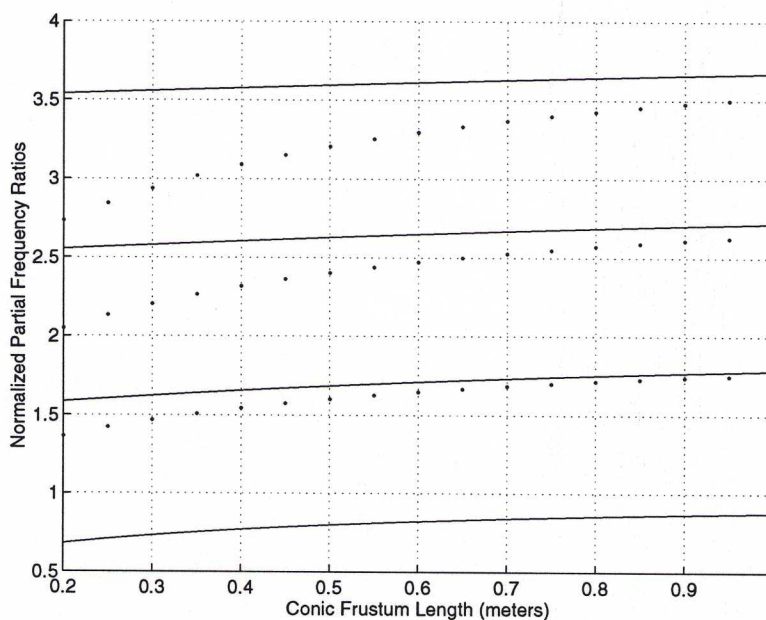


Fig. 2.5. Partial frequency ratios for a closed-open conic section versus frustum length, for a cone of half angle 2° and small-end radius of 0.005 meters. The partial frequencies are normalized by f_0 , the fundamental resonance for an open-open pipe of the same length as the frustum.

a closed-open conic frusta of length 0.5 meters, small-end radius of 0.005 meters, and half angle of 2° . Benade mentions that this is characteristic of long, conical woodwind air columns in which the missing part of the cone at the apex is relatively short compared to the length of the body of the instrument (Benade, 1976, p. 444). The input to a conical air column can be viewed as a parallel combination of an acoustic inertance and a cylindrical waveguide, as discussed in conjunction with Eq. (1.68). The inertance term grows in magnitude with proximity of the truncation point to the cone apex. Thus, short truncation lengths produce an inertance which “short-circuits” low-frequency excitations, but leaves high-frequency energy unaffected. When the air column length is short, the first resonance frequency of the system is high enough to be unaffected by the inertance term. Long air columns, however, will have an associated low-frequency first resonance which is destructively

Normalized Partial Values for $\beta =$	
0.15	0.24
1	1
2.04	2.12
3.13	3.32
4.25	4.55

Table 2.1. The first four partial frequency ratios, relative to the first resonance frequency, for conical frusta defined by β equal to 0.15 and 0.24.

influenced by the inertance. This effect may be the cause for the poor response of the lowest few notes of saxophones. These pitches are typically difficult to produce at soft dynamic levels, and tend toward entrainment at the second resonance, in agreement with the resonance structure of Fig. 2.6.

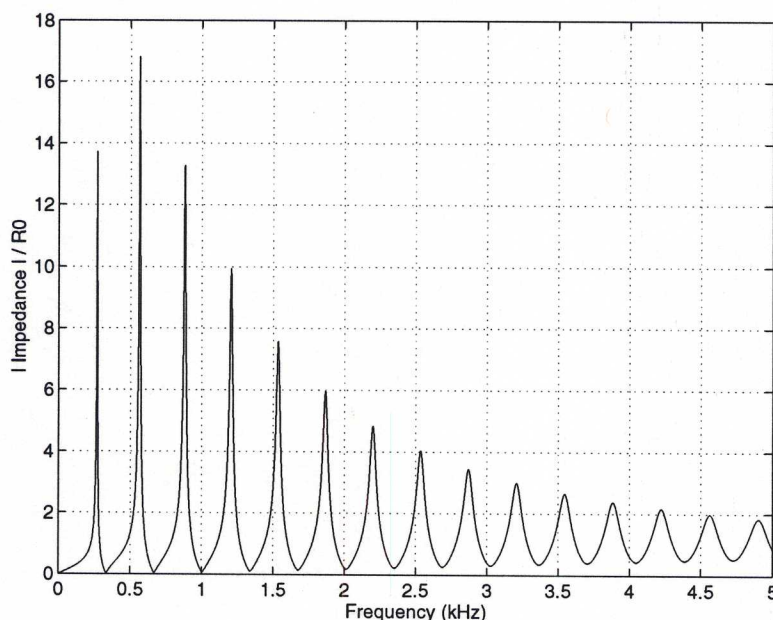


Fig. 2.6. The input impedance magnitude, relative to $R_0 = \rho c / S$ at its input end, of a conical frustum of length 0.5 meters, small-end radius 0.005 meters, and half angle of 2° .

In summary, the following effects produce deviations from perfect tuning in cylindrical-bored woodwind instruments:

- Open-end radiation causes the resonance frequencies of an air column to be compressed from perfect odd integer multiple relationships.
- Viscothermal boundary layer effects attenuate resonance peaks in proportion to frequency and flatten resonance frequencies in a manner inversely proportional to frequency.
- Temperature gradient effects may lower fundamental resonance frequencies in long tube lengths and raise higher partial frequencies.

Woodwind instruments with conical-bores will experience all of the above effects, and in addition:

- Effects related to truncation of the bore cause the resonance frequencies to be stretched from perfect integer multiples relationships.
- Effects related to truncation of the bore may attenuate the fundamental resonance in long tube lengths, so that excitation at the fundamental is detrimentally affected.

2.1.2 Perturbations

Various acoustic phenomena were analyzed in Section 2.1.1 which cause deviations from perfect tuning in musical instruments constructed from cylinders and cones. In this section, the effects of air-column perturbations are explored in order to gain insight into methods for the adjustment of misaligned resonances.

The resonance structure of a cylindrical bore can be modified in a well defined manner by making the pipe slightly conical convergent or divergent. The right side of Fig. 2.3 indicates the partial relationships for a nearly cylindrical, conical divergent air column. The fundamental resonance frequency of such a structure is seen to be higher than the uniform pipe and its partials are slightly compressed from exact odd integer ratios. Similarly, the resonances of a nearly cylindrical bore which decreases in cross-section away from the closed end are slightly stretched from exact odd integer multiples of the fundamental and the first resonance is lower than that of a uniform pipe (Benade, 1959, 1977).

In Section 1.4.2, methods for the analysis of sound-wave behavior in flaring horns were briefly discussed. While rapidly flaring horns, or bells, are a less significant component of woodwind instruments, very gradual flares over part or all of an air column's length may offer potential means for the adjustment of resonance frequency ratios. The analysis techniques developed in conjunction with flaring horns can thus be applied to woodwind bore shapes in this regard. In general, a one-dimensional analysis is made which assumes the existence of one-parameter waves propagating along the principal axis of the horn. As mentioned in Section 1.3, one-parameter waves are possible only in pipes of uniform cross-section and conical horns, respectively (Putland, 1993). Thus, the solutions obtained through these analyses are necessarily approximate. It is possible to estimate the acoustic behavior of sound waves in flaring horns by assuming either plane or spherical wave front shapes. While spherical wave fronts offer a better approximation to the actual wave front shapes in flaring horns, plane-wave approximations are reasonably accurate for small flare rates and horns of small cross-sectional area (Benade and Jansson, 1974*a,b*). It should be noted, however, that the plane-wave theory will always give a higher estimate of the normal mode frequencies of a structure than the spherical-wave approximation (Benade and Jansson, 1974*a*).

A family of horns whose cross-sectional radius is given by

$$a(x) = Cx^{-\epsilon} + Dx^{\epsilon+1}, \quad \text{for } x > 0, \quad (2.5)$$

is often studied because of its formal simplicity and because certain values of the constants ϵ , C , and D produce profiles which closely resemble sections of brass instruments. These horns are called *Bessel horns* because solutions to Webster's equation for such geometries, assuming planar wave front s, are given by (Pyle, 1975)

$$p(x) = x^{1/2} a^{-1}(x) [AJ_{\epsilon+1/2}(kx) + BY_{\epsilon+1/2}(kx)], \quad (2.6)$$

where A and B are constants determined by boundary conditions and J and Y are Bessel functions of the first and second kind, respectively. Benade (1959) discusses horn profiles in which the cross-sectional radius is given by Eq. (2.5) for $D = 0$ and negative values of ϵ . Included in this group are cylindrical ($\epsilon = 0$) and conical bores ($\epsilon = -1$). For horns defined by $\epsilon < -1$, Benade shows that the normal-mode frequencies are compressed from integer multiple ratios of the fundamental frequency. Bessel horns complete to their apex and ideally terminated at their open end form the complete set of possible wind instrument air column shapes which have normal-mode frequency ratios that are independent of horn length, within the plane-wave approximation mentioned previously (Benade, 1959). As was the case with conical bores, however, truncation of such a Bessel horn near its apex and application of a rigid termination will destroy this ideal behavior.

Another family of horns for which analytic solutions are relatively simple within the one-parameter plane-wave approximation are referred to as *exponential horns* because their cross-sectional radius is given by

$$a(x) = a_0 e^{mx}, \quad (2.7)$$

where m is the exponential flare constant and a_0 is the horn radius at the origin. Sinusoidal, steady-state solutions to Webster's equation for such geometries are given by

$$P(x, t) = \left[\frac{A}{a(x)} e^{-jbx} + \frac{B}{a(x)} e^{jbx} \right] e^{j\Omega t}, \quad (2.8)$$

where $b = \sqrt{k^2 - m^2}$. Using Eq. (1.33), the corresponding volume velocity is found to be

$$U(x, t) = \frac{S(x)}{a(x)\rho\Omega} [A(b - jm) e^{-jbx} - B(b + jm) e^{jbx}] e^{j\Omega t}. \quad (2.9)$$

From these expressions, the input impedance of an exponential horn, and thus its resonance frequencies, can be determined within the constraints of the plane-wave approximation. Figure 2.7 illustrates the profiles for two exponential horns of differing flare rate. The y -axis of the plot is magnified to make more apparent the horn flares; if viewed with equal grid spacings, these flares are much less obvious. For $m = 2$ and $a_0 = 0.005$ meters, the mouth and open-end radii of the horn are similar to those of the conical bore of an *E♭* alto saxophone of length 1 meter. In Fig. 2.8, the first four partial frequency ratios, relative to the fundamental frequency, are plotted for the two horn flare rates. The partial ratios are clearly dependent on horn length and, in general, depart significantly from integer multiples of the fundamental frequency. For horns of longer length, the partial ratios are compressed from integer relationships to an extent which is proportional to flare rate. In horns of short length, however, truncation effects dominate and cause the partials to be stretched from integer multiple ratios. This effect is more obvious for smaller flare rates, where the horn shape more closely resembles a cylindrical pipe. Just as the partial ratios of a cylindrical bore are slightly compressed from odd integer multiples when the pipe is made slightly conical divergent, so an additional slight flare will further compress these ratios. Figure 2.9 plots the partial frequency ratios of the exponential horns normalized by the fundamental resonance of an open-open

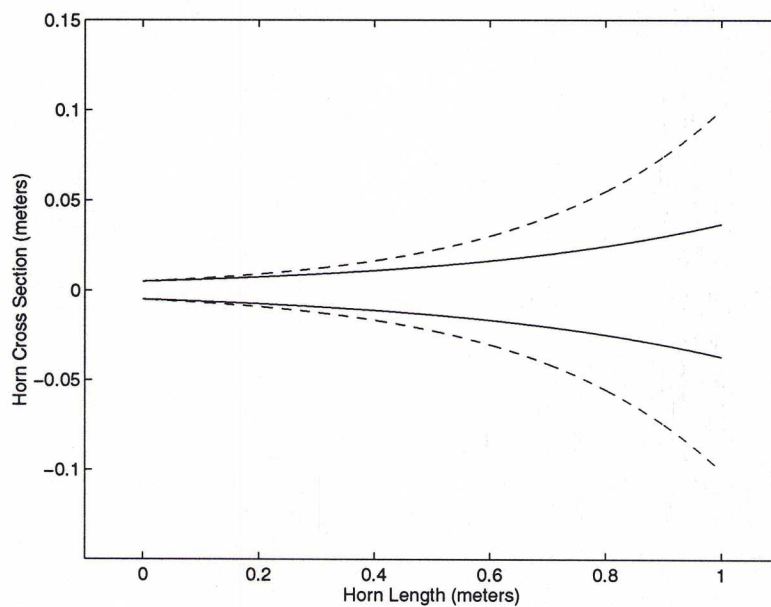


Fig. 2.7. Exponential horn profiles for flare parameters of $m = 2$ (—) and $m = 3$ (---).

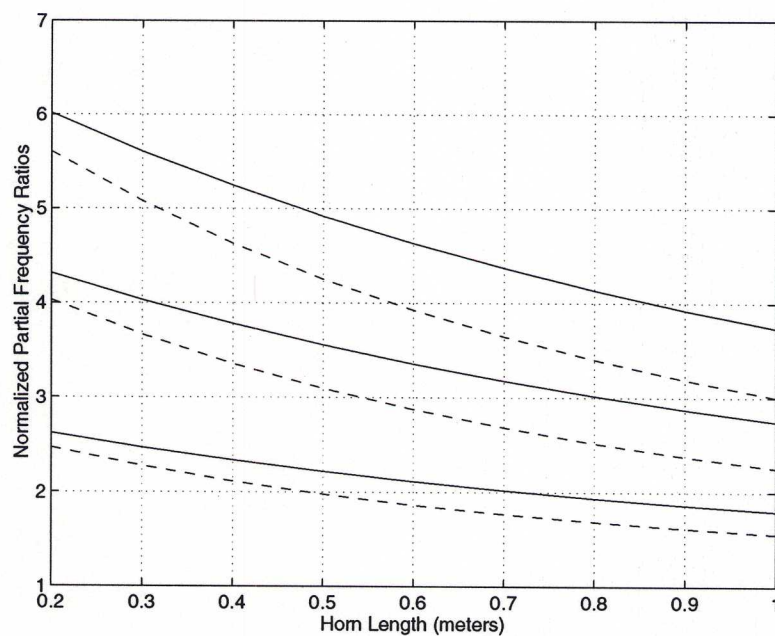


Fig. 2.8. Partial frequency ratios, relative to the fundamental resonance, for exponential horns defined by flare parameters of $m = 2$ (—) and $m = 3$ (---).

conic frustum of the same length. From this figure, it is easy to see that the fundamental resonance is most affected by both the truncation and horn flare, while the higher partials vary to a much lesser degree. Truncation effects cause the first resonance frequency to be lowered, corresponding to a longer effective bore length. Flares cause the first resonance frequency to be increased, which corresponds to a shorter effective bore length.

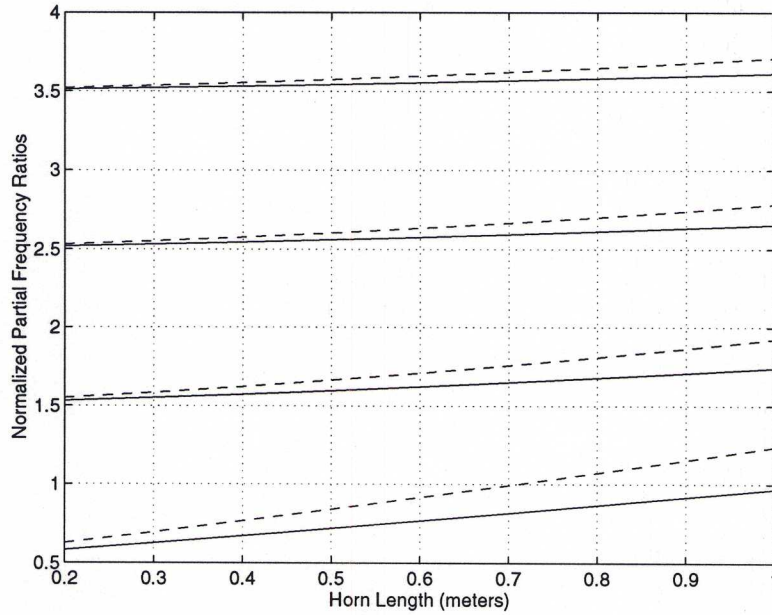


Fig. 2.9. Partial frequency ratios, relative to the fundamental resonance of an open-open conic frustum of the same length, for exponential horns defined by the flare parameters $m = 2$ (—) and $m = 3$ (---).

Flared horns improve sound radiation characteristics, relative to straight-sided pipes, by providing a gradual wave impedance transition from their mouth to the external environment. In this sense, the abrupt impedance mismatch at the open end of a cylindrical pipe results in poor radiation and high levels of sound wave reflection back into the bore. Low-frequency sound components are most affected by the flare of a horn, being reflected at relatively early stages in the horn, as compared to high-frequency components. Such behavior may be understood intuitively by assuming that each point along the curve of a flaring horn can be approximated by a piecewise conical section whose walls are tangent to the curve. In this way, a rapidly flaring horn section is represented by a cone of large central angle and short distance to its respective apex, while a less flared region is represented by a cone of smaller central angle and longer distance to its respective apex. As found in Section 1.3.2, the wave impedance of a cone is frequency-dependent and given by

$$Z_0(x) = \frac{\rho c}{S(x)} \left(\frac{jkx}{1 + jkx} \right), \quad (2.10)$$

where x is measured from the cone apex. Thus, the local wave impedance within a flared horn, as

estimated using Eq. (2.10), is lower for low-frequency wave components at any particular location. Frequency-dependent reflections occur when the change in wave impedance is excessively rapid from one region of the flare to the next. As a result, the lowest normal modes of a flaring horn occur at higher frequencies than those associated with unflared pipes of the same length. High-frequency normal modes are less affected by the flared horn and will travel further along the horn axis before being reflected, if at all. High-frequency partials are altered only slightly by the flaring horn and the overall partial ratios, relative to the first resonance frequency, are compressed. When the horn length is short, however, truncation effects may obscure such behavior. In this context and without regard for the influences of toneholes and a mouthpiece, the length-dependent partial stretching effects caused by truncation of a conical bore can be partially offset by incorporating a slight flare, particularly along the upstream regions of the air column.

Localized perturbations of an air column's cross section can be employed to modify distinct resonance frequencies, as discussed by Benade (1976). Reducing the diameter of an air column near a standing-wave pressure maximum will raise the pressure there and produce a greater local impedance to air flow. If the corresponding flow is small, the stiffness of the air in this region will increase and result in a higher frequency for this particular mode. Constricting an air column near a volume velocity maximum will produce slightly less flow for a fixed pressure differential. The inertance property of the air in this region will thus be increased, which corresponds to a decrease in the standing-wave frequency. From these observations, it is straight-forward to deduce that "a localized enlargement of the cross-section of an air column lowers the natural frequency of any mode having a large pressure amplitude at the position of the enlargement and raises the natural frequency of any mode having a pressure node at the position of the enlargement." (Benade, 1976, p. 474) By keeping track of various normal mode pressure distributions within an air column, modifications to particular resonance frequencies can be achieved. To facilitate such a task, it is possible to determine *perturbation weight functions* which indicate the effect of local bore diameter variations on the various normal modes. In general, the upstream portion of a woodwind bore is common to all modes, while the downstream segment is significant only for those tones produced by closing all or most of the toneholes. Thus, attempts to modify an instrument's resonance structure should begin at the upper end of the bore and continue downward.

In summary, the following woodwind air column perturbations and their associated effects were discussed:

- Making a cylindrical bore slightly conical divergent will raise its fundamental resonance and compress the partial frequency ratios from odd integer multiples.
- Making a cylindrical bore slightly conical convergent will lower its fundamental resonance and stretch the partial frequency ratios from odd integer multiples.
- If the walls of a conical frustum are flared, the partial frequency ratios of the flared structure

will be compressed in comparison to those of the conical frustum. In particular, the fundamental resonance frequency is raised, while the higher partials are affected to a much lesser extent.

- A localized enlargement of an air column will lower the natural frequency of any mode having a standing-wave pressure maximum at the position of the enlargement.
- A localized enlargement of an air column will raise the natural frequency of any mode having a standing-wave pressure minimum at the position of the enlargement.

2.1.3 The Saxophone's "Parabolic" Cone

Having discussed the properties of woodwind air columns, as well as potential perturbations of such, it is interesting to investigate Adolphe Sax's invention of the saxophone and his curious bore shape specification. An excerpt from the patent for the saxophone, as translated by Hemke (1975), reads:

Struck by these different drawbacks, I have looked for a means of remedying these situations by creating an instrument, which by the character of its voice can be reconciled with the stringed instruments, but which possesses more force and intensity than the strings. This instrument is the Saxophone. The Saxophone is able to change the volume of its sounds better than any other instrument. I have made it of brass and in the form of a parabolic cone to produce the qualities which were just mentioned and to keep a perfect equality throughout its entire range. The Saxophone embouchure uses a mouthpiece with a single reed whose interior is very wide and which becomes narrower at the part which is fitted to the body of the instrument (Hemke, 1975, p. 48).

It is nowadays assumed that the air column of a saxophone is principally conical in shape, but for a few modifications at distinct points along its length to account for tuning errors. Thus, the specification of a *parabolic cone* in the construction of the saxophone is surprising. Hemke pursues this issue in detail and states that "Sax was profoundly concerned with acoustics and proportions and this statement therefore exemplifies a relevant distinction in the mind of Adolphe Sax" (Hemke, 1975, p. 59). Unfortunately, Sax himself never provided a more detailed explanation of the parabolic cone's shape. As a result of Sax's first court case (in defense of the saxophone patent), the selected panel of experts reached the following conclusion on 2 November 1847:

...but above all the tube of the instrument, in place of being cylindrical as the clarinet and the bathyphone, forms a cone of which the walls have a specific curvature and which the Sax patent designates under the name of parabolic cone (Halévy *et al.*, 1848).

Jaap Kool provides a more detailed explanation of the shape of the parabolic cone, while viewing a saxophone built by Sax, as follows:

If we remove the mouthpiece and neck of an alto saxophone so that we could look into the main tubing, it would easily reveal that the forward side of the inner wall (that is, the side where most tone holes are found) is not entirely straight, but rather forms a

curve. We cannot see the beginnings of the tone holes all at the same time, but by slowly turning it upward, they successively appear. If we turn the instrument a quarter turn on its own axis, we discover that an absolutely straight course leads into the interior. This side wall thus widens downward in a straight line. Another quarter turn once again shows an outward-running curve, while the next wall again reveals an absolutely straight course. From this, it follows that the almost circular cross-section at the top of the tube takes on a continuously more elliptical shape toward the bottom. Furthermore, the tone holes do not lie in a straight line, but rather in a parabolic curve running outward. In this way, the diameter of the bore does not increase uniformly, but rather by a continuously smaller percentage (Kool, 1987, pp. 82–83).

Kool provides a sketch, similar to that of Fig. 2.10, that clarifies his description. The accuracy of his analysis is unclear, however, as he made no detailed measurements to substantiate his observations. The last sentence of the above quotation and the sketch provided seem to indicate that the diameter of the bore along the “parabolic” axis is always smaller than that along the straight-sided axis. It seems likely that an air column constructed in this way would be made to form a circular cross-section at the point where it meets the bow, and from there form a straight-sided cone for the remainder of its length.

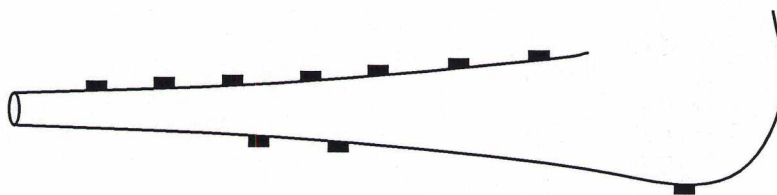


Fig. 2.10. The profile of an alto saxophone built by Adolphe Sax, in exaggerated proportions [after (Kool, 1987)].

The term “parabolic cone” is itself misleading, as there is no known common geometric surface given by this name. What is generally referred to as a “cone” is defined in terms of quadratic surfaces as a *circular cone*, as shown in Fig. 2.11(a). The walls of this structure are straight and of the same angle of inclination in both the $x - z$ and $y - z$ planes. Cross sections of the circular cone in the $x - y$ plane are always circular. An *elliptic cone*, Fig. 2.11(b), also has straight walls, though the angle of inclination differs in the $x - z$ and $y - z$ planes. Cross sections of an elliptic cone in the $x - y$ plane are elliptical in shape. While Kool’s description of the parabolic cone indicates straight walls in one plane, the distinguishing feature appears to be curved walls in the other plane. Figure 2.11(c) illustrates a structure with curved walls which is called an *elliptic paraboloid*, though this curvature is opposite to that described by Kool. Finally, there is a shape defined as a *hyperboloid of one sheet*, Fig. 2.11(d), which has the correct curvature, but no straight walls. Thus, the parabolic cone could be defined as tracing hyperbolas in one plane and lines which intersect at the “cone” apex in the other. Since such a surface is not confocal, it does not fall into the easily representable quadratic shapes shown in Fig. 2.11 and a concise mathematical formula to represent this surface is not possible. Several views of a parabolic cone are shown in Fig. 2.12. These plots were obtained

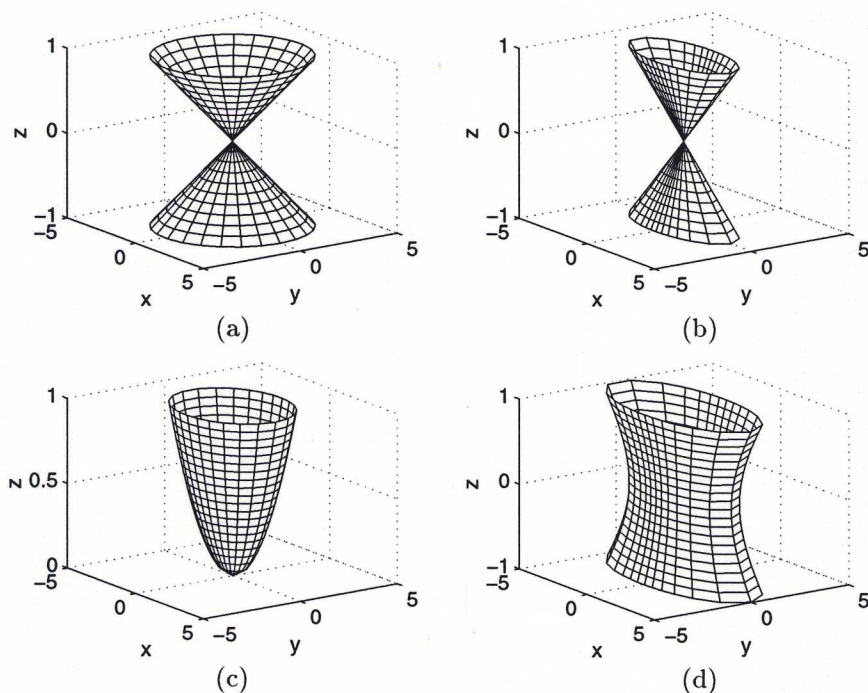


Fig. 2.11. Quadratic surfaces: (a) Circular cone; (b) Elliptic cone; (c) Hyperboloid of one sheet; (d) Elliptic paraboloid.

by modifying the equations of an elliptic cone, so that the focus along one plane is varying. This particular structure was defined such that its cross section at $z = 1$ is circular, as shown in the $x - y$ cross section of Fig. 2.12. For $0 \leq z < 1$, the cross sections are elliptical. Perhaps the term “hyperbolic” cone would be more accurate, but because of its own deficiency together with the historical precedent of Sax’s description, such a shape will continue to be referred to as a parabolic cone in this study.

While Sax’s use of the term “parabolic cone” to describe the shape of the saxophone air column is rightfully confusing, interpretations regarding the acoustical function of such a shape are a more important issue to this study. Georges Kastner, in his early method book for the saxophone, wrote:

A foremost particularity of the saxophone rests in its cone being parabolic throughout its entire length whereas the tubes of other instruments form a concave and generally cylindrical cone throughout their greater length; in the saxophone the vibrations occur along its entire length by means of undulations against the walls, but in the others (ophicleide, trumpet, trombone) the undulations vibrate from one end of the tube to the other (Kastner, 1846).

A similar interpretation is given by Henri Radiquer in the Lavignac *Encyclopédie de la musique et dictionnaire du Conservatoire*.

Now the tube is a parabolic cone in which the vibrations do not behave as in the cylindrical tube of the clarinet and in the conical tube of the oboe, where they directly follow

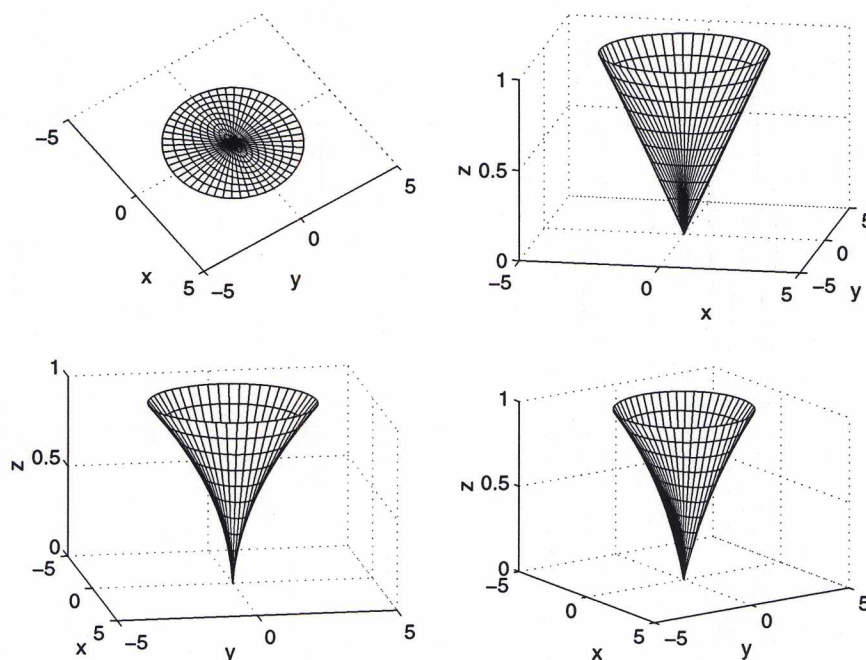


Fig. 2.12. Various views of a "Parabolic cone."

the straight line of the interior of the tube. In the tube of the saxophone the vibrations are reflected from one wall to the other and roll along as intersecting rings between the two curved interior lines of the tube (Radiguer, 1931).

Kastner had worked on his book in collaboration with Sax to some degree between 1844 and 1845, prior to the saxophone patent application (Hemke, 1975, p. 51). Given Sax's skill as an instrument builder and his reasonable understanding of acoustics for the time, it is unlikely that he himself wrote that description. It is, of course, ridiculous to suggest that transverse oscillations between the walls of the cone form the principal modes of vibration in this instrument. And while detailed analysis of higher mode propagation in musical instrument air columns was yet to be carried out in Kastner's time, Sax designed the instrument for length changes *along* its length, rather than by widening its bore width. What is clear, however, is that Sax considered the "parabolic" shape of the cone to be an important and distinguishing aspect of the saxophone.

In his book of 1931, Jaap Kool "explains" Sax's use of the parabolic cone.

Sax chose this parabolic shape intentionally. We know that the sound waves, exactly as light waves (say, off a mirror), are reflected. From an echo, for example, we know, that under certain circumstances the emitted sound is reflected back to its starting point. This reflection is the greatest, that is, it is most complete when the sound is reflected from the focal point of one parabolic body to the focal point of another parabolic body. This means, in practice, that one can direct the course of sound waves in a desired direction. . . . Sax employed all these parabolic surfaces and their effects in the saxophone. First of all, the parabolic inner walls operate like the convex mirror, diffusing the sound

and, at the same time, reflecting it into the tube's interior. This is how the uniquely sonorous, mellow, and at the same time, somewhat hollow sound of the saxophone is produced, which on inferior instruments is easily associated with a ventriloquial note. Still dissatisfied, Sax put in three other small parabolic concave surfaces, or slight curves. If we list the diameters of the tone holes in succession, it becomes obvious to us that these diameters do not regularly increase as the gradually increasing diameter of the tube would cause. On three occasions, we find that a lower tone requires a smaller tone hole than the preceding higher tone. ... At these three places Sax once again employed small parabolic bulges in the opposite direction of the overall curve, which extends across the entire instrument. ... These inward-turning parabolic surfaces operate like the concave lens, that is, they focus the sound. Since at the opposite wall – directly in the vertex of the parabola – there is respectively a tone hole, these surfaces simultaneously effect an easier escape of the sound waves.

American firms, as well as some European firms, are putting more and more inexpensive saxophones on the market, which often totally forego the parabolic shape. Such instruments sound harsh and slightly raspy like a Jew's harp. Strangely enough, by no means does every reputable saxophone factory calculate the exact shape of the bodies of their saxophones according to the scientific-acoustical laws (Kool, 1987, pp. 83–87).

While it may seem foolish to devote such space and energy to the writings of one obviously untrained in the fundamental principles of acoustics, Jaap Kool's statements remain, uncorrected in a recently released translation, an accepted explanation of sound wave behavior in a parabolic cone and its effect on saxophone tone quality. To this day, there are professional saxophonists that seek out old saxophones constructed with the parabolic conical shape, claiming that they allow a more focused sound and better flexibility of tone quality.

Using the acoustic observations discussed in previous sections, it should be possible to estimate the effects that a parabolic cone, in contrast to a circular cone, has on the sound of the saxophone. Based on the observations of Section 2.1.2, it is expected that the partial ratios of this structure will vary with air column length. It is assumed that only the straight portion of the air column, between its neckpipe and lower bow, is shaped as the parabolic cone. Within these limits, it is possible to approximate the shape of a parabolic cone using an exponential horn of equal mouth and open-end radii, as shown in Fig. 2.13. Remembering that the walls of the parabolic cone are curved along one plane only, it is reasonable to expect that the actual acoustic behavior of this bore structure will fall somewhere between that of the truncated cone and the exponential horn. Figure 2.14 plots the partial frequency ratios of both the closed-open conical frustum and the combined cone/exponential horn structure for various lengths, normalized by the fundamental resonance of an open-open conic section of the same length. In general, the fundamental resonance frequency of the cone/exponential horn structure is slightly lower than that of the closed-open conic frustum, while the upper partials are only slightly affected by the wall curvature. To determine the resonance frequencies for Fig. 2.14, the input impedance was calculated at the mouth of the neckpipe. Thus, the partial stretching effects caused by truncation and closure at the mouth of the bore are overestimated. Under playing conditions, a mouthpiece can potentially replace the missing cone section and greatly minimize, or

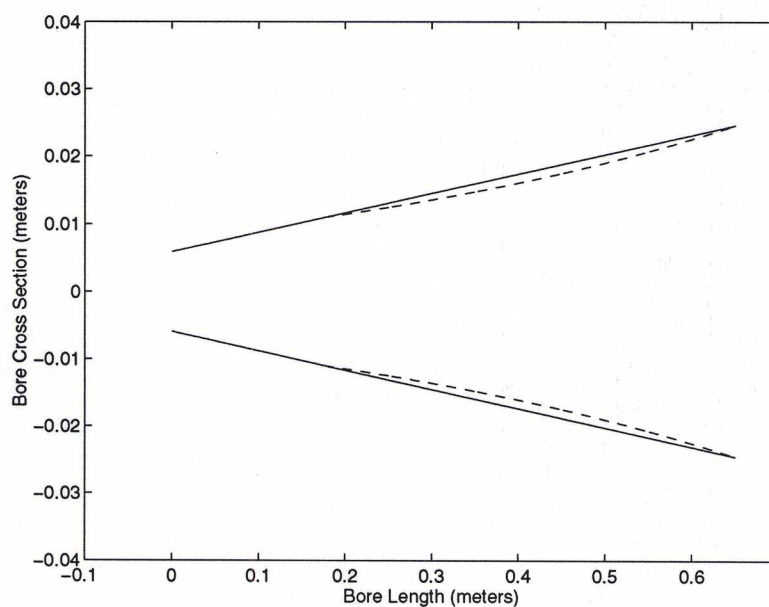


Fig. 2.13. Profile of an alto saxophone bore, up to its lower bow. The bore section between the neckpipe and lower bow is represented by a conical frustum (—) and an exponential horn (---).

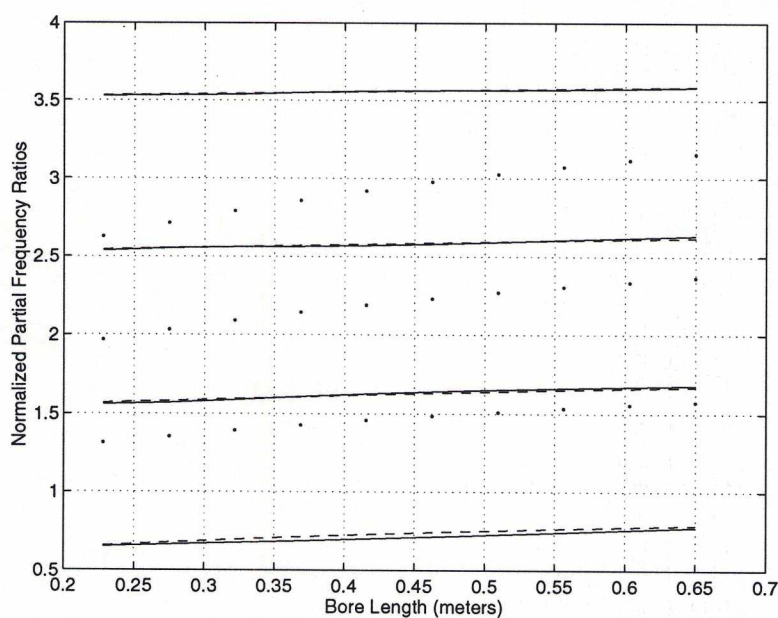


Fig. 2.14. Partial frequency ratios, relative to the fundamental resonance of an open-open conic section of the same length, of a combined cone/exponential horn structure (—) and a closed-open conical frustum (---). The dotted lines indicate exact integer multiple relationships to the first closed-open conical frustum resonance.

eliminate, the stretching of the resonances.

It appears that the parabolic conical bore prescribed by Adophe Sax produces negligible differences in resonance frequency placement versus a pure conical bore. The acoustic behavior of a woodwind instrument air column is greatly complicated by the presence of toneholes and a mouthpiece. Thus, it is likely that the unique qualities associated with saxophones of this shape (and era) are most attributable to other factors, as well as further possible bore deformities. In general, saxophones which have the parabolic conical shape also have a “darker” tone quality. Such behavior might be attributed to a misalignment of higher partials, preventing these harmonics from fully cooperating in the regime of oscillation and thus creating a sound which has less high spectral energy. It is difficult to determine the reasons an instrument might be considered to “focus” better, though this quality could be associated with proper alignment of the lowest and strongest resonances of an air column. In this case, an instrument design might sacrifice high harmonic alignment to achieve better alignment of the lowest resonances. Beyond such speculation, it is clear that the shape of the saxophone has evolved since its invention around 1840.

A check by the writer of various modern saxophones indicates these instruments follow a well defined conical shape and the parabolic forms observed by Kool in the early Sax saxophone have virtually been discarded. This modification of the bore resulted in a change in the saxophone’s timbre, but the principle of its mode of vibration remained the same, i.e. it operated as an open tube (Hemke, 1975, p. 67).

Given the above conclusion regarding the potential effects a parabolic cone might have on the sound of the saxophone, it is interesting that Sax considered this component to be the primary distinguishing feature of his instrument.

By consciously imposing parabolic curves on a conically formed instrument, Sax created an entirely new instrument. He had searched for a particular instrument possessing unique qualities – a new orchestral bass voice, an instrument with the particular ability to reconcile the brass with the strings and a brass instrument with superior intonation. Adolphe Sax invented an instrument which combined a single reed with a *parabolic* conical tube. He did not invent, nor [did he] claim to have invented an instrument which combined a single reed with a *conical* tube (Hemke, 1975, pp. 69–70).

2.2 Woodwind Toneholes

Toneholes are an essential and characteristic feature of all woodwind instruments, allowing variations of an air column’s length so as to produce a full scale of sounding pitches. Benade (1960) made useful and accurate low-frequency observations of the behavior of woodwind toneholes by analyzing them in terms of lattice structures, or as groups of open and closed holes. Keefe (1981) extended the theory of toneholes by making accurate analyses of an individual tonehole, and then determining the extent of tonehole interactions. His method allowed computer modeling of a complete tonehole lattice, assuming that the tonehole interactions are minimal. The mathematical details of these

approaches were discussed in Section 1.4.3. The present discussion is more oriented to the woodwind instrumentalist, seeking to define in general terms the acoustical behavior of toneholes. This background sets the stage for a short course in practical tonehole alteration techniques. While not a comprehensive discussion, several methods are outlined which have proven extremely useful over the years for correcting tuning errors in woodwind instruments. Finally, the fundamental operation of register holes is reviewed with an emphasis on their effect on saxophone intonation. These concepts offer an opportunity to introduce issues related to oral cavity manipulation.

2.2.1 The Tonehole Lattice

Benade (1960) provided the first mathematical descriptions of the acoustic behavior of woodwind toneholes which could potentially be used in the design of a complete woodwind instrument. As mentioned in Section 1.4.3, his analysis assumed that the tonehole lattice (THL) is adequately modeled in terms of uniformly spaced holes of equal size. Within a lattice of closed holes along a cylindrical pipe, Eqs. (1.118) and (1.119) express low-frequency approximations to the wave impedance and phase velocity. From these expressions, the closed-THL “effective” cross-sectional area is given by

$$S_{\text{eff}} \approx \pi a^2 \left[1 + \frac{1}{2} D^{(c)} \right], \quad (2.11)$$

for $D^{(c)} = \frac{1}{2}(b/a)^2(t/s) \ll 1$, where a is the main bore radius, b is the tonehole radius, t is the height of the tonehole, and $2s$ is the interhole spacing. The length correction due to the slower phase velocity is

$$\Delta l = l \left\{ \frac{r - [1 - (v_c/c)]}{1 - r[1 - (v_c/c)]} \right\}, \quad (2.12)$$

where r is the fractional length of the air column occupied by the closed side holes. It is also possible to estimate the length correction due to a single unit cell of the closed-hole THL. In the low-frequency limit, this length is given by (Benade, 1960)

$$E \approx 2s \left(\sqrt{1 + D^{(c)}} - 1 \right). \quad (2.13)$$

In order to determine the length correction for an entire closed-hole lattice using Eq. (2.13), it is necessary to sum the estimates for each of the closed toneholes. Despite the fact that the finger holes of real musical instruments are not of uniform spacing and equal size, this approach remains valid in the low-frequency limit if the parameter $D^{(c)}$ is constant, so that the wave impedance (or S_{eff}) and phase velocity are the same when evaluated anywhere along the pipe. For a fixed air column radius a and wall thickness t , this constraint sets up a necessary relationship between the interhole spacing $2s$ and the hole radius b . The toneholes are typically spaced and sized to form a chromatic scale. Semitones in the equal-tempered tuning system are related by the ratio $2^{1/12} \approx 1.06$, so to a first approximation, $2s \approx 0.06L$, where L is the position of the tonehole measured from the upper end of the air column. In such an idealized instrument, the tonehole radii will necessarily increase

with distance L to maintain a constant value of $D^{(c)}$. Because the closed-hole lattice has an effective cross-section which is greater than an unpierced pipe of the same radius, it might seem reasonable to increase the radius of the top portion of the air column where no toneholes exist, in order to maintain a constant effective wave impedance along the pipe.

Benade (1960) made the observation that only the first two or three open toneholes along a woodwind air column have significant influence on the behavior of low-frequency sound waves. For this reason, he was able to further apply lattice theory to the open-hole portion of a woodwind instrument. In the low-frequency limit, the open-hole lattice forms a “mass-like” termination to a set of closed holes, as discussed in conjunction with Eq. (1.120). Further, there is a *cutoff frequency* below which the propagation wave number [Eq. (1.121)] in such a structure is real and above which it is imaginary. Thus, low-frequency sound components are exponentially attenuated within the open THL, while high-frequency components propagate through it with an imaginary wave number approaching jk . The cutoff frequency can be determined from Eq. (1.121) by setting $\Gamma^{(o)} = 0$, with the result

$$f_c = \frac{c}{2\pi s} \sqrt{\frac{D^{(o)}}{1 + \frac{2}{3}D^{(o)}}}, \quad (2.14)$$

where c is the speed of sound and $D^{(o)} = \frac{1}{2}(b/a)^2(s/t_e)$ (Keefe, 1990). At frequencies much higher than cutoff, the characteristic impedance approaches Z_0 , or the wave impedance of a cylindrical bore.

Keefe (1990) updated the results of Benade (1960) to account for the complex series impedance component of a tonehole. For the tonehole structure of a typical clarinet, he found that the series impedance produces an approximate 20% shift in closed-THL parameters versus only about 2% for open-THL parameters. Thus, the series impedance terms are much more important for closed-hole lattice calculations.

These closed-form solutions can be used as an aid in the design of musical instruments. Keefe (1989) presents an approach developed by Benade and updated to include the series impedance effects. Using the closed-hole lattice constraints mentioned previously, initial estimates of the tonehole dimensions can be made. These values, together with information regarding the excitation mechanism and air column shape, are input to an iterative computer program which determines optimal tonehole positions along the bore. Given reasonably accurate data regarding the effective length of the excitation mechanism, this method can produce good instrument designs for pitches below the THL cutoff frequency.

2.2.2 The Single Tonehole

The theory of the single woodwind tonehole, as determined by Keefe (1981, 1990), was presented in Section 1.4.3. Because tonehole interactions are generally minimal, this theory can be applied by linear superposition to an entire tonehole lattice as well. In this way, it is possible to calculate the

acoustic behavior of a series of toneholes to reasonable accuracy. Furthermore, the effect of small modifications to tonehole parameters may be carefully investigated.

On a more general level, the relationships derived in conjunction with tonehole lattices can be used to determine the result of simple adjustments to a single tonehole. From the open-hole lattice length correction [Eq. (1.122)] and $D^{(o)}$, it is apparent that an increase in the radius of the first open tonehole will raise the frequencies of the corresponding air column resonances below the cutoff frequency. Variations to the height t of the first open tonehole have inverse effects on the corresponding air column resonance frequencies. That is, an increase in the tonehole height lowers the resulting fundamental frequency. Further, reducing the keypad height above the first one or two open toneholes along an air column will lower the frequency of the corresponding first resonance. In general, such modifications will have the greatest influence on low-frequency resonances and could potentially produce unexpected consequences on higher-register behavior.

While the various air column and tonehole design issues discussed briefly in this chapter and clearly stated by Benade (1976) may seem directed toward the instrument maker, it should be pointed out that performers have the ability to make many simple, yet significant, mechanical modifications to their instruments in order to improve response and intonation. Appropriate air column perturbations, as well as direct alterations to the position and height of a tonehole, are typically too difficult to be made by the performer. However, basic tonehole modifications are reasonably straight-forward and make it possible to lower the pitch of most notes on a woodwind instrument. Raising the pitch of a particular note via tonehole adjustments would entail removing portions of the instrument and thus are not considered viable in this context. One particularly effective technique involves the use of so-called *tonehole liners* (Caravan, 1979). A quarter-moon shaped wedge of material, or a tonehole liner, can be cemented to the upstream side of a tonehole to increase the effective length of the air column when that hole is open. Such a technique should be used only when the notes produced by a particular first open hole are too high in frequency in all registers, or when a tuning compromise between upper and lower registers is acceptable. The tonehole liner, of course, also reduces the effective diameter of the hole, which produces the same tuning result. Because tonehole liners form an extension of the air column wall, it is best to make them from a rigid material to reduce potential boundary layer losses. That said, tonehole liners are most commonly constructed from cork. Tonehole key heights can also be adjusted to make tuning corrections. Moving a key pad closer to a tonehole increases the effective length of the tonehole, which in turn, lowers the frequency of the note produced by the open hole. As mentioned in connection with air column adjustment principles, these modifications should begin at the upper end of a bore and progress toward its open end. An oversized tonehole liner or a very low key pad height can cause a “stuffy” response.

Though slightly more ambitious, the response of a wind instrument may be improved by smoothing any sharp edges within its air column (Benade, 1976; Hoekje, 1995). Sharp edges can cause

increased turbulence at lower blowing pressures, which in turn produces more internal damping. Rounding the corners of toneholes can significantly postpone and regularize the onset of turbulence in a woodwind and allow the instrument to play well over an extended range (Benade, 1976, pp. 500–501).

2.2.3 Register Holes

Most musical instruments have evolved or were designed in such a way as to take advantage of higher axial modes of vibration in order to extend their playing range. The ability to select a particular mode of oscillation is an inherent component of flute and brass instrument excitation mechanisms. As discussed in Section 1.5, however, single- and double-reed excitation mechanisms operate well below their resonance frequencies, and for this reason they are particularly subservient to the resonance structure of the air column to which they are attached. In order to entrain oscillations in these instruments at higher resonances, the normal mode structure of their air columns can be modified so as to destructively influence fundamental mode operation, and thus indirectly force production at higher, more stable resonance frequencies. The register hole is designed for this purpose. It is also possible to use oral cavity manipulations and lip pressure variations to entrain oscillations at higher air-column resonances, though such changes are more difficult to control. Register shifts are greatly facilitated through the use of a register hole.

Benade (1976) states that a register hole, or vent, must fulfill two functions. At soft dynamic levels, the hole must selectively reduce the magnitude of the air column's first resonance peak to a value less than that of the second resonance, and so encourage the reed to oscillate at the frequency of the second resonance. At greater dynamic levels, however, the increased strength of higher resonances may combine to support a regime of oscillation based on the first resonance, even when the second peak is of greater magnitude. In this case, a register vent must shift the frequency of the first resonance peak so that it is incapable of joining a regime of oscillation supported by higher air-column resonances. In both cases, reed oscillations are emphasized based on the second (or higher) axial mode of the air column.

In order to perform selective damping of first mode resonances, a register vent must be of very small radius and short length, so that it behaves as an acoustic resistance. To execute its second function, a register hole must be so proportioned that it behaves as an acoustic inertance. For practical reasons, a single register hole is designed to meet both of these requirements. (Benade, 1976, p. 458) provides formulas that properly relate a register hole's effective height t_e and radius b to the local bore radius a and length. In conical-bored instruments, this relationship is given by

$$\left(\frac{b}{a}\right)^2 \left(\frac{L}{t_e}\right) = 3.253, \quad (2.15)$$

where L is the length of the complete cone for the note of interest, while for cylindrical-bored

instruments,

$$\left(\frac{b}{a}\right)^2 \left(\frac{L}{t_e}\right) = 0.757. \quad (2.16)$$

In general, the *physical* tonehole height t (from which the *effective* tonehole height can be approximated as $t_e \approx t + 1.5b$) should be made as short as possible in order to give the register hole the desired resistive properties.

A register hole must be so located that it has a significant effect on the first resonance of an air column but little or no effect on the second resonance. Placing a register vent near a first-mode standing-wave pressure antinode and at a second-mode standing-wave pressure node will meet these requirements. Translating these conditions, the register hole should be located approximately one-third of the distance from the excitation mechanism of a cylindrical-bored instrument to its first open hole and approximately one-half the distance from the imaginary apex of a conical-bored instrument to its first open hole.

The second register of all woodwind instruments encompasses at least a dozen semitones, and so it would appear that these instruments should have an equal number of appropriately positioned register vents. Practical considerations make such a scenario impossible, so that the instrument designer must determine the optimal number and locations of register holes needed to produce responsive and “in-tune” second register behavior. Assuming proper alignment of the first and second resonances of an air column, a register hole will produce perfect octave or twelfth relationships only for those notes used in its design. Other second register notes produced using the same register hole will be raised in frequency by an amount proportional to the magnitude of the difference of the ideal, desired frequency and the register hole design frequency.

Modern saxophones have two register holes which function for the written range $D5 - G5\sharp$ and $A5 - F6\sharp$, respectively. The notes $D6 - F6\sharp$ on all saxophones are produced with toneholes intended for use only in the second register, so that the placement of these toneholes can be appropriately modified to account for misplaced register-hole effects. Thus, the best tuning compromise that can be made on such instruments is to design the register holes for proper operation at the notes $F5$ and $B5$, respectively. Notes on either side of these values will be sharp to a certain extent. Because the saxophone octave mechanism is automated to function with a single key, there appears to be little reason an additional one or two register holes could not be integrated into the existing scheme, without any inconvenience to the performer. The *Loomis Double Resonance Alto Saxophone* did just this, incorporating an extra register hole on the saxophone neckpipe for the notes $C6\sharp - F6$ (Cohen, 1991a,b). This instrument was primarily designed to eliminate all cross-fingerings within the conventional range of the saxophone, but only six prototypes were built by Loomis in the 1920's. Other instrument manufacturers, such as Selmer, Conn, and Evette Schaeffer, experimented in the first half of the twentieth century with as many as four saxophone register holes, though these features never became standard (Cohen, 1991c,d).

It is nowadays common that single-reed woodwind instrumentalists develop the ability to extend

the playing range of their instrument beyond the conventional fingering limits using third and higher resonances of the air column. Because all register keys are designed for use in the second register only, it is necessary that the performer find *cross-fingerings* which set up appropriate air column resonance structures (Benade, 1976, pp. 460–462). In conjunction with these unconventional fingerings, however, oral cavity manipulations are necessary to further emphasize desired regimes of oscillation and properly control extended register notes[†]. These topics will be further discussed in subsequent sections.

2.3 The Single-Reed Excitation Mechanism

In Section 1.5, the single-reed excitation mechanism was analyzed as a complete unit. In this section, the mouthpiece and reed are evaluated separately. In particular, the mouthpiece cavity is known to have significant control over an instrument's sound spectrum, as well as its intonation and response. Saxophone mouthpiece chamber geometries are of particular concern in this analysis. Next, a variety of literature with regard to reeds is reviewed and commented upon. In general, a professional performer's insight, together with reasonable grounding in acoustic fundamentals, is often necessary to winnow the wheat from the chaff.

2.3.1 Mouthpieces

The single-reed mouthpiece forms an extension of the woodwind air column which allows the attachment of a wooden cane reed in such a way that it can function as a pressure controlled air valve. The mouthpiece cavity does not form a uniform continuation to either a cylindrical or conical bore, and as a result, propagating sound waves within the chamber are scattered in complex ways. The inside geometry of the mouthpiece is critical in determining the response, timbre, and intonation of the overall instrument. Most attempts to accurately determine the specific relationships between geometric proportions and acoustical behavior, however, have failed. Benade and Richards (1983) conducted an important analysis of oboe reed and staple proportions which has relevance for all conical-bored instruments.

Benade (1959, 1977, 1976) estimated the influences of mouthpiece cavities on low-frequency sound waves. When attached to a *cylindrical* pipe, the mouthpiece chamber effectively extends the air column by an amount equivalent to its volume, to first approximation. Thus, a variation of cavity size affects the lowest resonances in equal proportions and does not alter their ratios to any

[†]Oral cavity manipulations of this sort are easily demonstrated with an *E♭* alto saxophone air column kindly donated to this author by The Selmer Company, Inc. This instrument has no holes along its entire length, thus eliminating any potential resonance structure modifications attributable to toneholes or register vents. Using a normal mouthpiece and reed combination, it is possible to sound individually and with reasonable control any of the first ten to twelve resonances of the air column, solely through oral cavity manipulations (no variation of lip tension).

great extent. At higher frequencies, however, the mouthpiece length correction becomes frequency-dependent and can have important consequence on tuning and tone color. That having been said, mouthpiece proportions have greater influence on conical air column resonances than cylindrical air column resonances.

The first known description of the saxophone mouthpiece was provided by Adolph Sax in his patent letter of March 20th, 1846. "The Saxophone embouchure uses a mouthpiece with a single reed whose interior is very wide and which becomes narrower at the part which is fitted to the body of the instrument" (Hemke, 1975, p. 48). Early saxophones fitted with such a mouthpiece elicited the following description by Hector Berlioz:

These newly gained orchestral voices have rare and valuable qualities. In the high range they are soft yet penetrating. In the low range they are full and rich and in the middle range they are very expressive. On the whole it is a timbre quite its own, vaguely similar to that of the violoncello, the clarinet and the English horn with a half metallic admixture which gives it an altogether peculiar expression. . . .

The high tones of low saxophones have a plaintive and sorrowful character; their low tones, however, have a sublime and as it were, priestly calm (Berlioz, 1856, p. 400).

The development of jazz in the 1930's and the use of saxophones in dance bands stimulated changes to the original saxophone mouthpiece design (Rascher, 1954; Leeson, 1960). Forced to compete with the more powerful brasses, saxophonists sought out any means possible to improve the dynamic range of their instruments. Modifications to the interior shape of the mouthpiece proved to be the easiest and most effective way to produce the desired tone quality changes. By narrowing and lengthening the mouthpiece chamber, a more strident, loud, and "edgy" tone quality was produced, which had a more penetrating character. Today, a large variety of mouthpiece designs are available to the saxophonist, though those intended for jazz use dominate the market. As a result, the full tonal potential of the saxophone remains unknown to most audiences and produces delighted words of praise when heard on such rare occasions.

In general, it is difficult to discuss musical tone quality without using subjective terms. The problem stems from an attempt to specify timbre, or the features of the spectrum of a sound. Further, terms such as "bright" and "dark" are comparative in nature and thus, they must be based on some accepted reference or standard. Despite these difficulties, it is widely acknowledged that a tone identified as "bright" will have more high-frequency spectral energy than a tone regarded as "dark."

The saxophone mouthpiece has been the focus of a great deal of conjecture and incompetent "acoustic" analysis by performers. Though rather simple in its acoustic capacity, a more valuable study was conducted by Wyman (1972) to determine the effect of alto saxophone mouthpiece chamber design on tone quality. His experiments consisted primarily of playing tests which were subjectively rated by performers. Further, he analyzed radiated spectra to form a comparative basis for his analysis. His first conclusion was:

In comparing the five basic mouthpiece types used in this study, differences were observed in the way tone quality varied with changes in dynamic level. At the *pp* level, differences between mouthpieces are not pronounced. In mouthpiece chambers producing a dark tone the upper harmonics appeared gradually as the dynamic level was increased. In chambers producing a brighter tone a more abrupt increase in upper harmonic strength was evident between *pp* and *mf* than between *mf* and *ff* (Wyman, 1972, p. 120).

(Benade, 1976, pp. 441-447) describes the behavior of the *clarinet* nonlinear excitation mechanism. At very soft playing levels, the internal sound produced by a pressure-controlled reed valve is characterized by very little harmonic energy above the fundamental component. Between *pp* and *mf* and before the reed begins to beat against the mouthpiece lay, the amplitude p_n of the n th harmonic will grow with respect to the amplitude p_1 of the fundamental by the formula $p_n = \alpha p_1^n$, where α is a constant. Thus, the amplitudes of the higher resonances will grow quickly in this range. Once the reed begins to beat, this relationship is no longer valid, and the higher harmonic amplitudes will tend to grow in a way that parallels the growth of the fundamental. Conical bores generate larger pressures on the reed than cylindrical bores, so that a saxophone reed begins to beat against the mouthpiece lay at much softer dynamic levels. For very soft saxophone reeds, beating may occur at all playing levels. Thus, the harmonic amplitudes will tend to grow in a way that parallels the growth of the fundamental over most of a saxophone's dynamic range. However, the internal spectrum consists primarily of frequencies below the open tonehole-lattice cutoff frequency, so that spectral content is essentially fixed at playing levels of *mf* and higher. Wyman further noted:

The amount of brightness in the tone is primarily controlled by the baffle shape. A small baffle-to-reed angle tends to promote a bright tone. Since proper tuning requires about the same chamber volume from all types, the brighter types with their low roof contours tend to have longer chambers. Their smaller cross-section area necessitates greater length in order to provide the proper volume. Within each of the five basic chamber types the chamber length is directly proportional to the brightness of tone it will produce.

When the side walls are flat rather than concave, the resulting constriction is similar to that caused by the lowering of the roof height. Flat side walls usually necessitate lengthening of the chamber. Even with flat side walls the tone quality can remain quite dark if the volume of the chamber can be increased by some means other than lengthening. Two of the test mouthpieces having flat sidewalls achieve this by using a large baffle-to-reed angle and a high roof line. One of these two mouthpieces also has a large inner chamber for added volume, allowing it to be still shorter in length.

Within each of the five basic types of chamber, the higher the maximum roof height is, the darker the tone will be (Wyman, 1972, p. 121).

The various components of a single-reed mouthpiece are illustrated in Fig. 2.15. The contour drawn represents a particularly "open" or wide cavity shape, similar to the original design of Adolphe Sax. The baffle is considered that portion of the roof which extends a short distance from the inside edge of the tip rail. In general, a short and open mouthpiece chamber is associated with a dark tone quality, while a long and narrow chamber is associated with a relatively brighter tone quality.

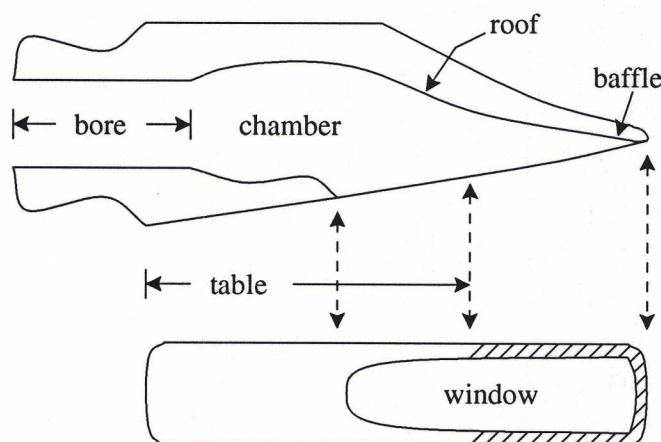


Fig. 2.15. An early saxophone mouthpiece design.

Benade and Richards (1983) conducted a theoretical analysis on the influence of reed and staple proportion adjustments on the air column normal modes of an oboe. By approximating the reed and staple with a cylindrical and conical section, respectively, they derived a closed-form solution from which the effect of simple geometric variations could be determined. In particular, they found that the reed and staple assembly should be so proportioned that its total volume is equivalent to that of the missing conical section at the top of the instrument. This requirement is based on the low-frequency behavior of the structure, since a cavity is characterized by its volume in the long-wavelength limit but not by its particular shape. Further, the lowest natural frequency of the assembly should match that of the missing conical tip so that their behaviors are comparable in the vicinity of this frequency. When correctly proportioned, the reed structure functions in place of the missing conical section and can correct some or most of the effects of conical bore truncation. The motion of the reed, damping in the reed and lips, and oral cavity effects all make large contributions to the *effective* volume of the reed assembly, which is much greater than its geometrical volume. Thus, while the dimensions of the model assembly will not be directly applicable, these observations can provide practical guidance in the adjustment of the reed structure of a real oboe.

Given the analysis of Benade and Richards (1983), it is reasonable to expect that a saxophone mouthpiece which produces a characteristically “dark” tone quality destructively influences the higher partials of the air column. In this sense, a long and narrow mouthpiece chamber may form a better continuation of the conical bore to its apex, and allow more high harmonic participation in the regime of oscillation.

To test this theory, transmission-line models of an alto saxophone mouthpiece and ideal conical air column structure were developed, using techniques described in Sections 1.3.1 and 1.3.2. The two hypothetical structures shown in Fig. 2.16 were used to approximate the shapes of a short, open

saxophone mouthpiece and a long, narrow mouthpiece. Their dimensions were based on typical alto

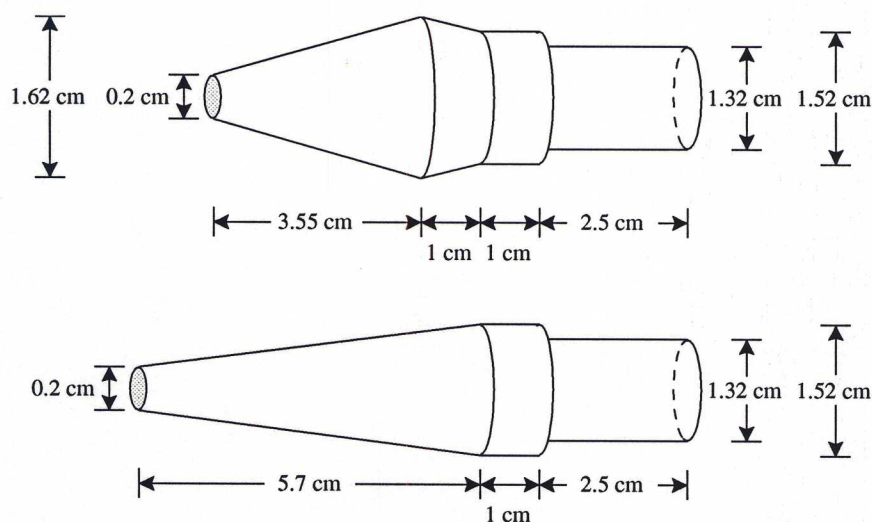


Fig. 2.16. Approximate saxophone mouthpiece structures: (top) Wide chamber design; (bottom) Narrow chamber design.

saxophone mouthpiece and bore measurements and subsequently refined such that their geometric volumes closely matched the volume of the missing conical tip. The calculations were intended only to highlight the differences between the two mouthpiece structures, so that matching of their first resonant frequencies to that of the missing conical section was not performed. The cylindrical sections on the right of each structure correspond to the cylindrical portion of the neckpipe and the cylindrical portion of the mouthpiece which fits over the neckpipe end. The slight increase in diameter occurs at the point where the neckpipe ends inside the mouthpiece.

The calculated input impedances of the complete mouthpiece and air column structures are shown in Fig. 2.17. Of particular interest, the resonance structure produced with the narrow chamber mouthpiece has a significantly greater high-frequency emphasis. The mouthpieces appear to impose formants on the air column resonant structure. Figure 2.18 illustrates the partial frequency ratios for the mouthpieces and conical air columns of varying length. While the narrow mouthpiece provides better normal mode tuning for shorter air column lengths, the tuning effect of these different designs seems negligible. It is likely that the mouthpiece geometries could be modified to produce better resonance alignment, though the purpose of this analysis was simply to determine any significant differences between the two designs.

Of practical consequence to the saxophone performer, the constraints imposed on saxophone mouthpiece designs imply proper proportioning between the mouthpiece and the neckpipe of the instrument. Musicians typically adjust their mouthpiece position on the neckpipe for correct pitch, but this adjustment also affects the overall partial alignment of the instrument. Thus, as Benade points out, “Saxophone players would lead much easier lives if the mouthpiece cavities used on their

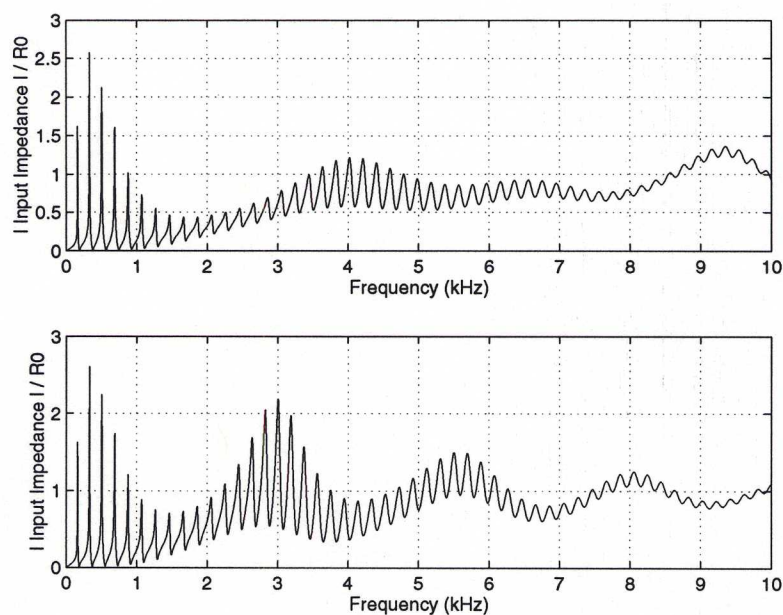


Fig. 2.17. Theoretical mouthpiece and air column structure input impedances, relative to $R_0 = \rho c/S$ at the input of the structure: (top) Wide chamber design; (bottom) Narrow chamber design.

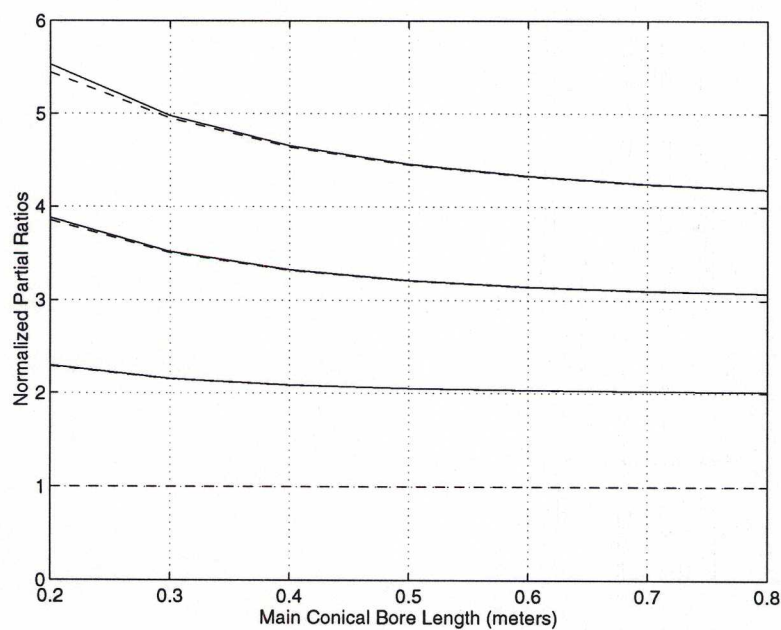


Fig. 2.18. Normalized partial frequency ratios for the theoretical mouthpiece and air column structures vs. air column length: (—) Wide chamber design; (---) Narrow chamber design.

instruments were fitted as meticulously to their instruments as are the double reeds used by their colleagues" (Benade, 1976, p. 472).

2.3.2 Reeds

The wooden cane reed used on reed woodwinds acts as a pressure-controlled air valve at the input of the instrument. As discussed in Section 1.5, the reed is typically modeled as a second-order, linear oscillator, an approximation which is reasonably accurate for small amplitude vibrations (Backus, 1963). For larger amplitudes, it is expected that nonlinearities occur. The resonance frequency of a clarinet reed falls somewhere in the range 2-3 kHz and can be modified by the player via lip position and lip pressure. Moving the lower lip away from the reed tip produces less damping. Greater lip pressure forces the reed closer to the curved mouthpiece lay, reducing its effective vibrating mass while at the same time, increasing its stiffness due to bending. All three factors will cause the reed resonance frequency to rise. Because it is driven at frequencies much lower than its resonance frequency, the reed is said to operate in a stiffness-dominated region where its motion is essentially "in-phase" with the driving pressure.

Backus (1961) measured the vibrations of a clarinet reed under artificial blowing conditions. He determined that for soft tones, the reed aperture does not close completely during the oscillatory cycle and the reed motion is nearly sinusoidal. At loud dynamic levels, the aperture is almost completely closed for about one-half cycle and completely open for the other half.

The resonance frequencies of an air column terminated by a compliant structure, or reed, are lowered by the reed's presence (Weber, 1830). If the reed formed a perfectly rigid termination, the air-column resonance frequencies would be lowered yet a little further. Alterations to the reed's natural frequency produce small but parallel changes to the air-column modes well below this frequency, and have greater impact on modes which lie near the reed resonance frequency. These effects, however, are reduced by reed damping (Benade, 1976, p. 436).

The reed woodwind performer uses lip pressure variations to affect changes in the reed aperture spacing, which in turn produce changes in the sounding frequency. *Vibrato* on single-reed woodwind instruments is primarily achieved in this way. The player applies an initial lip pressure to set the desired average reed aperture spacing, which is slightly smaller than the opening size when the reed is untouched. Further lip pressure under playing conditions causes the sounding frequency to increase, while less lip pressure lowers the sounding frequency. As one pushes the reed close to the mouthpiece facing, flow is constricted and sound production is negatively affected, setting an upper limit on the range of positive frequency variation. Likewise, the reed aperture can be opened only as far as its initial rest position, which limits negative frequency variations. Negative frequency shifts are easier to produce by lip pressure changes. Thus, vibrato is characterized by more negative than positive frequency deviation from the unmodified frequency to which it is applied. The range of frequency variation possible via lip pressure changes is typically on the order of a semitone or

smaller. Bak and Dømler (1987) explain the increase in sounding frequency produced by greater lip pressure as resulting from a gradual “shortening” of the reed’s length when it is pushed against the curved portion of the mouthpiece lay. This in turn reduces the reed’s flexibility and effectively reduces the length of the air column. This phenomenon might also be explained as resulting from an increase in the reed’s resonance frequency as it is bent toward the mouthpiece facing, in conjunction with the behavior mentioned in the preceding paragraph.

Performers typically notice a decrease in sounding frequency with an increase in blowing pressure. Bak and Dømler (1987) analyzed this relationship under artificial blowing conditions and determined that blowing pressure and frequency are positively correlated. Similar behavior in connection with reed organ pipes is reported by Bouasse and Fouchée (1930) and Hirschberg *et al.* (1990). Bak and Dømler were led to conclude that a performer simultaneously (and unconsciously) reduces lip pressure with an increase in blowing pressure, and as a result the sounding frequency decreases.

Thompson (1979) suggests that the reed woodwind performer adjusts the resonance frequency of the reed to correspond to a harmonic of the fundamental in order to stabilize notes which have only a single resonance peak below the air-column cutoff frequency. This author has noted a tendency to gradually modify reed damping, via lip position changes, over the range of the saxophone, such that less damping is used for higher notes. For extreme high register playing, this technique is often critical. However, while lower amounts of damping serve to increase the reed’s natural frequency, it seems unlikely that a performer would make such modifications on a note-by-note basis. Rather, the decrease in applied damping is believed to stabilize oscillations by keeping the reed resonance sufficiently high that the reed continues to function in its stiffness-dominated operating range. Thompson provides a series of “Musicians’ experiments” to support his analysis, though most of these are unconvincing. One example, in particular, is highly questionable.

As a final example of the application of the ideas presented in this paper, many of the saxophone mouthpiece facing designs prevalent in the 1920’s were such that the reed frequency could not be raised much above the playing frequency of notes in the top of the second register. The notes written at about *D6* could be achieved as reed regimes, but it was not possible to play many notes in the third register of the instrument. It was also not possible to play the second register without opening the register hole, because the reed frequency was too low to add energy to the oscillation at a higher component. More recent mouthpiece facing designs have allowed the reed frequency to be raised to a range analogous to that of the clarinet so that the third register is possible and the second register can be played without the register hole (Thompson, 1979).

Given the fact that Adolphe Sax demonstrated a three octave range on the saxophone in the 1840’s (Rascher, 1970), the validity of this example is unlikely. Further, this author has performed on saxophone mouthpieces (and instruments) from the 1920’s and has never had difficulty achieving a range of at least three and a half octaves.

Performers of reed woodwinds are typically affected by instrument response problems when they

travel to locations of significant elevation difference from their normal place of practice. By considering the reed's role as a pressure-dependent air valve, it is reasonable to expect variations in reed response between different elevations. At high elevations, the ambient air pressure is lower. Thus, the pressure variations within the air column will oscillate about a lower ambient pressure value. Because the reed functions properly for a particular range of pressure differences across it and because the average mouthpiece pressure will be lower (because of the lower ambient pressure), the performer will need to compensate for these effects by producing a greater oral cavity pressure than normal. In this sense, the reed behaves as if it were stiffer, which is the experience typically described in such an environment.

The reeds of musical instruments are wet before they are played, in order to increase their elasticity. Typically, these reeds are then allowed to dry after they have been used. As a result of this continuous wetting and drying, reeds tend to warp and eventually crack or "wear out." Performers can make life a lot easier for themselves by not allowing their reeds to dry. This author maintains an air-tight reed container in which a small sponge is kept wet. Warping problems are avoided by fastening the reeds to small pieces of plexiglass. Mold growth is greatly reduced by soaking the sponge in *Listerine*[®], which has a high alcohol content. In this way, reeds have been known to last over five years, as opposed to the more typical duration of a month or two.

2.4 The Oral Cavity

Wind instrument performers have long held that manipulations of their oral cavity play an important role in the performance of their instruments. At the same time, those in the acoustics community have generally ignored windway influences, or dismissed them as unimportant to the operation of the instrument. During the 1980's, however, such effects became the subject of great debate and a variety of studies were conducted.

There are several reasons why the influence of the oral cavity, or the upstream air column, was underestimated by acousticians. Benade (1985) shows that accurate analysis of wind instrument behavior is possible even when the oral cavity is ignored, due to symmetry of the upstream/downstream systems. Further, controlled manipulations of the vocal tract require years of practice to master, and in many instances, such techniques are beyond the ability of all but the professional musician. Thus, even acousticians of solid musical competence might never realize the possibilities offered by subtle oral cavity manipulations.

Many musicians have conducted studies themselves to show that windway variations are indeed an integral part of their performance technique. In one such example, Clinch *et al.* (1982) made X-ray fluoroscopic examinations of players' vocal tract shapes under performance conditions to determine the relationship between sounding frequency and vocal tract resonance frequencies. While the pictures showed interesting tendencies on the part of the performer, the acoustic analysis was

extremely limited. In general, Clinch *et al.* overestimated the role of the vocal tract, concluding that the upstream resonance frequencies *must* match those of the downstream system. Inherent in their conclusion, they incorrectly assumed that the reed drives the instrument air column. In fact, both the upstream and downstream air columns control the reed operation.

Backus (1985) correctly understood the symmetry of the upstream and downstream systems, stating that a player's windway can have significant influence over the reed oscillations only if its impedance is of similar or greater magnitude than that of the instrument air column. Based on his measurements of the vocal tract impedance, however, he concluded that the oral cavity has negligible effect on the tone of the instrument. It would appear that the swept-frequency measurement technique employed by Backus was inappropriate for use on the highly variable windway system. In an experiment with a clarinet under artificial blowing conditions, he found that effects were evident when the upstream system had resonances of comparable magnitude, but the resultant changes in sound quality were dismissed as insignificant. Had Backus explored these effects when the downstream resonance structure was weaker, his conclusions might have been different.

Benade (1985) and Hoekje (1986) present the most systematic and convincing analysis of the ways in which a player's windway might have an influence on sound production in wind instruments. The flow through the reed orifice can be expressed in terms of the upstream and downstream impedances Z_u and Z_d , the upstream and downstream pressures on the reed P_u and P_d , the reed impedance Z_r , and the pressure difference across the reed $P_\Delta = P_d - P_u$, as

$$U = \frac{P_d}{Z_d} + \frac{P_\Delta}{Z_r}, \quad (2.17a)$$

$$-U = \frac{P_u}{Z_u} + \frac{P_\Delta}{Z_r}. \quad (2.17b)$$

The first term on the right of each equation represents that component of the flow given by the acoustic pressure at the entryway of each respective air column. The second term represents the portion of the flow which fills the void left by the moving reed. Equations (2.17a) and (2.17b) can be combined to form the relationship

$$P_\Delta = U (Z_u + Z_d) \parallel Z_r, \quad (2.18)$$

which says that the pressure across the reed is proportional to the sum of the upstream and downstream impedances in parallel with the reed impedance. The reed impedance is typically very large compared with the other impedances, so that its role in the oscillation process is less consequential. Considerations of the nonlinear multicomponent regeneration process imply that, while a change in either the upstream or downstream impedance has considerable influence on the resultant sound spectrum on the *same* side of the reed, such a change has much less affect on the spectrum produced on the opposite side of the reed (Benade, 1985; Hoekje, 1986).

Impedance measurements of a player's windway made by Benade (1985), Hoekje (1986), and Wilson (1996) demonstrate that it is possible to shape the windway in such a way as to create

resonances that are significantly stronger than any of those found in a real instrument air column. It is also possible to shape the windway in such a way that it has no important resonances, and this shape is typically assumed by wind players in order to avoid undesired upstream effects. Thus, several situations can arise in which the upstream impedance can have significant impact on the reed oscillations and the radiated sound. In particular, when the downstream impedance structure is characterized by only a single resonance peak, a strong upstream resonance can be used to create multiphonic sounds. A strong windway resonance can also be used to stabilize a regime of oscillation, or in some instances, to completely dominate the resultant sound spectrum.

Many contemporary saxophone techniques, such as “altissimo” register playing and delicate multiphonic regimes, require highly refined control of windway shape variations. One exercise for the development of these skills calls for pitch bends via oral cavity manipulations. While high second register notes, approximately above written *B*5, can be lowered in this way by up to a perfect fourth, low register notes are largely invariable. Such behavior agrees well with the observations of Benade and Hoekje, as low register notes on saxophones are supported by several instrument air column resonances. In this case, the regime of oscillation is well entrained by the downstream system and largely unaffected by upstream manipulations. The cutoff frequency for an alto saxophone, however, is about 830 Hz, so that second (and higher) register notes are typically sustained by a single instrument air-column resonance (Benade and Lutgen, 1988). For these notes, it is possible to arrange a strong resonant peak in the player’s windway which can be used to take control of the oscillatory regime and bend the sounding pitch via oral cavity shape changes. Similar behavior was measured by Wilson (1996) in clarinet performance. Personal experience with this technique indicates that upstream manipulations can only be used to *lower* the sounding pitch from its initial, downstream-dominated frequency value. When started from high altissimo notes, the performer experiences discontinuities in the pitch bend at locations of lower downstream air column resonances. Thus, it would appear that upstream control and variation of the oscillatory regime cannot *continuously* occur across a strong downstream resonance. Pitch bends which rise in frequency are achieved by starting the note under the influence of an upstream resonance, which is subsequently increased in frequency via vocal tract variation up to the downstream resonance peak frequency. Jazz “scoops,” as well as the opening clarinet solo in the orchestrated version of George Gershwin’s *Rhapsody in Blue*, are well known examples of this technique.

2.5 Contemporary Performance Techniques

During the second half of the twentieth century, composers and musicians have made use of a variety of performance techniques which typically involve the creation of unconventional sounds and effects on traditional acoustic instruments. For wind instruments, the use of multiphonics, extended register playing, quarter tones, vocal sounds, and timbre variations has become commonplace in

contemporary music performance. In several cases, the production of these effects is dependent on oral cavity manipulations, as previously discussed. Several of these techniques are analyzed here in terms of their acoustic behavior.

2.5.1 Multiphonics

The production of multiphonics using woodwind instruments became widespread in the 1960's, and pedagogic studies soon followed which provided various tables of fingerings and their associated pitches (Bartolozzi, 1967; Caravan, 1974). Several detailed acoustical analyses appeared in the 1970's, though there were discrepancies between their conclusions (Benade, 1976; Backus, 1978).

Caravan (1974) notes that, because most multiphonic fingerings involve an open tonehole high on the air column and several closed holes below it, the resulting sounds can often be analyzed in terms of two simultaneous bore lengths. Figure 2.19 indicates a clarinet multiphonic fingering and the associated written notes that it produces. The written *D*4 is produced by the upper bore length, which is terminated by the highest open hole on the air column. This fingering alone would normally generate a written *E*4, but the presence of the lower closed holes flattens its pitch. The highest open hole then functions as a register hole for the longer bore length, which is terminated by the open holes near the bottom of the air column. The third, fifth, and seventh harmonics of the longer air column length would approximately produce the notes *D*5, *B*5, and a slightly flat *F*6, respectively. Instead, the third harmonic sounds an *F*5 because of the "misplaced" register hole, while the seventh harmonic approximately sounds an *E*6. Caravan's observations are essentially related to the locations of the air column resonances, which are created by a vented, long tube length and an unvented shorter bore length.



Fig. 2.19. A *B* \flat clarinet multiphonic fingering and the corresponding written notes it produces.

(Benade, 1976, pp. 559–567) analyzes the spectral content of a multiphonic sound in terms of the nonlinear, heterodyning action of the reed. Those components of the sound which contribute most directly to the maintenance of oscillation have frequencies quite near the strongest input impedance peaks. As these peaks are typically not harmonically aligned, due to the non-traditional fingering, the reed is able to oscillate in several different regimes simultaneously. Heterodyned spectral components may arise at frequencies where cooperation with an air column resonance is not favored.

Backus (1978) finds that multiphonic sounds can be well analyzed in terms of just two independently generated main components, one associated with the lowest air column resonance and the other with the third or fourth resonance. Through the action of the reed, oscillations based on

the higher bore resonance are amplitude modulated by the lower resonance, producing heterodyne components based solely on multiples of these two frequencies. Backus cites Benade's work and questions the complexity of his analysis, indicating that the same conclusions could be reached by considering only two resonance frequencies.

Benade (1976) and Backus (1978) base their analyses of multiphonic sounds on the relationship between measured input impedances and heterodyne components. Caravan's analysis is certainly less rigorous in terms of its acoustical basis, but it does lend an intuition to the situation not provided by the others. It would appear that the two resonance approach of Backus, in combination with that of Caravan, provides the best description of multiphonic sound production in woodwinds.

2.5.2 The Saxophone's Altissimo Register

The saxophone, as designed by Adolphe Sax, had a conventional playing range extending from written *B3* to *F6* (Berlioz, 1856). However, an early article on the instrument indicates a three octave range (Berlioz, 1842). Berlioz wrote this description after a visit by Adolphe Sax, in which the inventor demonstrated his new musical instrument. Thus, it is clear that Sax made use of "non-traditional" cross-fingerings to extend the range of his instrument, a technique commonly used on most other woodwind instruments in those days. Nonetheless, it appears that this technique proved difficult for early saxophonists to master and was largely discarded at a relatively early stage in the saxophone's development. A patent filed in 1880 by Sax, as translated by Hemke, reads:

The *E♭* alto saxophone - the most prevalent saxophone and the one most favorable for military bands represents the viola part of a string quartet. Its lower range falls short of the extreme low limit of the violin family by one tone. I have lengthened the tube in order to gain two semitones, *B3♭* and *A3*, which represent the transposed pitches of *D3♭* and *C3*.

Realizing that an analogous situation exists in the upper register, I have added keys to play high *F6♯* and high *G6*. *F6♯* to be fingered with the right hand and high *G6* with the left. You should be able, nevertheless, if you prefer, to use the other fingerings. In order to facilitate the production of the high notes, I employ a fourth octave key, which contrary to the usual practice, is not fingered with the thumb, but operates through a mechanism articulated to the upper register keys themselves. This method of operation can be used for every high note[†] (Hemke, 1975, pp. 77-78).

Thus, Sax found it necessary to provide additional toneholes on the instrument in order to extend its upper range, even though it was obvious to him that "other fingerings" existed for this purpose.

There is now evidence that several saxophonists from the first half of the twentieth century ventured beyond the conventional *F6* limit, though most of these individuals did not seek to educate or hand down their acquired skill (Rascher, 1970). Of notable exception, however, is the pioneering saxophone virtuoso, Sigurd Rascher, who inspired some of the most prominent composers of his time

[†]The third octave key was provided by Sax as an alternate method for producing the notes *A4* - *C5♯*, based on the second resonances of the longest tube lengths of the instrument. This hole was located near the left hand thumb.

to produce a large repertoire employing the saxophone's extended, or "altissimo" range. Through his examples and writings, Rascher almost single-handedly brought about the changes necessary to make extended register playing as accessible as it is today.

In general, cross-fingerings and oral cavity manipulations can be found to extend the *E \flat* alto saxophone's upper range by another octave and a half. These notes are produced using third and higher resonances of the instrument. Production and control of these notes, particularly above *B6* on an alto saxophone, often requires the use of a stiff reed, which has a high resonance frequency. In this way, the reed resonance can be sufficiently maintained above the fundamental frequency, as discussed in Section 2.3.2. An alto saxophone reed has an estimated natural frequency range of about 1-3 kHz. Henry Brant's *Concerto for E \flat Alto Saxophone and Orchestra* (1947) calls for a high *B7 \flat* , which has a corresponding frequency of 2.2 kHz. Playing experiments on most of the members of the saxophone family indicate that all of their upper ranges are commonly limited to about 2 kHz.

As previously discussed, oral cavity manipulations play an important part in stabilizing extended register notes. These notes have fundamental frequencies which are higher than the open-THL cutoff frequency, so that the air column resonances on which they are based are not nearly as strong as those used in the conventional playing range. Vocal tract influences are then used to stabilize such oscillations, as well as the reed resonance.

As might be expected, slurring among extended register notes is often difficult to control. A little thought and experimentation should make it obvious that such slurs are reasonably easy when attempted between notes produced using the same air column resonance, but nearly impossible when changing resonances.

2.5.3 Additional Contemporary Techniques

The production of quarter tones on woodwind instruments is certainly not straight-forward, as these instruments are provided with toneholes designed to produce only the conventional twelve-tone octave. As a result, various non-traditional cross-fingerings and tonehole configurations must be used to produce the desired sounding frequencies. It sometimes occurs that a particular quarter tone fingering can not be found, in which case the performer is forced to "lip down" the pitch by the appropriate amount.

Timbre variations are commonly produced on woodwind instruments by closing toneholes below the first open fingerhole. In effect, the performer is changing the open-THL cutoff frequency via changes in the interhole spacing. These variations alter the resultant sound spectrum via modifications to the upper sound components, but leave the fundamental frequency largely unaffected. Timbre changes can also be created by alternating between traditional fingerings designed to produce the same note.

Several extended performance techniques involve *breath pressure modulations*, or the superposition of higher frequency components over the steady breath pressure. *Flutter tonguing*, accomplished

using either the tongue or uvula (velum), results in the addition of a 15 – 30 Hz signal to the breath pressure stream. Growling and singing are produced by audio rate modulations of the breath pressure.

Chapter 3

Digital Waveguide Modeling of Single-Reed Woodwinds

A primary objective of this work is to detail the implementation of the acoustic principles described in Chapters 1 and 2 using the discrete-time technique of *digital waveguide modeling*. Hirschman (1991) considered many of these same issues, though that work was principally concerned with the efficient synthesis of woodwind sounds and less so with the accuracy of results in comparison to detailed acoustical studies of individual instrument components. A more recent study by Välimäki (1995) dealt with several aspects of digital waveguide modeling of woodwind instruments, such as fractional delays, toneholes, and the junctions between cylindrical and conical sections. The present work combines the most current understanding of all single-reed woodwind instrument acoustic principles in a complete model, suitable for use by physicists conducting detailed acoustic studies or musicians wishing to perform real-time, virtual computer-music instruments.

The use of digital waveguides was first proposed by Smith (1985) for the efficient simulation of reverberation. The modeling of musical instruments using this technique was subsequently described in (Smith, 1986). Digital waveguide modeling is an efficient and accurate method for time-domain simulation of one-dimensional wave propagation, which has gained increasing popularity in the field of musical acoustics research since the publication of McIntyre *et al.* (1983). The theory of digital waveguide modeling has been well summarized in (Smith, 1996*b*).

The frequency-domain analysis of musical instrument acoustic behavior provides much information regarding the linear components of these systems, as seen in Chapter 1. Nonlinear behavior, however, is best examined and determined in the time-domain. Thus, for the development of complete instrument models which include a nonlinear excitation mechanism, efficient and accurate methods for time-domain simulation are necessary. Digital waveguide techniques can be used to accomplish this task. Further, frequency-domain characterizations of instrument components, such

as air-column junctions and toneholes, can be incorporated into a digital waveguide model in a straight-forward manner. In terms of traditional methods for computer synthesis of musical instruments, digital waveguides offer complete modularity and flexibility to an extent never before possible with additive synthesis or sampling techniques. While the development of digital waveguide models requires significant familiarity with musical instrument acoustic properties, the resulting “virtual” instruments provide unsurpassed “physical” control of their behavior.

It is interesting to compare the digital waveguide approach with more traditional continuous-time analysis methods, as briefly discussed in Section 1.3.4. A recent paper by Ayers (1996) presents a continuous-time model of a brass instrument air column and lumped mouthpiece arrangement which has direct parallels to digital waveguide methods. Because this theory is eventually discretized for implementation and because the use of delay lines can drastically reduce computational costs, it appears that Ayers (1996) could benefit by incorporating waveguide techniques.

3.1 Modeling Sound Propagation in One Dimension

This section reviews the fundamentals of digital waveguide modeling as related to wave propagation in air, and is derived in large part from (Smith, 1996b). Sound propagation in air was discussed in Section 1.1 and the scalar wave equation for plane-wave pressure propagation in one dimension was found to be

$$\frac{\partial^2 p}{\partial x^2} = \frac{1}{c^2} \frac{\partial^2 p}{\partial t^2}. \quad (3.1)$$

A variety of other plane-wave variables, including particle displacement and velocity, can be similarly expressed in this form. D’Alembert published a general solution to Eq. (3.1) in 1747 of the form

$$p(x, t) = f(t - x/c) + g(t + x/c). \quad (3.2)$$

The functions $f(\cdot)$ and $g(\cdot)$ are completely general and continuous and can be interpreted as arbitrarily fixed waveshapes that travel in opposite directions along the x -axis with speed c . This representation of wave propagation is referred to as the *traveling-wave solution* to the one-dimensional wave equation.

Digital waveguide modeling is based on the traveling-wave representation of one-dimensional wave propagation. The individual traveling-wave amplitudes are sampled in both time and space. The temporal sampling interval is T seconds, which corresponds to a sampling rate $f_s \triangleq 1/T$. The spatial sampling interval is given most naturally by $X \triangleq cT$ meters, or the distance traveled by sound in one temporal sampling interval. In this way, each traveling-wave component moves left or right one spatial sample for each time sample. Using the change of variables

$$\begin{aligned} x &\rightarrow x_m = mX \\ t &\rightarrow t_n = nT, \end{aligned}$$

Eq. (3.2) becomes

$$\begin{aligned}
 p(t_n, x_m) &= f(t_n - x_m/c) + g(t_n + x_m/c) \\
 &= f(nT - mX/c) + g(nT + mX/c) \\
 &= f[(n - m)T] + g[(n + m)T].
 \end{aligned} \tag{3.3}$$

This representation can be further simplified by suppressing T and defining

$$p^+(n, m) \triangleq f(nT, mT) \quad p^-(n, m) \triangleq g(nT, mT),$$

where the superscripts $+$ and $-$ denote wave travel to the right and left, respectively. The resulting expression for total pressure at time n and location m is given as the sum of the two traveling-wave components

$$p(t_n, x_m) = p^+(n - m) + p^-(n + m). \tag{3.4}$$

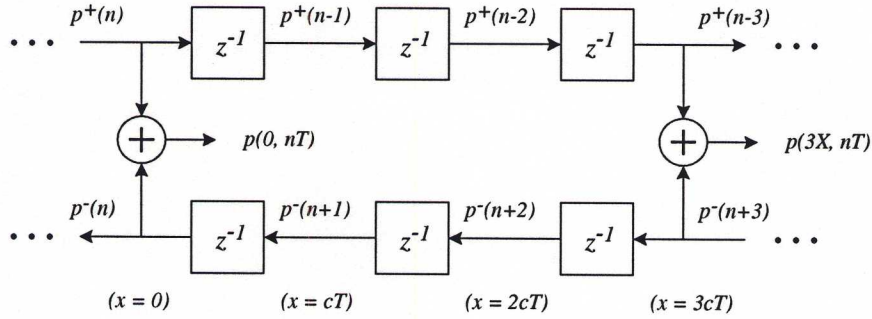


Fig. 3.1. Digital waveguide implementation of ideal, lossless plane-wave propagation in air [after (Smith, 1996a)]. The z^{-1} units represent one-sample delays.

Figure 3.1 depicts a digital waveguide section which implements the traveling-wave solution of Eq. (3.4) using bi-directional delay lines. The upper delay line simulates the term $p^+(n - m)$ as the output of an m -sample delay line with input $p^+(n)$. The lower delay line simulates the term $p^-(n + m)$ as the *input* to an m -sample delay line with *output* $p^-(n)$. The total or physical pressure at any location in the waveguide is given by the sum of the upper and lower delay lines, as shown for the points $x = 0$ and $x = 3X$. The model is exact at these sampling instants, to within the numerical precision of the samples themselves, provided that the waveshapes traveling within the structure are initially bandlimited to less than half the sampling frequency f_s . To obtain an output at non-integer values of X , a variety of spatial interpolation techniques are available using fractional delay filters (Välimäki, 1995).

While sound propagation in air is typically analyzed and simulated in terms of pressure wave components, as in the previous analysis, it is also possible to describe such motion in terms of velocity or displacement wave variables. In general, the propagation of any wave variable can be

simulated using digital waveguides, given that the wave equation can be expressed in terms of this variable and that a traveling-wave solution exists.

This study is primarily concerned with one-dimensional wave propagation. It should be noted, however, that two- and three-dimensional wave propagation can also be modeled using digital waveguide techniques. Two-dimensional waveguide modeling of acoustic structures was first reported by Van Duyne and Smith (1993). A more recent paper (Van Duyne and Smith, 1996) summarizes the simulation of wave propagation in three-dimensions using waveguide techniques. While one-dimensional waveguide models perfectly simulate ideal, lossless wave propagation, higher dimensional waveguide structures exhibit direction-dependent dispersion characteristics.

3.2 Modeling Lumped Acoustic Systems

Digital waveguides provide a highly efficient means for the simulation of one-dimensional wave propagation. Many acoustic phenomena however, such as wave propagation at the end of an open tube or at the junction of a woodwind tonehole, are most easily simulated in terms of their lumped behavior, as discussed in Section 1.2. That is, rather than attempt to simulate the complex interaction of waves in these structures, it is more convenient to use a lumped impedance description that is only concerned with the output of the system given a particular frequency-dependent input. In order to incorporate such lumped elements in digital waveguide models, it is necessary to express these lumped impedances in terms of traveling-wave parameters and then to convert such expressions to discrete-time filters.

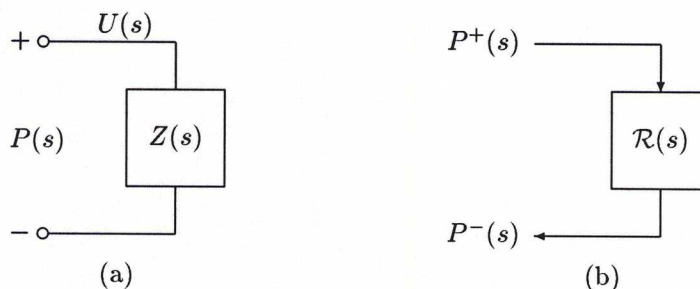


Fig. 3.2. Lumped impedance block diagrams [after (Smith, 1996a)]: (a) Impedance representation; (b) Digital waveguide representation.

Figure 3.2a shows the impedance representation of a general lumped series impedance $Z(s)$, where $s = \sigma + j\Omega$ is the Laplace transform frequency variable. For implementation within the context of a digital waveguide simulation, this representation must be recast in terms of a traveling-wave reflectance, as shown in Fig. 3.2b. The decomposition of pressure and volume velocity wave variables into their traveling-wave components is written in the frequency domain for any fixed

position as

$$P(s) = P^+(s) + P^-(s) \quad U(s) = U^+(s) + U^-(s). \quad (3.5)$$

Pressure and volume velocity traveling-wave components are related for plane-wave propagation in acoustic structures by

$$P^+(s) = Z_0 U^+(s) \quad P^-(s) = -Z_0 U^-(s), \quad (3.6)$$

where Z_0 is the real valued characteristic wave impedance in the structure. Using these relationships, the impedance $Z(s)$ of Fig. 3.2a can be transformed to a plane-wave pressure reflectance as

$$\begin{aligned} P(s) &= Z(s)U(s) \\ P^+(s) + P^-(s) &= Z(s) [U^+(s) + U^-(s)] \\ &= Z(s) \left[\frac{P^+(s) - P^-(s)}{Z_0} \right] \\ \mathcal{R}(s) &\triangleq \frac{P^-(s)}{P^+(s)} = \left[\frac{Z(s) - Z_0}{Z(s) + Z_0} \right]. \end{aligned} \quad (3.7)$$

This expression is similar to that found in Section 1.3.1 for the pressure wave reflectance in cylindrical bores. Spherical-wave pressure and volume velocity traveling-wave components in acoustic structures are related by a space- and frequency-dependent characteristic impedance, as discussed in Section 1.3.2. These relationships are given by

$$P^+(x, s) = Z_0(x, s) U^+(x, s) \quad P^-(x, s) = -Z_0^*(x, s) U^-(x, s), \quad (3.8)$$

where $Z_0(x, s)$ is the complex valued characteristic wave impedance and $Z_0^*(x, s)$ denotes the para-conjugate of $Z_0(x, s)$. Thus, for structures in which spherical-wave propagation occurs, such as conical bores, a lumped series impedance $Z(x, s)$ can be transformed to a pressure wave reflectance as

$$\begin{aligned} P(x, s) &= Z(x, s)U(x, s) \\ P^+(x, s) + P^-(x, s) &= Z(x, s) [U^+(x, s) + U^-(x, s)] \\ &= Z(x, s) \left[\frac{P^+(x, s)}{Z_0(x, s)} - \frac{P^-(x, s)}{Z_0^*(x, s)} \right] \\ \mathcal{R}(x, s) &\triangleq \frac{P^-(x, s)}{P^+(x, s)} = \left[\frac{Z(x, s)Z_0^*(x, s) - Z_0(x, s)Z_0^*(x, s)}{Z(x, s)Z_0(x, s) + Z_0(x, s)Z_0^*(x, s)} \right]. \end{aligned} \quad (3.9)$$

This expression is similar to that found in Section 1.3.2 for the pressure wave reflectance in conical bores. It is common to simulate propagating pressure waves in reed-driven woodwind instruments, because their excitation mechanism is pressure controlled. Instruments which are excited by an air jet, however, are best simulated in terms of propagating volume velocity waves. Relationships similar to the preceding reflectances result when derived in terms of volume velocity waves.

For implementation of the reflectance in the digital domain, it is necessary to convert the continuous-time filter to an appropriate discrete-time representation. A variety of techniques exist for this purpose (Smith, 1983; Oppenheim and Schaffer, 1989). In this study, use is generally made of either the bilinear transform or an equation-error minimization technique which matches both frequency response magnitude and phase.

The bilinear transform (Oppenheim and Schaffer, 1989, pp. 415-430) is an algebraic transformation between the continuous-time and discrete-time frequency variables s and z , respectively. It is therefore appropriate only when a closed-form filter representation in s exists. Using the substitution

$$s = \alpha \frac{1 - z^{-1}}{1 + z^{-1}}, \quad (3.10)$$

the discrete-time counterpart to a continuous-time transfer function $H_c(s)$ is given by

$$H_d(z) = H_c\left(\alpha \frac{1 - z^{-1}}{1 + z^{-1}}\right).$$

The bilinear transform maps the entire continuous-time frequency space, $-\infty \leq \Omega \leq \infty$, onto the discrete-time frequency space $-\pi \leq \omega \leq \pi$. Continuous-time dc ($\Omega = 0$) maps to discrete-time dc ($\omega = 0$) and infinite continuous-time frequency ($\Omega = \infty$) to the *Nyquist frequency* ($\omega = \pi$). Thus, a nonlinear *warping* of the frequency axes occurs. However, since the $j\Omega$ -axis in the s plane is mapped exactly once around the unit circle of the z plane, no aliasing occurs. The constant α is typically given by $\alpha = 2/T$, where T is the discrete-time sampling interval. This parameter (α) provides one degree of freedom for the mapping of a particular finite continuous-time frequency to a particular location on the z -plane unit circle. The warping of frequencies is given for the discrete-time frequency in terms of α and Ω as

$$\omega = 2 \arctan(\Omega/\alpha).$$

Because of the nonlinear compression of the frequency axis, use of the bilinear transformation should be limited to filters with a single transition band (lowpass and highpass) or resonance (narrow bandpass and bandstop).

Numerous methods exist for the design of digital filters based on a given system frequency response. A technique based on equation-error minimization is used in several instances in this study, particularly when a desired frequency response is known but a closed-form solution is impossible. The theory of equation-error techniques is discussed in (Smith, 1983, pp. 47-50, 98-103). Given a desired continuous complex spectrum $H_c(e^{j\Omega})$, this method attempts to find a stable digital filter of the form

$$H_d(z) \triangleq \frac{B_d(z)}{A_d(z)}, \quad (3.11)$$

where

$$\begin{aligned} B_d(z) &\triangleq b_0 + b_1 z^{-1} + \cdots + b_{n_b} z^{-n_b} \\ A_d(z) &\triangleq 1 + a_1 z^{-1} + \cdots + a_{n_a} z^{-n_a}, \end{aligned}$$

with n_b and n_a given, such that the L^2 norm of the equation-error

$$\|A_d(e^{j\Omega})H_c(e^{j\Omega}) - B_d(e^{j\Omega})\|_2 = \|A_d(e^{j\Omega})\|_2 \cdot \|H_c(e^{j\Omega}) - H_d(e^{j\Omega})\|_2 \quad (3.12)$$

is minimized with respect to the filter coefficients. Both spectral phase and magnitude are matched while allowing arbitrary numerator and denominator orders. Smith (1983) points out that the equation-error norm is equivalent to the norm $\|H_c(e^{j\Omega}) - H_d(e^{j\Omega})\|_2$, but weighted by the poles of the filter to be designed. An equation-error method is implemented in *MATLAB*® by the function *invfreqz*.

3.3 Modeling Woodwind Instrument Bores

The acoustic behavior of wind-instrument air columns has traditionally been described in the frequency-domain, where such characteristics as normal-mode frequencies and decay rates and tonehole-lattice cutoff frequencies are easily identifiable. The requirements for wind-instrument bores, as discussed in Section 1.3, are also typically stated in terms of frequency-domain constraints. Research on wind-instrument nonlinear excitation mechanisms and their complex coupling with the air column, as well as interest in the simulation of a complete wind instrument, however, has led to the development of time-domain models of wind-instrument sound production. The time-domain analysis of woodwind bores was briefly explored in Section 1.3.4. The linear time-domain response of an air column is represented by either its impulse response $h(t)$ or its reflection function $r(t)$. The impulse response is the pressure response at the bore entrance to the introduction of a unit volume velocity impulse. Because the entryway is represented by a closed end after the impulse is introduced, $h(t)$ is a slowly decaying function. The reflection function is the pressure response at the entrance of the air column to the introduction of a unit pressure impulse. There are no reflections at the bore entryway for this response function, so that it decays to zero much more quickly than the impulse response. Traditional computational methods for the simulation of time-domain pressure propagation in a complete wind instrument involve the convolution of mouthpiece pressure with an air column response function during each time sample period. In this respect, $r(t)$ serves to greatly reduce the number of mathematical operations necessary for calculation of the model output. Digital waveguide modeling of wave propagation in wind-instrument air columns incorporates the advantages of the reflection function approach, and further reduces computational requirements by “pulling out” the delay inherent in $r(t)$ and implementing it in the form of digital delay lines.

It was previously noted [Section 1.3] that the requirements for wind-instrument bores are *perfectly* satisfied by one-parameter waves, which are possible only in rectangular, circular cylindrical, and spherical coordinates, corresponding to pipes of uniform cross-section and conical horns, respectively (Putland, 1993). Woodwind bores are mostly cylindrical or conical in shape, and variations from these ideals can be approximated by cylindrical and conical sections. In this section, it will be

shown that digital waveguides provide an efficient means for the simulation of one-parameter wave propagation in cylindrical and conical bores.

3.3.1 Cylindrical Bores

In Section 1.3.1, the three-dimensional Helmholtz equation was solved in circular cylindrical coordinates. By applying appropriate boundary conditions, it was found that for musical purposes, wave motion in wind instruments with cylindrical bores is adequately represented by plane-wave propagation along the length of the pipe.

The simulation of one-dimensional plane-wave propagation in cylindrical bores using digital waveguides follows directly from the discussion of Section 3.1. The one-dimensional wave equation for plane waves,

$$\frac{\partial^2 p}{\partial x^2} = \frac{1}{c^2} \frac{\partial^2 p}{\partial t^2}, \quad (3.13)$$

accurately represents lossless wave propagation along the central axis of a cylindrical tube, subject to the boundary conditions at both its ends. The discrete-time and -space traveling-wave simulation of this wave propagation is then given by

$$p(t_n, x_m) = p^+(n - m) + p^-(n + m) \quad (3.14)$$

as previously shown. In Section 1.3.1, the behavior of a finite length cylindrical bore was approximated for low-frequency sound waves by assuming that pressure is equal to zero at the open end of the tube. This boundary condition is met with an inversion of traveling-wave pressure components at the open end, so that the sum of the left- and right-going waves is zero. Figure 3.3 represents the digital waveguide implementation of lossless plane-wave pressure propagation in an ideally terminated cylindrical tube. The negative one multiplier at $x = L$ implements the low-frequency, open-end

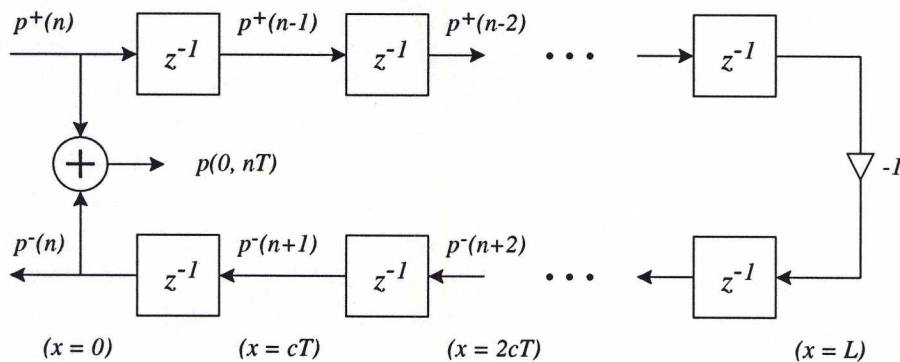


Fig. 3.3. Digital waveguide implementation of ideal, lossless plane-wave propagation in a cylindrical tube. The z^{-1} units represent one-sample delays.

approximation for traveling-wave pressure reflection. The system of Fig. 3.3 is a discrete-time and

-space implementation of an ideal cylindrical bore reflection function. As derived in Section 1.3.1, the reflectance seen from the entrance of a cylindrical tube of length L is given by

$$\mathcal{R}(\Omega) = e^{-2jkL} \left[\frac{Z_L(\Omega) - Z_0}{Z_L(\Omega) + Z_0} \right], \quad (3.15)$$

where Z_0 is the real characteristic wave impedance of the cylindrical pipe, and $Z_L(\Omega)$ is the load impedance at $x = L$. For $Z_L(\Omega) = 0$, which corresponds to zero pressure at $x = L$, $R(\Omega) = -e^{-2jkL}$. The resulting continuous-time reflection function $r(t) = -\delta(t - 2L/c)$ is found as the inverse Fourier transform of $\mathcal{R}(\Omega)$ when viscothermal losses are ignored. This time delay is realized in the digital domain by the delay lines of Fig. 3.3. Digital delay lines are easily implemented in computer software, requiring only a fetch, store, and pointer update at each time sample. Digital waveguide implementations thus offer an extremely efficient means for the modeling of acoustic behavior within a wind-instrument air column. The structure of Fig. 3.3 can be converted to that of a lattice digital filter by commuting the delays of the upper delay line to the lower delay line. The lattice filter scattering junctions are unnecessary in this case because of the uniform characteristic impedance inside the ideal cylindrical bore.

The open end of a cylindrical pipe is poorly represented by a load impedance $Z_L(\Omega) = 0$, as discussed in conjunction with sound radiation in Section 1.4.1. In general, the acoustic properties of the end of the wind-instrument bore are characterized by a non-zero and complex valued load impedance and this impedance can be expressed as a lumped traveling-wave reflectance, as given by the bracketed term of Eq. (3.15) and described in Section 3.2. Figure 3.4 represents the digital waveguide implementation of plane-wave pressure propagation in a cylindrical tube terminated by the reflectance $\mathcal{R}_L(z)$. Thermal and viscous boundary layer losses are neglected in this model. The

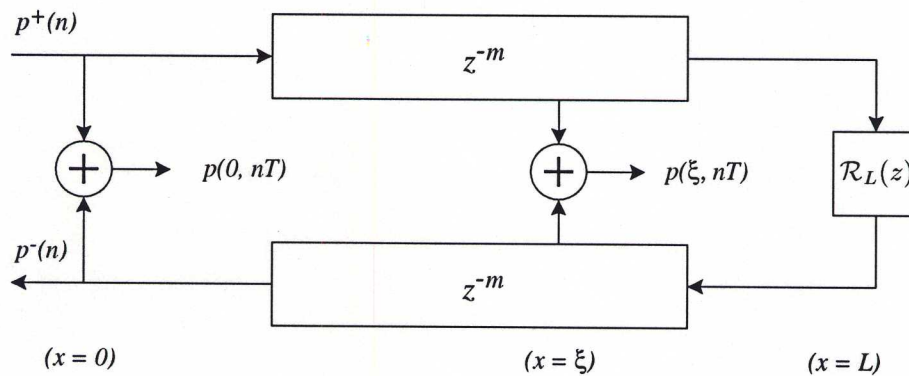


Fig. 3.4. Digital waveguide implementation of plane-wave propagation in a cylindrical tube, neglecting viscothermal losses.

waveguide structure of Fig. 3.4 can be further simplified by limiting observation of physical pressure to the input of the tube. Then, by linearity and time-invariance, the digital filter representing $\mathcal{R}_L(z)$ can be “pushed” through the lower delay line to its output and a single delay line used for

the simulation, as shown in Fig. 3.5. In general, a digital waveguide model with a single observation point can be implemented using one delay line as long as it is possible to “tap” into and out of any point on the delay line.

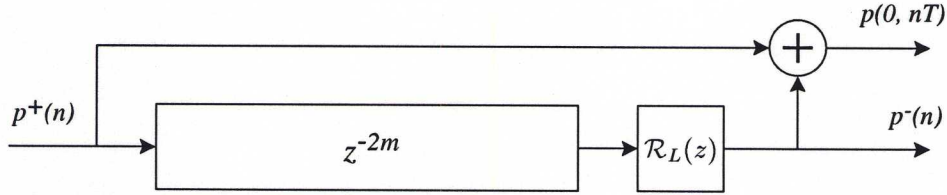


Fig. 3.5. Simplified digital waveguide implementation of plane-wave propagation in a cylindrical tube using a single delay line and neglecting viscothermal losses. The pressure observation point is constrained to the entryway of the bore.

The impulse response $h(t)$ of a wind-instrument air column, defined as the inverse Fourier transform of its input impedance, implies an acoustic feedback loop because of the inherent closure of the bore entryway after the introduction of a volume velocity unit impulse. The infinite termination impedance of the closed end results in a non-inverting reflection of pressure, so that the waveguide model of a closed-open cylindrical bore is as shown in Fig. 3.6. The waveguide “input impedance” is found by calculating the system impulse response and transforming it to the frequency domain using the discrete Fourier transform (DFT). If $\mathcal{R}_L(z)$ is approximated for low-frequency sound waves by a simple inversion, the impulse response of the feedback system of Fig. 3.6 will be periodic and of infinite duration. The Fourier transform of the resulting infinite length periodic impulse train will then simplify to $j \tan(kL)$, which is equivalent to the input impedance found analytically for a closed-open cylindrical bore in Section 1.3.1.

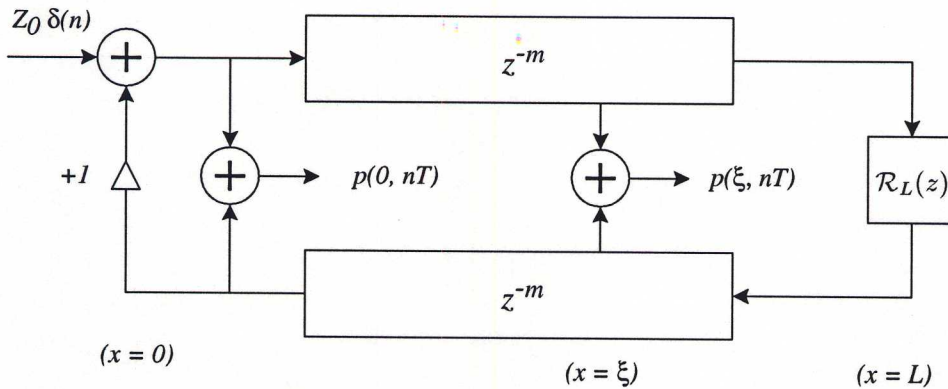


Fig. 3.6. Digital waveguide model of a closed-open cylindrical bore.

In comparison to traditional time-domain bore simulation techniques, the digital waveguide bore implementation offers high efficiency without sacrificing accuracy. The lumped open-end reflectance

filter $\mathcal{R}_L(z)$ is generally adequately implemented using a first- or second-order digital filter. Thus, just a single short convolution/filtering operation is necessary in this model.

Evanescent transverse modes in cylindrical bores can dissipate energy if appropriately excited. Within woodwind instruments, evanescent mode dissipation will most likely take place near bore discontinuities, such as the excitation mechanism, toneholes, and bells. While such effects are generally insignificant, it is possible to develop three-dimensional waveguide mesh structures to account for higher order mode behavior (Van Duyne and Smith, 1993, 1996; Savioja *et al.*, 1994). At a sampling rate of 44.1 kHz, the spatial sampling interval of a digital waveguide system is approximately 7.87 millimeters. As previously noted in Section 1.3.1, the lowest two cutoff frequencies for transverse modes in the cylindrical bore of a flute are approximately 11.96 kHz and 19.8 kHz. Three-dimensional mesh structures provide frequency resolution only up to about a quarter of the sampling rate (Van Duyne and Smith, 1996), so that a 3D bore mesh implementation should be highly oversampled. The necessity for fractional delay interpolation and the resulting attenuation could make such a model of minimal benefit. Further, wave dispersion in 3D mesh implementations could interfere with the accuracy of the fundamental propagating mode, which does not occur in the one-dimensional model.

3.3.2 Conical Bores

It was found in Section 1.3.2 that, for musical purposes, sound propagation in conical air columns can be well modeled by one-dimensional spherical waves traveling along the length of the bore. The one-dimensional wave equation for spherical pressure waves,

$$\frac{1}{x} \frac{\partial^2(xp)}{\partial x^2} = \frac{1}{c^2} \frac{\partial^2 p}{\partial t^2}, \quad (3.16)$$

accurately represents lossless pressure wave propagation along the central axis of a conical tube, subject to the boundary conditions at both its ends. The continuous-time traveling-wave solution to this equation is

$$p(x, t) = \frac{f(t - x/c)}{x} + \frac{g(t + x/c)}{x}, \quad (3.17)$$

where the functions $f(\cdot)$ and $g(\cdot)$ are completely general and continuous and can be interpreted as arbitrarily fixed waveshapes that travel in opposite directions along the x -axis with speed c . This expression is similar to that for plane waves with the exception that spherical pressure traveling-wave components are inversely proportional to their distance from the cone apex. As was shown in Section 3.1, a solution of this form can be discretized in time and space and given by (Smith, 1991)

$$p(t_n, x_m) = \frac{p^+(n - m)}{x} + \frac{p^-(n + m)}{x}. \quad (3.18)$$

In Section 1.3.2, the behavior of a finite length conical bore was approximated for low-frequency sound waves by assuming that pressure is equal to zero at the open end of the tube. This boundary

condition is met with an inversion of traveling-wave pressure components at the open end, so that the sum of the left- and right-going waves is zero. Figure 3.7 represents the digital waveguide implementation of ideal, lossless spherical-wave propagation in an ideally terminated conical tube. Aside from the $1/x$ scale factors, which are implemented at observation points, the cylindrical and

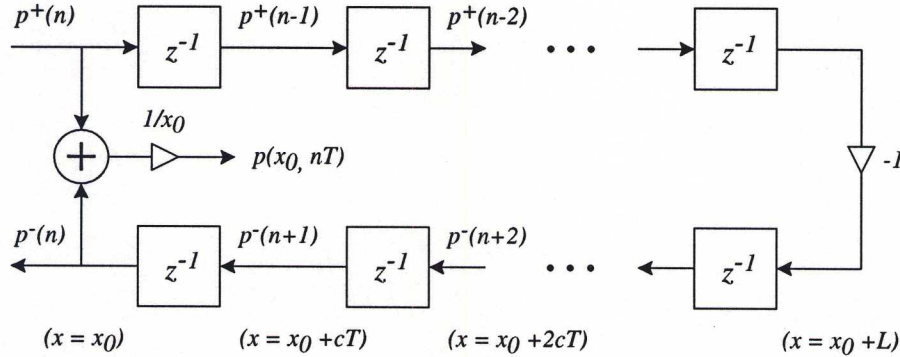


Fig. 3.7. Digital waveguide implementation of ideal, lossless spherical-wave propagation in a conical tube [after (Smith, 1996a)].

conical waveguide implementations are exactly the same. Further, if the system input and output are measured at the same location, the $1/x$ scale factor is unnecessary. Differences between the two systems, however, arise at discontinuities.

The system of Fig. 3.7 is an efficient discrete-time and -space implementation of the ideal pressure reflection function for conical bores. As derived in Section 1.3.2, the pressure wave reflectance seen from the entrance of a conical tube which is terminated with a load impedance $Z_L(\Omega)$ at $x = L$ is given by

$$\mathcal{R}(x, \Omega) = e^{-2jkL} \left[\frac{Z_L(\Omega)Z_0^*(L, \Omega) - Z_0(L, \Omega)Z_0^*(L, \Omega)}{Z_L(\Omega)Z_0(L, \Omega) + Z_0(L, \Omega)Z_0^*(L, \Omega)} \right], \quad (3.19)$$

where $Z_0(x, \Omega)$ is the complex characteristic wave impedance of the cone. The waveguide implementation of Fig. 3.7 corresponds to $Z_L(\Omega) = 0$, for which $\mathcal{R}(x, \Omega) = -e^{-2jkL}$. For a general (and more physical) non-zero $Z_L(\Omega)$, however, the bracketed term of Eq. (3.19) specifies the lumped traveling-wave reflectance of the load, as discussed in Section 3.2.

In Section 1.3.2, it was observed that pressure and volume flow traveling-wave components grow increasingly out of phase as they approach the cone apex. This behavior is defined by the complex characteristic impedance of conical air columns. The boundary condition imposed by a rigid termination requires that volume flow normal to the boundary equal zero. Where spherical volume velocity traveling-wave components reflect with an inversion, so that their sum is zero, spherical pressure traveling-wave components reflect with a phase angle $2 \angle Z_0(x, \Omega)$. In the case of a complete cone, $\angle Z_0(0, \Omega) = 90^\circ$, and pressure traveling-wave components reflect from the cone apex with a 180° phase shift (or an inversion). The physical pressure at the cone tip for this case can be found in the limit as $x \rightarrow 0$ by l'Hopital's rule. Expressing the pressure at position x in the bore in terms

of sinusoidal traveling-wave components,

$$p(x, t) = \left[\frac{P^+}{x} e^{-jkx} + \frac{P^-}{x} e^{jkx} \right] e^{j\omega t}, \quad (3.20)$$

where P^+ and P^- are complex amplitudes and sinusoidal time dependence is assumed, $p(0, t)$ is found to approach $2jkP^-$ as $x \rightarrow 0$ for all time. For use in musical instruments, however, conical bores are always truncated to some extent. Figure 3.8 illustrates a divergent conical bore truncated

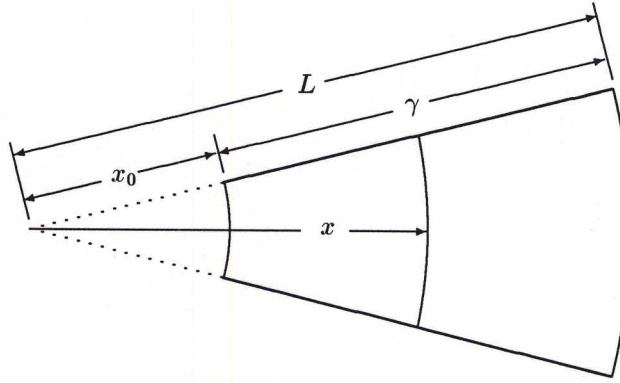


Fig. 3.8. Divergent conical section rigidly terminated by a spherical cap at x_0 .

and rigidly terminated at a distance x_0 from its apex. The pressure reflectance at x_0 is found from the boundary condition $U(x_0) = 0$, such that

$$\begin{aligned} U^+(x_0) + U^-(x_0) &= 0 \\ \frac{P^+(x_0)}{Z_0(x_0)} - \frac{P^-(x_0)}{Z_0^*(x_0)} &= 0 \\ \Rightarrow \frac{P^+(x_0, s)}{P^-(x_0, s)} &= \frac{Z_0(x_0, s)}{Z_0^*(x_0, s)} = \frac{jkx_0 - 1}{jkx_0 + 1} \\ &= \left. \frac{x_0 s - c}{x_0 s + c} \right|_{s=jk/c}, \end{aligned} \quad (3.21)$$

where s is the Laplace transform variable and c is the speed of sound in air. As $x_0 \rightarrow 0$, the reflectance approaches negative one as observed above. Using the bilinear transform, this expression can be discretized as follows

$$\frac{P^+(x_0, z)}{P^-(x_0, z)} = \frac{-a_1 - z^{-1}}{1 + a_1 z^{-1}}, \quad (3.22)$$

where

$$a_1 = \frac{c - \alpha x_0}{c + \alpha x_0} \quad (3.23)$$

and α is the bilinear transform constant which controls frequency warping. For proper phase matching at low frequencies, α can be set equal to $2f_s$. Equation (3.22) is a first-order discrete-time allpass

filter. This filter structure implements the $2 \angle Z_0(x, \Omega)$ frequency-dependent phase delay experienced by pressure traveling-wave components reflecting from a rigid termination in a conical waveguide. The upper plot of Fig. 3.9 illustrates the continuous-time phase response of the reflectance given by Eq. (3.21) and the discrete-time phase response of the digital filter of Eq. (3.22). The lower plot of Fig. 3.9 indicates the allpass filter coefficient value as a function of cone truncation. As $x_0 \rightarrow 0$, the filter becomes unstable because $a_1 \rightarrow 1$ and the allpass pole falls on the unit circle. Thus, the truncation filter cannot be used to simulate a complete cone, but in this case the reflectance is simply negative one anyway.

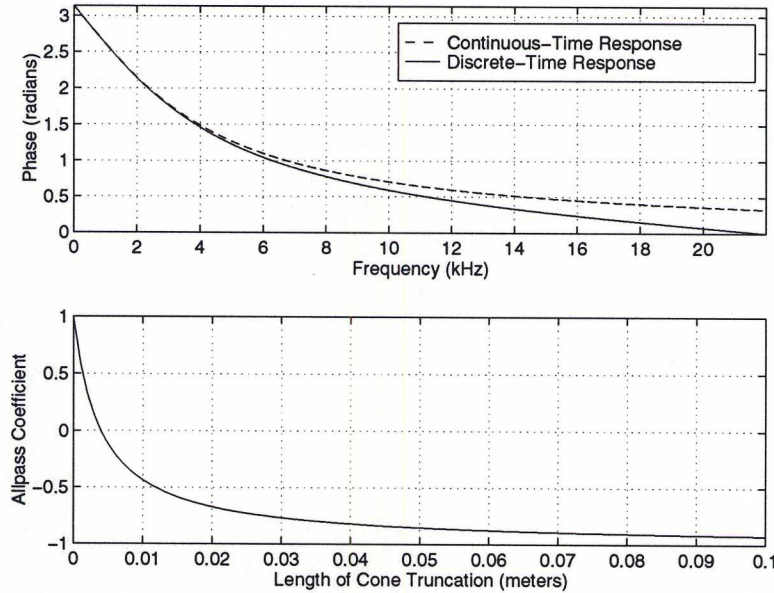


Fig. 3.9. The conical truncation reflectance: (top) Continuous-time and discrete-time filter phase responses; (bottom) Digital allpass filter coefficient value versus x_0 .

The digital waveguide implementation of a closed-open conic section is shown in Fig. 3.10. The cone truncation reflectance filter is represented by $\mathcal{R}_{x_0}(z)$. The waveguide “input impedance” $h(x_0, n)$ for this system can be determined by calculating its response to a unit volume velocity impulse and transforming it to the frequency domain using the DFT. The continuous-time pressure response to a volume velocity impulse is given by the inverse Fourier transform of the characteristic impedance $Z_0(x, \Omega)$. This function was determined in Section 1.3.4 [Eq. (1.105)] as

$$h^+(x, t) = \frac{\rho c}{S(x)} \left[\delta(t) - \frac{c}{x} e^{-(c/x)t} \epsilon(t) \right], \quad (3.24)$$

where $\epsilon(t)$ is the Heaviside unit step function. It is necessary to determine a digital filter which appropriately models the response of $h^+(x, t)$ in the discrete-time domain. The spherical-wave characteristic impedance is given in terms of its Laplace transform as

$$H_c^+(x, s) = Z_0(x, s) = \frac{\rho c}{S(x)} \left(\frac{xs}{c + xs} \right), \quad (3.25)$$

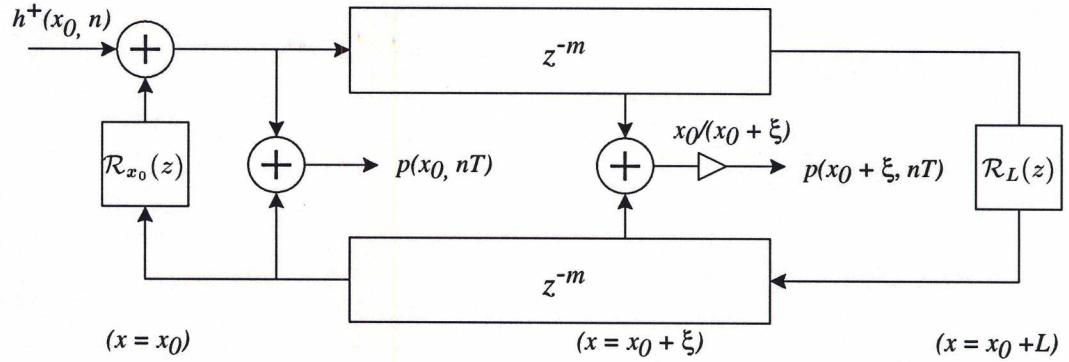


Fig. 3.10. Digital waveguide implementation of a closed-open truncated conical section excited at $x = x_0$.

where $S(x)$ is the spherical-wave surface area at x . Using the bilinear transform, an equivalent discrete-time filter is given by

$$H_d^+(x, z) = \left(\frac{\rho c}{S(x)} \right) \left(\frac{\alpha x}{c + \alpha x} \right) \frac{1 - z^{-1}}{1 + a_1 z^{-1}}, \quad (3.26)$$

where α is the bilinear transform constant and a_1 is equal to the allpass truncation filter coefficient given in Eq. (3.23). The impulse response $h(x_0, n)$ of a closed-open truncated cone is found from the digital waveguide structure of Fig. 3.10 as the pressure response at $x = x_0$ to the impulse response $h^+(x_0, n)$. Because the cone is excited at $x = x_0$, output scale factors are appropriately weighted by x_0 . Figure 3.11 is a plot of $h(x_0, n)$, calculated using a Levine and Schwinger model of the open-end radiation and neglecting viscothermal losses.

Salmon (1946a) and Benade (1988) proposed a transmission-line conical waveguide model directly analogous to that described above. Shown in Fig. 3.12, Benade's model represents a conic section by a cylindrical waveguide, a pair of "inertance" terms, and a transformer whose "turns ratio" is equal to the ratio P_{x_0}/P_L . The digital waveguide truncated cone model implements the cylindrical waveguide section using delay lines, as previously described, and the transformer operation wherever a physical pressure measurement is taken. Benade derived the inertance terms from the analytic expressions for input admittance, as seen from the small and large ends of the conic section. Both inertances are of the form

$$Z(x, s) = M(x)s = \frac{\rho x}{S(x)}s, \quad (3.27)$$

where $S(x)$ is the surface area of the spherical wave front, x is the distance from the imaginary cone tip, and ρ is the density of air, though $M(L)$ seen looking into the large end of the cone is negative. When the cone is fitted with a rigid spherical cap at $x = x_0$, U_{x_0} is zero and the inertance $M(x_0)$ terminates the bore. In this sense, a conical bore which is truncated and stopped at its small end behaves like a cylindrical waveguide section terminated by a "masslike" impedance. The

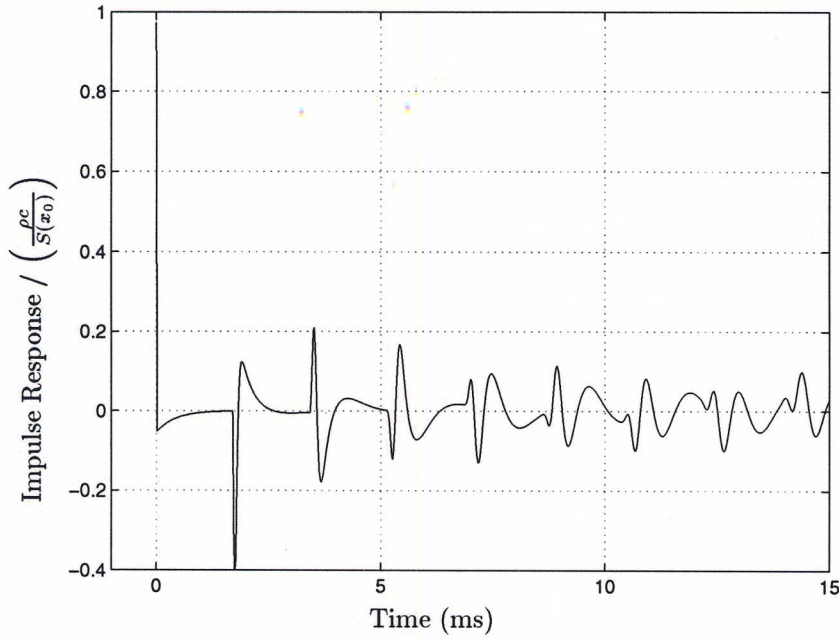


Fig. 3.11. Impulse response of conical bore closed at $x = x_0$ and open at $x = L$. Open-end radiation is approximated by a 2nd-order discrete-time filter and viscothermal losses are ignored.

corresponding pressure traveling-wave reflectance is given by

$$\begin{aligned}
 Z(x_0, s) &= M(x_0)s = -\frac{P(x_0, s)}{U(x_0, s)} \\
 &= -\frac{P^+(x_0, s) + P^-(x_0, s)}{U^+(x_0, s) + U^-(x_0, s)} \\
 &= -R_0(x_0) \frac{P^+(x_0, s) + P^-(x_0, s)}{P^+(x_0, s) - P^-(x_0, s)} \\
 \mathcal{R}(x_0, s) &\triangleq \frac{P^-(x_0, s)}{P^+(x_0, s)} = \frac{Z(x_0, s) - R_0(x_0)}{Z(x_0, s) + R_0(x_0)} \\
 &= \frac{x_0 s - c}{x_0 s + c},
 \end{aligned} \tag{3.28}$$

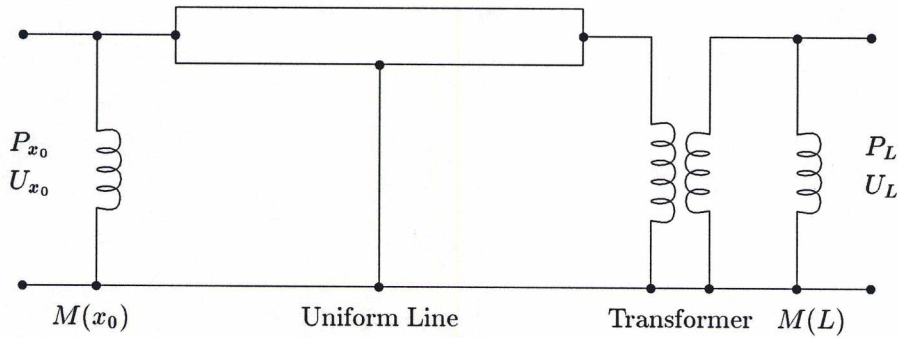


Fig. 3.12. Equivalent circuit of a conical waveguide [after Benade (1988)].

where $R_0(x) = \rho c/S(x)$ is the real, locally defined characteristic impedance of the cylindrical waveguide. The negative sign in the initial impedance relationship arises because volume velocity through the inertance $M(x_0)$ is flowing in the negative direction. This reflectance is the same as that found in Eq. (3.21). If the open end of the bore is approximated by a low-frequency load impedance $Z_L(s) = 0$, the negative inertance $M(L)$ will be short circuited. When a more physical, non-zero load impedance is incorporated, the large end of the bore is terminated by the parallel combination of $Z_L(s)$ and $M(L)$. Rewriting $M(L)$ as $R_0(L)L/c$, the pressure traveling-wave reflectance at the large, open end of the bore is given in terms of the parallel impedance $Z_{\parallel} = Z_L \parallel (M(L)s)$ as

$$\begin{aligned}
 \mathcal{R}(L, s) &\triangleq \frac{P^-(L, s)}{P^+(L, s)} = \frac{Z_{\parallel} - R_0(L)}{Z_{\parallel} + R_0(L)} \\
 &= \frac{LR_0(L)Z_Ls + R_0(L)[cZ_L - LR_0(L)s]}{LR_0(L)Z_Ls - R_0(L)[cZ_L - LR_0(L)s]} \\
 &= \frac{Z_LR_0(L)[Ls + c] - R_0^2(L)Ls}{Z_LR_0(L)[Ls - c] + R_0^2(L)Ls} \\
 &= \frac{Z_LZ_0^*(L, s) - Z_0(L, s)Z_0^*(L, s)}{Z_LZ_0(L, s) - Z_0(L, s)Z_0^*(L, s)},
 \end{aligned} \tag{3.29}$$

where

$$Z_0(L, s) = \frac{R_0(L)Ls}{Ls + c} \tag{3.30}$$

is the complex characteristic impedance of a conical bore at $x = L$. This expression is equivalent to the bracketed term of Eq. (3.19), or the spherical-wave reflectance for pressure. Benade's conical waveguide circuit thus provides an alternate interpretation of wave behavior in conical bores which closely parallels the digital waveguide implementation.

3.3.3 Diameter and Taper Discontinuities

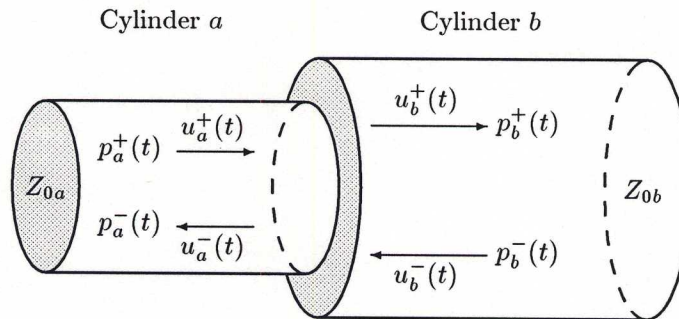


Fig. 3.13. Junction of two cylindrical tube sections.

Diameter discontinuities are generally avoided in wind-instrument bore profiles, but sometime occur at the junction of instrument sections, such as between the mouthpiece and neck of a saxophone.

These discontinuities will also be encountered in the approximation of complex bore shapes using cylindrical pipe sections. At the boundary of two discontinuous and lossless cylindrical sections, Fig. 3.13, there will be a change of characteristic impedance which results in partial reflection and transmission of traveling-wave components. Assuming continuity of pressure and conservation of volume flow at the boundary,

$$P_a^+(\Omega) + P_a^-(\Omega) = P_b^+(\Omega) + P_b^-(\Omega) \quad (3.31)$$

and

$$\frac{1}{Z_{0a}} [P_a^+(\Omega) - P_a^-(\Omega)] = \frac{1}{Z_{0b}} [P_b^+(\Omega) - P_b^-(\Omega)], \quad (3.32)$$

where Z_{0a} is the characteristic impedance of cylindrical section a . Solving for $P_a^-(\Omega)$ and $P_b^+(\Omega)$ at the junction,

$$\begin{aligned} P_a^-(\Omega) &= \left(\frac{Z_{0b} - Z_{0a}}{Z_{0b} + Z_{0a}} \right) P_a^+(\Omega) + \left(\frac{2Z_{0a}}{Z_{0b} + Z_{0a}} \right) P_b^-(\Omega) \\ &= \mathcal{R}_{ab} P_a^+(\Omega) + (1 - \mathcal{R}_{ab}) P_b^-(\Omega) \end{aligned} \quad (3.33a)$$

$$\begin{aligned} P_b^+(\Omega) &= \left(\frac{2Z_{0b}}{Z_{0b} + Z_{0a}} \right) P_a^+(\Omega) - \left(\frac{Z_{0b} - Z_{0a}}{Z_{0b} + Z_{0a}} \right) P_b^-(\Omega) + \\ &= (1 + \mathcal{R}_{ab}) P_a^+ - \mathcal{R}_{ab} P_b^- \end{aligned} \quad (3.33b)$$

where \mathcal{R}_{ab} is the reflectance for the junction of cylinders a and b . \mathcal{R}_{ab} is given by

$$\mathcal{R}_{ab} = \frac{Z_{0b} - Z_{0a}}{Z_{0b} + Z_{0a}} \quad (3.34)$$

$$= \frac{S_a - S_b}{S_a + S_b}, \quad (3.35)$$

where S_a is the cross-sectional area of section a . The relationships of Eqs. (3.33a) and (3.33b) are referred to as *scattering equations*. The reflectance \mathcal{R}_{ab} can also be obtained from Eq. (3.15) by assuming an infinite length for section b , so that $Z_L = Z_{0b}$. Because \mathcal{R}_{ab} is real and frequency-independent, the time-domain reflection function $r_{ab}(t)$ and the frequency-domain reflectance are equal for cylindrical tube junctions. The scattering equations are implemented by the structure shown in Fig. 3.14a, which was first derived for an acoustic tube model used in speech synthesis (Kelly and Lochbaum, 1962). Equations (3.33a) and (3.33b) can also be written in the form

$$P_a^-(\Omega) = P_b^-(\Omega) + P_\Delta(\Omega) \quad (3.36a)$$

$$P_b^+(\Omega) = P_a^+(\Omega) + P_\Delta(\Omega), \quad (3.36b)$$

where

$$P_\Delta(\Omega) = \mathcal{R}_{ab} [P_a^+(\Omega) - P_b^-(\Omega)].$$

In this way, the Kelly-Lochbaum scattering junction can be implemented with a single multiply, as shown in Fig. 3.14b (Markel and Gray, 1976). Smith (1987) points out that junction passivity is guaranteed for $-1 \leq r_{ab}(t) = \mathcal{R}_{ab}(\Omega) \leq 1$.

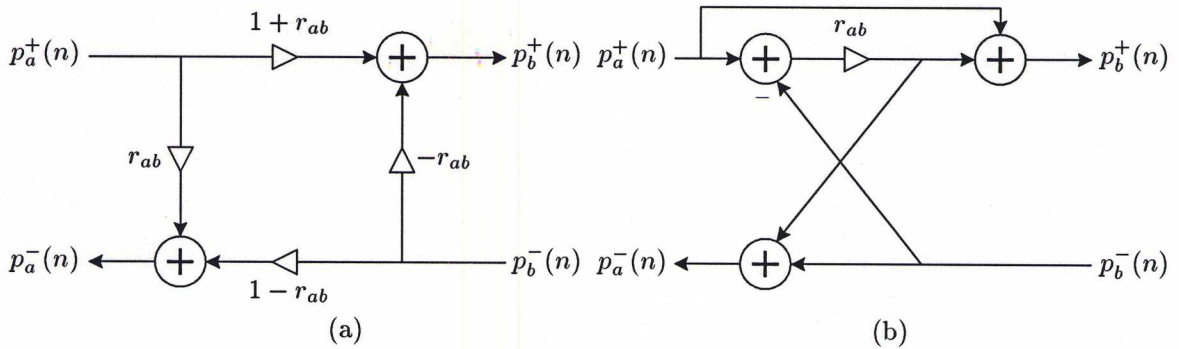


Fig. 3.14. (a) The Kelly-Lochbaum scattering junction for diameter discontinuities in cylindrical bores; (b) The one-multiply scattering junction [after (Markel and Gray, 1976)].

The digital waveguide implementation of lossless wave propagation in two discontinuous cylindrical sections is shown in Fig. 3.15. In this way, any combination of co-axial cylindrical sections

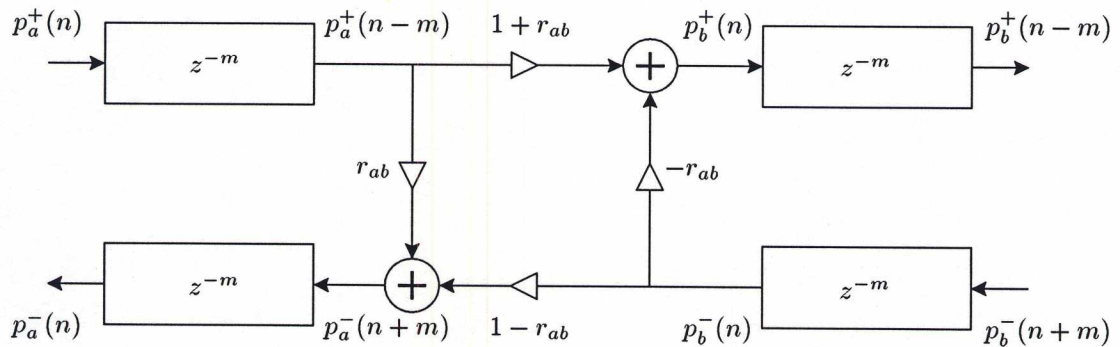


Fig. 3.15. The digital waveguide model of two discontinuous cylindrical sections.

can be modeled using only digital delay lines and one-multiply scattering junctions. The hypothetical non-uniform bore shape first illustrated in Section 1.3.1 is shown again in Fig. 3.16 with its approximation by cylindrical sections. The input impedance of such a structure was previously calculated using transmission-line matrices. The discrete-time input impedance $Z(\omega)$ determined from a cylindrical section digital waveguide approximation of the non-uniform bore is shown in Fig. 3.17.

It is possible to derive similar expressions for reflection and transmission functions at the junctions of conical tubes, though the frequency and axial dependency of the characteristic impedance for spherical waves complicates the results in comparison to the cylindrical tube case. At the boundary of two discontinuous and lossless conical sections, Fig. 3.18, the abrupt change in diameter and rate of taper will cause scattering of traveling wave components. Assuming continuity of pressure and

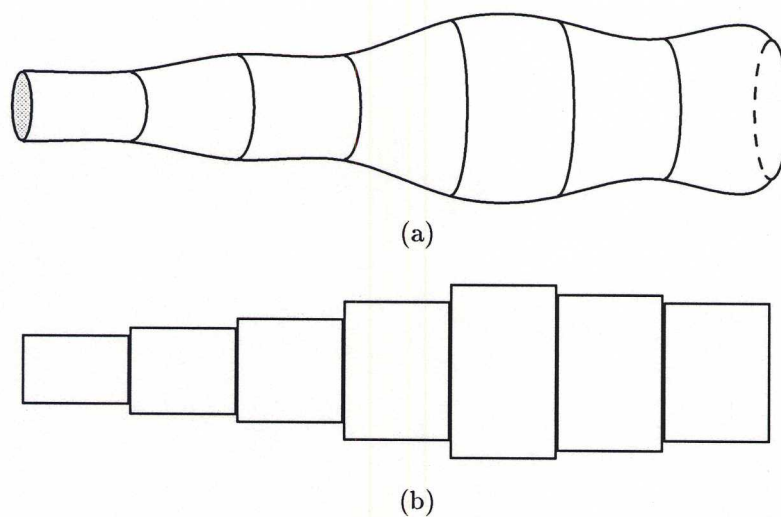


Fig. 3.16. (a) A non-uniform bore and (b) its approximation in terms of cylindrical sections.

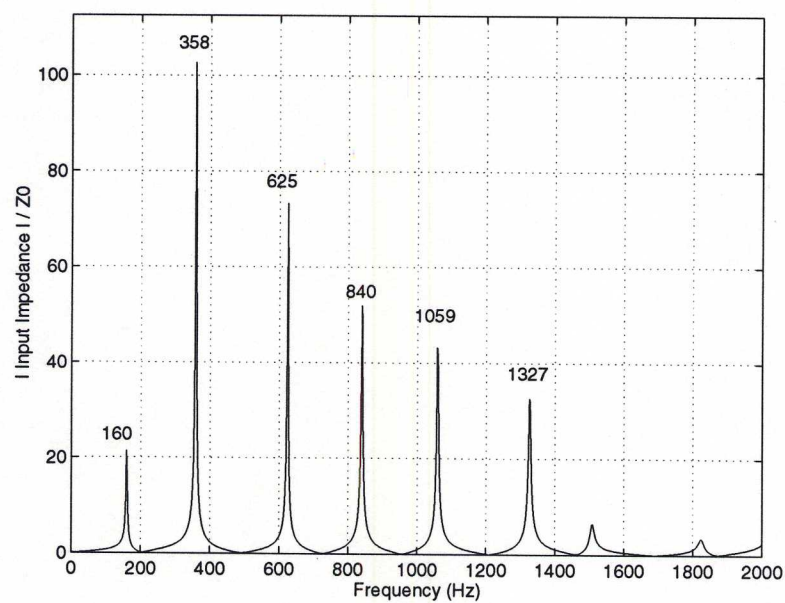


Fig. 3.17. Input impedance magnitude, normalized by Z_0 at $x = 0$, calculated using a digital waveguide model of the cylindrical section structure shown in Fig. 3.16(b).

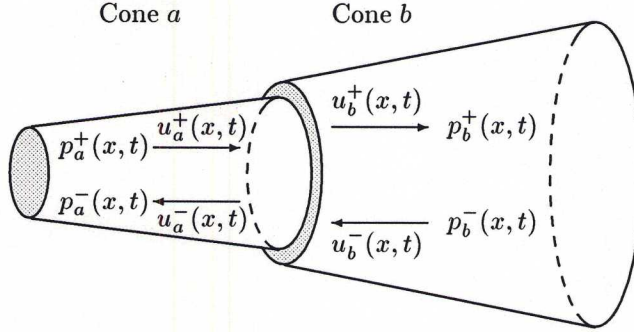


Fig. 3.18. Junction of two conical tube sections.

conservation of volume flow at the boundary,

$$P_a^+(\Omega) + P_a^-(\Omega) = P_b^+(\Omega) + P_b^-(\Omega) \quad (3.37)$$

and

$$P_a^+(\Omega)Y_{0a}(\Omega) - P_a^-(\Omega)Y_{0a}^*(\Omega) = P_b^+(\Omega)Y_{0b}(\Omega) - P_b^-(\Omega)Y_{0b}^*(\Omega), \quad (3.38)$$

where Y_{0a} is the characteristic admittance for section a at the boundary looking in the positive x direction. The characteristic admittance for spherical waves in a cone is given by

$$Y_0(x, \Omega) = \frac{1}{Z_0(x, \Omega)} = \frac{S(x)}{\rho c} \left(1 + \frac{1}{jkx} \right) \quad Y_0^*(x, \Omega) = \frac{1}{Z_0^*(x, \Omega)} = \frac{S(x)}{\rho c} \left(1 - \frac{1}{jkx} \right), \quad (3.39)$$

where $Y_0(x, \Omega)$ applies to traveling-wave components propagating away from the cone apex in the positive x direction and $Y_0^*(x, \Omega)$ to traveling-wave components propagating toward the cone apex in the negative x direction. Solving for $P_a^-(\Omega)$ at the junction,

$$P_a^-(\Omega) = \left[\frac{Y_{0a}(\Omega) - Y_{0b}(\Omega)}{Y_{0a}^*(\Omega) + Y_{0b}(\Omega)} \right] P_a^+(\Omega) + \left[\frac{Y_{0b}(\Omega) + Y_{0b}^*(\Omega)}{Y_{0a}^*(\Omega) + Y_{0b}(\Omega)} \right] P_b^-(\Omega). \quad (3.40)$$

The frequency-dependent scattering coefficient which relates $P_a^-(\Omega)$ to $P_a^+(\Omega)$ is

$$\begin{aligned} \mathcal{R}^-(\Omega) &= \frac{Y_{0a}(\Omega) - Y_{0b}(\Omega)}{Y_{0a}^*(\Omega) + Y_{0b}(\Omega)} \\ &= \frac{B - 1}{B + 1} - \frac{2B\gamma}{(B + 1)(j\Omega + \gamma)}, \end{aligned} \quad (3.41)$$

where B is the ratio of wave front surface areas S_a/S_b at the boundary and γ is given by

$$\gamma = -\frac{c}{S_a + S_b} \left(\frac{S_a}{x_a} - \frac{S_b}{x_b} \right) \quad (3.42)$$

(Martínez and Agulló, 1988; Gilbert *et al.*, 1990a). This *reflectance* is given a negative superscript to indicate scattering in the negative x direction. The parameters x_a and x_b are measured from the (imaginary) apices of cones a and b , respectively, to the discontinuity. $\mathcal{R}^-(\Omega)$ could also have been

found in terms of impedances from Eq. (3.19) by assuming an infinite length for conical section b with a resulting load impedance equal to Z_{0b} . Similarly, the expression for $P_b^+(\Omega)$ at the junction is

$$P_b^+(\Omega) = \left[\frac{Y_{0a}(\Omega) + Y_{0a}^*(\Omega)}{Y_{0b}(\Omega) + Y_{0a}^*(\Omega)} \right] P_a^+(\Omega) + \left[\frac{Y_{0b}^*(\Omega) - Y_{0a}^*(\Omega)}{Y_{0b}(\Omega) + Y_{0a}^*(\Omega)} \right] P_b^-(\Omega), \quad (3.43)$$

and the reflectance which relates $P_b^+(\Omega)$ to $P_b^-(\Omega)$ is

$$\begin{aligned} \mathcal{R}^+(\Omega) &= \frac{Y_{0b}^*(\Omega) - Y_{0a}^*(\Omega)}{Y_{0b}(\Omega) + Y_{0a}^*(\Omega)} \\ &= \frac{1 - B}{1 + B} - \frac{2\gamma}{(1 + B)(j\Omega + \gamma)}. \end{aligned} \quad (3.44)$$

(Välimäki, 1995). This reflectance is given a positive superscript to indicate scattering in the positive x direction. The scattering equations can then be expressed in terms of $\mathcal{R}^-(\Omega)$ and $\mathcal{R}^+(\Omega)$ as

$$P_a^-(\Omega) = \mathcal{R}^-(\Omega)P_a^+(\Omega) + [1 + \mathcal{R}^+(\Omega)]P_b^-(\Omega) \quad (3.45a)$$

$$P_b^+(\Omega) = [1 + \mathcal{R}^-(\Omega)]P_a^+(\Omega) + \mathcal{R}^+(\Omega)P_b^-(\Omega). \quad (3.45b)$$

It is possible to define *transmittances* which indicate scattering through the junction as $\mathcal{T}^+(\Omega) = 1 + \mathcal{R}^-(\Omega)$ and $\mathcal{T}^-(\Omega) = 1 + \mathcal{R}^+(\Omega)$. These expressions are equally valid when either acoustic section is cylindrical, rather than conical. Replacing cone a by a cylindrical section, $x_a = \infty$ and S_a is given by the cylinder's cross-sectional area at the discontinuity.

Whereas the junction scattering coefficients for cylindrical bore diameter discontinuities were real and constant, these expressions are frequency-dependent and must be transformed to discrete-time filters for time-domain implementation. Figure 3.19(a) illustrates the general scattering junction implementation for diameter and taper discontinuities in conical bores. Because $\mathcal{R}^-(\Omega)$ and $\mathcal{R}^+(\Omega)$ are

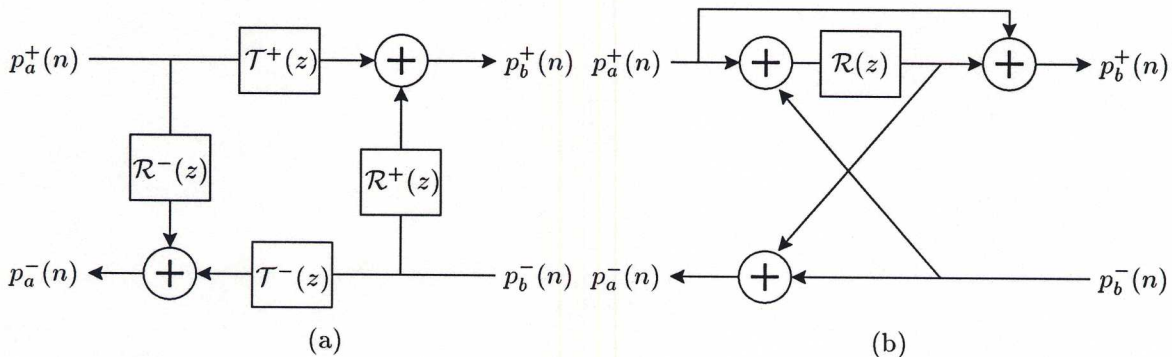


Fig. 3.19. (a) The scattering junction for diameter and taper discontinuities in conical bores; (b) The one-multiply scattering junction for a taper discontinuity only [after (Välimäki, 1995)].

different, the one-multiply form of the scattering junction implementation is not possible. However, the wave front surface areas are often approximated by cross-sectional areas at the discontinuity, which is reasonable only for small changes in taper rate and cross-section. By making this approximation, the reflectances \mathcal{R}^- and \mathcal{R}^+ become identical for a discontinuity of taper only. In this case,

a one-multiply scattering junction implementation is possible, as shown in Fig. 3.19(b) (Välimäki, 1995). Strictly speaking, however, the propagating wave fronts in cones are spherical and thus \mathcal{R}^- and \mathcal{R}^+ will never be identical, even for a simple taper discontinuity.

Equation (3.41) can be transformed to the time domain, resulting in the reflection function

$$r^-(t) = \frac{B-1}{B+1}\delta(t) - \frac{2B}{(B+1)}\gamma e^{-\gamma t}\epsilon(t), \quad (3.46)$$

where $\delta(t)$ is the Dirac impulse and $\epsilon(t)$ is the Heaviside unit step function (Martínez and Agulló, 1988). An appropriate discrete-time filter is found by making the bilinear transform frequency variable substitution in Eq. (3.41) with the result

$$\mathcal{R}^-(z) = \frac{B-1}{B+1}\delta(n) - \frac{2B\gamma/(\alpha+\gamma)}{(B+1)}\left(\frac{1+z^{-1}}{1-a_1z^{-1}}\right), \quad (3.47)$$

where $\delta(n)$ is the unit sample sequence or discrete-time impulse, γ is as given in Eq. (3.42), α is the bilinear transform constant, and

$$a_1 = \frac{\alpha - \gamma}{\alpha + \gamma} \quad (3.48)$$

is the first-order filter pole location in the z -plane. Unfortunately, $\mathcal{R}^-(z)$ is unstable for negative γ , which occurs any time cone b has a lower rate of taper than cone a . Equivalently, $\mathcal{R}^-(\Omega)$ has no causal inverse Fourier transform for negative γ . Agulló *et al.* (1992) rederived expressions for the reflection functions associated with conical discontinuities using time-domain analyses only to demonstrate the validity of Eq. (3.46) for negative γ as well. This corresponds to a growing exponential in the reflection function $r^-(t)$. Much debate has been waged over the existence and/or passivity of the growing exponential terms. The reflectance is a junction characteristic which is “blind” to the boundary conditions upstream or downstream from it. Physically realistic boundary conditions in such cases, however, will always limit the time duration over which the growing exponential can exist. Experimental measurements of reflection functions due to discontinuities have verified this general behavior (Agulló *et al.*, 1995). It should be noted, however, that limited exponential growth of the reflection function or impulse response of a physically feasible system is dependent on the summation of an infinite number of growing exponential terms. In other words, reflections at a junction for which γ is negative must continue forever in order to guarantee stability of the system.

The implementation of an unstable digital filter to simulate an air column junction of decreasing taper rate, as given by the theory above, is extremely problematic and generally impossible in a synthesis environment. It is often possible to calculate the “impulsive” behavior of an acoustic system containing growing exponentials in double-precision floating-point environments, though simulations over longer time durations will tend to grow unstable due to precision limits in the digital domain. Figure 3.20 illustrates two possible cylinder-cone section combinations. Because γ is positive (or the taper rate widens) for the junction in Fig. 3.20(a), the system reflection function will be characterized by decreasing exponential terms. Figure 3.21 is a plot of the discrete-time reflection function and impulse response of the cylinder-diverging cone structure illustrated in Fig. 3.20(a), as calculated

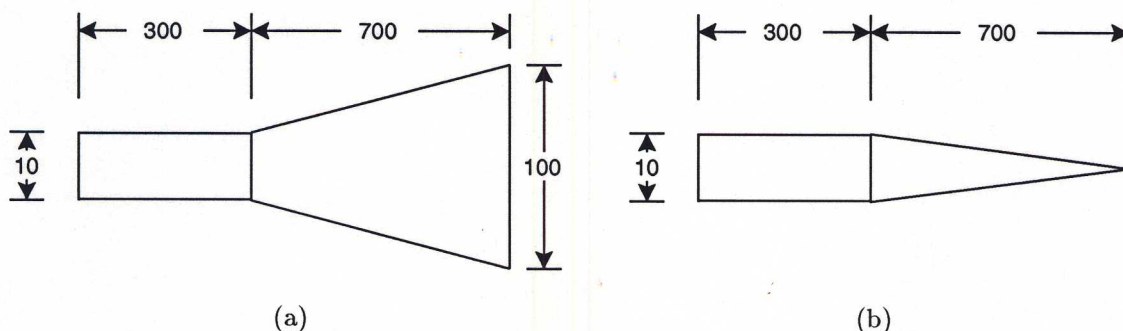


Fig. 3.20. (a) Cylinder-diverging cone junction; (b) Cylinder-converging cone junction. All lengths are in millimeters.

using digital waveguide techniques. The decaying exponential terms are obvious in both responses and the reflection function is seen to decay much faster than the impulse response. Further, both plots compare well to those of (Agulló *et al.*, 1988, p. 1610). Figure 3.22 is a plot of the discrete-time

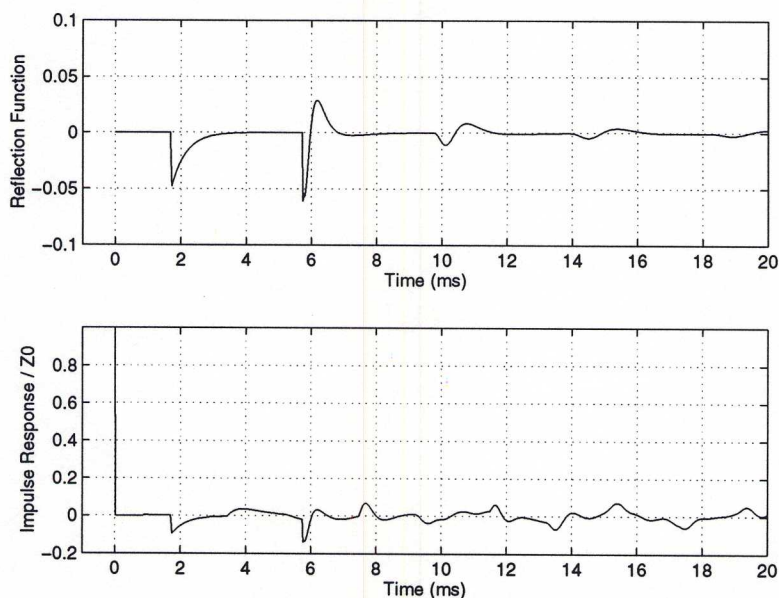


Fig. 3.21. (top) Discrete-time reflection function $r(n)$ and (bottom) discrete-time impulse response, normalized by Z_0 of the cylinder, calculated using a digital waveguide model of the cylinder-diverging cone structure shown in Fig. 3.20(a).

reflection function of the cylinder-converging cone structure illustrated in Fig. 3.20(b), as calculated using digital waveguide techniques. The growing exponential terms are limited in time and the overall response decays to zero within about 15 milliseconds. If this model is run for a long period of time, however, internal state overflow and precision errors lead to unstable growth. The impulse response of this system is of infinite duration in the absence of viscothermal losses and attempts to calculate $h(n)$ likewise result in unstable growth.

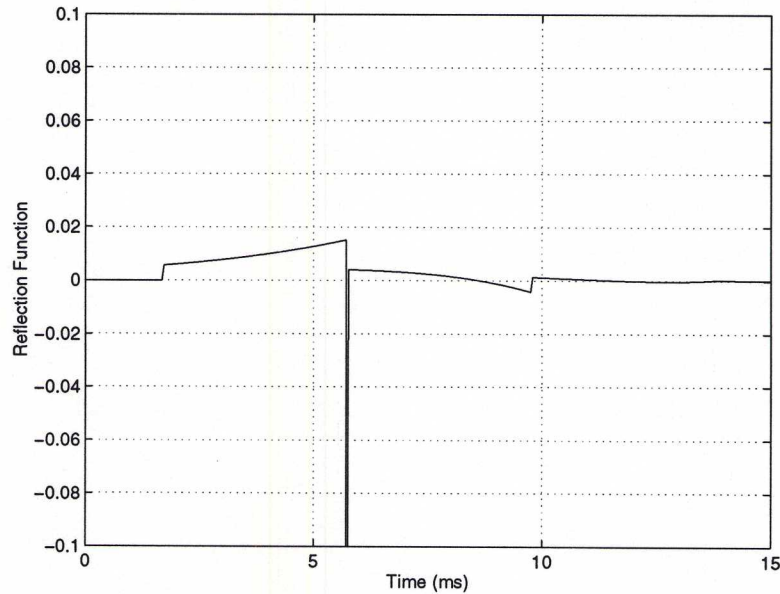


Fig. 3.22. Discrete-time reflection function $r(n)$ calculated using a digital waveguide model of the cylinder-converging cone structure shown in Fig. 3.20(b).

It is obvious that alternative methods are necessary for the digital simulation of such a system. While the individual reflection function characterization of the junction is problematic, the overall response of the composite acoustic system is stable. Thus, it is possible to lump together several acoustic sections to form a stable filter. This is done at the cost of model accessibility; that is, the detailed behavior of wave propagation at locations within the lumped section is unknown. One approach is to implement the reflection function of Fig. 3.22 with a *finite impulse response* (FIR) filter. In this case, the filter coefficients are simply given by the discrete-time values of $r(n)$ over its non-zero length. At a sampling rate of 44.1 kHz, the FIR filter for this system could be truncated to about 600 coefficients. The downside to such a solution, however, is its relative inefficiency with respect to the digital waveguide implementation. Further, a reflection function description of this sort is appropriate at the termination of a waveguide implementation, but not at points internal to the model. Another potential solution involves zeroing out the internal states of the unstable filters when reflection activity has decayed to negligible levels. This technique is based on the observation that filter instability tends to occur after signal levels have decayed away. The internal reflections themselves tend to limit the growth of the filter states. This approach is reasonable for determining short duration signals, such as air column reflection functions. The hypothetical non-uniform bore shape first illustrated in Section 1.3.2 is shown again in Fig. 3.23 with its approximation by conical and cylindrical sections. This structure has six internal junctions, of which those between sections two and three, four and five, and five and six, are unstable. The bore shape as a whole, however, represents a stable system because successive internal and open-end reflections

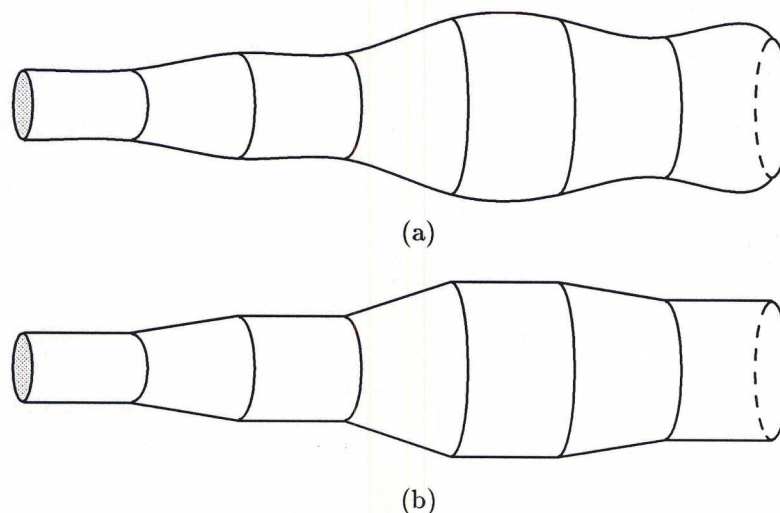


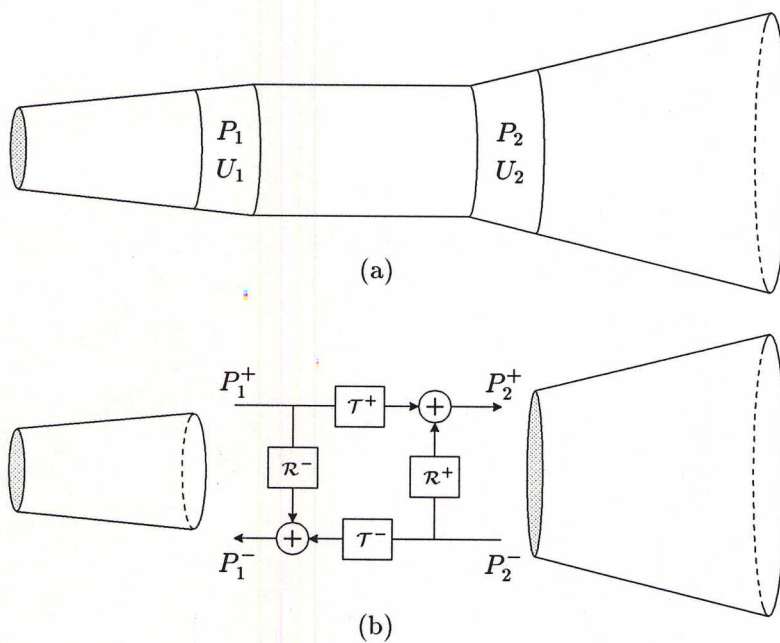
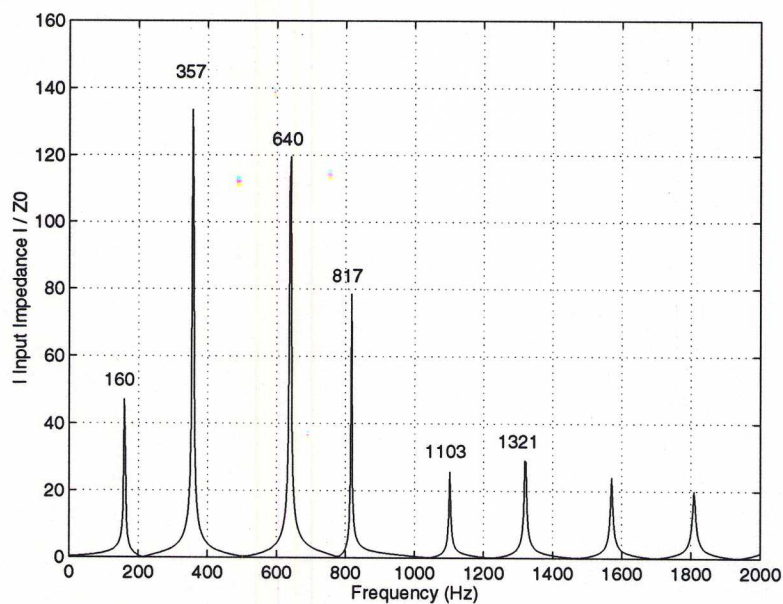
Fig. 3.23. (a) A non-uniform bore and (b) its approximation in terms of conical and cylindrical sections.

cancel out the growing exponential terms. The input impedance of this structure was previously calculated using transmission-line matrices. The discrete-time input impedance $Z(\omega)$ determined in a double-precision, floating point environment from a conical and cylindrical section digital waveguide approximation of the non-uniform bore is shown in Fig. 3.24.

For discrete- and real-time implementations, the use of unstable digital filters is unacceptable. A solution to this problem is possible by lumping an unstable junction together with a stable one, to produce a scattering junction characterized by stable digital filters. Such an approach is illustrated in Fig. 3.25. The bore profile of Fig. 3.25a requires the implementation of unstable scattering junction reflectance and transmittance filters if each junction is explicitly modeled. In particular, the junction between the first divergent conical section and the cylindrical section is unstable in the digital domain. However, if the overall taper rate of the composite system is increasing (that is, the right-most section taper rate is greater than that of the left-most section), a lumped model for the inner sections can be determined which is implemented by a single, stable scattering junction.

The cascading of digital waveguide reflectance and transmittance filters is nontrivial. Instead, the approach used here is to express the bore profile in terms of its frequency-domain, transmission-matrix representation. The appropriate matrices are then cascaded together and this representation is transformed to waveguide coordinates. Finally, appropriate discrete-time filters are designed. The inner bore profile of Fig. 3.25a is typically represented by a series of three transmission matrices, as

$$\begin{aligned}
 \begin{bmatrix} P_1 \\ U_1 \end{bmatrix} &= \begin{bmatrix} a_1 & b_1 \\ c_1 & d_1 \end{bmatrix} \begin{bmatrix} a_2 & b_2 \\ c_2 & d_2 \end{bmatrix} \begin{bmatrix} a_3 & b_3 \\ c_3 & d_3 \end{bmatrix} \begin{bmatrix} P_2 \\ U_2 \end{bmatrix} \\
 &= \begin{bmatrix} A & B \\ C & D \end{bmatrix} \begin{bmatrix} P_2 \\ U_2 \end{bmatrix}
 \end{aligned} \tag{3.49}$$



where

$$\begin{bmatrix} A & B \\ C & D \end{bmatrix} = \prod_{i=1}^3 \begin{bmatrix} a_i & b_i \\ c_i & d_i \end{bmatrix}. \quad (3.50)$$

Each matrix in Eq. (3.49) is given by the appropriate conical and cylindrical transmission-matrix parameters, as discussed in Section 1.3. In order to avoid implementing the cylinder-conical section junctions, it is necessary to include a short portion of the conical section lengths on either side of both junctions in the overall lumped system. In this case, the complete cylindrical section will be lumped together with short conical sections on both its ends. It is desirable to keep the lengths of the conical sections short, so as to avoid unnecessary phase delay in the digital filters to be designed.

To render these relationships in the digital waveguide domain, it is necessary to transform the spherical-wave transmission-matrix coordinates of pressure and volume velocity to waveguide coordinates, as

$$\begin{bmatrix} P_1 \\ U_1 \end{bmatrix} = \begin{bmatrix} P_1^+ + P_1^- \\ \frac{P_1^+}{Z_{01}} - \frac{P_1^-}{Z_{01}^*} \end{bmatrix}, \quad \begin{bmatrix} P_2 \\ U_2 \end{bmatrix} = \begin{bmatrix} P_2^+ + P_2^- \\ \frac{P_2^+}{Z_{02}} - \frac{P_2^-}{Z_{02}^*} \end{bmatrix}, \quad (3.51)$$

where Z_{01} is the complex valued characteristic impedance determined at the input of the first conical section and Z_{01}^* is its complex conjugate. Waveguide pressure variables on both sides of the junction are related by

$$\begin{bmatrix} P_1^- \\ P_2^+ \end{bmatrix} = \begin{bmatrix} \mathcal{R}^- & \mathcal{T}^- \\ \mathcal{T}^+ & \mathcal{R}^+ \end{bmatrix} \begin{bmatrix} P_1^+ \\ P_2^- \end{bmatrix}, \quad (3.52)$$

where

$$\mathcal{R}^- = \frac{Z_{01}^* (BZ_{02}^* - DZ_{01}Z_{02}^* + AZ_{02}Z_{02}^* - CZ_{01}Z_{02}Z_{02}^*)}{Z_{01}Z_{02}^* (B + DZ_{01}^* + AZ_{02} + CZ_{01}^*Z_{02})} \quad (3.53a)$$

$$\mathcal{T}^- = \frac{Z_{01}^* (AD - BC) (Z_{01}Z_{02} + Z_{01}Z_{02}^*)}{Z_{01}Z_{02}^* (B + DZ_{01}^* + AZ_{02} + CZ_{01}^*Z_{02})} \quad (3.53b)$$

$$\mathcal{T}^+ = \frac{Z_{02} (Z_{01}^*Z_{02}^* + Z_{01}Z_{02})}{Z_{01}Z_{02}^* (B + DZ_{01}^* + AZ_{02} + CZ_{01}^*Z_{02})} \quad (3.53c)$$

$$\mathcal{R}^+ = \frac{Z_{02} (BZ_{01} + DZ_{01}Z_{01}^* - AZ_{01}Z_{02}^* - CZ_{01}Z_{01}^*Z_{02}^*)}{Z_{01}Z_{02}^* (B + DZ_{01}^* + AZ_{02} + CZ_{01}^*Z_{02})}, \quad (3.53d)$$

calculated using Eqs. (3.49) and (3.51). Figure 3.25b illustrates the digital waveguide implementation of the lumped inner sections, as well as the outer bore segments which are modeled by standard waveguide techniques, as previously discussed. There is no need for additional conical waveguide input and output “inertance” filters, as these terms are included in the lumped scattering junction equations. This is based on the fact that there is no back-scattering at the junction of conical sections of equal taper and diameter.

An implementation of this theory was made for a structure with approximate sectional lengths of 0.2, 0.05, and 0.3 meters, each rounded to its nearest integer delay length of 25, 6, and 38 samples at a sampling rate of 44.1 kHz, and sectional radii of 0.6, 1.3, and 2.7 centimeters. Conical sections

of one delay each were lumped together with the cylindrical segment and modeled by appropriately designed discrete-time scattering filters. For this purpose, the *MATLAB*® function *invfreqz* was used with low-frequency weighting functions to design fourth-order transmittance and reflectance filters based on the continuous-time responses of Eqs. (3.53a)–(3.53d). Figures 3.26 and 3.27 plot the input impedance magnitudes and impulse responses for this bore profile, as calculated using frequency-domain transmission-matrix and time-domain digital waveguide techniques. Low-order scattering junction digital filters are somewhat difficult to design for the lumped section, in part due to the phase delay associated with propagation along its length. However, this phase delay can be extracted from the continuous-time transmittance responses and implemented by delay lines, in series with lower-order, modified transmittance filters, as depicted in Fig. 3.28. It is important to maintain the overall passivity of the scattering junction during the filter design process. That is, design errors in the reflectance and/or transmittance filters may cause an inappropriate gain at a particular frequency which destabilizes the junction behavior. The design process should thus be checked by verifying that the sum of \mathcal{R}^- and \mathcal{T}^- and the sum of \mathcal{R}^+ and \mathcal{T}^+ have magnitudes less than or equal to the corresponding continuous-time functions for all frequencies. This problem can be reduced by incorporating viscothermal losses in the cascaded transmission-matrix coefficients.

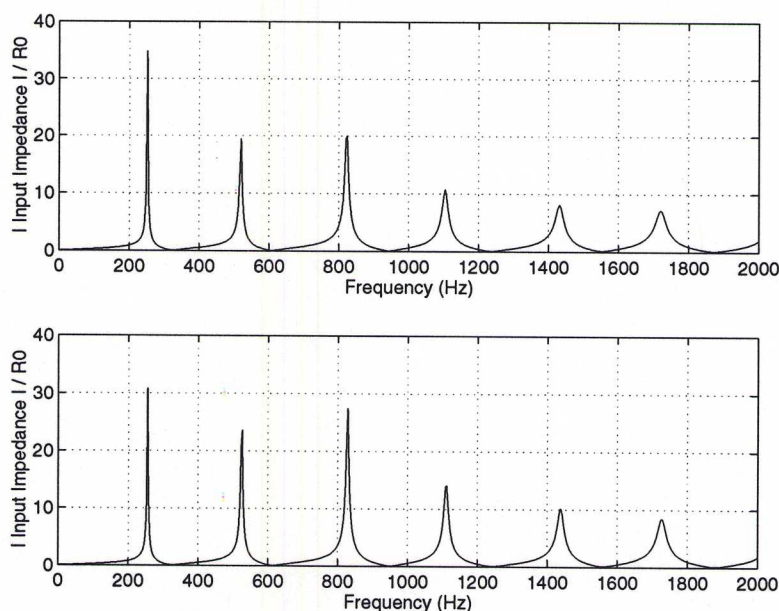


Fig. 3.26. Input impedance magnitude, normalized by $R_0 = \rho c/S(x)$ at the bore input, calculated using (top) transmission matrices and (bottom) a lumped section digital waveguide model as illustrated in Fig. 3.25(b).

The lumped section approach just discussed could also be derived by cascading waveguide matrix coefficients, determined from the transmission matrix elements by the appropriate substitution of waveguide variables. It is not possible, however, to cascade waveguide matrices which are in the form of Eq. (3.52) (van Walstijn and de Bruin, 1995).

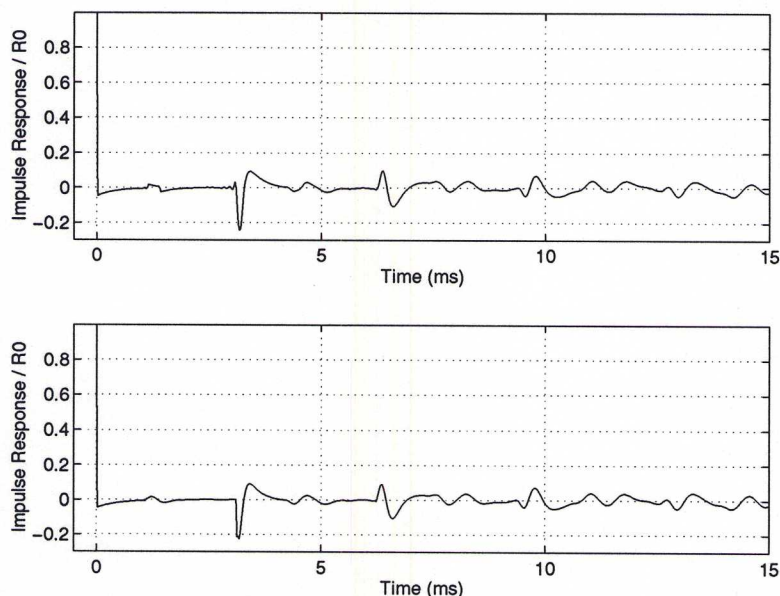


Fig. 3.27. Impulse response, normalized by $R_0 = \rho c/S(x)$ at the bore input, calculated using (top) transmission matrices and (bottom) a lumped section digital waveguide model as illustrated in Fig. 3.25(b).

3.3.4 Fractional Delay Lengths

Sound propagates with an approximate speed of 347.23 meters per second at a temperature of 26.85°C (Benade, 1968). The spatial sampling interval at 44.1 kHz is thus approximately 7.87 millimeters. The distances between various component parts of musical instruments seldom fall at perfect multiples of this interval, so that non-integer delay-line lengths are necessary for digital waveguide models. A significant body of work has been generated on this topic (Laakso *et al.*, 1994; Välimäki, 1995). The most useful methods for achieving fractional delay lengths in the context of digital waveguide modeling include *Lagrange* and *allpass* interpolation. Lagrange interpolation is

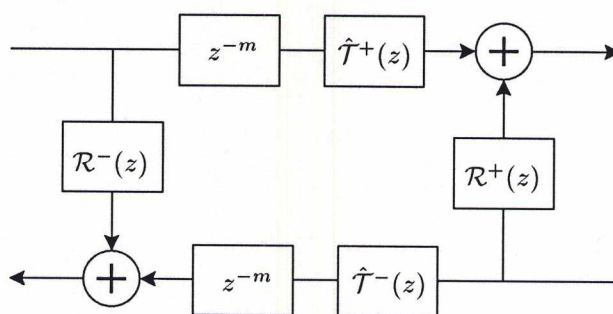


Fig. 3.28. The digital waveguide lumped section scattering junction with extracted linear phase terms and modified reflectance and transmittance filters.

typically implemented as either a first- or third-order finite impulse response (FIR) filter. The first-order Lagrange interpolator performs simple linear interpolation between two consecutive samples. The coefficients of the general Lagrange interpolator are given by

$$h(n) = \prod_{k=0, k \neq n}^N \frac{D - k}{n - k} \quad \text{for } n = 0, 1, 2, \dots, N \quad (3.54)$$

where D is the fractional delay and N is the order of the filter. Normalization of the coefficients found using Eq. (3.54) is necessary to preserve unity gain at DC. In order to keep the filter gains at or below unity over all frequencies, the delay and filter order should fall in the range $(N-1)/2 \leq D \leq (N+1)/2$ for odd N and $(N/2) - 1 \leq D \leq (N/2) + 1$ for even N (Välimäki, 1995). Further, for lowest error, values in the range $(N-1)/2 \leq D \leq (N+1)/2$ should be maintained for both even and odd order filters. Figure 3.29 shows the frequency response and phase delay of first-order Lagrange interpolation filters for delays in the range $0 \leq D \leq 1$. Figure 3.30 provides the same information for third-order

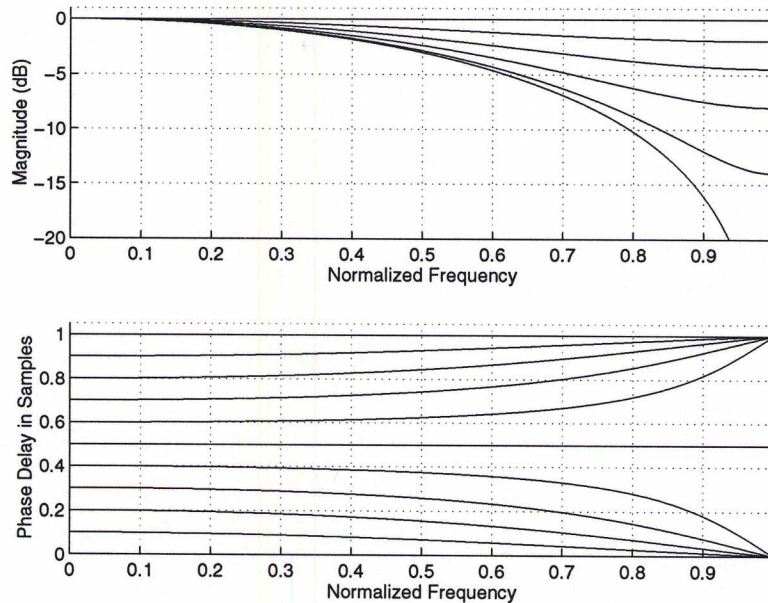


Fig. 3.29. Frequency response and phase delay of first-order, Lagrange interpolation filters for 11 delay values in the range $0 \leq D \leq 1$ [after (Jaffe and Smith, 1983)].

filters and delay values in the range $1 \leq D \leq 2$. The magnitude characteristics for both plots reveal signal attenuation to some extent for all non-integer delay length Lagrange interpolators. The phase characteristics further indicate dispersion at high frequencies. Even-order filters are also useful and generally provide improved frequency response at the cost of nonlinear phase delay. However, for dynamic fractional delay applications, the even order filters require switching at half sample points to maintain delay values within the range given above, rather than on integer sample points (as with odd order filters).

The use of allpass filters for achieving fractional delay in digital waveguide systems was first

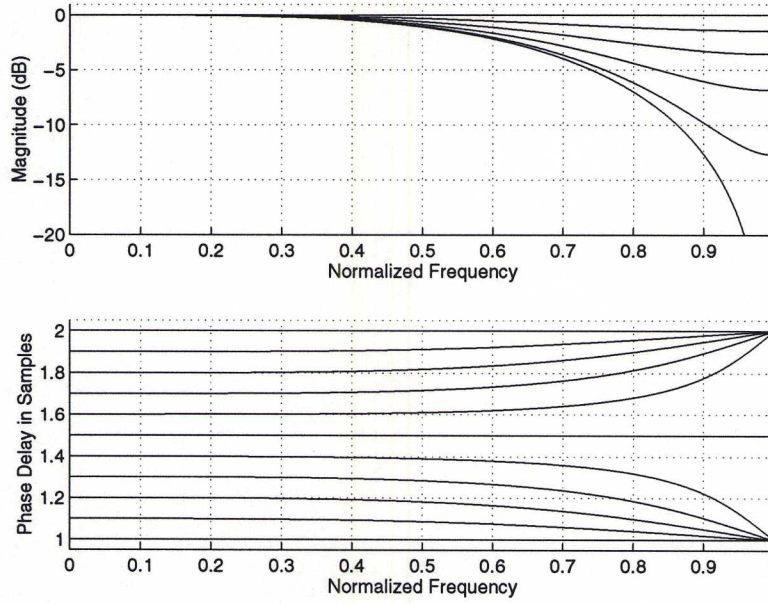


Fig. 3.30. Frequency response and phase delay of third-order, Lagrange interpolation filters for 11 delay values in the range $1 \leq D \leq 2$ [after (Jaffe and Smith, 1983)].

discussed by Smith (1983). Allpass filters have unity gain over all frequencies but variable phase delay properties. For this reason, they offer a means for achieving fractional delay with no frequency magnitude distortion (as was present to some extent in the Lagrange filters). Allpass interpolation is adequately performed using a first order allpass filter with a phase delay calculated to match the desired spacing at a particular frequency. However, the allpass filter has an infinite impulse response (IIR) and this response can affect desired time-domain performance. The coefficients of a general order (N) allpass filter are given by (Laakso *et al.*, 1992; Välimäki, 1995)

$$a_k = (-1)^k \binom{N}{k} \prod_{n=0}^N \frac{D - N + n}{D - N + k + n} \quad \text{for } k = 0, 1, 2, \dots, N \quad (3.55)$$

where D is the desired fractional delay and

$$\binom{N}{k} = \frac{N!}{k!(N-k)!} \quad (3.56)$$

is the binomial coefficient. In the first-order case, the allpass coefficient is thus found as

$$a_1 = -\frac{D-1}{D+1}. \quad (3.57)$$

Figure 3.31 shows the phase delay of first-order allpass interpolation filters for delays in the range $0 \leq D \leq 2$. While it is possible to get a wide range of low-frequency delay values from an allpass filter, it is best to limit this range around the order of the filter (in this case, $D = 1$). A delay range of $0.5 \leq D \leq 1.5$ corresponds to a coefficient range of $0.33 \geq a_1 \geq -0.2$. With such values, the

allpass filter displays maximally flat phase delay response together with the fastest decaying impulse response, a desired characteristic when dealing with dynamic delay values and their associated transient responses.

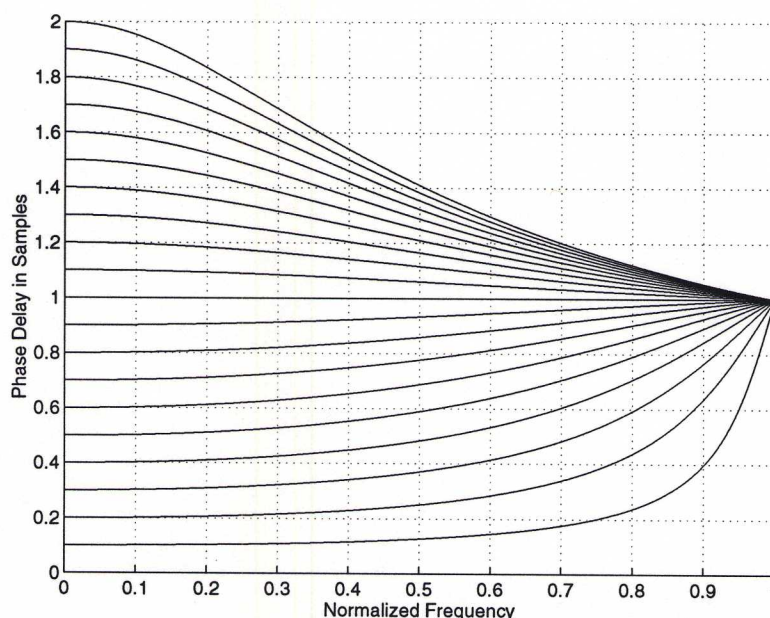


Fig. 3.31. Phase delay of first-order, allpass interpolation filters [after (Jaffe and Smith, 1983)].

In general, the phase delay characteristic of allpass filters is less linear than that of Lagrange interpolators. A nonlinear phase delay implemented within a digital waveguide feedback loop results in inharmonicities among the higher system normal modes or harmonic attenuation in steady-state, periodic waveforms. For this reason and because the impulse response of FIR filters is always much shorter than that of IIR systems, the Lagrange interpolator is better suited for most digital waveguide implementations. An exception to this rule, however, occurs for short string implementations, where the flat magnitude frequency response of the allpass filter is more important than a flat phase delay response.

Figure 3.32 displays the first 500 samples of an ideally terminated cylindrical waveguide bore implementation, using fractional delay filters to approximate a bore length of 20.275 samples or 0.15964 meters at a sampling rate of 44.1 kHz. The ideal, continuous-time response would consist of a single, negative unit impulse at a time of 0.9195 milliseconds, or the time necessary for the pulse to travel to the open end of the bore and back, followed by alternating unit pulses at equal time intervals. In the discrete-time simulation, the pulse is spread between the closest adjoining samples to the desired delay length. The impulse response of the first-order Lagrange interpolated bore is seen to decay over time, despite the absence of any dispersive element in the loop (aside from the Lagrange interpolation filter). This is a result of the frequency magnitude characteristic of the

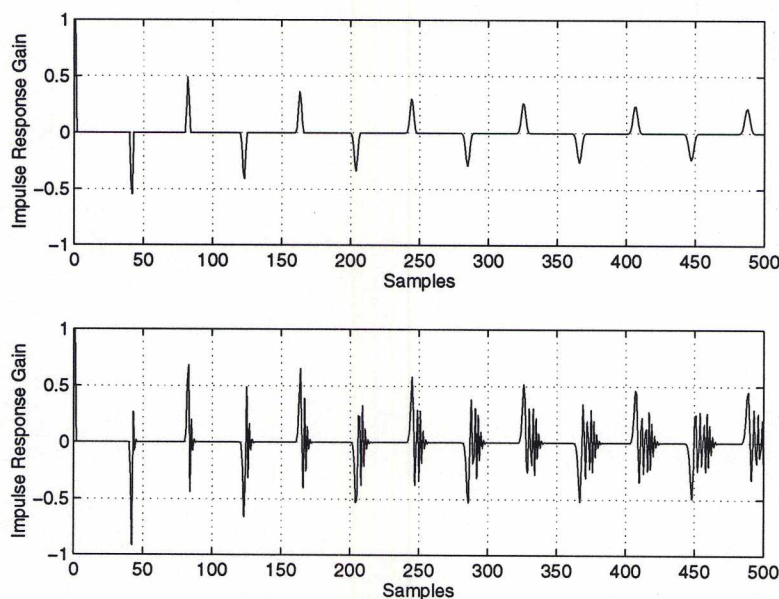


Fig. 3.32. Impulse response of digital waveguide system using (top) first-order Lagrange interpolation and (bottom) first-order allpass interpolation.

Lagrange interpolator. The impulse response of the allpass interpolated bore exhibits no attenuation, however, the much longer impulse response of the IIR interpolation filter is obvious. Assuming the bore model will incorporate loss filters, the allpass response will normally be quickly attenuated and the transient response will not be aurally noticeable. However, Lagrange interpolation is better suited for instances where visual comparison of time-domain response functions is made to continuous-time waveforms.

Within a single digital waveguide model, a large number of fractional delay filters may be needed to implement such discontinuities as toneholes. The combined effect of these “cascaded” filters can be significant. Cook (1995) illustrates the worst-case magnitude and phase errors of a waveguide flute model with eight toneholes. It should be noted that early reflections in such a model will be less affected by the combined fractional delay losses than those portions of the signal that propagate through many or all of the tonehole junctions. It may be possible to reduce the effect of these errors, however, by commuting appropriate boundary-layer losses with the fractional-delay filters.

3.3.5 Boundary-Layer Effects

An analysis of viscous and thermal losses in rigid cylindrical tubes was provided in Section 1.3.3. These effects were characterized by a modified wave propagation number $k = \Omega/v_p - j\alpha$, where v_p is the phase velocity and α is an attenuation coefficient per unit length. The parameters v_p and α vary with frequency and duct radius (at a constant temperature) and are given in Section 1.3.3. In this representation, the thermoviscous losses are *distributed* over the length of the pipe. Within a digital

waveguide system, it is necessary to lump these effects by replacing each unit sample delay with a digital filter designed to approximate the attenuation and phase delay incurred over the distance cT . The continuous-time filter $H(\Omega)$ which represents lossy wave propagation over this distance is found as

$$H(\Omega) = e^{-jkx} = e^{-\alpha cT} e^{-j\Omega cT/v_p}. \quad (3.58)$$

$H(\Omega)$ can be expressed in terms of the discrete-time frequency variable z as

$$H(z) = e^{-\alpha cT} z^{-c/v_p}. \quad (3.59)$$

The frequency response of $H(z)$ is shown in Fig. 3.33. Except at low frequencies, the phase delay

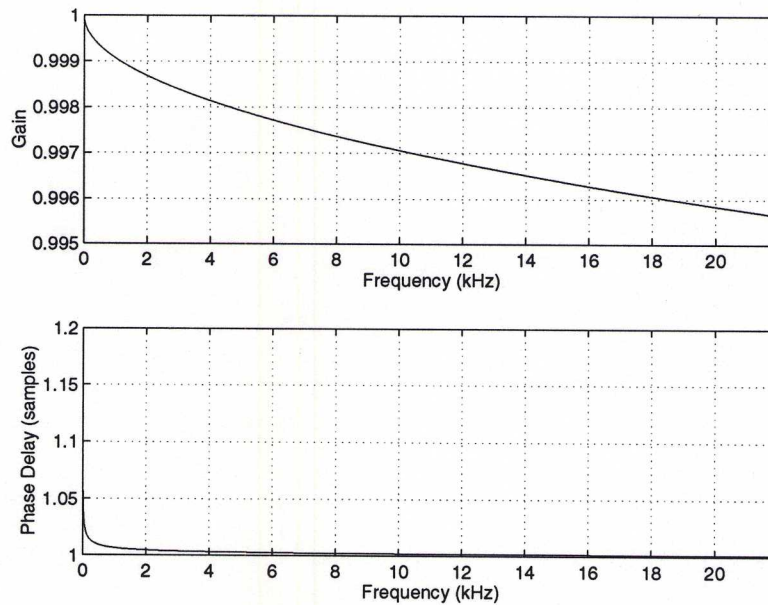


Fig. 3.33. Frequency response of the filter $H(z)$: Magnitude (top); Phase delay (bottom).

is close to that of a unit sample delay. The attenuation is minimal over the distance cT , but does become significant for distances on the order of woodwind instrument bore lengths. A digital filter can be designed to approximate the ideal response of $H(z)$ by commuting a linear phase attenuation filter, representing the term $e^{-\alpha cT}$, with an allpass filter which models the phase delay term z^{-c/v_p} . Alternatively, an IIR filter can be designed to match both the phase delay and attenuation characteristics. Thermoviscous losses over fractional delay lengths are similarly modeled by appropriately designed digital filters. However, the attenuation and/or dispersion inherent in fractional delay interpolation techniques will usually be greater than the thermoviscous effects themselves.

The use of $H(z)$ in a digital waveguide model is represented in Fig. 3.34. Each unit delay is replaced by a separate implementation of $H(z)$. By doing so, however, inaccuracies in the digital filter approximation to $H(\Omega)$ are compounded throughout the system. More importantly, the computational performance of the model is completely destroyed because the efficiency of the digital

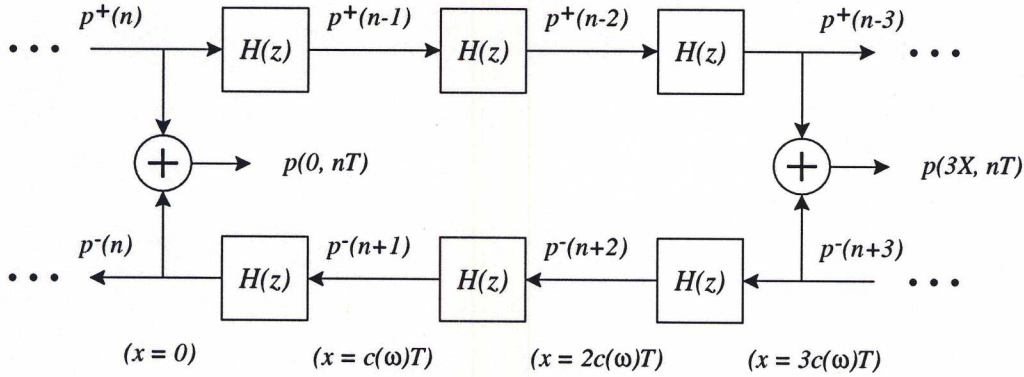


Fig. 3.34. Digital waveguide implementation of lossy plane-wave propagation in air [after (Smith, 1996a)]. The unit delays have been incorporated into $H(z)$.

waveguide technique is dependent upon the use of delay lines to represent lossless wave propagation. Instead, linearity of the woodwind bore model allows the effects of thermoviscous losses to be “lumped” or commuted together, as shown in Fig. 3.35. The filters $H_b^m(z)$ represent the commuted losses only, or equivalently $z^m H^m(z)$. Figure 3.36 shows the response of a 5th-order IIR filter, designed using an equation-error minimization technique, versus the ideal response of $H_b^{76}(\Omega)$, or the commuted phase delay and attenuation over 76 unit sample delay lengths. The loss filter(s) can even be commuted with other filters in the system, such as the open-end reflection filter $\mathcal{R}_L(z)$, thereby reducing computational complexity even further. Commutation of losses is simple when the desired observation point is located at either end of the bore. However, when it is desired that an implementation allow an arbitrary observation point, the commuted losses need be carefully accounted for.

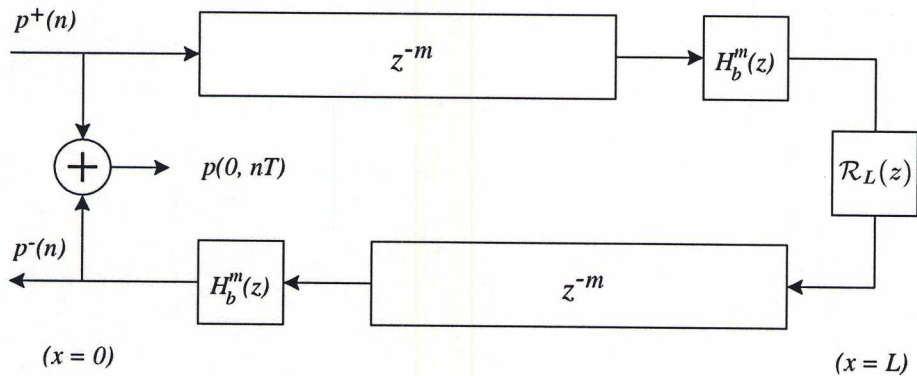


Fig. 3.35. Commuted thermoviscous losses in a digital waveguide cylindrical air column implementation.

Boundary layer effects in conical bores may be estimated by dividing the conical bore into cylindrical sections and deriving loss filters based on the average radius of each segment. For computational efficiency, the loss filters can then be commuted as was done above.

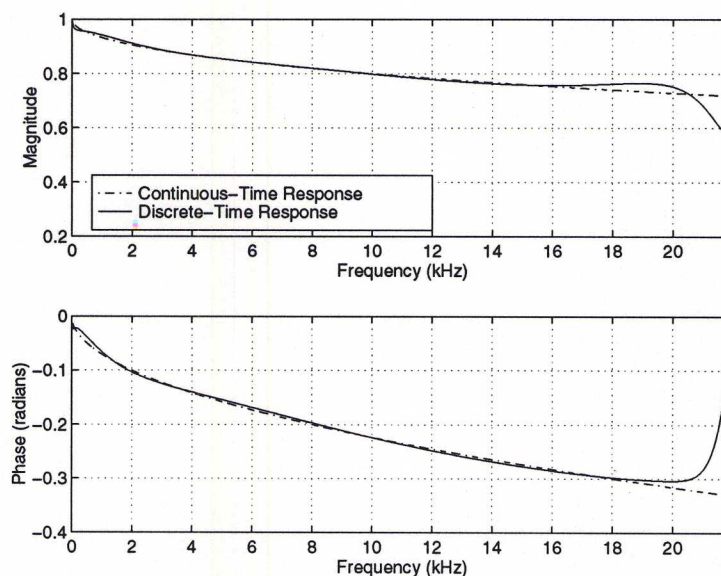


Fig. 3.36. Continuous-time filter $H_b^{76}(s)$ and 5th-order discrete-time filter $H_b^{76}(z)$ responses.

3.4 Modeling Sound Radiation

In Section 1.4, the acoustic behavior of propagating sound waves in horns, near toneholes, and at the ends of non-flaring cylindrical pipes was briefly discussed. Such structures completely define a wind instrument's sound radiation and internal reflection characteristics. Because the dimensions of these acoustic elements are typically much smaller than the wavelengths of sound propagating through them, they are well approximated by lumped responses. The efficiency of digital waveguide techniques rests primarily in the simulation of lossless, one-dimensional traveling-waves. Within this scheme, the lumped responses of acoustic sound radiating components are well modeled by FIR or IIR digital filters.

3.4.1 Non-Flaring Ends

In most woodwind instruments, sound radiation is primarily accomplished via a tonehole lattice. For this reason, the open ends of such instruments typically exhibit little or no flare. Two theoretical models of sound reflection at non-flaring bore ends were discussed in Section 1.4.1. The results of Lord Rayleigh (1896) were obtained by assuming an infinite flange at the end of the bore. Subsequently, Levine and Schwinger (1948) obtained an explicit solution for the radiation of sound from an unflanged circular pipe.

For implementation within the digital waveguide context, it is necessary to design digital filters which accurately model the continuous-time characteristics mentioned above. Good discrete-time approximations to both solutions are best obtained using frequency-domain digital filter design

methods. Figure 3.37 plots the continuous-time and discrete-time approximations to the frequency magnitude and phase responses, respectively, of the Levine and Schwinger unflanged cylindrical duct solution. The result is a digital filter of second order, obtained using the equation-error filter design method discussed in Section 3.2. In this case, the filter was designed for a pipe radius of 0.008 meters, which falls near the typical dimensions of both clarinet and flute bores. Similar results can be obtained for the Rayleigh solution but are not shown here.

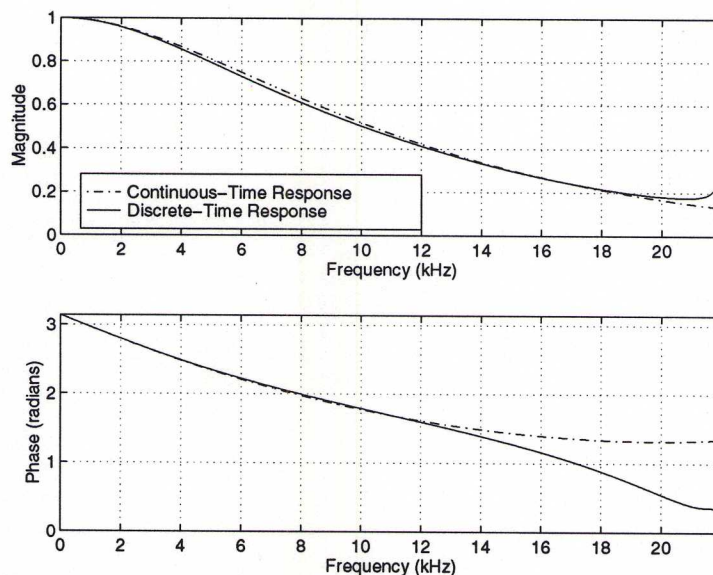


Fig. 3.37. Continuous-time and digital filter magnitude and phase characteristics for the Levine and Schwinger reflectance in a cylindrical duct of radius 0.008 meters.

Open-end reflections in a digital waveguide model were previously represented by a general reflectance filter $\mathcal{R}(z)$. From Fig. 3.37, this reflectance is characterized by a lowpass digital filter. The corresponding open-end transmittance is given by $\mathcal{T}(z) = 1 + \mathcal{R}(z)$, which displays a highpass filter characteristic. The open-end transmittance may be implemented in two ways, as depicted in Fig. 3.38. These two schemes are equivalent, though the bottom representation of Fig. 3.38 is obviously a more efficient means for calculating the residual, transmitted sound. However, the implementation of two separate filters may be desired in order to allow better control over model output sound quality.

As mentioned in Section 1.4.1, an explicit theoretical solution for sound radiation at the open end of a conical bore has yet to be derived. Caussé *et al.* (1984) suggest scaling the cylindrical pipe open-end radiation impedance Z_R by the ratio of plane- and spherical-wave surface areas (S_p/S_s) at the end of the conic frusta. The resulting load impedance at the end of an open conical bore is then given by

$$Z_{R'} = \frac{S_p}{S_s} Z_R. \quad (3.60)$$

A corresponding conical bore open-end reflectance is determined by substituting Eq. (3.60) into

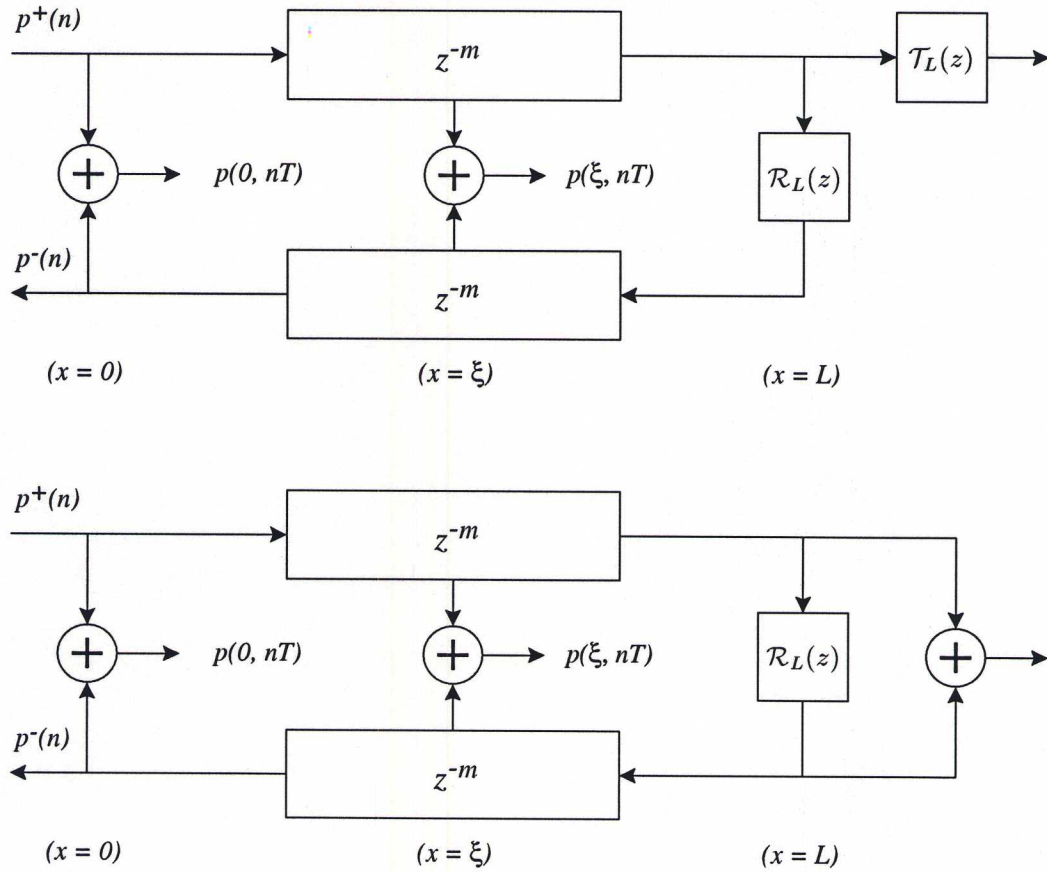


Fig. 3.38. Sound radiation filter implementations in a digital waveguide cylindrical duct model: (top) Complementary transmittance filter [after (Smith, 1986)]; (bottom) Residual sound output.

Eq. (3.9) as

$$\mathcal{R}_{R'}(x, s) = \left[\frac{Z_{R'}(x, s)Z_0^*(x, s) - Z_0(x, s)Z_0^*(x, s)}{Z_{R'}(x, s)Z_0(x, s) + Z_0(x, s)Z_0^*(x, s)} \right]. \quad (3.61)$$

This is equivalent to determining the reflectance which results from the parallel combination of $Z_{R'}$ and the conical bore open-end inertance. In practice, however, the complex spherical-wave characteristic impedance is nearly real at the end of a conical bore, so that the substitution

$$\mathcal{R}_{R'}(x, s) = \frac{(S_p/S_s)Z_R(x, s) - Z_0}{(S_p/S_s)Z_R(x, s) + Z_0} \quad (3.62)$$

is adequate in most contexts. Since the Levine and Schwinger solution is given in the form of a plane-wave reflectance $\mathcal{R}_R(s)$, the substitution

$$\mathcal{R}_{R'}(s) = \frac{\gamma + \mathcal{R}_R(s)}{1 + \gamma\mathcal{R}_R(s)} \quad (3.63)$$

results, where

$$\gamma = \frac{S_p - S_s}{S_p + S_s}.$$

The explicit theoretical solution determined by Levine and Schwinger for sound radiation from an unflanged cylindrical pipe is valid for frequencies in the range $0 \leq ka \leq 3.8$. This range is often inadequate for digital waveguide simulations involving large open-end radii, for such instruments as saxophones, and standard digital audio sampling rates. Therefore, the Levine and Schwinger solution was smoothly extended out to a range $ka \leq 20$, as shown in Fig. 3.39. The magnitude extension was achieved by concatenating a scaled version of $(ka)^{-3}$ to the tail of the theoretical results. Similarly, the length correction extension was achieved by concatenating a scaled version of $(ka - 3)^{-2}$ to the tail of the corresponding theoretical results.

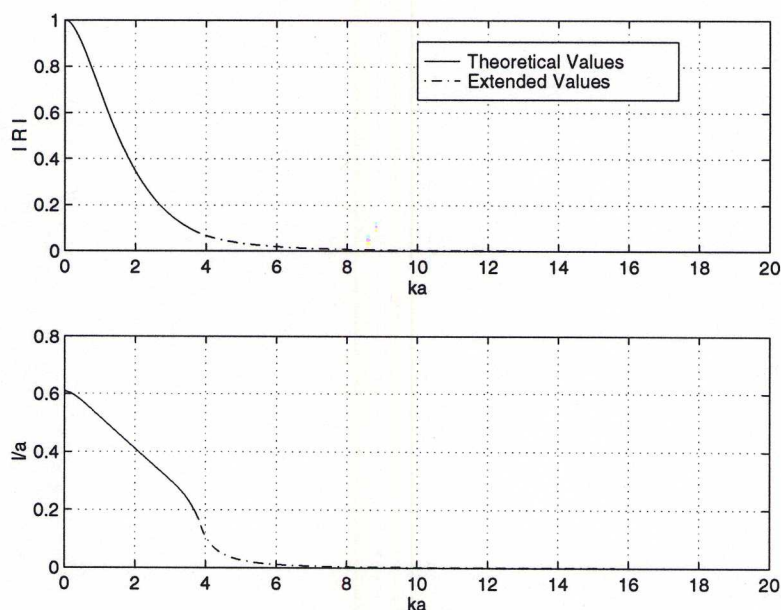


Fig. 3.39. Levine and Schwinger unflanged open end reflectance magnitude and length correction extensions.

3.4.2 Horns

Digital waveguides have been shown to efficiently simulate wave propagation described by the one-dimensional wave equation. Plane waves in cylindrical bores and spherical waves in conical bores are thus well modeled in this manner. Most wind instruments are not perfectly cylindrical or conical throughout their length, though a major portion of their air columns are generally well approximated by a single cylindrical or conical section. For regions in which an air column flares rapidly, however, an alternative means is necessary to model the internal wave behavior. In Section 1.4.2, it was mentioned that general horn shapes can be approximated with cylindrical and/or conical sections. The use of cylindrical digital waveguide sections in this way was previously reported by Cook (1988).

The air columns of woodwind instruments are nearly uniform throughout most of their length. Flared sections of short length sometimes occur near the end of woodwind bores, though significant

sound propagation in these sections is generally limited to instances when all or most of the instrument's toneholes are closed. For these reasons, a detailed discussion of flaring horns will not be presented in this study. Wave propagation in structures other than pipes of circular and rectangular cross-section and cones is necessarily multi-dimensional (Putland, 1993), and digital waveguides do not efficiently model this type of wave behavior. However, because horns are typically found only at the end of bores which are mostly cylindrical or conical in shape, the horn characteristic can be modeled by a lumped impedance or reflectance while wave propagation in the cylindrical or conical section can be modeled using digital waveguides. A method for determining the reflectance of a horn of general shape is discussed by Berners and Smith (1994).

3.4.3 Toneholes

The fundamental acoustic properties of toneholes were discussed in Chapter 1. The model described by Keefe (1990) is the most current and accurate representation for a tonehole unit, assuming interactions between adjacent toneholes are negligible. In this description, acoustic variables are related by a transmission matrix of series and shunt impedance parameters. Keefe's original derivation of the tonehole parameters was based on a symmetric T section, as shown in Fig. 3.40 (Keefe, 1981). The series impedance terms, Z_a , result from an analysis of anti-symmetric pressure distribution, or

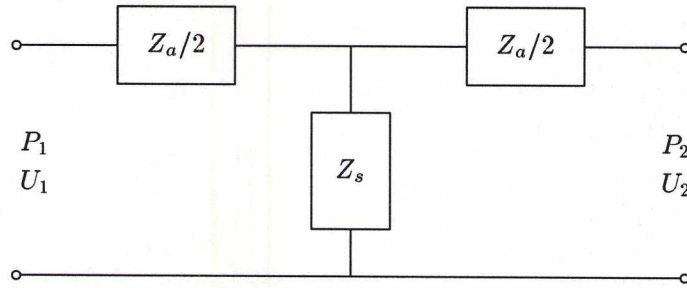


Fig. 3.40. T section transmission line element representing the tonehole.

a pressure node, at the tonehole junction. In this case, volume flow is symmetric and thus equal across the junction. The shunt impedance term, Z_s , results from an analysis of symmetric pressure distribution, or a pressure anti-node, at the tonehole junction. In this case, pressure is symmetric and equal across the junction. The transmission matrix which results under this analysis is given by

$$\begin{aligned} \begin{bmatrix} P_1 \\ U_1 \end{bmatrix} &= \begin{bmatrix} 1 & Z_a/2 \\ 0 & 1 \end{bmatrix} \begin{bmatrix} 1 & 0 \\ Z_s^{-1} & 1 \end{bmatrix} \begin{bmatrix} 1 & Z_a/2 \\ 0 & 1 \end{bmatrix} \begin{bmatrix} P_2 \\ U_2 \end{bmatrix} \\ &= \begin{bmatrix} 1 + \frac{Z_a}{2Z_s} & Z_a \left(1 + \frac{Z_a}{4Z_s} \right) \\ Z_s^{-1} & 1 + \frac{Z_a}{2Z_s} \end{bmatrix} \begin{bmatrix} P_2 \\ U_2 \end{bmatrix}. \end{aligned} \quad (3.64)$$

Based on the fact that $|Z_a/Z_s| \ll 1$, Eq. (3.64) can be reduced to the form

$$\begin{bmatrix} P_1 \\ U_1 \end{bmatrix} = \begin{bmatrix} 1 & Z_a \\ Z_s^{-1} & 1 \end{bmatrix} \begin{bmatrix} P_2 \\ U_2 \end{bmatrix}, \quad (3.65)$$

which is the basic tonehole unit cell used by Keefe in transmission-matrix calculations. The values of Z_a and Z_s vary according to whether the tonehole is open (o) or closed (c) and are repeated here for convenience as

$$Z_s^{(o)} = Z_0(a/b)^2 (jkt_e + \xi_e), \quad (3.66a)$$

$$Z_s^{(c)} = -jZ_0(a/b)^2 \cot(kt), \quad (3.66b)$$

$$Z_a^{(o)} = -jZ_0(a/b)^2 kt_a^{(o)}, \quad (3.66c)$$

$$Z_a^{(c)} = -jZ_0(a/b)^2 kt_a^{(c)}. \quad (3.66d)$$

Definitions and descriptions of the various parameters in Eqs. (3.66a) – (3.66d) can be found in Section 1.4.3.

To render these relationships in the digital waveguide domain, it is necessary to transform the plane-wave transmission-matrix coordinates of pressure and volume velocity to waveguide coordinates, as

$$\begin{bmatrix} P_1 \\ U_1 \end{bmatrix} = \begin{bmatrix} P_1^+ + P_1^- \\ Z_0^{-1} (P_1^+ - P_1^-) \end{bmatrix}, \quad \begin{bmatrix} P_2 \\ U_2 \end{bmatrix} = \begin{bmatrix} P_2^+ + P_2^- \\ Z_0^{-1} (P_2^+ - P_2^-) \end{bmatrix}, \quad (3.67)$$

where Z_0 is the characteristic impedance of the cylindrical bore, which is equal on both sides of the tonehole. Waveguide pressure variables on both sides of the tonehole are related by

$$\begin{aligned} \begin{bmatrix} P_1^- \\ P_2^+ \end{bmatrix} &= \begin{bmatrix} \mathcal{R}^- & \mathcal{T}^- \\ \mathcal{T}^+ & \mathcal{R}^+ \end{bmatrix} \begin{bmatrix} P_1^+ \\ P_2^- \end{bmatrix} \\ &= \frac{1}{(2Z_0 + Z_a)(2Z_0 + Z_a + 4Z_s)} \begin{bmatrix} 4Z_a Z_s + Z_a^2 - 4Z_0^2 & 8Z_0 Z_s \\ 8Z_0 Z_s & 4Z_a Z_s + Z_a^2 - 4Z_0^2 \end{bmatrix} \begin{bmatrix} P_1^+ \\ P_2^- \end{bmatrix}, \\ &\approx \frac{1}{Z_a Z_s + 2Z_0 Z_s + Z_0^2} \begin{bmatrix} Z_a Z_s - Z_0^2 & 2Z_0 Z_s \\ 2Z_0 Z_s & Z_a Z_s - Z_0^2 \end{bmatrix} \begin{bmatrix} P_1^+ \\ P_2^- \end{bmatrix} \end{aligned} \quad (3.68)$$

calculated using Eqs. (3.64) and (3.67) and then making appropriate simplifications based on the fact that $|Z_a/Z_s| \ll 1$. Figure 3.41 depicts the waveguide tonehole two-port scattering junction in terms of these reflectances and transmittances. This structure is analogous to the four-multiply Kelly-Lochbaum scattering junction (Kelly and Lochbaum, 1962). It is interesting to note that direct transformation of Eq. (3.65) to waveguide coordinates results in

$$\begin{bmatrix} P_1^- \\ P_2^+ \end{bmatrix} = \frac{1}{Z_a Z_s + 2Z_0 Z_s + Z_0^2} \begin{bmatrix} Z_a Z_s - Z_0^2 & 2Z_0(Z_s - Z_a) \\ 2Z_0 Z_s & Z_a Z_s - Z_0^2 \end{bmatrix} \begin{bmatrix} P_1^+ \\ P_2^- \end{bmatrix}, \quad (3.69)$$

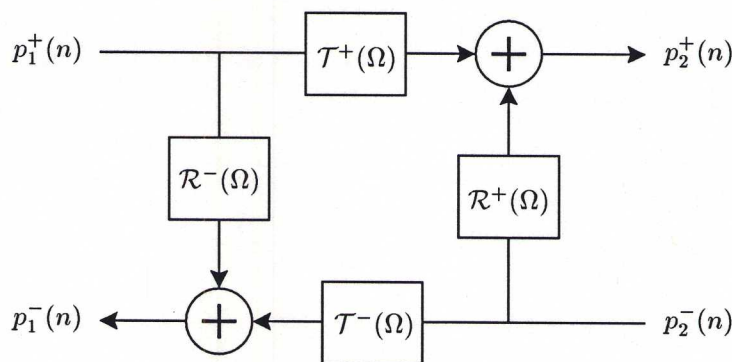


Fig. 3.41. Tonehole two-port scattering junction.

for which the two transmittances are unequal, indicating non-symmetric wave propagation at the junction of the tonehole. However, by again assuming $|Z_a/Z_s| \ll 1$, the two transmission terms converge, as expected from the original symmetric T section derivation of the tonehole parameters.

It is necessary to derive appropriate digital reflectance and transmittance filters to model the behavior represented by Eq. (3.68). While the series impedance terms are easily expressed in terms of the Laplace transform frequency variable, and subsequently can be transformed to the discrete-time domain using the bilinear transform, the shunt impedance terms are given by distributed cotangent and tangent factors which are not well represented in the Laplace domain. Consequently, the digital waveguide tonehole reflectance and transmittance filters are best designed using general digital filter design techniques. Figure 3.42 plots the continuous-time magnitude and phase characteristics of the *closed-hole* reflectance, together with the response of a two pole/two zero digital filter approximation. The discrete-time filter was designed using the equation-error method previously discussed in Section 3.2. Figure 3.43 plots the continuous-time magnitude and phase characteristics of the *open-hole* reflectance, together with the response of a one pole/two zero digital filter approximation. The open-hole discrete-time filter was designed using Kopec's method (Smith, 1983, p. 46), in conjunction with the equation-error method. That is, a one-pole model $\hat{H}_1(z)$ was first fit to the continuous-time response, $H(e^{j\Omega})$. Subsequently, the inverse error spectrum, $\hat{H}_1(e^{j\Omega})/H(e^{j\Omega})$ was modeled with a two-pole digital filter, $\hat{H}_2(z)$. The discrete-time approximation to $H(e^{j\Omega})$ was then given by $\hat{H}_1(z)/\hat{H}_2(z)$. The first step of the design process captures the peaks of the spectral envelope, while the second step models the "dips" in the spectrum. These particular calculations were performed for a tonehole of radius $b = 4.765$ millimeters, minimum tonehole height $t_w = 3.4$ millimeters, tonehole radius of curvature $r_c = 0.5$ millimeters, and air column radius $a = 9.45$ millimeters. The results of Keefe (1981) were experimentally calibrated for frequencies less than about 5 kHz, so that the continuous-time responses evident in the figures are purely theoretical above this limit. Therefore, the discrete-time filter design process was weighted to produce better matching at low frequencies.

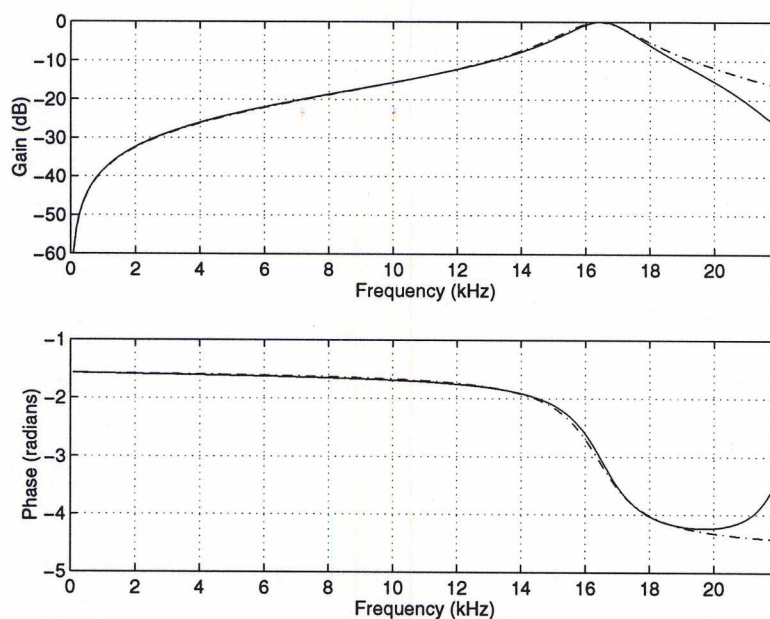


Fig. 3.42. Two-port tonehole junction closed-hole reflectance, derived from Keefe (1981) shunt and series impedance parameters [(---) continuous-time response; (—) discrete-time filter response]. (top) Reflectance magnitude; (bottom) Reflectance phase.

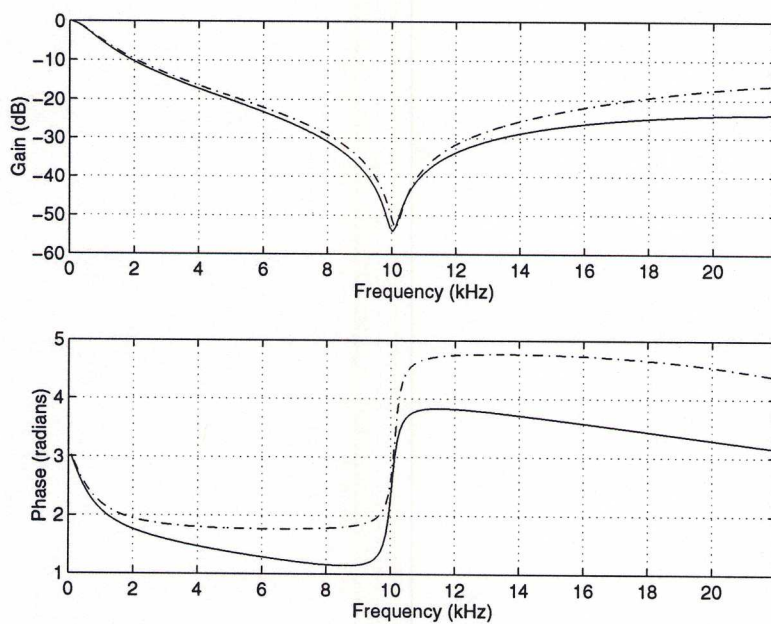


Fig. 3.43. Two-port tonehole junction open-hole reflectance, derived from Keefe (1981) shunt and series impedance parameters [(---) continuous-time response; (—) discrete-time filter response]. (top) Reflectance magnitude; (bottom) Reflectance phase.

Figures 3.44, 3.45, and 3.46 plot the reflection functions calculated for a six-hole flute, as described in (Keefe, 1990). The upper plots in each figure were calculated using continuous-time transmission-matrix parameters, and the plotted reflection functions were determined as the inverse Fourier transform of the corresponding reflectances. These responses are equivalent to those provided by Keefe (1990), though scale factor discrepancies exist due to differences in open-end reflection models and lowpass filter responses. The lower plots were calculated from a digital waveguide model using two-port tonehole scattering junctions. Differences between the continuous- and discrete-time results are most apparent in early, high-frequency, closed-hole reflections. The continuous-time reflection functions were low-pass filtered to remove time-domain aliasing effects incurred by the inverse Fourier transform operation and to better correspond with the plots of Keefe (1990). By trial and error, a lowpass filter with a cutoff frequency around 4 kHz was found to produce the best match to Keefe's results. The digital waveguide results were obtained at a sampling rate of 44.1 kHz and then lowpass filtered to a 10 kHz bandwidth, corresponding to that of Keefe (1990). Further lowpass filtering is inherent from the Lagrangian, delay-line length interpolation technique used in this model (Välimäki, 1995). Because such filtering is applied at different locations along the air column, a cumulative effect is difficult to accurately determine. The first tonehole reflection is affected by only two interpolation filters, while the second tonehole reflection is affected by four filtering operations. This effect is most responsible for the minor discrepancies apparent between the plots.

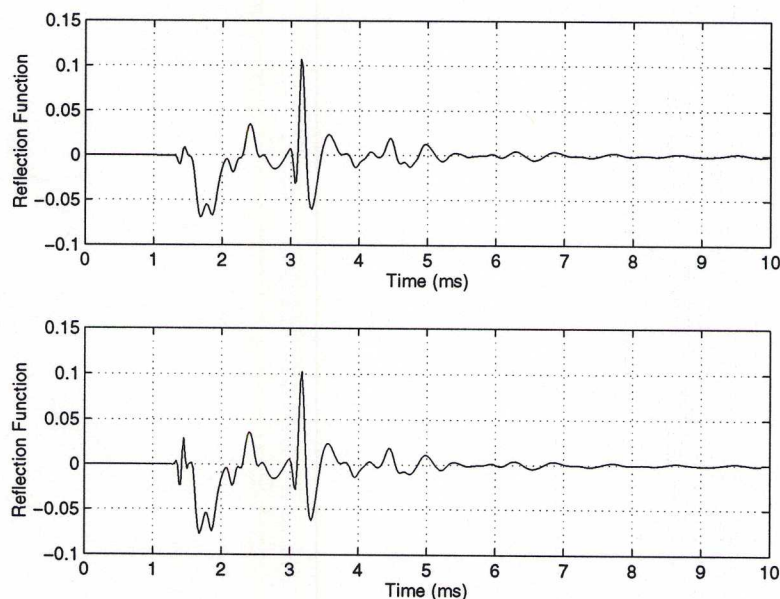


Fig. 3.44. Reflection functions for note *B* (all six finger holes open) on a simple flute [see (Keefe, 1990)]. (top) Transmission-line calculation; (bottom) Digital waveguide implementation.

The Keefe tonehole model transforms directly into a two-port digital waveguide scattering junction. In such a form, however, sound radiation from the tonehole is not explicitly determined. For

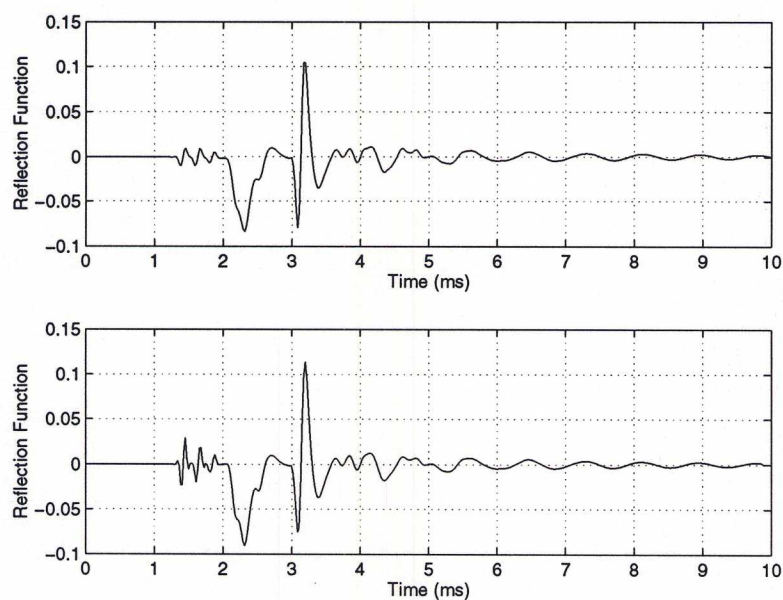


Fig. 3.45. Reflection functions for note *G* (three finger holes closed, three finger holes open) on a simple flute [see (Keefe, 1990)]. (top) Transmission-line calculation; (bottom) Digital waveguide implementation.

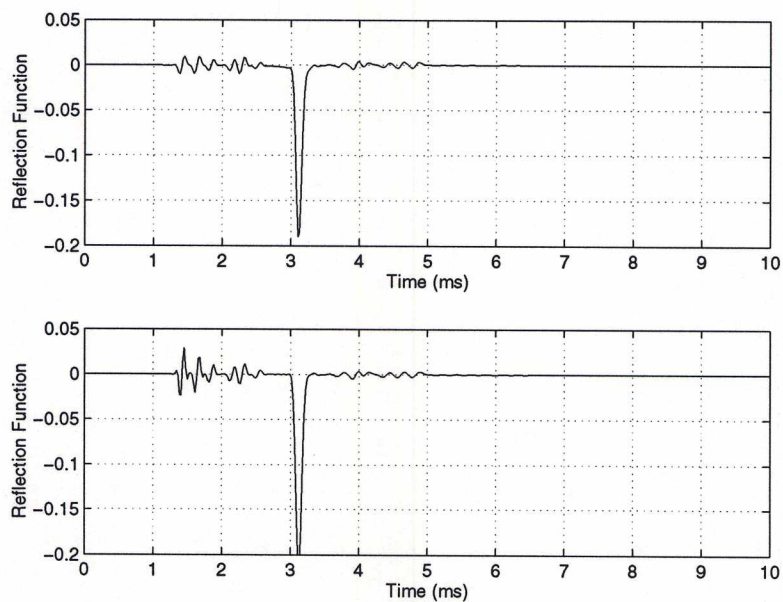


Fig. 3.46. Reflection functions for note *D* (all six finger holes closed) on a simple flute [see (Keefe, 1990)]. (top) Transmission-line calculation; (bottom) Digital waveguide implementation.

this, it is necessary to examine the restrictions implied at the junction of several acoustic pipes. Smith (1987) discusses the constraints on a general N-port junction of acoustic tubes. According to Kirchoff's node equations, the junction is governed by conservation of volume flow,

$$\sum_{i=1}^N U_i = 0, \quad (3.70)$$

and pressure continuity,

$$P_1 = P_2 = \dots = P_J, \quad (3.71)$$

where P_J is the junction pressure. Sound radiation at the junction can occur only from an open tonehole, which is characterized by the shunt impedance term $Z_s^{(o)}$. Thus, it is possible to design a tonehole pressure transmission filter from $Z_s^{(o)}$ through which the junction pressure P_J can be filtered to determine the radiated sound pressure.

A tonehole junction may also be represented by a lossless three-port junction, as shown in Fig. 3.47. The three-port junction models sound wave interaction at the intersection of the air column and tonehole, as determined by conservation of volume flow and continuity of pressure. Wave propagation within the tonehole itself can subsequently be modeled by another waveguide and the reflection/transmission characteristics at its end by an appropriate digital filter. This tonehole model is then attached to the appropriate branch of the three-port junction. The bore characteristic admittance Y_0 is equal on either side of the junction, while the real tonehole characteristic admittance is Y_{0th} . Because this is a junction of three cylindrical pipes, and each pipe has a real and

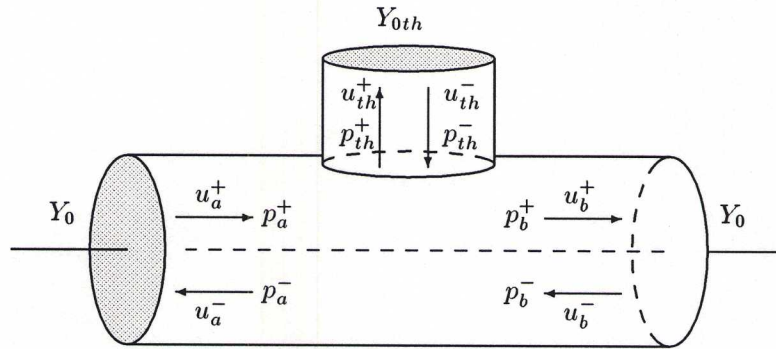


Fig. 3.47. The three-port tonehole junction where a side branch is connected to a uniform cylindrical tube [after (Välimäki, 1995)].

constant characteristic admittance, the scattering equations can be determined directly in the time-domain. By expressing Eqs. (3.70) and (3.71) in terms of traveling waves of pressure, the pressure traveling-wave components leaving the junction are given by

$$p_a^-(t) = \frac{-Y_{0th}p_a^+(t) + 2Y_0p_b^-(t) + 2Y_{0th}p_{th}^-(t)}{Y_{0th} + 2Y_0} \quad (3.72a)$$

$$p_b^+(t) = \frac{2Y_0p_a^+(t) - Y_{0th}p_b^-(t) + 2Y_{0th}p_{th}^-(t)}{Y_{0th} + 2Y_0} \quad (3.72b)$$

$$p_{th}^+(t) = \frac{2Y_0 p_a^+(t) + 2Y_0 p_b^-(t) + [Y_{0th} - 2Y_0] p_{th}^-(t)}{Y_{0th} + 2Y_0}. \quad (3.72c)$$

The internal bore frequency-independent reflection coefficients are equal and given by

$$r_0 \triangleq r_a = r_b = \frac{-Y_{0th}}{Y_{0th} + 2Y_0} = \frac{-Z_0}{Z_0 + 2Z_{0th}}, \quad (3.73)$$

while the tonehole frequency-independent reflection coefficient is

$$r_{th} = \frac{Y_{0th} - 2Y_0}{Y_{0th} + 2Y_0} = \frac{Z_0 - 2Z_{0th}}{Z_0 + 2Z_{0th}} = -1 - 2r_0 \quad (3.74)$$

Using the reflection coefficient r_0 , the three-port scattering junction equations for pressure wave components can be simplified as

$$p_a^-(t) = r_0 p_a^+(t) + [1 + r_0] p_b^-(t) - 2r_0 p_{th}^-(t) \quad (3.75a)$$

$$p_b^+(t) = [1 + r_0] p_a^+(t) + r_0 p_b^-(t) - 2r_0 p_{th}^-(t) \quad (3.75b)$$

$$p_{th}^+(t) = [1 + r_0] p_a^+(t) + [1 + r_0] p_b^-(t) - [1 + 2r_0] p_{th}^-(t). \quad (3.75c)$$

(Välimäki, 1995, p. 47) states that a one-multiply form of the three-port scattering equations is not possible, though this is probably due to errors in his corresponding equations. From the above expressions, a one-multiply implementation is given by

$$p_a^-(t) = p_b^-(t) + w \quad (3.76a)$$

$$p_b^+(t) = p_a^+(t) + w \quad (3.76b)$$

$$p_{th}^+(t) = p_a^+(t) + p_b^-(t) - p_{th}^-(t) + w, \quad (3.76c)$$

where

$$w = r_0 [p_a^+(t) + p_b^-(t) - 2p_{th}^-(t)]. \quad (3.77)$$

An implementation of these equations is shown in Fig. 3.48.

To complete the digital waveguide three-port tonehole implementation, it is necessary to determine an appropriate model for the tonehole section itself, and then attach this model to the junction. The spatial sampling interval at a sampling rate of 44.1 kHz is approximately 7.87 millimeters. It is thus possible to implement the tonehole structure as a short, fractional delay, digital waveguide and apply an appropriate reflectance at its end. Depending on the tonehole geometry, the reflectance at the end of an open tonehole may be approximated by either a flanged (Lord Rayleigh, 1896) or unflanged (Levine and Schwinger, 1948) solution. When the tonehole is closed, an infinite impedance (or a pressure reflection without inversion) is appropriate. Given typical tonehole heights, however, a lumped reflectance model of the tonehole, which accounts for both the propagation delay and end reflection, is more appropriate and easily implemented with a single low-order digital filter. In this sense, incoming tonehole pressure $p_{th}^-(t)$ is calculated from the outgoing tonehole pressure $p_{th}^+(t)$ and the tonehole reflection function, while the corresponding pressure radiated from the open tonehole

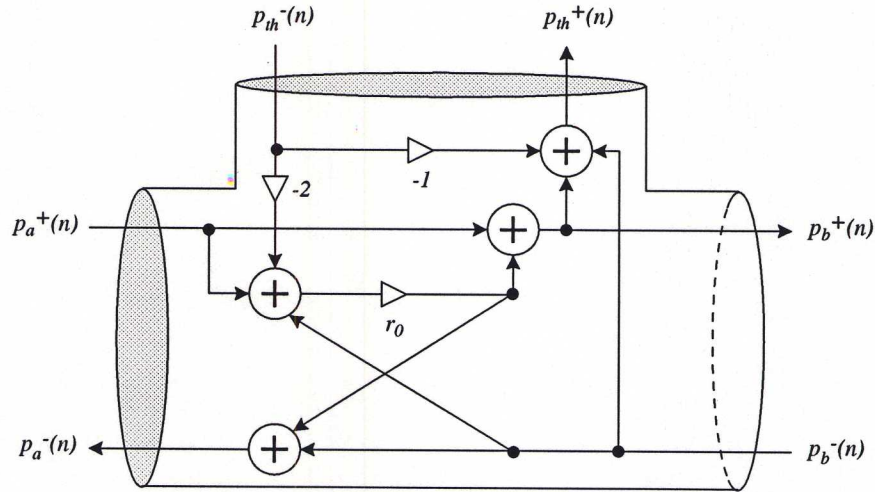


Fig. 3.48. Tonehole three-port scattering junction implementation in one-multiply form.

is given by convolution of $p_{th}^+(t)$ with the tonehole transmission function. Välimäki *et al.* (1993) approximated an open tonehole in the low-frequency limit by an acoustic inertance for implementation in the context of digital waveguide systems. Unfortunately, these authors appear to have equated a frequency-dependent input impedance description of the tonehole to the real and constant characteristic impedance term Z_{0th} in the equations above. The input impedance of the open finger hole, seen from the main bore, is given in terms of an acoustic inertance as

$$Z_{th}(s) = \frac{\rho t}{S_{th}} s, \quad (3.78)$$

where ρ is the density of air, t is the effective height [Eq. (1.125)], S_{th} is the cross-sectional area of the hole, and $s = \sigma + j\Omega$ is the Laplace transform frequency variable. The tonehole reflectance is then given by

$$\mathcal{R}_{th}(s) \triangleq \frac{P_t^-(s)}{P_t^+(s)} = \frac{Z_{th}(s) - Z_{0th}}{Z_{th}(s) + Z_{0th}} = \frac{ts - c}{ts + c}, \quad (3.79)$$

where c is the speed of sound. Equation (3.79) is easily transformed to a discrete-time filter using the bilinear transform as

$$\mathcal{R}_{th}(z) = \frac{a_1 - z^{-1}}{1 - a_1 z^{-1}}, \quad (3.80)$$

where

$$a_1 = \frac{t\alpha - c}{t\alpha + c} \quad (3.81)$$

and α is the bilinear transform constant which controls frequency warping. In this case, a low-frequency discrete-time fit is achieved for $\alpha = 2f_s$. The discrete-time reflectance $\mathcal{R}_{th}(z)$ is a first-order allpass filter, which is consistent with reflection from a “masslike” impedance. This model, however, does not contain a real or resistive component which would correspond to radiation losses from the open hole. Thus, the inertance model of the tonehole is lossless and is appropriate only

for low sampling rate implementations. Figure 3.49 plots the reflection functions determined from a digital waveguide three-port tonehole model of a flute using an inertance model of the open tonehole. Closed toneholes were simply represented by the junction scattering coefficient and direct reflection.

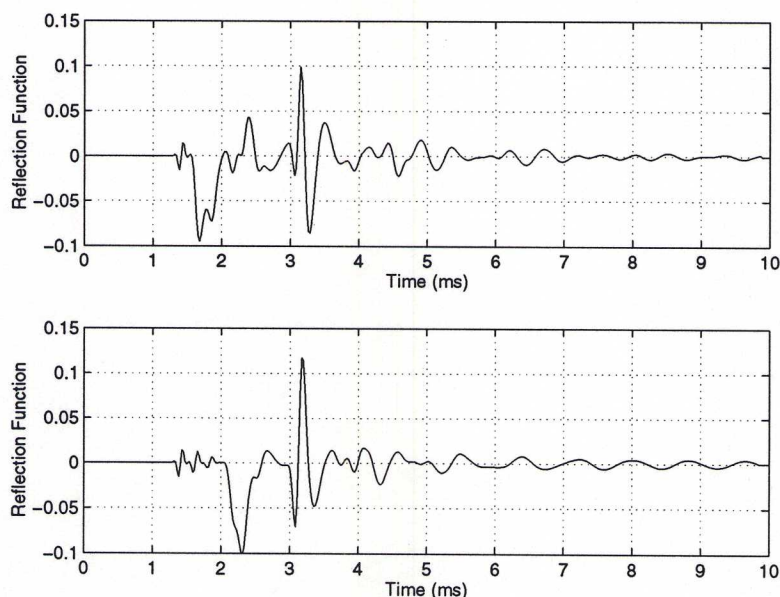


Fig. 3.49. Reflection functions for notes *B* (top) and *G* (bottom) on a six-hole flute, determined using a digital waveguide three-port tonehole junction implementation and an inertance approximation for the tonehole driving-point impedance.

A more accurate model of the open finger-hole reflectance can be determined from a continuous-time cylindrical tube model with open-end radiation, and a corresponding digital filter designed by frequency response matching techniques. The results of Keefe (1981) can be incorporated by designing this filter from the open-tonehole shunt impedance $Z_s^{(o)}$. An appropriate continuous-time reflectance filter for the tonehole branch of the junction is found using Eq. (3.7) as

$$\mathcal{R}(s) = \left[\frac{Z_s^{(o)}(s) - Z_{0th}}{Z_s^{(o)}(s) + Z_{0th}} \right], \quad (3.82)$$

where s is the Laplace transform frequency variable. Figure 3.50 plots the continuous-time magnitude response of two tonehole branch reflectances, as determined from Eq. (3.82) and by explicit calculation of the propagation and Levine and Schwinger open-end reflection characteristics. The open-tonehole shunt impedance, $Z_s^{(o)}$, is based in part on an *ideal* open-end reflectance model, as given by the $\tan(kt)$ factors in t_e . Because of this, $Z_s^{(o)}$ overestimates high-frequency reflections at the open end of the tonehole, as seen in Fig. 3.50, in comparison with the explicit waveguide model. Results from a digital waveguide implementation based on the explicit tonehole reflectance model are shown in Fig. 3.51 and are seen to closely parallel the digital waveguide loaded two-port implementation.

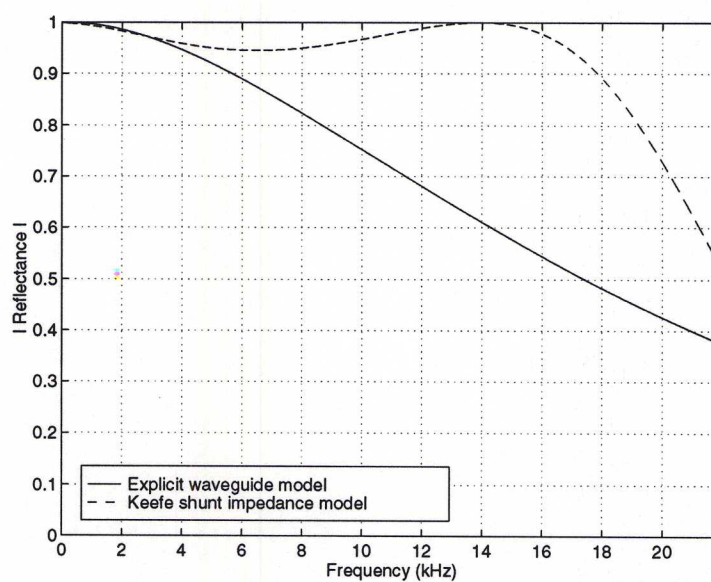


Fig. 3.50. Continuous-time magnitude responses for two open-tonehole reflectance models.

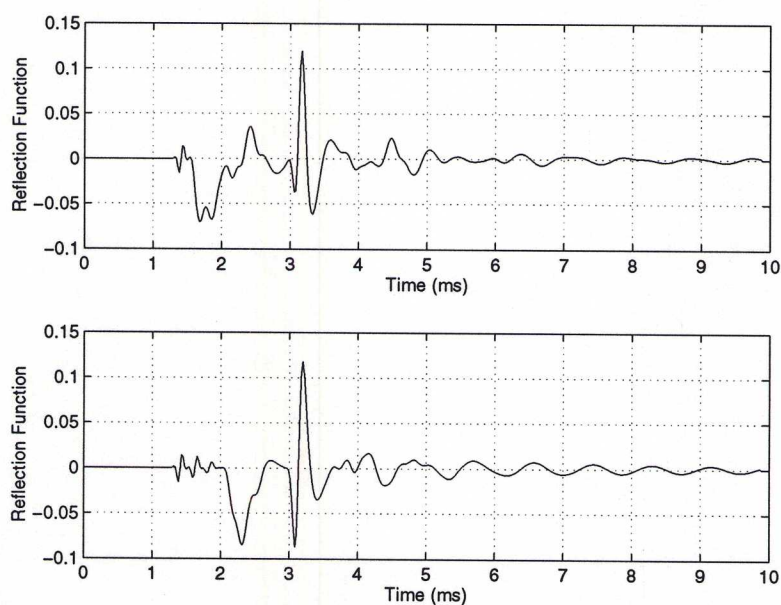


Fig. 3.51. Reflection functions for notes *B* (top) and *G* (bottom) on a six-hole flute, determined using a digital waveguide three-port tonehole junction implementation and an explicit open cylinder approximation for the tonehole driving-point impedance.

The three-port tonehole junction reflection coefficient $R_0(\Omega)$ used by Välimäki *et al.* (1993) to implement a finger hole in a digital waveguide system is given by

$$R_0(\Omega) = -\frac{Z_0}{Z_0 + 2Z_{th}(\Omega)}, \quad (3.83)$$

where $Z_{th}(\Omega)$ is the driving-point impedance of the tonehole. While $R_0(\Omega)$ was incorrectly formulated in the *three-port* context [compare with Eq. (3.73)], it is interesting to note that this expression is equivalent to the *two-port* reflectance given by Eq. (3.68) when the series impedance Z_a is neglected. It turns out that a loaded two-port junction with a driving-point load admittance Y_L is mathematically equivalent to an “unloaded” three-port junction in which one branch is characterized by a complex characteristic admittance Y_L . Thus, the tonehole implementation of Välimäki *et al.* (1993) represents a loaded two-port tonehole model without series impedances.

The digital waveguide three-port tonehole junction implementation corresponds to the Keefe model with series impedance terms neglected. In general, the series impedance terms are much less critical to the model performance than the shunt impedance. Further, the series terms have more influence on closed-hole results than those for open-holes. These impedances represent negative length corrections, to account for the dimensions of the tonehole in relation to the pipe lengths around it. In other words, when modeled by a simple shunt impedance, the tonehole theoretically exists at a dimensionless point along the bore. A low-frequency approximation to this length correction can be easily incorporated in a digital waveguide system by subtracting the length correction from the waveguide bore lengths on either side of the tonehole. Frequency-dependent length corrections can be implemented by appropriately designed allpass digital filters along the waveguide (Smith, 1996a).

A theoretical model of tonehole closure has not been developed. The open and closed models proposed by Keefe (1981) are mutually exclusive. That is, a single mathematical representation of these two states is not possible under this theory. In a digital waveguide context, it is possible to design simple digital filters for which the coefficients may be slowly varied in time to capture the basic behavior of a closing tonehole. This is particularly straight-forward when the closed-hole behavior is modeled by simple reflection without phase delay (Välimäki *et al.*, 1993). Further, it is possible to implement cross-fading techniques between the open and closed filters to simulate the real behavior. Clearly, however, a new theoretical model is needed which captures the behavior of the two states together. One such model is discussed in Section 4.1.1 in conjunction with register holes. The open hole is modeled by an inertance, in series with a time-varying resistance. As the hole is closed, the resistance increases to infinity and perfect reflection results. This effect may also be simulated by varying the acoustic mass parameter of the tonehole inertance, such that perfect reflection occurs as the mass approaches infinity.

3.5 Modeling the Nonlinear Excitation Mechanism

Musical instruments are most clearly distinguished from one another by their transient characteristics, which in turn are defined primarily by a particular method of excitation. Such wind-blown instruments as saxophones, trumpets, and flutes, for example, are discerned by their various pressure-driven excitation methods. Thus, in the computer generation of music instrument sounds, the success of a given model is most dependent on the nonlinear excitation mechanism. Unfortunately, research regarding air-driven reed mechanisms is at a relatively early stage and much is not understood about their operation.

The basic operation of the nonlinear excitation mechanism in single-reed woodwind instruments was discussed in Section 1.5. Summarizing, the reed acts as a pressure controlled valve which allows energy into the instrument for the initialization and maintenance of oscillations in the acoustic resonator. The movement of the reed controls the volume flow through the reed channel and into the mouthpiece, which is typically determined from the Bernoulli equation for steady flow. The oral

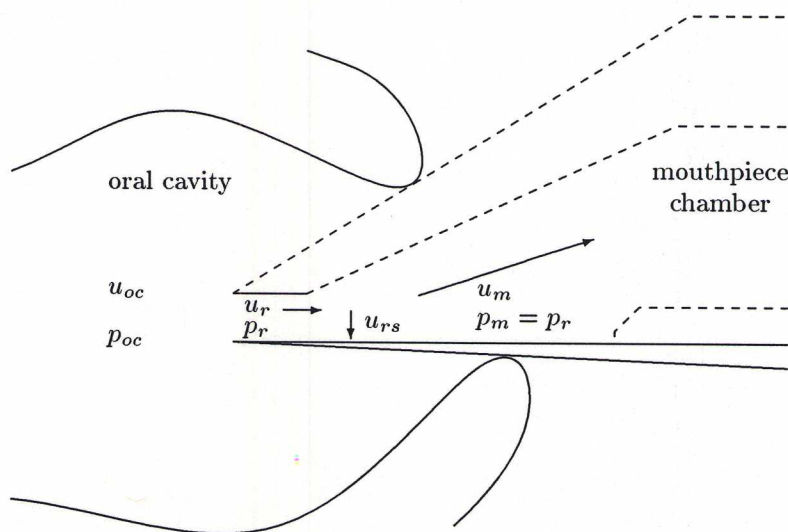


Fig. 3.52. The volume flow and pressure relationships for a single-reed oral cavity/mouthpiece geometry.

cavity is viewed as a large tank with essentially constant pressure p_{oc} and zero volume flow u_{oc} . By conservation of energy, Bernoulli's equation gives

$$u_r = w y \left(\frac{2p_{\Delta}}{\rho} \right)^{1/2} \text{sgn}(p_{\Delta}), \quad (3.84)$$

where y and w are the height and width of the reed channel, respectively, and ρ is the density of air.

Because the lowest reed resonance is typically much higher than fundamental playing frequencies in clarinets and saxophones, a single-reed system is often modeled as a memory-less nonlinearity.

This is equivalent to assuming the mass of the reed is zero or the reed resonance frequency is infinity. Assuming the force on the reed is equal to $S_r \cdot p_\Delta$, where S_r is the effective surface area of the reed exposed to p_Δ , the displacement of the reed from its equilibrium position y_0 is given by Hooke's law

$$y = y_0 - \frac{S_r \cdot p_\Delta}{k}. \quad (3.85)$$

Figure 3.53 is repeated from Section 1.5 and illustrates the nonlinear *dynamic* volume flow characteristic which results by combining this expression and Eq. (3.84) for a constant oral cavity pressure $p_{oc}/p_C = 0.4$, where p_C is the pressure necessary to push the reed against the mouthpiece facing and completely close the reed channel. The volume flow is initially zero because $p_r \leq p_{oc} - p_C$. In this range, the reed channel pressure is negative, which in conjunction with the positive oral cavity pressure, serves to pull the reed against the mouthpiece lay. As p_r increases in the range $p_{oc} > p_r > p_{oc} - p_C$, the reed channel volume flow increases rapidly, but then decreases as p_r approaches p_{oc} and a resultant $p_\Delta = 0$. When the reed channel pressure exceeds the oral cavity pressure, negative flow into the mouth occurs.

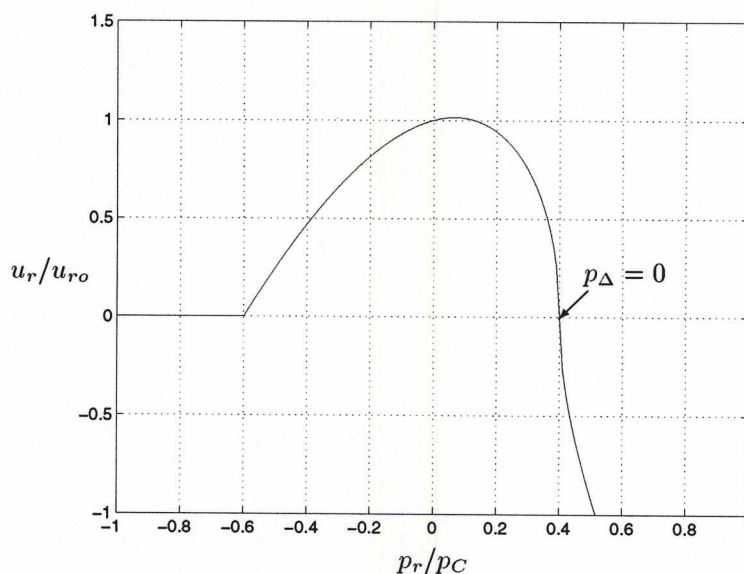


Fig. 3.53. Dynamic flow through a pressure controlled valve blown closed for $p_{oc}/p_C = 0.4$.

This section discusses three nonlinear excitation techniques for use within the context of digital waveguide modeling. The first two methods are based upon ideas originally presented by McIntyre *et al.* (1983), which were then formulated in terms of traveling-wave components for efficient implementation using digital waveguides (Smith, 1986; Cook, 1991). The final method is based on a dynamic model of the reed and directly incorporates the volume flow relationships discussed in Section 1.5.

3.5.1 The Pressure-Dependent Reflection Coefficient

McIntyre *et al.* (1983) discussed the time-domain synthesis of clarinet sounds and incorporated a nonlinear volume flow characteristic similar to that of Figure 3.53. Their procedure assumed continuity of volume velocity at the reed/bore junction and involved the simultaneous solution of a linear equation relating pressure to volume flow in the bore and a nonlinear approximation to Eq. (3.84), which related pressure to volume flow through the reed. As an efficient alternative to this process within the context of digital waveguide modeling, Smith (1986) proposed modeling the reed/bore boundary with a memory-less reflection coefficient that varies in response to the difference in oral cavity (p_{oc}) and bore pressures (p_b). In this way, the essential nonlinear behavior of the reed is attained using an extremely simple calculation, though "higher order" dynamic reed behavior is sacrificed.

The reed system is represented by a lumped acoustic impedance $Z_r(p_\Delta)$, over which the pressure p_Δ acts. In this sense, $Z_r(p_\Delta)$ roughly corresponds to the impedance represented by the reed opening, whose size varies with pressure drop p_Δ across the reed. The volume flow through the reed opening is then given by

$$u_r(p_\Delta) = \frac{p_\Delta}{Z_r(p_\Delta)}. \quad (3.86)$$

The volume flow in the bore is

$$u_b = \frac{p_b^+ - p_b^-}{Z_{0b}}, \quad (3.87)$$

where Z_{0b} is the characteristic impedance of the air column at the reed/bore intersection, p_b^+ is the outgoing pressure traveling-wave component, and p_b^- is the incoming pressure traveling-wave component from the bore. Assuming continuity of volume velocity at the reed/bore junction,

$$\frac{p_\Delta}{Z_r(p_\Delta)} = \frac{p_b^+ - p_b^-}{Z_{0b}}, \quad (3.88)$$

where

$$p_\Delta \triangleq p_{oc} - [p_b^+ + p_b^-]. \quad (3.89)$$

Equation (3.88) can be solved for the outgoing pressure traveling-wave component, with the result (Smith, 1986)

$$\begin{aligned} p_b^+ &= \left[\frac{Z_r(p_\Delta) - Z_{0b}}{Z_r(p_\Delta) + Z_{0b}} \right] p_b^- + \left[\frac{Z_{0b}}{Z_r(p_\Delta) + Z_{0b}} \right] p_{oc} \\ &= r(p_\Delta) p_b^- + \frac{1 - r(p_\Delta)}{2} p_{oc} \\ &= r(p_\Delta) \left[p_b^- - \frac{p_{oc}}{2} \right] + \frac{p_{oc}}{2}, \end{aligned} \quad (3.90)$$

where the pressure-dependent reflection coefficient is defined as

$$r(p_\Delta) \triangleq \frac{Z_r(p_\Delta) - Z_{0b}}{Z_r(p_\Delta) + Z_{0b}}. \quad (3.91)$$

A solution to Eq. (3.90) is difficult because $r(p_\Delta)$ is dependent on p_Δ , which itself is a function of p_b^+ . It is possible, however, to use the dynamic volume flow characteristic shown in Fig. 3.53 to define the behavior of $Z_r(p_\Delta)$ as

$$Z_r(p_\Delta) = \frac{p_\Delta}{u_r(p_\Delta)}, \quad (3.92)$$

which in turn defines $r(p_\Delta)$ via Eq. (3.91). Figure 3.54 plots several pressure-dependent reflection coefficient curves for various values of reed stiffness and equilibrium tip opening. These plots are

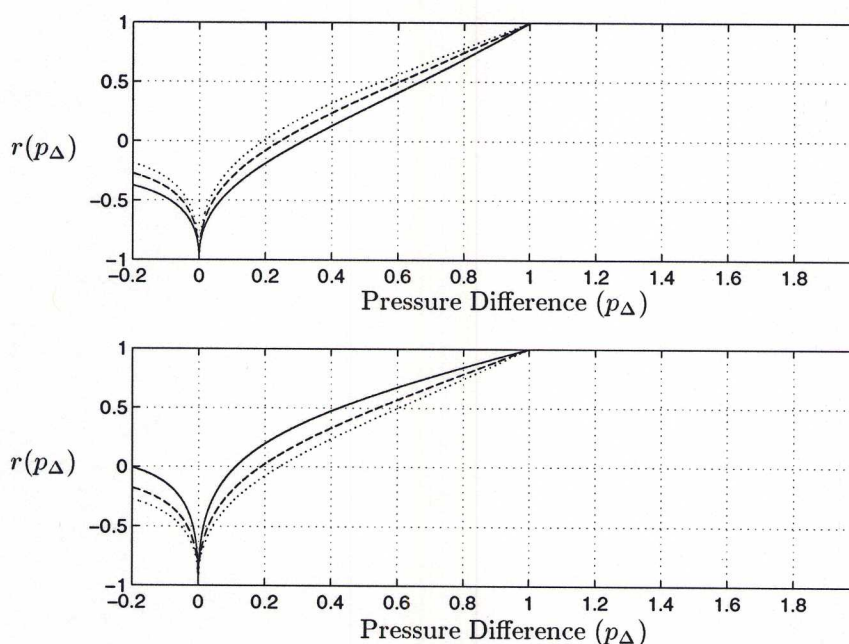


Fig. 3.54. Pressure-dependent reflection coefficient curves versus reed stiffness (top) [reed resonances of 2500 Hz (—), 3000 Hz (---), 3500 Hz (···)] and equilibrium reed tip opening (bottom) [$y_0 = 1.5$ mm (—), 1.0 mm (---), 0.5 mm (···)].

based on a normalized value of p_C , or the pressure necessary to close the reed channel. Values of p_Δ greater than one indicate beating of the reed against the mouthpiece lay and complete reflection of incoming bore pressure. For $p_\Delta = 0$, the reflection coefficient approaches negative one, corresponding to pressure traveling-wave inversion at an open-tube end. When $p_\Delta < 0$, the bore pressure is greater than the oral cavity pressure, and negative flow through the reed channel results. These reflection coefficient curves result from the assumption that reed channel pressure and mouthpiece chamber pressure are equivalent, due to kinetic energy losses in the turbulent region just beyond the reed channel (Hirschberg *et al.*, 1995, p. 314). If the reed channel and mouthpiece junction were modeled by two cylindrical sections and conservation of pressure were assumed, positive reflection coefficient values generally greater than 0.5 would result. Thus, use of the reflection coefficient curves of Fig. 3.54 requires proper modeling of the mouthpiece chamber taper in order to form an appropriate transition between the narrow reed channel and the main air column. Given this

reflection coefficient characteristic, it is only necessary to find an approximation to p_Δ . In a recursive, discrete-time calculation, it is possible to approximate $p_\Delta(n)$ by $p_\Delta(n-1)$ or to calculate $p_\Delta(n)$ using $p_b^+(n-1)$. Further, current values of either quantity could be extrapolated from previous values. For sufficiently high sampling rates and because the pressure traveling-wave components in the bore are lowpass filtered by the open-end reflectance and tonehole filters, such approximations prove reasonably accurate. In this way, the new outgoing pressure traveling-wave component (p_b^+) is determined from Eq. (3.90).

Smith (1986) proceeds with a solution to Eq. (3.90) by defining a function $G(p_\Delta) \triangleq Z_{0b} u_r(p_\Delta) = p_\Delta Z_{0b}/Z_r(p_\Delta)$, and the term $p_\Delta^+ \triangleq p_{oc}/2 - p_b^-$, so that Eq. (3.88) can be written

$$G(p_\Delta) = 2p_\Delta^+ - p_\Delta. \quad (3.93)$$

By plotting $G(p_\Delta)$ and $2p_\Delta^+ - p_\Delta$ on the same graph and finding their point of intersection $G(p_\Delta^*)$, the outgoing pressure traveling-wave component is found as $p_b^+ = p_{oc} - p_b^- - p_\Delta^*$.

For efficient synthesis in the digital waveguide context, Smith (1986) implements a table lookup technique containing

$$\hat{r}(p_\Delta^+) = r(p_\Delta^*(p_\Delta^+)), \quad (3.94)$$

such that the outgoing pressure traveling-wave component is found from Eq. (3.90) as

$$p_b^+ = -\hat{r}(p_\Delta^+)p_\Delta^+ + \frac{p_{oc}}{2}. \quad (3.95)$$

A digital waveguide implementation of this expression is shown in Fig. 3.57a. Because an appropriate table of $\hat{r}(p_\Delta^+)$ values can require a significant amount of memory, it is sometimes desirable to express the reflection coefficient in terms of a simple mathematical expression. Realistic woodwind sounds have been generated using (Smith, 1986)

$$\hat{r}(p_\Delta^+) = \begin{cases} 1 + m(p_\Delta^+ - p_C), & p_\Delta^+ < p_C \\ 1, & p_\Delta^+ \geq p_C \end{cases} \quad (3.96)$$

Figure 3.55 displays a sample reflection coefficient table that has been used in synthesizing clarinet sounds, together with the corresponding reed volume flow $\hat{u}_r(p_\Delta^+)$, as determined from Eqs. (3.86) and (3.91). This particular table is based on normalized oral cavity pressure. The pressure necessary to close the reed channel (p_C) is equal to one. Values of p_Δ^+ greater than one indicate beating of the reed against the mouthpiece lay and complete reflection of incoming bore pressure. Corresponding reed volume flow is equal to zero for values of $p_\Delta^+ \geq p_C$. Values of differential pressure less than one correspond to partial reflection of p_b^- at the junction and partial transmission of p_{oc} into the bore. When $p_\Delta^+ < 0$, the bore pressure is greater than the oral cavity pressure, and negative flow through the reed channel results. For this particular table, the desired “negative resistance” region of operation occurs for $0.5 < p_\Delta^+ \leq 1$.

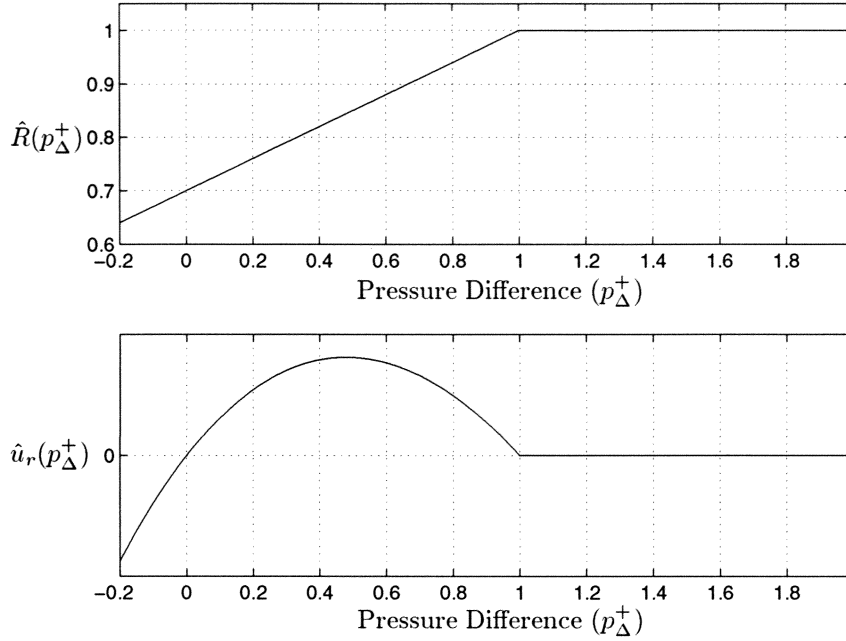


Fig. 3.55. An example reflection coefficient table $\hat{r}(p_{\Delta}^+)$ (top), and the corresponding reed volume flow $\hat{u}_r(p_{\Delta}^+)$ (bottom).

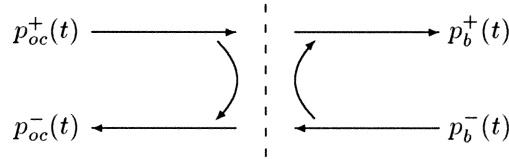


Fig. 3.56. The reed/bore scattering junction.

3.5.2 The Reed-Reflection Polynomial

Another approach to the implementation of a nonlinear excitation mechanism in the context of digital waveguide modeling of wind instruments is referred to as the reed-reflection polynomial (Cook, 1992). This technique is similar in concept to the pressure-dependent reflection coefficient, in that the reed/bore is modeled by a pressure-dependent scattering junction, though in this case the junction reflection and transmission properties are assumed to depend on $p_{oc}^+ - p_b^-$, rather than the more physical p_{Δ} defined in Eq. (3.89). The polynomial model is derived by considering the reed/bore junction as shown in Fig. 3.56. Because the volume flow through the reed is small, the reed/bore junction represents a large impedance. When the reed is closed, perfect non-inverting pressure reflections occur on both sides of the junction, so that $p_{oc}^+ - p_b^- = p_{oc}/2 - p_b^- = p_{\Delta}^+$, as defined in the previous section. Continuing with this crude approximation, the portion of p_b^- reflected back into the bore is given by $p_b^- \cdot r(p_{\Delta}^+)$, while the portion of the oral cavity pressure which

is transmitted into the bore is given by $p_{oc}^+ [1 - r(p_\Delta^+)]$. Then p_b^+ is given by

$$p_b^+ = p_{oc}^+ - [p_{oc}^+ - p_b^-] r(p_\Delta^+). \quad (3.97)$$

Approximating $r(p_\Delta^+)$ by a second order polynomial function, Eq. (3.97) simplifies to

$$p_b^+ \approx p_{oc}^+ - [c_1(p_{oc}^+ - p_b^-) + c_2(p_{oc}^+ - p_b^-)^2 + c_3(p_{oc}^+ - p_b^-)^3]. \quad (3.98)$$

A digital waveguide implementation of this expression is shown in Fig. 3.57b.

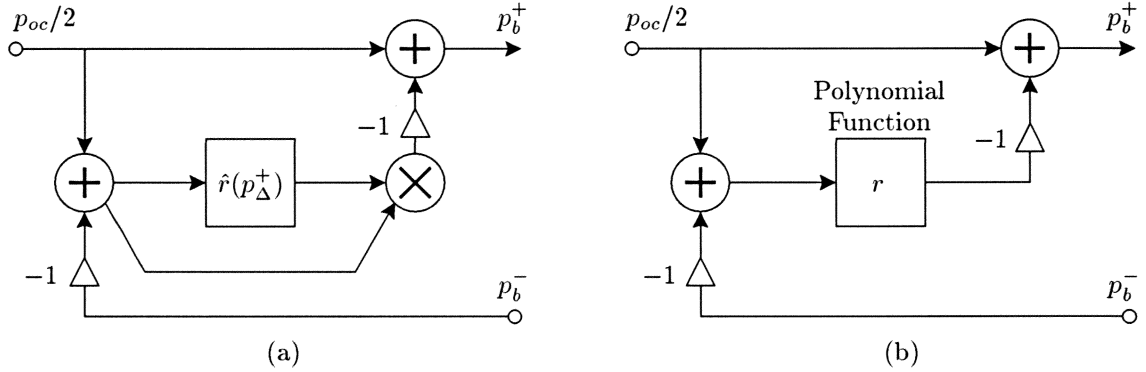


Fig. 3.57. (a) The pressure-dependent reflection coefficient digital waveguide implementation; (b) The reed-reflection polynomial digital waveguide implementation.

This reed implementation method has proven efficient and effective for real-time DSP synthesis (Cook, 1992; Scavone, 1995). Unfortunately, the process of determining appropriate polynomial coefficients is rather arbitrary. It is possible, however, to relate the polynomial coefficients to a polynomial approximation of the pressure-dependent reflection coefficient through a matrix transformation (Cook, 1991).

3.5.3 The Dynamic Woodwind Reed Model

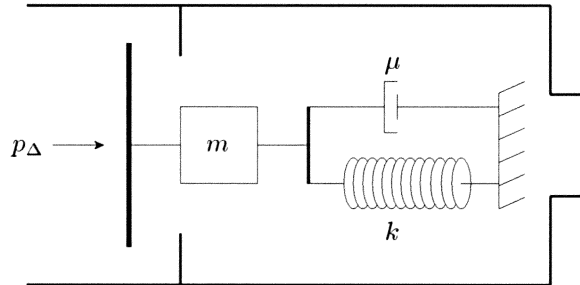


Fig. 3.58. The single-reed as a mechanical oscillator blown closed.

In contrast to the reed models previously discussed, all of which ignored the mass of the reed, the dynamic reed model seeks to accurately model the motion of the reed and its beating against the

mouthpiece lay. In functioning as a pressure controlled valve, the position of the reed at any instant governs the volume flow that is injected at the reed/bore junction. The reed is represented by a linear mass-spring-damper system which is acted upon by the difference in oral cavity and bore pressures, as shown in Fig. 3.58. The relationship between applied force and the resulting reed displacement, and the corresponding Laplace transform are given by

$$m \frac{d^2 y}{dt^2} + \mu \frac{dy}{dt} + ky = f_r(t) \iff [ms^2 + \mu s + k] Y(s) = F_r(s), \quad (3.99)$$

where the reed equilibrium position is redefined from Section 1.5 as $y = 0$ and displacement toward the mouthpiece facing is positive. Both the oral-cavity and the bore pressures act upon the reed, so that the resultant force on the reed is

$$F_r(s) = S_r \cdot P_\Delta(s) = S_r \cdot [P_{oc}(s) - P_b(s)], \quad (3.100)$$

where S_r is the effective surface area of the reed exposed to P_Δ . The surface area S_r is typically bounded by the width of the reed at its tip and the distance from the reed tip to the player's lower lip.

The transfer function that relates reed displacement to applied force is found from Eq. (3.99) as

$$\begin{aligned} \frac{Y(s)}{F_r(s)} &\triangleq H_r(s) = \frac{1}{ms^2 + \mu s + k} \\ &= \frac{1/m}{s^2 + (\mu/m)s + \omega_0^2} \end{aligned} \quad (3.101)$$

where $\omega_0^2 = k/m$ is the natural frequency of the mass-spring system in the absence of damping. Using the bilinear transform to convert from continuous to discrete time, the digital transfer function results

$$\begin{aligned} H_r(z) &= \frac{(1 + 2z^{-1} + z^{-2})}{(k + \alpha^2 m + \alpha\mu) + 2(k - \alpha^2 m)z^{-1} + (k + \alpha^2 m - \alpha\mu)z^{-2}}, \\ &= \frac{(1 + 2z^{-1} + z^{-2})}{(m\omega_0^2 + \alpha^2 m + \alpha\mu) + 2m(\omega_0^2 - \alpha^2)z^{-1} + (m\omega_0^2 + \alpha^2 m - \alpha\mu)z^{-2}}, \end{aligned} \quad (3.102)$$

where α is the bilinear transform constant used to control frequency warping. The bilinear transform performs a nonlinear warping of the continuous-time frequency axis to the discrete-time frequency space. The constant α can be set to match any particular finite continuous-time frequency to a specific location on the z -plane unit circle as

$$\alpha = \frac{\Omega}{\tan(\omega/2)}. \quad (3.103)$$

In this case, α should be determined using the reed resonance frequency. The displacement found by passing $S_r \cdot p_\Delta(n)$ through this biquad section is subtracted from the equilibrium tip opening (y_0) to produce the aperture spacing. Inelastic beating of the reed is assumed, such that the reed is forced against the lay and held there until the driving force decreases below $k \cdot y_0$, the force necessary to

hold the spring stretched by y_0 . Hirschman (1991) implemented a variable elastic beating model within the reflection coefficient scheme. The reed filter $H_r(z)$ must be reset with the appropriate initial conditions each time this occurs. Figure 3.59 represents a transposed direct form II biquad filter structure that could be used to implement the reed filter. The appropriate internal state values to be used when the reed first begins to separate from the lay can be determined by inspection of the filter structure, given that the previous filter inputs and outputs are assumed to be $k \cdot y_0$ and y_0 , respectively. In this case, the initializing values for the filter's internal states should equal

$$s_1 = k \cdot y_0 (b_1 + b_2) + y_0 (a_1 + a_2) = y_0 (1 - k b_0) \quad (3.104a)$$

$$s_2 = k \cdot y_0 \cdot b_2 + y_0 \cdot a_2 = y_0 (k b_2 + a_2). \quad (3.104b)$$

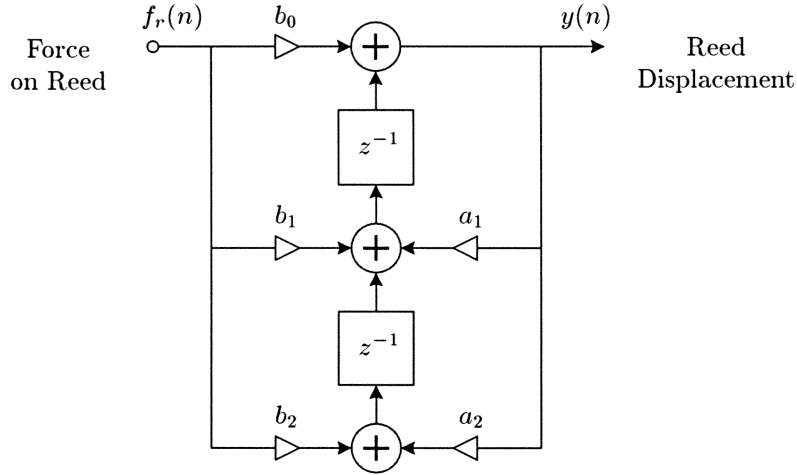


Fig. 3.59. Second-order reed filter $H_r(z)$.

As discussed in Section 1.5, the Bernoulli flow equation provides a reasonable approximation to the volume flow through the reed channel of a single-reed woodwind instrument. By conservation of energy and assuming an oral cavity volume flow of zero,

$$\begin{aligned} u_r(t) &= w [y_0 - y(t)] \cdot v(t) \\ &= w [y_0 - y(t)] \cdot \left[\frac{2p_\Delta(t)}{\rho} \right]^{\frac{1}{2}} \end{aligned} \quad (3.105)$$

where w is the width of the reed channel, $y(t)$ is the time-varying height of the reed aperture, and ρ is the density of air.

The flow through the reed channel is assumed to separate from the wall and form a free jet into the mouthpiece, as noted by Hirschberg *et al.* (1994, 1995) and discussed in Section 1.5. The free jet is inherently unstable and breaks down into vortical structures which are eventually dissipated by turbulence. In the turbulent region, viscous dissipation of kinetic energy is dominant, so that

pressure recovery is not expected in the mouthpiece region beyond the reed channel. Instead, the mouthpiece pressure is assumed equal to the reed channel pressure and conservation of volume flow to hold in the mouthpiece chamber. For dynamic regimes of flow, u_r leaving the reed channel is divided into two parts, u_{rs} and u_m , as shown in Fig. 3.52. The flow u_m enters the mouthpiece chamber, while the motion of the reed surface results in a flow $u_{rs} = S_r(dy/dt)$. The reed surface flow component u_{rs} is easily implemented in discrete time by a digital differentiator. Using a “leaky” differentiator, the appropriate filter is given by

$$\frac{U_{rs}(z)}{Y(z)} = S_r \frac{1 - z^{-1}}{1 + g z^{-1}}, \quad (3.106)$$

where $g \approx 0.999$. Subtracting the output of this filter from the reed channel flow, the volume flow at the mouthpiece/bore junction is

$$u_m(t) = u_r(t) - u_{rs}(t) = u_b(t) = u_b^+(t) + u_b^-(t) = \frac{p_b^+(t) - p_b^-(t)}{Z_{0b}}, \quad (3.107)$$

where $Z_{0b} = \rho c/S_b$ is the constant acoustic characteristic impedance of a cylindrical bore of cross-sectional area S_b . $p_b^+(t)$ represents the traveling-wave component of pressure entering the bore from the reed channel while $p_b^-(t)$ represents the traveling-wave component of pressure entering the reed/bore junction from the bore. Solving for $p_b^+(t)$ and substituting from Eq. (3.105),

$$\begin{aligned} p_b^+(t) &= Z_{0b} \cdot [u_r(t) - u_{rs}(t)] + p_b^-(t) \\ &= w[y_0 - y(t)] \cdot Z_{0b} \cdot \left[\frac{2p_\Delta(t)}{\rho} \right]^{\frac{1}{2}} - Z_{0b} \cdot u_{rs}(t) + p_b^-(t), \end{aligned} \quad (3.108)$$

where $u_{rs}(t)$ is determined as the output of the differentiator of Eq. (3.106). This calculation can be simplified for real-time DSP implementation by the use of a look-up table. In order to implement Eq. (3.108) in discrete time, it is necessary to use an approximation to $p_\Delta(n)$ because of its dependence on $p_b^+(n)$. Given sufficiently high sampling rates and the fact that the bore oscillations are lowpass filtered by the open-end reflectance and tonehole filters, a reasonable approximation that has produced acceptable results when implemented is $p_\Delta(n) = p_{oc}(n) - [p_b^+(n-1) + p_b^-(n-1)]$.

Figure 3.60 plots the onset of oscillations in a simple digital waveguide clarinet using the various excitation models discussed in this section. The air column is modeled as a pure cylinder without toneholes and incorporates a discrete-time Levine and Schwinger open-end reflection implementation. In comparison to the first two excitation methods, the dynamic reed model takes longer to reach its steady-state oscillatory regime. This model also exhibits undesirable initial transient behavior when the oral cavity pressure is first applied. This behavior can be attributed to the lack of “back pressure” in the bore during initial “blowing” conditions. The model of Eq. (3.108) is based on *steady-state* air column and flow relationships. For an initial pressure disturbance, the air column appears anechoic and the input impedance at zero frequency is given by the bore wave impedance, instead of its small steady-state value. As a result, the dynamic reed model is plagued by an unphysical gain factor

when the excitation is first initiated. This excitation model also requires the use of an appropriately designed mouthpiece chamber taper, to provide proper scaling of pressure between the turbulent region just beyond the reed channel and the main bore, as discussed in conjunction with Fig. 3.54.

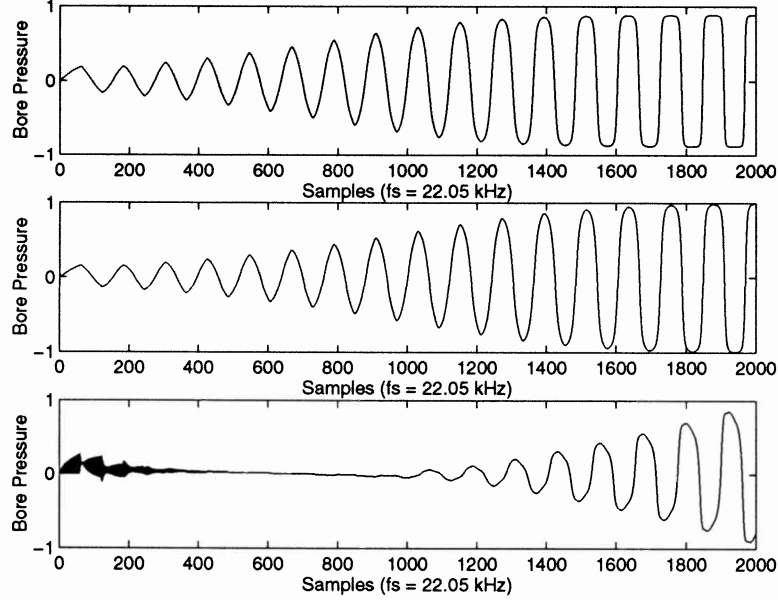


Fig. 3.60. Oscillation onsets for digital waveguide clarinet implementations: (top) Pressure-dependent reflection coefficient; (middle) Reed-reflection polynomial; (bottom) Dynamic reed model.

3.5.4 Excitation Mechanisms Attached to Truncated Cones

All of the nonlinear excitation techniques discussed thus far have assumed the input bore section to be of cylindrical shape. If the excitation mechanism is attached to a truncated conical section, then the bore characteristic impedance at the input is complex, rather than purely real and constant. Considering the derivation of the dynamic woodwind reed model, Eq. (3.107) is then rewritten in the frequency domain using the Laplace frequency variable $s = \sigma + j\Omega$ as

$$U_m(s) = U_r(s) - U_{rs}(s) = U_b(x, s) = U_b^+(x, s) + U_b^-(x, s) = \frac{P_b^+(x, s)}{Z_{0b}(x, s)} - \frac{P_b^-(x, s)}{Z_{0b}^*(x, s)} \quad (3.109)$$

where

$$Z_{0b}(x, s) = \frac{\rho c}{S_b(x)} \left(\frac{x s}{c + x s} \right) \quad (3.110)$$

is the complex characteristic impedance of a conical bore at a distance x from its imaginary apex, c is the speed of sound in air, and $S_b(x) = 2\pi x^2(1 - \cos \theta)$ is the surface area of a spherical wave front at position x in a cone of half-angle θ . Solving for $P_b^+(x, s)$,

$$P_b^+(x, s) = Z_{0b}(x, s) \cdot [U_r(s) - U_{rs}(s)] + \frac{Z_{0b}(x, s)}{Z_{0b}^*(x, s)} P_b^-(x, s)$$

$$= \frac{\rho c}{S_b(x)} \left(\frac{x s}{c + x s} \right) \cdot [U_r(s) - U_{rs}(s)] + \left(\frac{x s - c}{x s + c} \right) P_b^-(x, s). \quad (3.111)$$

This continuous-time expression is easily transformed to discrete time using the bilinear transform as

$$P_b^+(x, z) = \frac{\rho c}{S(x)} \left(\frac{\alpha x}{c + \alpha x} \right) \frac{1 - z^{-1}}{1 + a_1 z^{-1}} \cdot [U_r(z) - U_{rs}(z)] + \left(\frac{-a_1 - z^{-1}}{1 + a_1 z^{-1}} \right) P_b^-(x, z), \quad (3.112)$$

where α is the bilinear transform constant and

$$a_1 = \frac{c - \alpha x}{c + \alpha x}.$$

For both filters, a good fit at low frequencies can be attained by setting the bilinear constant $\alpha = 2f_s$, where f_s is the discrete-time sampling rate. Thus, the conical bore excitation mechanism requires an additional two first-order filtering operations. The filter multiplying $P_b^-(x, z)$ is the first-order allpass filter previously derived in conjunction with conical bore truncation and results from the “masslike” load at the cone truncation point. Since $|a_1| < 1 \forall c > 0, \alpha > 0$, and $x > 0$, the filters are always stable.

Chapter 4

Digital Waveguide Model Extensions and Calibration

The first part of the chapter offers a few extensions to conventional digital waveguide models that are inspired in part by the analysis of Chapter 2. In particular, the digital waveguide tonehole implementations presented in Section 3.4.3 offer an effective and efficient means for modeling woodwind register holes. Issues regarding placement and proportions of register vents are discussed, as well as a means for simulating the closing of the hole (which can also be applied to toneholes). The discussion in Section 2.3.1 regarding single-reed woodwind mouthpieces, together with the lumped-section modeling technique presented in Section 3.3.3, offer a means for modeling specific mouthpiece designs in the context of digital waveguide systems.

The use of physical models, as implemented using digital waveguide techniques, in new computer-music compositions and performances is becoming increasingly common. With this interest, new demands are being made for increased model flexibility. A recent paper (Scavone, 1996) that addresses some of these demands is included in the middle of this chapter. Several of the contemporary performance techniques briefly discussed in Section 2.5 are implemented in real-time digital waveguide models. Issues regarding the control of such expression using electronic musical controllers are then discussed.

The last part of this chapter is concerned with the calibration of digital waveguide models based on acoustical measurements. In general, most of the acoustic theory presented in Chapter 1 has been experimentally validated by frequency-domain measurement techniques. While it has been shown throughout this study that frequency-domain characterizations are easily incorporated into digital waveguide models, it is interesting to compare the time-domain responses of musical instruments to the results of time-domain simulations. The measurement of instrument air-column time-domain behavior has been gaining interest in recent years (Agulló *et al.*, 1995; Keefe, 1996). A study

previously conducted to investigate both linear and nonlinear instrument responses (Scavone and Cook, 1994) is reviewed at the end of this chapter.

4.1 Extensions to Digital Waveguide Models of Woodwinds

Chapter 3 presented digital waveguide modeling techniques for the most essential components of woodwind instruments. Virtual instruments implemented in that way produce convincing results and display a variety of behavior characteristic of their “real-world” counterparts. Several subtle refinements to these models are offered in this section. In particular, the implementation of register holes should provide more realistic behavior based on second air-column resonances. The choice of mouthpiece design, which is of such importance to real instrument performers, offers a means for shaping the overall timbre of the waveguide instrument.

4.1.1 Register Holes

Woodwind register holes were briefly discussed in Section 2.2.3. These holes are designed to function both as an acoustic inertance and an acoustic resistance. Proper register hole proportions to achieve this behavior are indicated in Section 2.2.3, as determined by Benade (1976). They are ideally placed about one-third of the distance from the excitation mechanism of a cylindrical-bored instrument to its first open hole and approximately one-half the distance from the imaginary apex of a conical-bored instrument to its first open hole. Sound radiation from a register hole is negligible.

Virtual instruments offer the ability to implement ideally positioned register holes for all second register notes, thus avoiding the necessary compromises made by woodwind instrument designers when deciding on the number and position of octave vents. The digital waveguide register hole is implemented by means of either a two-port or three-port scattering junction, as discussed with regard to toneholes in Section 3.4.3. For real-time implementations, it may be too computationally expensive to continually modify the air-column delay-line lengths on *both* sides of the junction, so that fixed junction locations may need to be specified, as on real instruments. Assuming that the stability of the second register note is not excessively affected by a slightly misplaced register hole junction, intonation problems can be compensated for by appropriate delay-line length adjustments for each particular note.

The open register hole is best modeled as a simple inertance in series with an acoustic resistance. In this case, the input impedance of the register hole, seen from the main bore, is given by

$$Z_{rh}^{(o)}(s) = \frac{\rho t}{S_{rh}} s + \xi, \quad (4.1)$$

where ρ is the density of air, t is the effective height [Eq. (1.125)], S_{rh} is the cross-sectional area of the hole, ξ is the acoustic resistance, and $s = \sigma + j\Omega$ is the Laplace transform frequency variable. The series impedance terms associated with toneholes are insignificant for register holes and can be

neglected. Thus, the register hole is represented in transmission-matrix form by

$$\begin{bmatrix} P_1 \\ U_1 \end{bmatrix} = \begin{bmatrix} 1 & 0 \\ Z_s^{-1} & 1 \end{bmatrix} \begin{bmatrix} P_2 \\ U_2 \end{bmatrix}, \quad (4.2)$$

where the shunt impedance is given by the input impedance of the open register hole, $Z_{rh}^{(o)}$. In waveguide coordinates, this expression is written

$$\begin{aligned} \begin{bmatrix} P_1^- \\ P_2^+ \end{bmatrix} &= \begin{bmatrix} \mathcal{R}^- & \mathcal{T}^- \\ \mathcal{T}^+ & \mathcal{R}^+ \end{bmatrix} \begin{bmatrix} P_1^+ \\ P_2^- \end{bmatrix} \\ &= \frac{1}{Z_0 + 2Z_s} \begin{bmatrix} -Z_0 & 2Z_s \\ 2Z_s & -Z_0 \end{bmatrix} \begin{bmatrix} P_1^+ \\ P_2^- \end{bmatrix}. \end{aligned} \quad (4.3)$$

The reflectances and transmittances are equivalent at this junction for wave components traveling to the right or to the left. As $\mathcal{T} = 1 + \mathcal{R}$, a one-filter form of the junction is possible, as diagrammed in Fig. 3.19b. An appropriate discrete-time filter implementation for \mathcal{R} can be obtained using the bilinear transform substitution, with the result

$$\mathcal{R}^-(z) = \mathcal{R}^+(z) = \frac{c(1 + z^{-1})}{(\zeta + \alpha\psi) + (\zeta - \alpha\psi)z^{-1}}, \quad (4.4)$$

where

$$\zeta = c + 2S_b\xi/\rho \quad \text{and} \quad \psi = 2S_bt/S_{rh}, \quad (4.5)$$

S_b is the cross-sectional area of the main air column, and α is the bilinear transform constant which controls frequency warping. In this case, a low-frequency discrete-time fit is achieved for $\alpha = 2f_s$.

The register hole can also be implemented in the form of a three-port scattering junction. The appropriate register-hole branch reflectance is then given by

$$\mathcal{R}_{rh}(s) \triangleq \frac{P_t^-(s)}{P_t^+(s)} = \frac{Z_{rh}^{(o)}(s) - Z_{0rh}}{Z_{rh}^{(o)}(s) + Z_{0rh}} = \frac{ts + \xi S_{rh}/\rho - c}{ts + \xi S_{rh}/\rho + c}, \quad (4.6)$$

where c is the speed of sound. Equation (4.6) can be transformed to a discrete-time filter using the bilinear transform as

$$\mathcal{R}_{rh}(z) = \frac{(t\alpha + \gamma - c) - (t\alpha - \gamma + c)z^{-1}}{(t\alpha + \gamma + c) - (t\alpha - \gamma - c)z^{-1}}, \quad (4.7)$$

where

$$\gamma = \frac{\xi S_{rh}}{\rho} \quad (4.8)$$

and α is given as above for a good low-frequency fit. The discrete-time reflectance $\mathcal{R}_{rh}(z)$ is a first-order digital allpass filter when $\xi = 0$, or when the register hole is characterized as an inertance only. For positive values of ξ , however, $\mathcal{R}_{rh}(z)$ takes on a highpass character. The three-port junction register-hole implementation requires a one-multiply scattering junction and one filtering operation for the register-hole branch. The two-port junction implementation requires a single filtering operation, and thus is more efficient.

It is interesting to note that the resistive term ξ in $Z_{rh}^{(o)}$ can be taken to infinity to simulate the closing of the hole. In this case, the two-port reflectance smoothly goes to zero. In the limit as $\xi \rightarrow \infty$, the two-port reflectance digital filter pole approaches negative one. However, the filter gain is sufficiently reduced for a pole location just inside the unit circle to allow acceptable simulation of a closed-hole state. Alternately, the filter pole position can be left constant and the filter gain smoothly ramped to zero to simulate the closing of the hole. This technique avoids transients which result when a filter pole is varied over time. The three-port register-hole branch reflectance suffers the same pole instability in the limit as $\xi \rightarrow \infty$, and is more difficult to use for simulation of the closing hole. Hole closure can also be simulated by increasing the acoustic mass of the register hole inertance. In this case, both the two-port and three-port reflectance filter poles approach positive one. Ramping the two-port filter gain to zero, as mentioned above, simulates this effect as well. These techniques are also applicable to toneholes.

4.1.2 Mouthpiece Models

Issues regarding single-reed woodwind instrument mouthpieces were discussed in Section 2.3.1. It was seen there that mouthpiece geometry variations can have significant influence on the timbre and intonation of a musical instrument. It is possible to model a mouthpiece in the digital waveguide domain by approximating it with cylindrical and conical sections, in a manner similar to that of Section 2.3.1. A saxophone mouthpiece of narrow chamber design is approximated in this way in Fig. 4.1. Such an approximation using digital waveguide techniques requires the implementation of

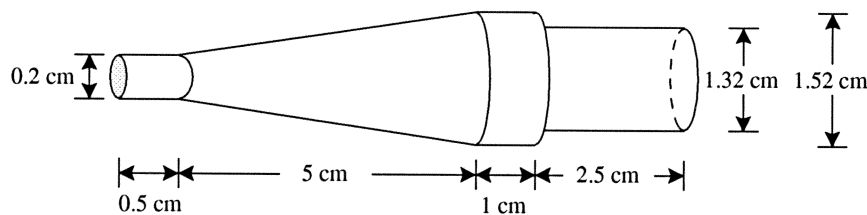


Fig. 4.1. A cylindrical and conical section approximation to a narrow chamber saxophone mouthpiece structure.

a scattering junction for each section junction. Further, at least one unstable scattering junction invariably occurs from this approximation, as would result at the conical-cylindrical section junction in Fig. 4.1. These problems can be avoided by incorporating the “lumped section” technique discussed in Section 3.3.3. In this way, part or all of mouthpiece structure is modeled by a single lumped-section scattering junction, as illustrated in Fig. 4.2. A scattering junction scale factor α can be “pulled out” of the transmittance terms and is given by the ratio of input to output wave front surface areas of the lumped section. It is associated with the transformer component of conical waveguides or similarly, the spreading of pressure across an expanding wave front surface area. In comparison to

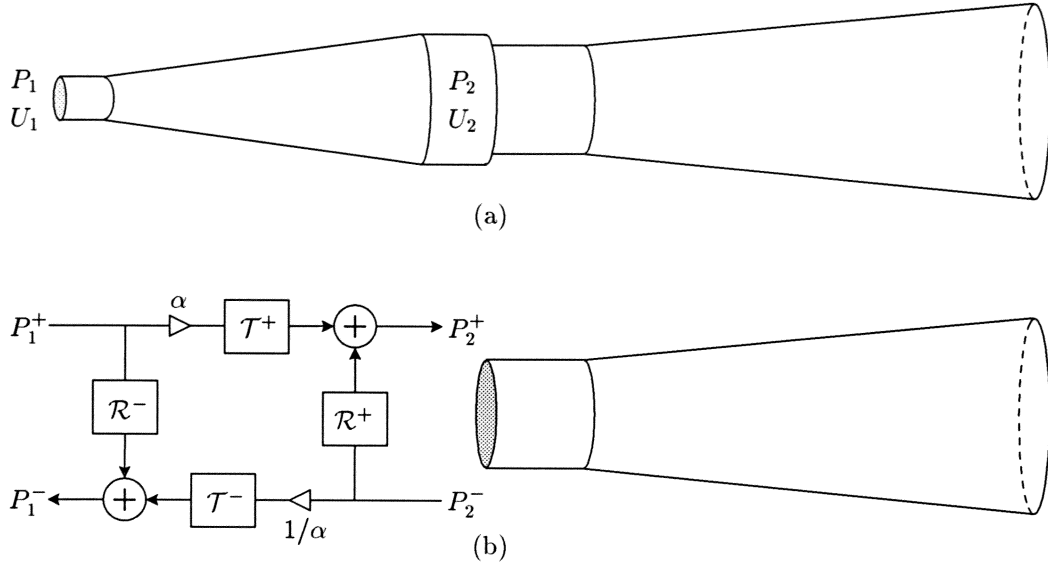


Fig. 4.2. (a) A saxophone mouthpiece and air column profile approximated by cylindrical and conical sections and (b) a lumped-section model which allows a stable digital waveguide filter implementation.

the mouthpiece profiles of Fig. 2.16, a short cylindrical section has been added at the input of the mouthpiece model to allow a stable lumped filter approximation. As was discussed regarding this technique in Section 3.3.3, stable lumped-section scattering filters can only be achieved when the taper rate of the right-most section is greater than that of the left-most section. Without the short cylindrical section, this condition is not met. Given the approximations already inherent in the sectioned-mouthpiece profile, the addition of this section is considered to have negligible influence on the overall behavior of the lumped model. Further, the various dimensions of the model can be modified in order to “fine-tune” the complete instrument intonation.

As discussed in Section 3.3.3, the lumped-section approach begins in the frequency domain. The appropriate transmission matrices which correspond to the individual sections are cascaded to produce a single, lumped transmission matrix characterization. These parameters are then transformed to waveguide coordinates via the substitutions documented throughout this study. It is particularly important that the wave impedance for spherical traveling-wave components be conjugated for propagation toward the cone apex. When the input and/or output of the lumped section is given by a cylindrical segment, the relationships of Eqs. (3.53a)–(3.53d) can be simplified, in that Z_0 and Z_0^* are equivalent for cylindrical pipes.

The scattering junction reflectance and transmittance frequency responses that result from these calculations can potentially be very difficult to approximate with discrete-time filters. The complexity of these filters grows with the number of sections and the inherent delay in the lumped structure. It is best then to lump as few sections as necessary to eliminate the unstable junction. In the case of the structure of Fig. 4.1, the three left-most sections can be lumped to obtain a stable

implementation and the remaining sections modeled individually using standard digital waveguide techniques. In this case, both the input and output sections are cylindrical, so that the expressions of Eqs. (3.53a)–(3.53d) reduce to

$$\mathcal{R}^- = \frac{B - DZ_{01} + AZ_{02} - CZ_{01}Z_{02}}{B + DZ_{01} + AZ_{02} + CZ_{01}Z_{02}} \quad (4.9a)$$

$$\mathcal{T}^- = \frac{Z_{01}(2AD - 2BC)}{B + DZ_{01} + AZ_{02} + CZ_{01}Z_{02}} \quad (4.9b)$$

$$\mathcal{T}^+ = \frac{2Z_{02}}{B + DZ_{01} + AZ_{02} + CZ_{01}Z_{02}} \quad (4.9c)$$

$$\mathcal{R}^+ = \frac{B + DZ_{01} - AZ_{02} - CZ_{01}Z_{02}}{B + DZ_{01} + AZ_{02} + CZ_{01}Z_{02}}. \quad (4.9d)$$

The lumped-section forward reflectance \mathcal{R}^+ frequency response and a 13th-order discrete-time approximation are shown in Fig. 4.3. The pole and zero locations in the z -plane for $\mathcal{R}^+(z)$ are shown in Fig. 4.4. In order to obtain good discrete-time approximations, it is generally necessary to “pull out” the inherent phase delay of the structure and implement it using delay lines in series with the filter, as illustrated in Fig. 3.28. For this particular case, phase delay was extracted from the reflectance responses, as well as the transmittances. The transmittance characteristics are well approximated by an 11th-order IIR filter, but are not shown here. The theoretical impulse response for the

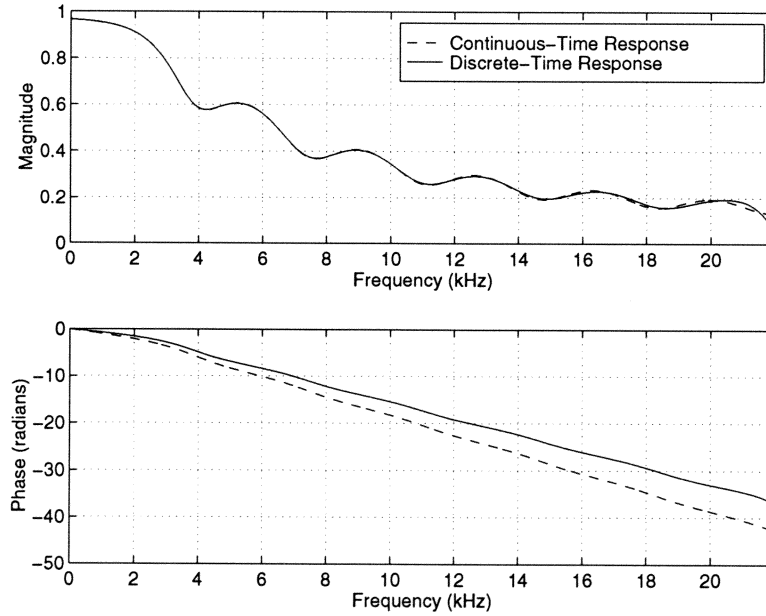


Fig. 4.3. Continuous- and discrete-time frequency responses for the forward reflectance \mathcal{R}^+ determined by lumping the three left-most sections of the mouthpiece shape of Fig. 4.1.

complete structure of Fig. 4.2 is shown in Fig. 4.5, as determined using transmission matrices and a lumped-section digital waveguide implementation. The right-most conical bore section was modeled for a length of 0.3 meters and an open-end radius of 0.018 meters. All section lengths, aside from

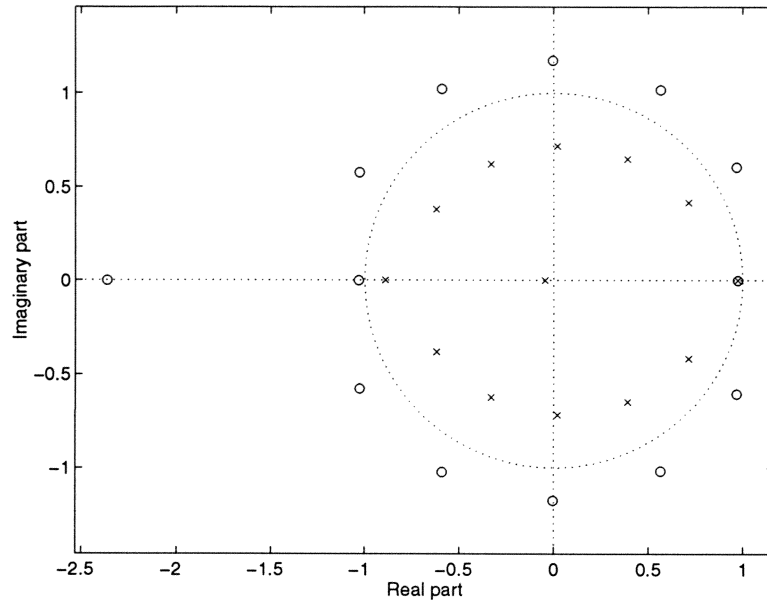


Fig. 4.4. Forward reflectance $\mathcal{R}^+(z)$ discrete-time filter approximation zero and pole locations in the z -plane.

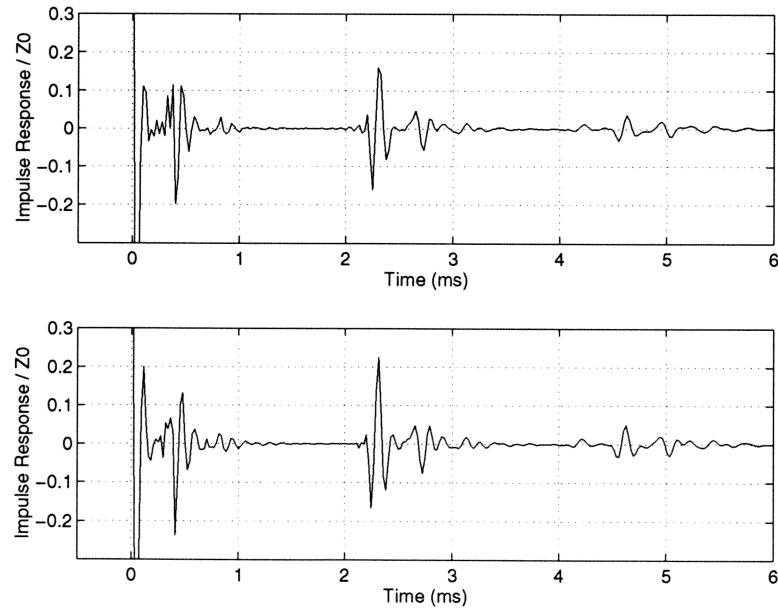


Fig. 4.5. Impulse response, normalized by $Z_0 = \rho c/S$ at the bore input, calculated using (top) transmission matrices and (bottom) a lumped section digital waveguide model as illustrated in Fig. 4.2(b).

those that were lumped, were rounded to the nearest integer delay at a sampling rate of 44.1 kHz.

The lumped-section mouthpiece implementation demonstrated here demands high-order digital filters to accurately model. For real-time digital waveguide implementations under current computer processor capabilities, it is unclear whether the benefits of such mouthpiece design flexibility are worth the added computational cost.

4.2 Performance Expression in Digital Waveguide Woodwind Models

Acoustical issues of woodwind instrument contemporary performance techniques were briefly discussed in Section 2.5. There is a growing demand by composers and musicians to use physical models in new compositions and performance settings. For these situations, the existing models need more flexibility so as to produce a wide variety of sounds, both similar to real instruments and sounds which would be physically impossible in the real world. This section is derived largely from a previously reported study (Scavone, 1996). The first part of this section presents methods for achieving such flexibility within the context of digital waveguide modeling. The control of these extensions using MIDI controllers is discussed in the second part of this section. The implementation of performance expression within the context of digital waveguide stringed-instrument models was previously discussed by Jaffe and Smith (1995), but issues of real-time MIDI control were not considered.

4.2.1 Implementation Issues

The expressive controls discussed here fall into three principal categories – attack variation, breath pressure modification, and bore manipulation. The attack or onset of sound generation in musical instruments is a particularly important aspect of instrument performance and offers enormous expressive flexibility to both the composer and performer. Further, this attack information is a critical element in distinguishing different instruments from one another. Breath pressure modifications, such as flutter tonguing, growling, and singing into the instrument, are possible in all wind instruments, though they are a more common element of woodwind instrument performance. The production of multiphonics, achieved by non-traditional fingerings, is particular to woodwind bores with tonehole lattices.

Attack Variation

A variety of attack styles are possible in woodwind instruments, ranging from breath attacks to extremely percussive, “slap tongue” effects. Most models typically implement only breath-like styles of attack. Hard tonguing effects are achieved by using the tongue to briefly push the reed against

the mouthpiece facing, stopping the reed vibrations and air flow into the mouthpiece. The rapid increase in pressure and air flow into the mouthpiece upon removal of the tongue from the reed, together with noise produced by this highly turbulent initial air flow, produces the resulting attack sound. Lighter tonguing effects are created by briefly interrupting the reed vibrations with the tongue and lesser degrees of flow interruption. The upper half of Fig. 4.6 represents a common method for implementing a breath attack. The breath noise scaler controls the level of noise present in the steady-state sound. A tongued attack is implemented with an additional burst of DC pressure and noise, as shown in the lower half of Fig. 4.6. The tonguing envelope controls the magnitude and duration of the attack and should have a shape of the form $x e^{-x}$. Scaling of the tonguing envelope corresponds to “hardness” of attack and provides an important performance expression control parameter. The relative degree of air flow stoppage is controlled with the tonguing noise scaler.

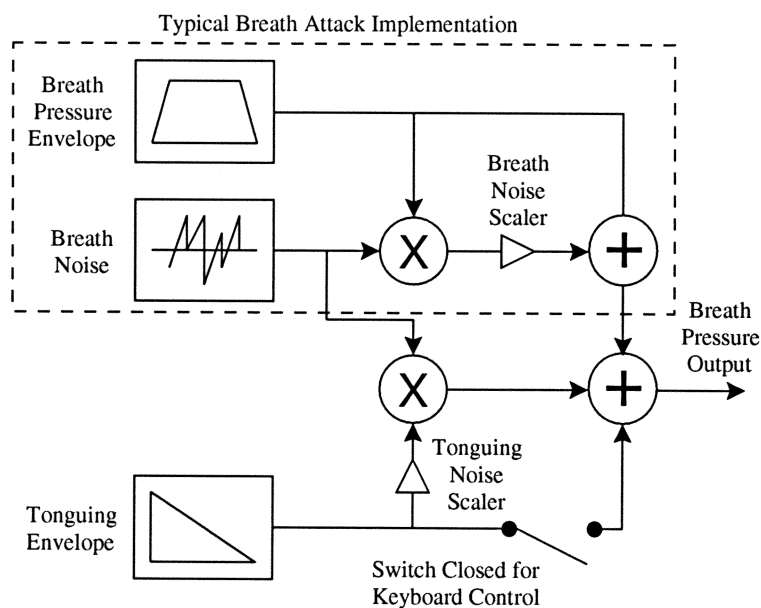


Fig. 4.6. A digital waveguide system for implementing tonguing variation.

Slap tonguing is an effect whereby the reed is pulled away from the mouthpiece lay using a suction force between the reed and tongue. When the elastic restoring force of the reed becomes greater than the suction force between the tongue and reed, the reed separates from the tongue and “slaps” against the mouthpiece lay. Varying amounts of breath pressure are then added to produce a range of effects from dry to fully sounding. Implementation of this effect can be accomplished in several ways. One method involves the recording of a dry slap with the mouthpiece removed from the instrument. This signal is then added to the normal breath pressure signal and input to the instrument’s nonlinear excitation. This effect can also be achieved by approximating the slap with

a predetermined filter impulse response, which is added to the breath pressure signal.

Breath Pressure Modulation

Several extended performance techniques involve the superposition of higher frequency components with the DC breath pressure applied to the instrument. This type of modification is referred to here as modulation, though not in the strict sense of amplitude or frequency modulation. Flutter tonguing, accomplished using either the tongue or the uvula (velum), simply amounts to the addition of a 15 – 30 Hz signal to the breath pressure. Growling and singing are audio rate modulations of breath pressure. One interesting non-physical extension possible in the digital domain is modulation with speech signals, particularly fricative sounds.

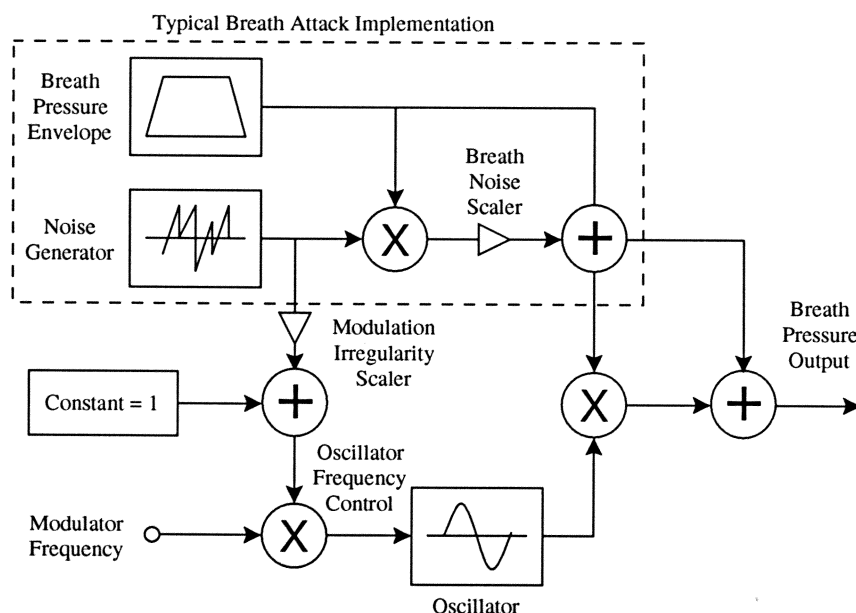


Fig. 4.7. A digital waveguide system for implementing breath pressure modulation.

The implementation of these effects can be achieved using the system depicted in Fig. 4.7. A sinusoidal signal of some desired modulation frequency is added to the original breath pressure and the modulation frequency is randomly varied around its mean to attain a more realistic modulation signal. Modulation of breath pressure with speech can be achieved using recorded signals, though memory considerations in real-time DSP implementations often make this prohibitively expensive. A more desirable implementation provides real-time digital input via a microphone, which can be scaled and added directly to the breath pressure signal. As discussed later in conjunction with wind controllers, a breath pressure sensor sampled in the range of 2 kHz would be ideal for breath pressure control and eliminate the need for most of the system in Fig. 4.7.

Multiphonics and Pitch Bending

Multiphonics are a common element of contemporary woodwind performance technique, as discussed in Section 2.5. Acoustically speaking, non-traditional fingerings produce air column resonances which are not harmonically related, but which are strong enough to entrain simultaneous inharmonic reed oscillations. The resulting tone is heard as comprised of two or more synchronous and distinct pitches, or as a tone with a rough and beating quality.

The most accurate method of modeling this phenomenon is to implement a full series of toneholes which exactly reconstruct the real instrument behavior. Unfortunately, the complexity of such a model would make real-time performance difficult to achieve under current technology. An efficient, though non-physical, technique for generating multiphonics is to add more bores to the model, each of different length. In terms of digital waveguide modeling, this corresponds to the addition of more delay lines and a summing operation for feedback to the excitation mechanism, as shown in Fig. 4.8. Each delay line represents a particular resonance and set of partials, while the input scalars roughly control their relative strengths.

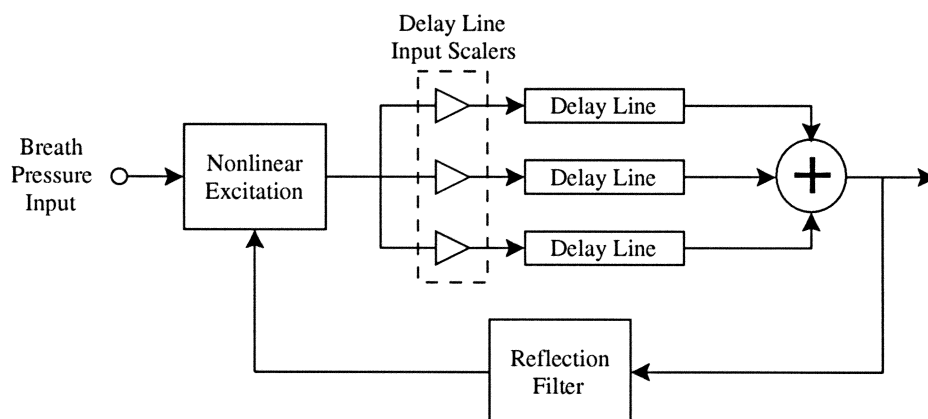


Fig. 4.8. An efficient digital waveguide system for implementing multiphonic tones.

Another performance technique is pitch bending. On single reed instruments, equilibrium reed position can be manipulated by the performer's lower jaw, allowing the sounding pitch to be lowered by as much as a quarter tone. Some increase in pitch is possible by tightening the embouchure but this effect is much less significant. Oral cavity manipulations allow a further lowering of pitch, the magnitude of which varies over the range of the instrument and can be greater than a fifth. This effect is most easily implemented in a digital waveguide context using a smooth delay line interpolation method. Linear and Lagrangian interpolation techniques produce no transients due to filter coefficient changes, but care must be taken to avoid signal discontinuities when changing delay lengths. For the small incremental delay length changes necessary for pitch bend, these techniques generally work well without producing audible discontinuities. Allpass interpolation can

prove troublesome because of the transients associated with coefficient modifications in a recursive filter structure. Two methods exist for minimizing these transients in waveguide models (Välimäki *et al.*, 1995; Van Duyne *et al.*, 1996).

4.2.2 Control Issues

Improving technology and the efficiency of digital waveguide techniques are resulting in synthesis models of unsurpassed flexibility. Unfortunately, it is quickly becoming obvious that such flexibility is difficult to control. Implementation of the expressive techniques discussed above is straight-forward and intuitive within the physical modeling context. Finding ways to control these behaviors in real time is far from simple given current MIDI standards and controller technology. It is obvious that MIDI was not designed to handle extended techniques. Is it possible to adequately control these parameters without inventing a new protocol? The clear choice for controlling woodwind synthesis models is a MIDI wind controller. However, the few wind controllers commercially available offer only basic features and prove inadequate for the control of most of the extended techniques previously discussed. The MIDI keyboard is also far from ideal in this context, but it must be supported for historical and pragmatic reasons. The limitations of the keyboard are sometimes circumvented by providing wind-like controllers, such as the breath pressure controller supplied with Yamaha's VL1 synthesizer. In order to accommodate the advantages and disadvantages of these two controller types, different control schemes are necessary for each.

Wind Controller Issues

Flexible attack control requires two degrees of freedom and can be achieved using both breath pressure and velocity MIDI messages. The breath pressure messages control the breath pressure envelope while velocity controls the tonguing noise level, or tonguing noise scaler in Fig. 4.6. In this way, a wide range of combinations of breath attack and tonguing level are possible. The Yamaha WX series of wind controllers generate both breath pressure and velocity MIDI messages via the pressure sensor in its mouthpiece. It is unclear how the velocity messages are determined in the WX controllers, though playing experiments show precise control of this parameter to be difficult. Of all the wind controllers commercially available at present, those of Yamaha are the only ones which generate breath-dependent velocity messages. Physically relevant breath velocity messages can be obtained, however, by differentiating the breath pressure signal, so that velocity control using controllers without MIDI velocity output can still be possible if implemented onboard the synthesizer or computer.

The performance techniques based on modulation of the breath pressure signal present significant challenges in developing a realistic means of control. The most physically accurate solution would incorporate a breath pressure sensor that is sensitive enough to detect the modulations in the performer's breath input. Audio rate modulations, however, would require pressure sensor sampling

rates on the order of 2 kHz. Under current MIDI standards, message rates can theoretically run as high as 1.5 kHz using running status and 2-byte messages, but such a strategy would be inefficient and hinder control of other aspects of the model. A more ideal solution would be to output breath sensor readings on a separate data line for real-time digital breath pressure input to the instrument model. Under the limitations of current wind controller technology, one possible scheme for the control of flutter tonguing and growling provides the performer with a foot switch mechanism that allows control of the modulation rate.

Multiphonics present an even greater control problem when using a wind controller. Potentially, non-traditional fingerings could be detected and output with special MIDI parameter values. The Synthophone wind controller provides this flexibility, allowing non-standard fingerings to be programmed with particular parameter values. However, the Yamaha WX and Akai EWI wind controllers output a standard MIDI key number for all fingerings without allowing the key combinations to be reprogrammed. This limitation might potentially be circumvented by using a particular MIDI program change message to control a “multiphonic” mode of operation, but any control scheme developed under this scenario would only function as a poor substitute to the desired behavior. Clearly, the programmable environment offered by the Synthophone should serve as a model for future wind controller development.

Keyboard Controller Issues

The mapping of MIDI keyboard control mechanisms to wind instrument expressive parameters is less obvious than when using a wind controller. However, the keyboard provides more flexibility than current wind controllers when used in conjunction with a breath pressure sensor. This is largely due to the fact that only one hand is needed to play the keys of the keyboard, leaving the other hand free to modify additional parameters. Without a breath pressure sensor, attack control via the keyboard is completely dependent on key velocity messages, resulting in significant loss of flexibility. In this context, low velocity values might be made to correspond to soft breath attacks and high velocity values to loud, hard tongued attacks. Lost in this scheme would be such effects as strong breath and lightly tongued attacks. The addition of a breath controller gives the keyboard musician much of the same attack flexibility enjoyed by users of wind controllers equipped with breath sensitive velocity detection.

As previously mentioned, natural control of breath pressure modulation requires a high breath pressure sampling rate. Until new controller technologies make this possible, the system of Fig. 4.7 can be implemented and the various modulation parameters can be assigned to such keyboard controllers as modulation wheels or foot pedals. In this instance, the keyboard’s wide array of controllers give it more flexibility than the wind controller.

Control of the multiphonic implementation of Fig. 4.8 using a keyboard can be achieved by

depressing multiple keys at the same time and assigning the various delay line lengths by the corresponding key numbers.

4.2.3 Summary

Physical models of woodwind instruments provide flexible control over a wide range of performance expression techniques. The implementation of these effects is reasonably straight forward because of the one-to-one correspondence between the model elements and physical elements. Unfortunately, control of these techniques is less straight forward, even when using a MIDI wind controller. With current technology, schemes can be developed which allow control of performance expression using both wind controllers and keyboards, though such control is not always intuitive or natural. The flexibility of physical modeling should result in the future development of new controller technologies that make such control more natural.

4.3 Calibrating Digital Waveguide Woodwind Models

The modeling of the various components of single-reed woodwind instruments using digital waveguide techniques, as discussed in Chapter 3, was based largely on theoretical studies described in acoustical reports. In most cases, however, acoustical measurements have been made to validate the theory. In the past, most acoustic theory was based in the frequency domain, and thus, most experimental measurements were made of air column impedances or other frequency-domain characteristics. As was seen in Chapter 3, frequency-domain descriptions of acoustic components are as easily incorporated into digital waveguide models as time-domain characterizations. That said, there is an increasing movement to measure wind instrument responses in the time domain, in order to verify time-domain theories.

4.3.1 Measuring Woodwind Instrument Responses in the Time Domain

Recent studies by Agulló *et al.* (1995) and Keefe (1996) have presented methods for the measurement of time-domain reflection functions, either associated with individual air-column discontinuities or complete instrument systems. The study of Agulló *et al.* (1995) was initiated for the purpose of verifying the reflection function theory of cylindrical-conical junctions. Their experimental setup was designed as shown in Fig. 4.9 such that an initial wide bandwidth, short duration pressure disturbance was initiated within a long cylindrical extension tube and reflections from the discontinuity could be measured by the microphones before reflections from either the conical section open end or the source reached the microphones. Deconvolution operations are critical to the success of such approaches and are the largest source of error, aside from achieving a reasonable excitation signal. Agulló *et al.* (1995) performed two deconvolution operations. The first was done to remove the response of the non-ideal driver from the excitation signal, while the second operation was performed

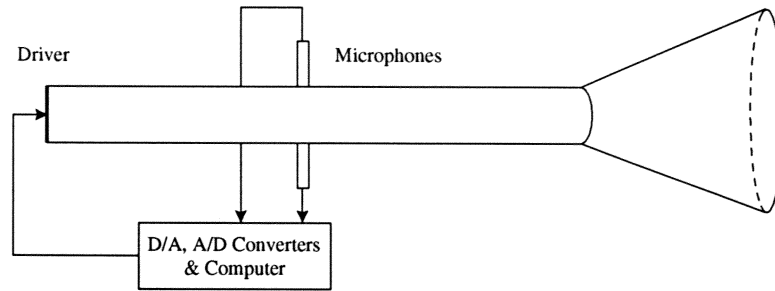


Fig. 4.9. The experimental setup of Agulló *et al.* (1995).

to determine the actual reflection function initiated by the non-ideal, bandlimited excitation. It would appear that only a single deconvolution was necessary for this procedure. Results of this study showed reasonable verification of the theory.

Keefe (1996) presented a slightly modified approach to the time-domain measurement of wind instrument air column response functions. This technique did not require the use of a cylindrical extension tube, but rather, a long calibration tube of similar diameter to that of the measured instrument bore. Use of the calibration tube eliminates the need to explicitly determine the driver response, and allows a calculation that requires only a single deconvolution operation. In this context, the measured reflection functions characterize the entire instrument air column and all of the various discontinuities within it. The measured responses are limited in duration to that of the calibration tube round-trip travel time.

4.3.2 Periodic Prediction for the Determination of Linear and Nonlinear Instrument Behavior

A study was conducted to investigate a wind instrument's linear and nonlinear behavior using periodic prediction techniques (Scavone and Cook, 1994). Central to this approach is the simplified model of a general wind instrument as given by Fig. 4.10, where the system observation point is defined at the output of the nonlinear element. The nonlinear element, or reed mechanism in

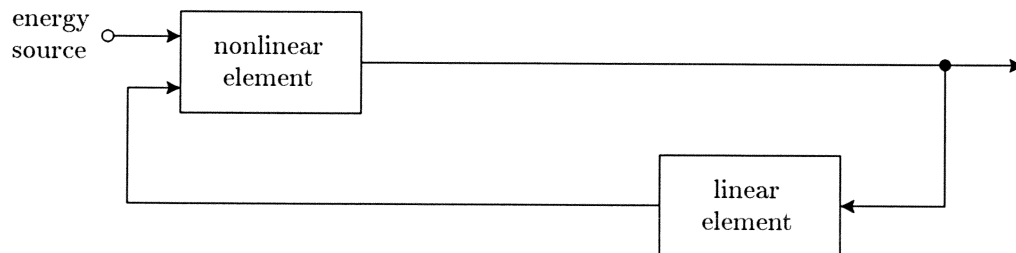


Fig. 4.10. A general wind instrument represented by linear and nonlinear elements in a feedback loop.

reed-woodwind instruments, excites a passive linear element, such as a cylindrical or conical bore. Feedback from the air column subsequently influences the operation of the excitation mechanism. In general, the linear element is characterized in the time domain by a reflection function or in the frequency domain by a frequency-dependent reflection coefficient or reflectance, as discussed in Section 1.3.4. For this study, the linear element is assumed to be a uniform waveguide with only a single discontinuity at its open end. Under this assumption, it is possible to “pull out” a propagation delay term from the time-domain reflection function which is roughly equivalent to the time necessary for sound waves to travel to the end of the air column and back. For a propagation delay of L seconds, the instrument system can then be represented as shown in Fig. 4.11. The

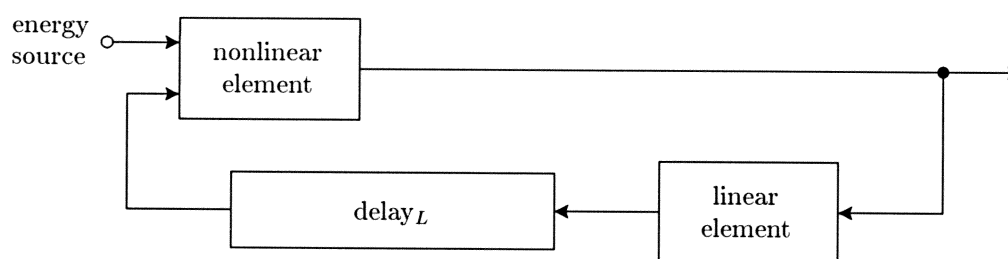


Fig. 4.11. A general wind instrument represented by linear, nonlinear, and delay elements in a feedback loop.

linear component now represents only the attenuation and phase delay associated with open-end radiation and thermoviscous losses to the tube walls, assuming the air column is a perfectly uniform cylinder. If the given air column is conical, then this term would further include the effects of mass loading at the input to the conical frustum. The nonlinear element represents the nonlinear action of the excitation mechanism only. Nonlinear acoustic phenomena which take place downstream from the mouthpiece and reed assembly are thus ignored or assumed negligible. It is well known that a clarinet air column acts as a quarter-wave resonator, such that an initial pressure disturbance in the mouthpiece must propagate along its length four times before completing a full period of oscillation. The air column of conical-bored instruments acts as a half-wave resonator. From this perspective, the linear and nonlinear filters are each applied once or twice per oscillatory period of the instrument output. A “pseudo-clarinet” was constructed as shown in Fig. 4.12 that roughly corresponds to the system of Fig. 4.11. Under blowing conditions, the internal pressure signal was recorded in the mouthpiece cavity and considered to be the output of the nonlinear element. This pressure actually represents the sum of the outgoing and returning traveling-wave components in the bore. For the purpose of this study, an assumption was made that this pressure is roughly proportional to the outgoing component only, given that the clarinet reed assembly is characterized by a reflection coefficient of negative one while the reed is closed against the mouthpiece facing. In practice, this assumption proved to be the “weak link” in the approach.

An attempt to identify linear and nonlinear characteristics in quasi-periodic steady-state musical

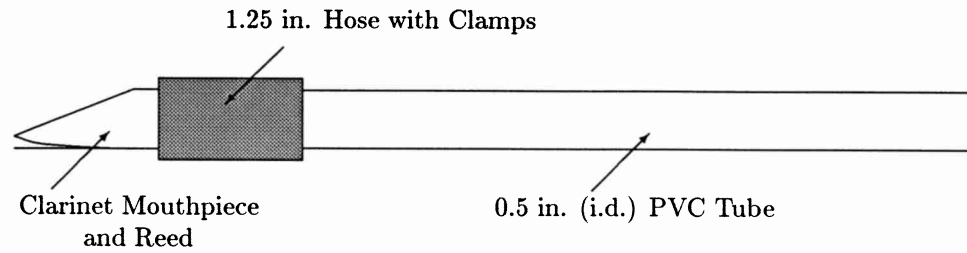


Fig. 4.12. An experimental “pseudo-clarinet” instrument.

tones is problematic because period to period variations are generally minimal. This is evident in Fig. 4.13, which shows a portion of a steady-state waveform measured inside the clarinet-like experimental instrument. All musical instruments capable of sustained oscillations operate in an

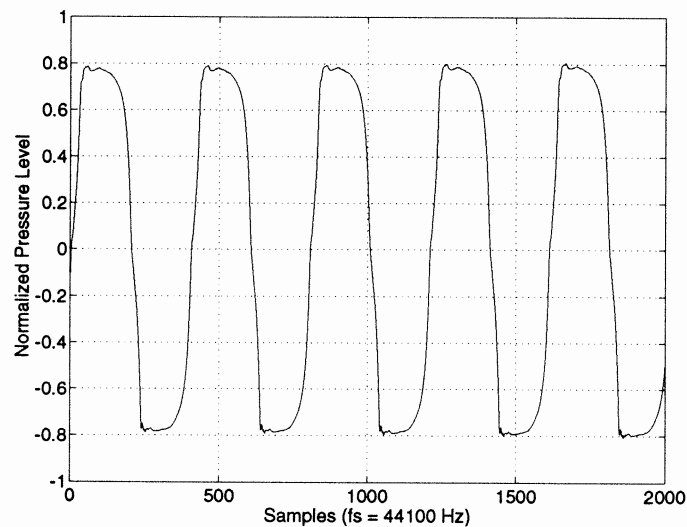


Fig. 4.13. Steady-state waveform measured inside the “pseudo-clarinet” instrument.

equilibrium condition set up between an excitation source, a passive nonlinear control mechanism, and a passive linear “lossy” element. A reed, for example, acts as a nonlinear pressure-controlled control valve, allowing energy supplied by a performer into the system to compensate for losses to its surrounding environment. As a result, the action of these two components “offset” one another and make attempts to simultaneously identify their individual characteristics difficult at best. Such a task is further complicated by the fact that during steady-state regimes, the linear and nonlinear elements generally function in only a limited subspace of their full operating range. Previously, Cook (1991) attempted to identify an instrument’s nonlinear characteristic assuming that the system’s linear characteristic can be ignored. The approach in this study was to first identify the instrument’s linear characteristic in the absence of its nonlinear excitation mechanism.

This was done by applying an impulsive or white-noise excitation source to the system and using linear periodic prediction on the resultant “impulse response.” The instrument was then “played” under normal conditions and an internal pressure signal was recorded. The previously identified linear filtering characteristic was removed from a delayed version of the measured output by inverse filtering to form the input signal used when performing the nonlinear periodic prediction.

Adaptive Linear Periodic Prediction

The difficulty in identifying a musical instrument’s linear filtering characteristic in the presence of the nonlinear element was previously mentioned. Thus, it is necessary to excite the system via an external, impulsive source and measure the associated system “impulse response” in the absence of the nonlinear element. If the excitation signal is applied at the same point that the associated response is measured, the system of Fig. 4.14 results. In this case, the measured response is given

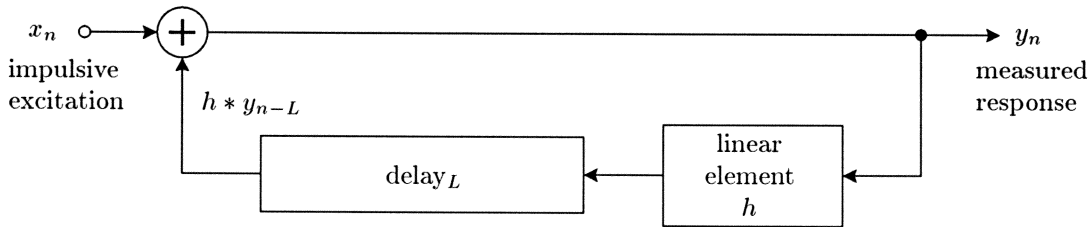


Fig. 4.14. A general wind instrument air column represented by delay and lumped linear elements in a feedback loop.

by

$$y_n = x_n + [h * y_{n-L}], \quad (4.10)$$

where the subscript n denotes the n th time step. It is clear that an impulse excitation signal will cause the linear filter’s impulse response to appear at the output L samples after it is introduced. This impulse response is then repeatedly convolved with itself as it propagates through the feedback loop. Most linear estimation techniques that have been applied to wind instrument air columns (Agulló *et al.*, 1995; Keefe, 1996) involve the generation of a known input signal and subsequent deconvolution of this signal from the measured output. The periodic prediction technique, however, avoids the deconvolution step and its inherent inaccuracies, and only requires that the excitation signal be wideband and of shorter duration than the roundtrip delay time L . Using the measured output L samples in advance as the desired signal (i.e. using periodic prediction), the linear element can be approximated by FIR filter coefficients. The structure of Fig. 4.15 represents the single-input, adaptive processor implemented for this purpose. The least-mean-square (LMS) algorithm was used to adapt the filter weights (Widrow and Stearns, 1985).

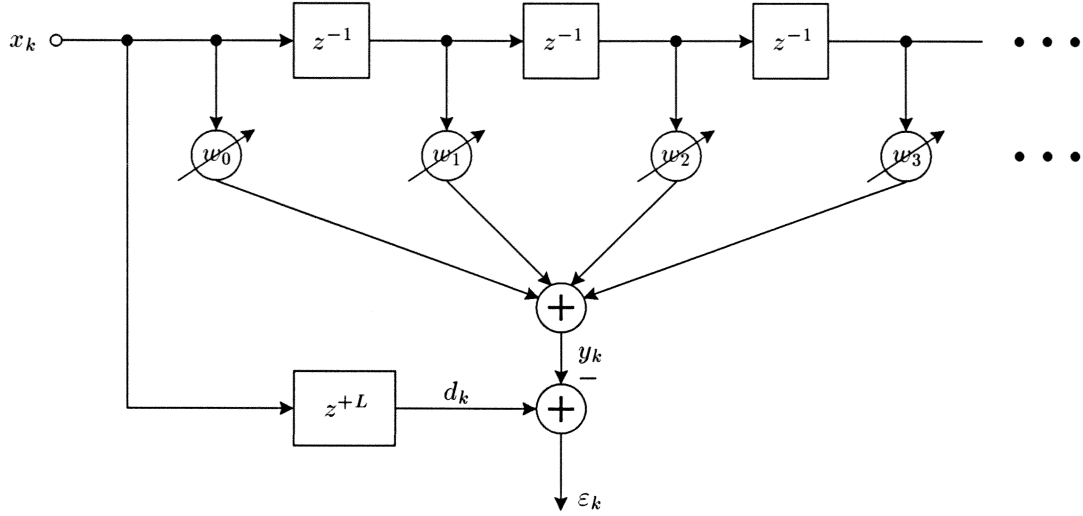


Fig. 4.15. An adaptive linear periodic forward predictor.

Adaptive Nonlinear Periodic Prediction

Several assumptions regarding the reed excitation mechanism were made for this analysis. The nonlinear element was first considered to be memory-less and essentially time-invariant in its steady state. Secondly, it was assumed that the nonlinearity is a function of the difference between breath pressure and returning bore pressure x_n , as defined in Fig. 4.16. Finally, the breath pressure was assumed constant during a steady-state excitation, so that the nonlinearity could be approximated by a polynomial function of x_n .

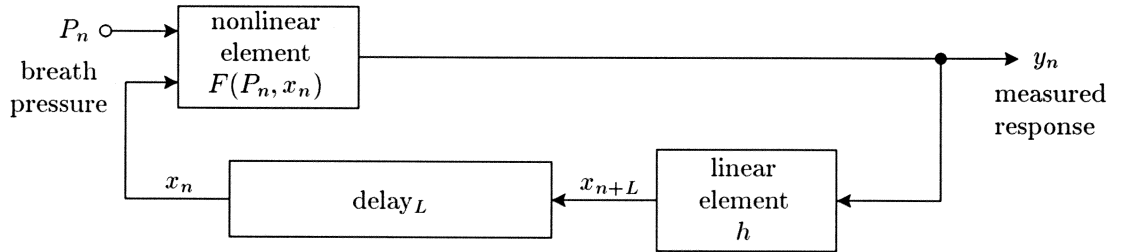


Fig. 4.16. The assumed wind instrument model used for the nonlinear prediction experiment.

To identify the nonlinear characteristic from the experimental instrument internal pressure signal, the influence of the linear element is first removed. Under normal operation, the input to the nonlinear function is given by

$$x_n = y_{n-L} * h. \quad (4.11)$$

An inverse filter is determined from the extracted linear predictor weights and applied to a delayed version of the measured output y_{n-L} . This signal then forms the input to the nonlinear predictor,

for which the desired response is given by the unfiltered y_n . Thus, the nonlinear predictor produces an approximation to y_n given an input of $x_n = y_{n-L} * h^{-1}$.

To perform the nonlinear prediction, a single-input, transversal filter was modified in order to create a nonlinear, periodic, forward predictor. This was accomplished by replacing the transversal filter's delay elements with multiplicative units, so that each adaptable weight is operating on a successive power of the input. This structure is shown in Fig. 4.17. Because it is assumed that the nonlinearity of the input signal is memory-less, no delay units are included. The adaptive nonlinear

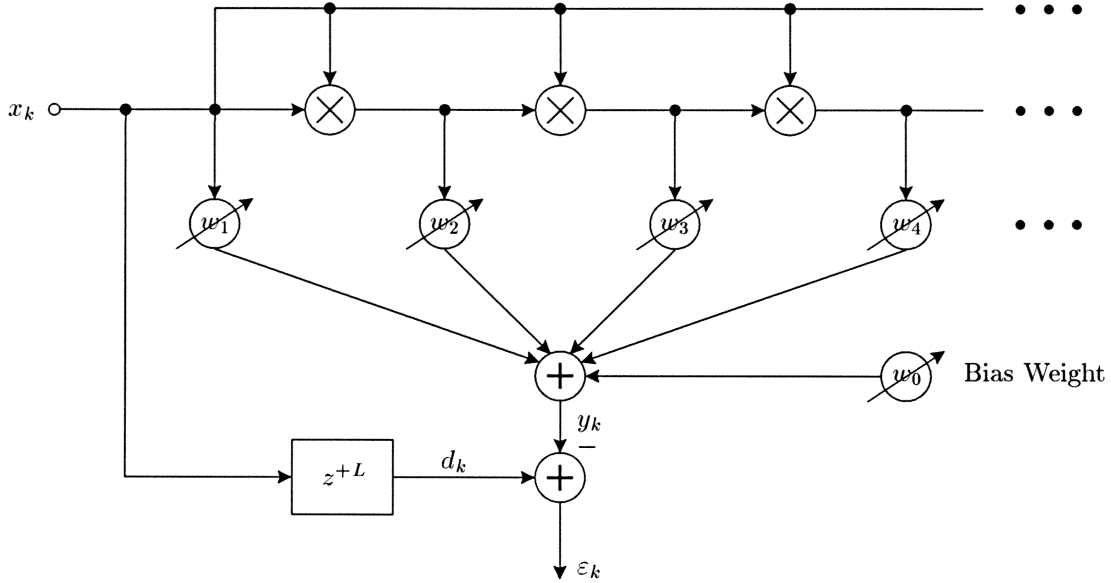


Fig. 4.17. An adaptive nonlinear periodic forward predictor.

predictor produces a least-mean-square approximation to y_n given an input of $x_n = y_{n-L} * h^{-1}$ by adapting coefficients of an N th order polynomial.

Following a discussion similar to that of Widrow and Stearns (1985), the input-output relationship which results from this configuration is

$$y_k = \sum_{j=0}^N w_{jn} x_k^j, \quad (4.12)$$

where N is the nonlinear predictor polynomial order. An input column vector to the adaptor can be written as

$$\mathbf{X}_k = \begin{bmatrix} 1 & x_k & x_k^2 & \cdots & x_k^N \end{bmatrix}^T. \quad (4.13)$$

As seen in Fig. 4.17, w_{0k} is a bias weight with an input equal to x_k raised to the power zero (equal to one over all time). The corresponding weight vector is given by

$$\mathbf{W}_k = \begin{bmatrix} w_{0k} & w_{1k} & \cdots & w_{Nk} \end{bmatrix}^T, \quad (4.14)$$

so that Eq. (4.12) can be written in vector notation as

$$y_k = \mathbf{X}_k^T \mathbf{W}_k = \mathbf{W}_k^T \mathbf{X}_k. \quad (4.15)$$

The desired signal is denoted by d_k . For convenience, the subscript k is dropped from the weight vector \mathbf{W} , because adaptation of the weights is not being considered at this point. The error is then given by

$$\varepsilon_k = d_k - y_k \quad (4.16)$$

$$= d_k - \mathbf{X}_k^T \mathbf{W} = d_k - \mathbf{W}^T \mathbf{X}_k, \quad (4.17)$$

and the instantaneous squared error is

$$\varepsilon_k^2 = d_k^2 + \mathbf{W}^T \mathbf{X}_k \mathbf{X}_k^T \mathbf{W} - 2d_k \mathbf{X}_k^T \mathbf{W}. \quad (4.18)$$

With the assumption that ε_k , d_k , and \mathbf{X}_k are statistically stationary, the expected value of Eq. (4.18) is

$$E[\varepsilon_k^2] = E[d_k^2] + \mathbf{W}^T E[\mathbf{X}_k \mathbf{X}_k^T] \mathbf{W} - 2E[d_k \mathbf{X}_k^T] \mathbf{W}. \quad (4.19)$$

Let \mathbf{R} be defined as the square matrix

$$\mathbf{R} = E[\mathbf{X}_k \mathbf{X}_k^T] = E \begin{bmatrix} 1 & x_k & x_k^2 & \cdots & x_k^N \\ x_k & x_k^2 & x_k^3 & \cdots & x_k^{N+1} \\ \vdots & \vdots & \vdots & & \vdots \\ x_k^N & x_k^{N+1} & x_k^{N+2} & \cdots & x_k^{2N} \end{bmatrix}. \quad (4.20)$$

While the main diagonal terms of this matrix are the mean squares of the input components, \mathbf{R} is not an “input correlation matrix,” as is the case for the standard linear transversal filter. \mathbf{R} is a symmetric, Hankel matrix which is constant along its anti-diagonals, singular, and of rank 1. The characteristic equation of this matrix is: $a(s) = \det(s\mathbf{I} - \mathbf{R}) = s^{n-1}(s - \lambda)$, where λ is the only possibly nonzero eigenvalue of \mathbf{R} and n is the matrix dimension. The single nonzero eigenvalue of \mathbf{R} is given by its trace, which in this case is the sum of the squares of the input vector \mathbf{X}_k .

Let \mathbf{P} be defined as the column vector

$$\mathbf{P} = E[d_k \mathbf{X}_k] = E \begin{bmatrix} d_k & d_k x_k & \cdots & d_k x_k^N \end{bmatrix}^T. \quad (4.21)$$

This vector is the set of cross correlations between the desired response and the input components. The mean-square error in Eq. (4.19) can be designated by ξ and expressed in the terms of Eqs. (4.20) and (4.21) as

$$\xi = E[\varepsilon_k^2] = E[d_k^2] + \mathbf{W}^T \mathbf{R} \mathbf{W} - 2\mathbf{P}^T \mathbf{W}. \quad (4.22)$$

Adaptation of the weights is performed using the LMS algorithm, whereby ε_k^2 itself is taken as an estimate of ξ . At each iteration in the adaptive process, the gradient estimate is of the form

$$\hat{\nabla}_k = \begin{bmatrix} \frac{\partial \varepsilon_k^2}{\partial w_0} \\ \vdots \\ \frac{\partial \varepsilon_k^2}{\partial w_N} \end{bmatrix} = 2\varepsilon_k \begin{bmatrix} \frac{\partial \varepsilon_k}{\partial w_0} \\ \vdots \\ \frac{\partial \varepsilon_k}{\partial w_N} \end{bmatrix} = -2\varepsilon_k \mathbf{X}_k. \quad (4.23)$$

The weight adjustment is given by

$$\begin{aligned} \mathbf{W}_{k+1} &= \mathbf{W}_k - \mu \hat{\nabla}_k \\ &= \mathbf{W}_k + 2\mu \varepsilon_k \mathbf{X}_k, \end{aligned} \quad (4.24)$$

where μ is a gain constant which regulates the speed and stability of adaptation. Convergence is guaranteed only if

$$0 < \mu < \frac{1}{\lambda_{\max}} \quad (4.25)$$

with

$$\lambda_{\max} = \text{tr}[\mathbf{R}] = \sum_{j=0}^N x_k^{2j} \quad (4.26)$$

as indicated earlier.

Relating Nonlinear Predictor Weights to General Nonlinear Functions

In reference to Fig. 4.16, the measured response y_n is the output of the nonlinear element. As previously mentioned, it is assumed that the instrument nonlinearity can be approximated by a general polynomial function of its input x_n , such as the third-order fit

$$F(x_n) \approx a_0 + a_1 x_n + a_2 x_n^2 + a_3 x_n^3. \quad (4.27)$$

It is further assumed that the nonlinearity is a function of the difference between the input mouth pressure P_n and the returning pressure from the bore x_n , which for constant P_n during a steady-state tone results in the relationship

$$\begin{aligned} y_n &= F(P_n, x_n) \\ &= F(P - x_n) \\ &\approx a_0 + a_1(P - x_n) + a_2(P - x_n)^2 + a_3(P - x_n)^3 \\ &= (a_0 + a_1 P + a_2 P^2 + a_3 P^3) - (a_1 + 2a_2 P + 3a_3 P^2)x_n + (a_2 + 3a_3 P)x_n^2 - a_3 x_n^3. \end{aligned} \quad (4.28)$$

The nonlinear predictor produces a least-mean-square approximation to y_n given an input x_n by adapting coefficients of an N th-order polynomial. In terms of the predictor weights, this is represented by the relation

$$y_n \approx w_0 + w_1 x_n + w_2 x_n^2 + w_3 x_n^3. \quad (4.29)$$

Thus, the weights of the nonlinear predictor are related to the coefficients of a nonlinear function of the differential pressure at the reed by

$$\begin{aligned} w_0 &= a_0 + a_1 P + a_2 P^2 + a_3 P^3 \\ w_1 &= -a_1 - 2a_2 P - 3a_3 P^2 \\ w_2 &= a_2 + 3a_3 P \\ w_3 &= -a_3, \end{aligned} \tag{4.30}$$

or in matrix form as

$$\begin{bmatrix} w_0 \\ w_1 \\ w_2 \\ w_3 \end{bmatrix} = \begin{bmatrix} 1 & P & P^2 & P^3 \\ 0 & -1 & -2P & -3P^2 \\ 0 & 0 & 1 & 3P \\ 0 & 0 & 0 & -1 \end{bmatrix} \begin{bmatrix} a_0 \\ a_1 \\ a_2 \\ a_3 \end{bmatrix}. \tag{4.31}$$

This transformation assumes that the nonlinearity is identified from a steady-state tone, which is produced by a constant input mouth pressure level. In real wind-driven musical instruments, the nonlinearity will be dependent on the input mouth pressure level. For the purpose of sound synthesis, however, it is often convenient to ignore this dependence and implement a single nonlinear characteristic. If the input breath pressure is normalized and it is assumed that $P \approx 1$ in the steady state, the transformation matrix in Eq. (4.31) reduces to a Pascal triangle

$$\begin{bmatrix} w_0 \\ w_1 \\ w_2 \\ w_3 \end{bmatrix} = \begin{bmatrix} 1 & 1 & 1 & 1 \\ 0 & -1 & -2 & -3 \\ 0 & 0 & 1 & 3 \\ 0 & 0 & 0 & -1 \end{bmatrix} \begin{bmatrix} a_0 \\ a_1 \\ a_2 \\ a_3 \end{bmatrix}. \tag{4.32}$$

From the extracted weights, it is then possible to determine the polynomial coefficients of a nonlinear function of the differential pressure at the reed by inverting Eq. (4.32) as

$$\begin{bmatrix} a_0 \\ a_1 \\ a_2 \\ a_3 \end{bmatrix} = \begin{bmatrix} 1 & 1 & 1 & 1 \\ 0 & -1 & -2 & -3 \\ 0 & 0 & 1 & 3 \\ 0 & 0 & 0 & -1 \end{bmatrix} \begin{bmatrix} w_0 \\ w_1 \\ w_2 \\ w_3 \end{bmatrix}. \tag{4.33}$$

It is possible to further represent this characterization of the excitation mechanism nonlinearity in terms of a pressure-dependent reed reflection coefficient $r(p_\Delta)$, as discussed in Section 3.5.1. The coupling of the mouthpiece/reed and instrument bore is modeled in terms of a two-port junction, with associated reflection and transmission coefficients. In terms of Fig. 4.16, y_n is formed by the partial reflection of x_n and the partial transmission of P at the junction of the instrument excitation mechanism and air column. The portion of x_n that is reflected back into the air column is given by $x_n r(p_\Delta)$ while the portion of the breath pressure which is transmitted through the junction and into the bore is given by $P[1 - r(p_\Delta)]$. The net output from the nonlinear junction is given by

$$y_n = P - r(p_\Delta) \cdot [P - x_n]. \tag{4.34}$$

The pressure-dependent reed reflection coefficient can then be approximated by a third-order polynomial function of the pressure difference at the reed, $p_\Delta = P - x_n$, as

$$r(P - x_n) \approx c_0 + c_1(P - x_n) + c_2(P - x_n)^2 + c_3(P - x_n)^3. \quad (4.35)$$

Using this form of the reed reflection coefficient and substituting into Eq. (4.34)

$$\begin{aligned} y_n = & (P - c_0P - c_1P^2 - c_2P^3 - c_3P^4) + (c_0 + 2c_1P + 3c_2P^2 + 4c_3P^3)x_n \\ & - (c_1 + 3c_2P + 6c_3P^2)x_n^2 + (c_2 + 4c_3P)x_n^3 - c_3x_n^4, \end{aligned} \quad (4.36)$$

which for $P = 1$ simplifies to

$$\begin{aligned} y_n = & (1 - c_0 - c_1 - c_2 - c_3) + (c_0 + 2c_1 + 3c_2 + 4c_3)x_n - (c_1 + 3c_2 + 6c_3)x_n^2 \\ & + (c_2 + 4c_3)x_n^3 - c_3x_n^4. \end{aligned} \quad (4.37)$$

The weights of the nonlinear predictor are related to the polynomial coefficients of r by comparing Eqs. (4.29) and (4.37) as

$$\begin{bmatrix} w_0 \\ w_1 \\ w_2 \\ w_3 \\ w_4 \end{bmatrix} = \begin{bmatrix} 1 & -1 & -1 & -1 & -1 \\ 0 & 1 & 2 & 3 & 4 \\ 0 & 0 & -1 & -3 & -6 \\ 0 & 0 & 0 & 1 & 4 \\ 0 & 0 & 0 & 0 & -1 \end{bmatrix} \begin{bmatrix} 1 \\ c_0 \\ c_1 \\ c_2 \\ c_3 \end{bmatrix}. \quad (4.38)$$

Inversely, a polynomial approximation to the pressure-dependent reed reflection coefficient can be determined from the nonlinear predictor weights by

$$\begin{bmatrix} 1 \\ c_0 \\ c_1 \\ c_2 \\ c_3 \end{bmatrix} = \begin{bmatrix} 1 & 1 & 1 & 1 & 1 \\ 0 & 1 & 2 & 3 & 4 \\ 0 & 0 & -1 & -3 & -6 \\ 0 & 0 & 0 & 1 & 4 \\ 0 & 0 & 0 & 0 & -1 \end{bmatrix} \begin{bmatrix} w_0 \\ w_1 \\ w_2 \\ w_3 \\ w_4 \end{bmatrix}. \quad (4.39)$$

By comparing Eqs. (4.36) and (3.98), the nonlinear predictor weights are seen to determine the coefficients of the reed reflection polynomial, as discussed in Section 3.5.2, for a constant breath pressure.

As an example of these concepts, the top graph of Fig. 4.18 displays a sample piecewise, nonlinear pressure-dependent reflection coefficient table effective in synthesizing clarinet-like sounds, together with a third-order polynomial approximation. Assuming normalized parameters, the input breath pressure P can range between zero and one and the incoming air column pressure x_n between negative one and one. Thus, the pressure difference is confined to the range $0 \leq P - x_n \leq 2$. For $P - x_n \geq 1$, the reflection coefficient output is one, which corresponds to having the reed

closed against the mouthpiece facing and full reflection of the incoming air column pressure. The third-order polynomial approximation to r can be transformed into a general fourth-order nonlinear function of x_n by the transformation of Eq. (4.38), assuming a constant breath pressure $P = 1$. The resulting function is shown in the lower plot of Fig. 4.18, together with that obtained by directly transforming the piecewise reflection coefficient using Eq. (4.34). For negative values of incoming air column pressure x_n , the nonlinear function output y_n is equal to its input x_n , corresponding to a closed reed and no addition of mouth pressure into the system. For most positive pressure levels, the function output is slightly greater than its input, corresponding to an open reed and a partial input of mouth pressure into the system. When $x_n = 1$, the nonlinear function output consists solely of transmitted breath pressure. The polynomial approximation to r is seen to transform fairly accurately, though with a slight negative bias at $x_n = 0$. The nonlinear predictor identifies a characteristic similar to that of the lower plot of Fig 4.18. Using Eq. (4.39), these weights can be transformed into a polynomial approximation of a pressure-dependent reflection coefficient for implementation in a digital waveguide single-reed instrument model.

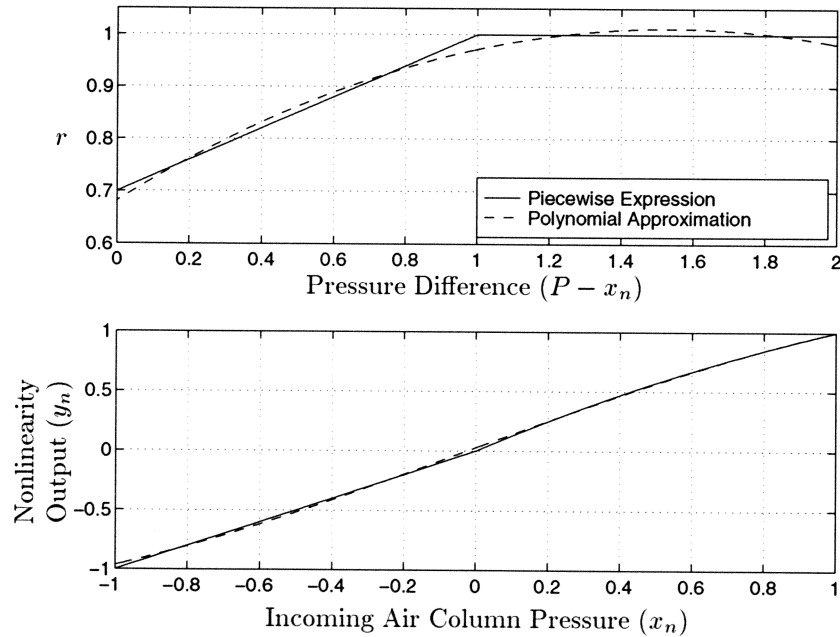


Fig. 4.18. An example piecewise reflection coefficient table and its polynomial approximation (top), and the corresponding general nonlinear function responses (bottom).

Linear Element Experimental Setup and Measurements

The objective of the first experiment is to obtain a system excitation response in the absence of the nonlinear element. It is also necessary that only a single propagation period be present in the measured signal, so that the periodic prediction technique can be applied. For these experiments, the

excitation signal and microphone were placed at either the same or at opposite ends of the instrument air column. The period of the recorded signal is then roughly equal to the time necessary for sound to propagation along two tube lengths. The only constraint on the excitation signal is that it contain significant energy over the frequency range of interest. In this case, results between about 100–5,000 Hz are completely acceptable.

The setup for this experiment is shown in Fig. 4.19. The clarinet mouthpiece was removed from the PVC tube and a cork stopper was placed at one end, through which an $\frac{1}{8}$ in. Panasonic microphone and earplug transmitter were inserted. The transmitter was driven by a square-wave generator, resulting in a sequence of alternating positive and negative impulse-like pressure signals somewhat proportional to the derivative of the square wave. The square-wave width and frequency were adjusted so that pulse reflections within the tube decayed below the surrounding noise level before a subsequent negative or positive edge was reached. The condenser microphone output was fed into a Singular Solutions A/D 64x analog-to-digital converter and the digital signal was recorded on a NeXT computer. Details regarding the equipment are provided in Appendix C.

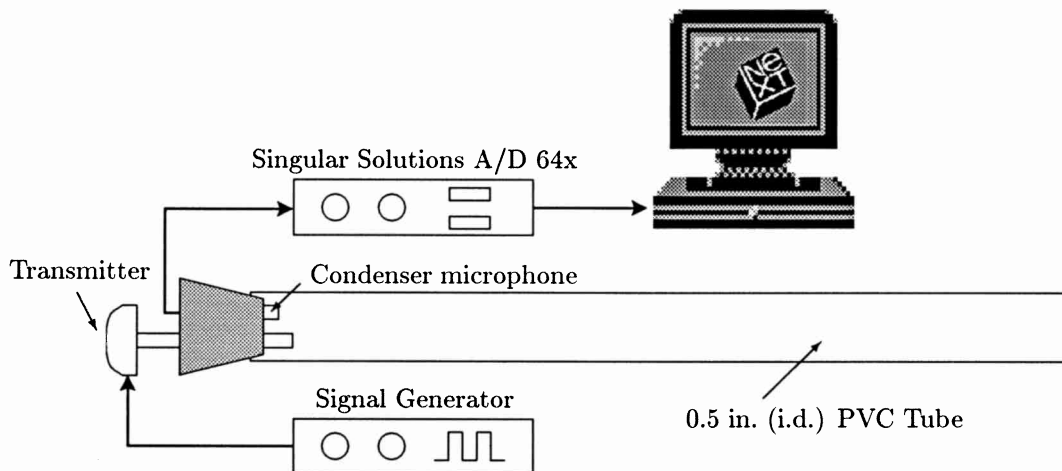


Fig. 4.19. Linear element experiment setup.

As will be shown, the air column response obtained by the procedure described above decayed rather rapidly and was of short duration. Therefore, another measurement was made by striking the palm of a hand against one end of the tube while recording the response at the other end with an external microphone. In this case, the palm was held against the tube, forming a closed end and the microphone recorded the tube response at its open end.

Figure 4.20 shows the recorded tube response given a single square wave input. The first group of reflections results from the positive edge of the pulse, while the second set is triggered by the pulse's negative edge. The positive and negative impulse separation is approximately 4083 samples, corresponding to an impulse frequency of about 10.8 Hz or an input square-wave frequency of 5.4

Hz.

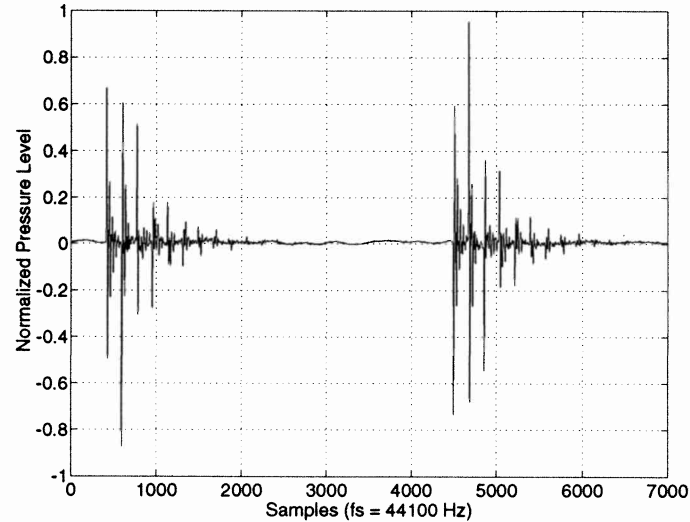


Fig. 4.20. Recorded response of the PVC tube.

Figure 4.21 shows the reflections resulting from the negative impulse only. That part of the signal contained within the first 200 samples represents the input fed directly by the transmitter. The greater signal strength of the first *reflection* relative to the input signal is attributable to the fact that the transmitter extends farther into the bore than the microphone. The expected inversion experienced by each subsequent reflection of the pressure signal at the PVC tube's open end is clearly visible in this figure. Figure 4.22 illustrates the tube response to the “palm-strike” excitation. As previously mentioned, the duration of this signal is significantly greater than that generated with the square-wave input signal.

Linear Periodic Prediction Results

A single-input, adaptive, periodic, transversal filter was implemented in *MATLAB*® for this portion of the study. The transmitter input signal, as measured by the internal microphone, and its spectral magnitude are shown in Fig. 4.23. As seen in the spectrum plot, the signal energy is mainly concentrated within the first 5000 Hz, with the highest components between about 1500–3000 Hz. The frequency peaks around 2800, 8400, and 14000 Hz are likely due to the resonance of the small pipe directing the signal into the PVC tube. The length of this pipe is approximately 3.1 cm, corresponding to a propagation distance of 12.4 cm given its one open end. An attempt to accurately identify a linear characteristic outside the input signal frequency range is useless because the accuracy of the adaptation process is directly related to the input signal energy in any particular frequency region. Therefore, the recorded signal was downsampled from 44.1 kHz to 9.9 kHz. This unconventional

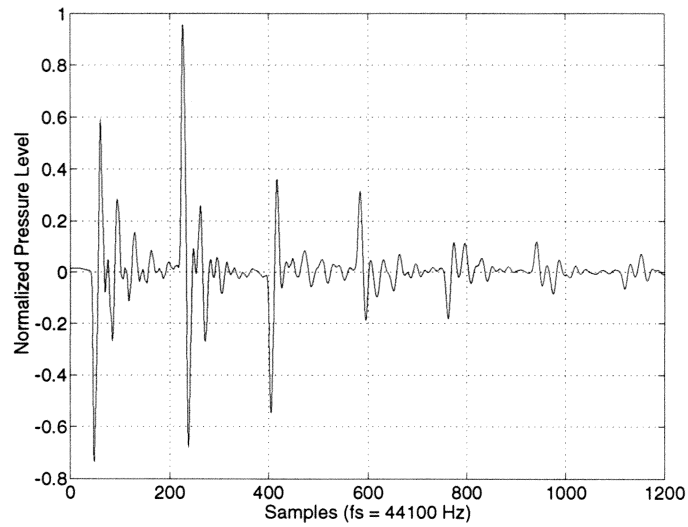


Fig. 4.21. Single pulse response in the PVC tube.

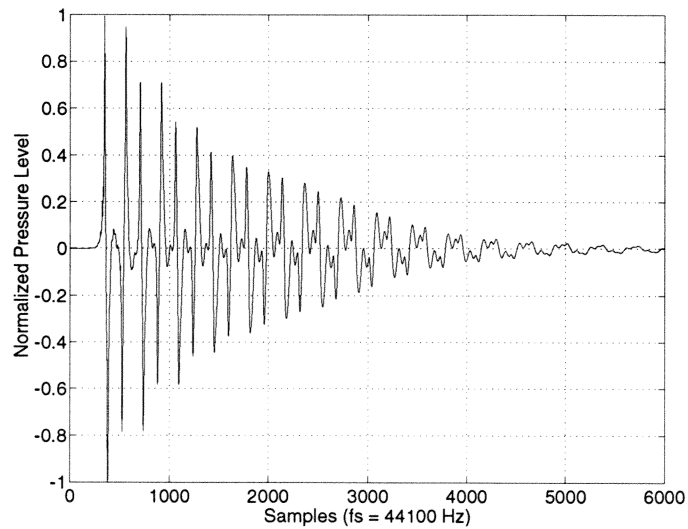


Fig. 4.22. Pulse response in the PVC tube via a palm-strike.

final sampling rate was chosen so that the signal period fell close to an integer value.

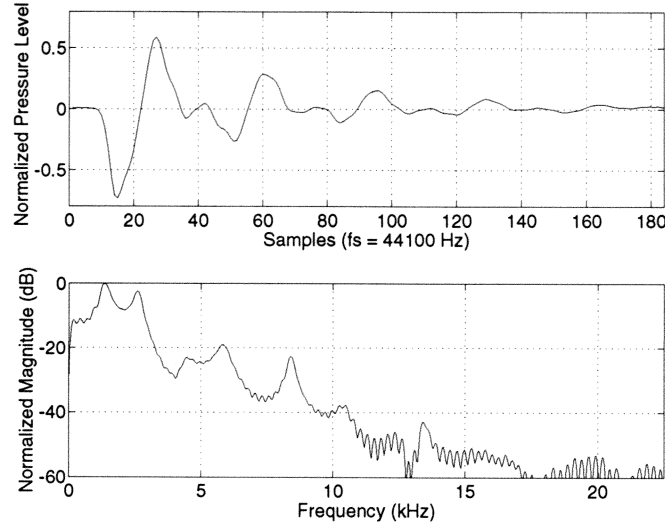


Fig. 4.23. Measured input signal: (top) Time domain; (bottom) Frequency domain.

Because the excitation response is of such short duration and also because it decays so rapidly, the predictor was configured to iterate through the data a specified number of times. For this signal, it was found that 50 iterations were necessary for the learning process to converge adequately. Seven weights were specified and the constant of adaptation was set to 0.04. The frequency response of the linear predictor weights is shown in Fig. 4.24. Thermal and dispersive losses in tubes increase with frequency, as well as radiation from the open end, and such a lowpass characteristic is evident in this figure. Not obvious from the magnitude plot is a 180 degree phase shift, or inversion, in the predicted response.

Linear periodic prediction was also performed on the “palm-strike” response of Fig. 4.22. Though this method of excitation was less rigorous than that using a signal transmitter, it proved effective in producing a longer duration and higher amplitude tube response. The first pulse in this signal, which represents the direct, palm generated excitation, is shown in Fig. 4.25, together with its associated frequency content. Before prediction was performed, the signal was somewhat arbitrarily downsampled to 11.025 kHz. Because this signal is of longer duration and magnitude than that of Fig. 4.23, the periodic predictor was able to adapt faster, and only 20 iterations were performed. The predicted linear characteristic using this response, as determined with 15 weights, is shown in Fig. 4.26.

The linear characteristics of Fig. 4.24 were determined to inaccurately represent the true linear filtering characteristic of the PVC tube, due largely to the high attenuation levels predicted. The cork stopper, through which the probe microphone and transmitter were inserted, represents just

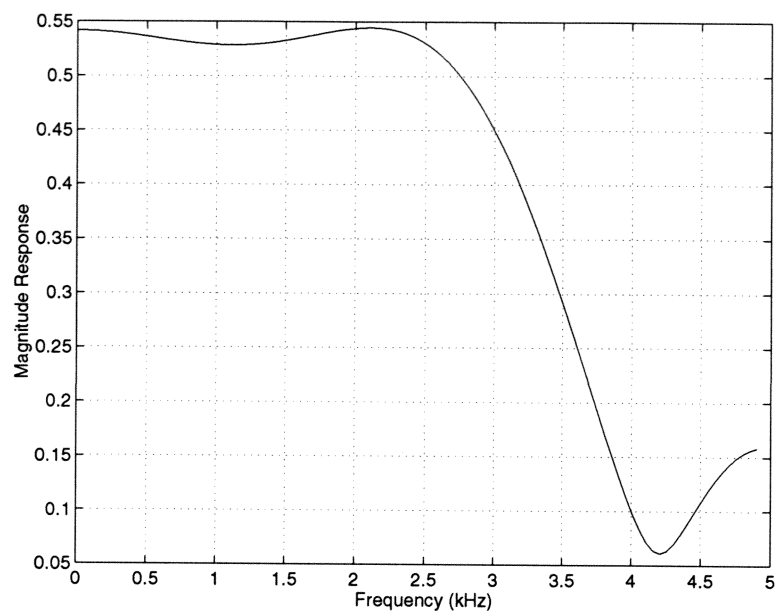


Fig. 4.24. Frequency Response Magnitude of Linear Weights.

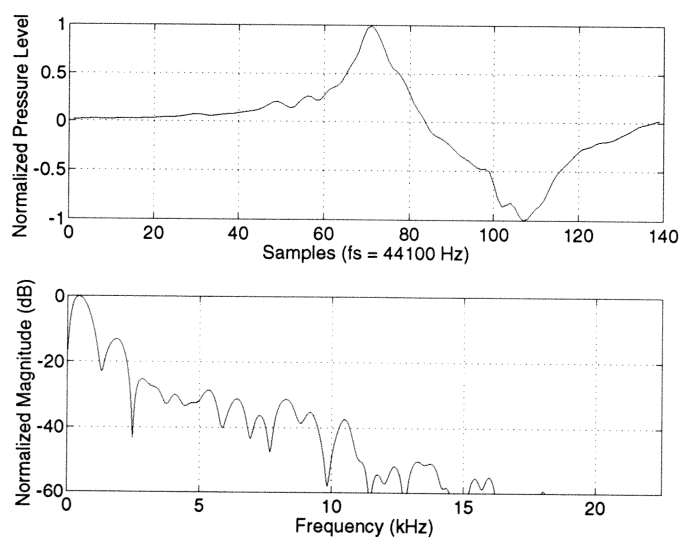


Fig. 4.25. Direct palm strike signal: (top) Time domain; (bottom) Frequency domain.

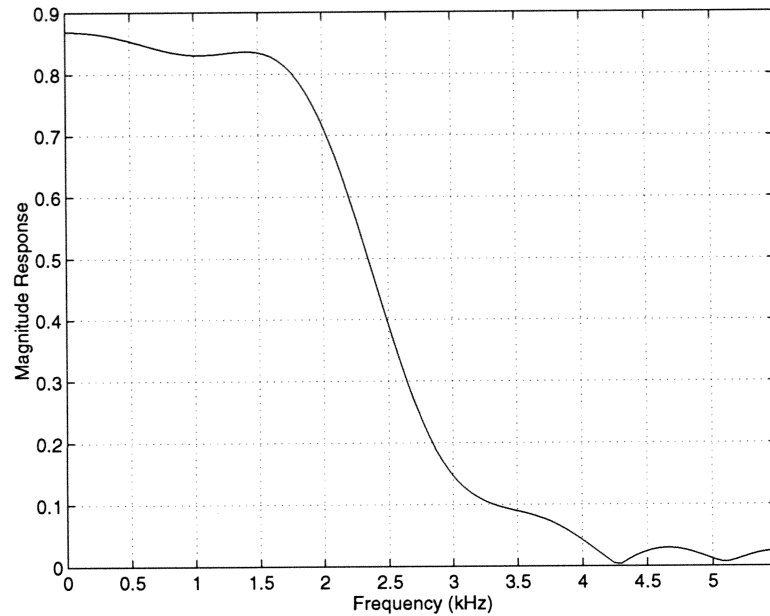


Fig. 4.26. Frequency response magnitude of the predicted linear weights using the palm strike excitation.

one likely source for extra losses in the system. Thus, the linear characteristic predicted from the “palm-strike” excitation was that used when performing the inverse filtering operation.

Nonlinear Element Experimental Setup and Measurements

The signal necessary as input to the nonlinear predictor is one obtained in the presence of the nonlinear excitation source. Thus, for this measurement the mouthpiece was re-attached to the PVC tubing and an Endevco 8510B-1 piezoresistive pressure transducer was used to measure the internal pressure signal. The setup for this experiment is shown in Fig. 4.27. In order to obtain a signal which might approximate the output of the reed nonlinearity, it was desired to have the microphone as close to the mouthpiece/reed as possible. Thus, the microphone was inserted through the reed near the back of the mouthpiece facing, in an area where reed vibrations are negligible. The pressure transducer output was fed into a Singular Solutions A/D 64x analog-to-digital converter and the digital signal was recorded on a NeXT computer. Figure 4.28 shows a portion of the signal recorded while the instrument is excited under normal reed operation. The signal period varies somewhat over the course of the recorded sound, but generally ranges between 402-403 samples, or about 9.1 ms.

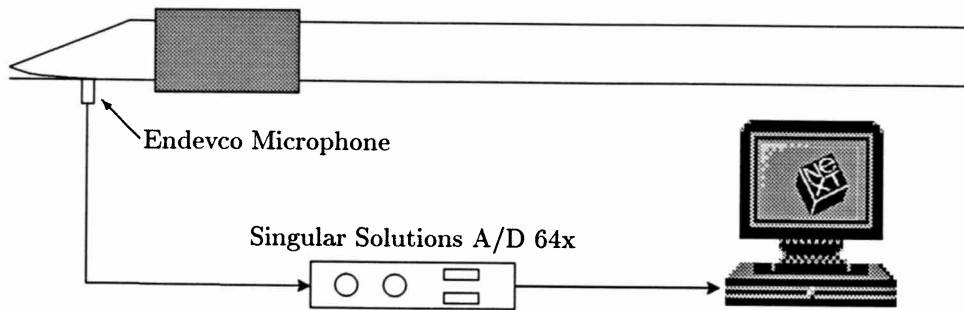


Fig. 4.27. Nonlinear element experiment setup.

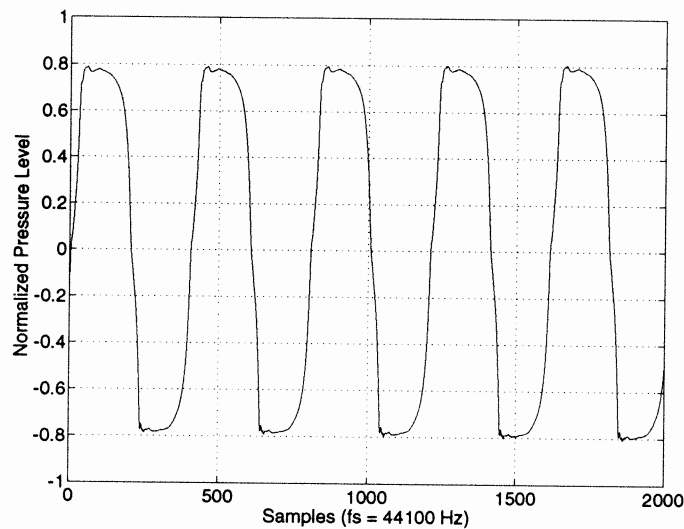


Fig. 4.28. Internal pressure signal in PVC tube under normal blowing conditions.

Nonlinear Periodic Prediction Results

A single-input, adaptive, periodic, nonlinear predictor was implemented in *MATLAB*[®] for this portion of the study. A simple digital waveguide clarinet model was developed based on the system diagram of Fig. 4.16 to test the nonlinear prediction procedure. The pressure-dependent reflection coefficient nonlinear excitation characteristic shown in Fig. 4.18 was used for this implementation. The resulting extracted nonlinear characteristics, as functions of the predictor weights, are shown in Figs. 4.29 and 4.30. In each case, the nonlinear predictor was iterated 15 times through the data, which was first inverse filtered to remove the effects of the linear element.

As seen in the figures, the nonlinear predictor was able to extract the nonlinear characteristic with reasonable accuracy. It should be noted, however, that the synthesized sounds were generated

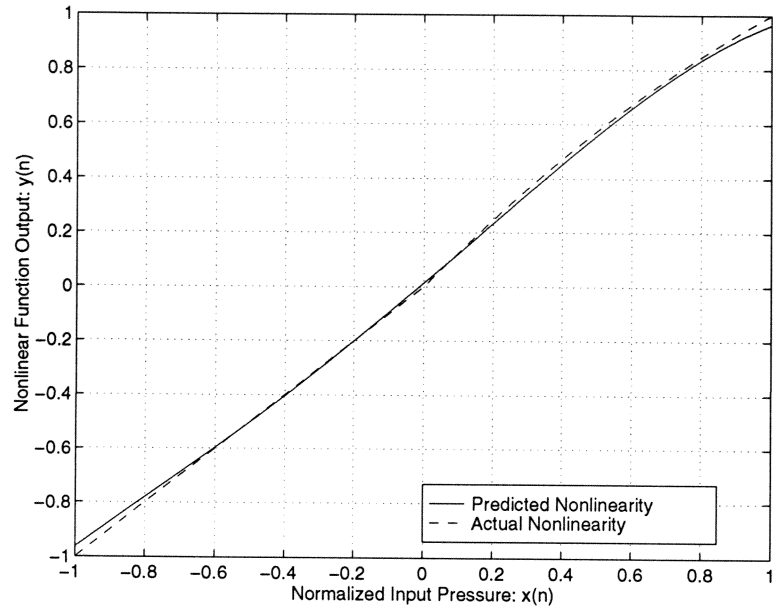


Fig. 4.29. Nonlinear polynomial function extracted from a synthesized sound.

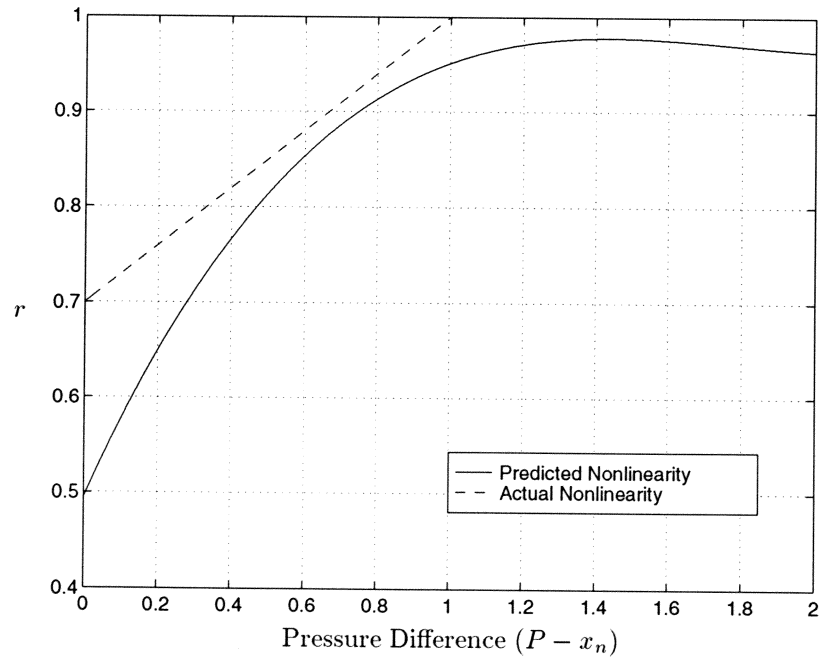


Fig. 4.30. Nonlinear reflection coefficient, as determined using nonlinear predictor weights which were extracted from a synthesized sound.

from a fixed nonlinear characteristic, and that the breath pressure was ramped up from zero to one during synthesis. Once a steady state regime is reached with these synthesis models, it is common for the nonlinear function to be significantly excited in only two small regions, as the signal is very “square-like.” By predicting through the transient portion of the synthesized signal, the nonlinear predictor was provided with more “information” about the nonlinearity and so it was better able to accurately adapt. As was mentioned previously, the nonlinear characteristic in real musical instruments changes with breath pressure. Thus, attempting to predict through transients in real sound recordings will theoretically not result in better nonlinear approximations.

The signal recorded under normal reed operation was sampled at a rate of 44.1 kHz. Its period was found to increase slightly from the beginning to the end of the sound. To apply an inverse filter designed from the previously determined linear characteristic, it was necessary that it be downsampled. Further, it was desired to perform the prediction separately using a transient portion and a steady-state section of the recorded sound and thus, in order that each portion’s respective period fell as close as possible to an integer value, the sound was downsampled to both 10.73 kHz and 10.691 kHz. The nonlinear polynomial functions predicted after inverse filtering are shown in Fig. 4.31, and their respective reflection functions in Fig. 4.32.

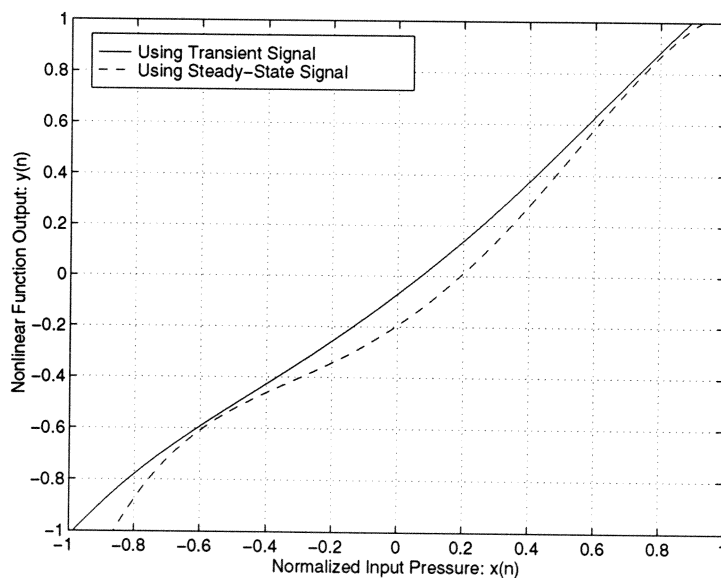


Fig. 4.31. Nonlinear polynomial functions extracted from the internal pressure signal measured in the experimental instrument.

All of the predicted nonlinear polynomial functions demonstrate unexpected results. From the discussion of Fig. 4.18, negative pressure levels of the input x_n were expected to produce an equal output level y_n , which corresponds to total reflection of the incoming bore pressure back into the bore. This would produce a function slope of positive one for negative values of x_n . Instead, most of the functions show a positive gain (y_n/x_n) greater than one somewhere in this region,

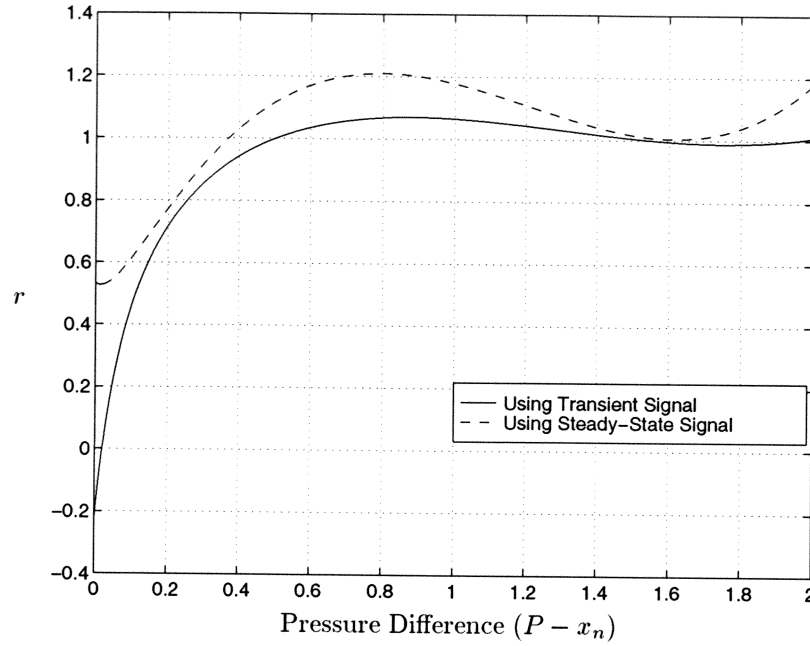


Fig. 4.32. Nonlinear reflection coefficient, as determined using nonlinear predictor weights which were extracted from the internal pressure signal measured in the experimental instrument.

implying an increase of negative pressure into the system (though the mouth pressure is positive). This is also evident in the reflection functions, corresponding to a reflection coefficient greater than one. Further, positive pressure levels of x_n were expected to produce an increased output level y_n due to the addition of mouth pressure into the system (and a corresponding gain greater than one). The histograms of Fig. 4.33 offer one clue to these behaviors. It is clear that the input is significantly isolated around just two regions, and never at a level exceeding 0.9. Thus, the polynomial approximations in these regions of low excitation cannot be assumed accurate. It is interesting to note that in the regions where the input signal contains significant energy, the predicted characteristics converge on a common result. It was seen that the polynomial function output level at $x_n = 1$ represents the breath pressure level (total transmission of bore pressure out the mouthpiece and total transmission of mouth pressure into the bore). All the predicted polynomial approximations at this point are greater than one, most likely the result of insufficient excitation energy. Thus, these characteristics do not obey the conservation of energy principles assumed of a two-port junction, and the polynomial reflection coefficient transformation relation is rendered invalid. In this case, it is necessary to perform the transformation using Eq. (4.34), evaluating the polynomial at individual points between negative one and positive one to obtain a respective reflection function.

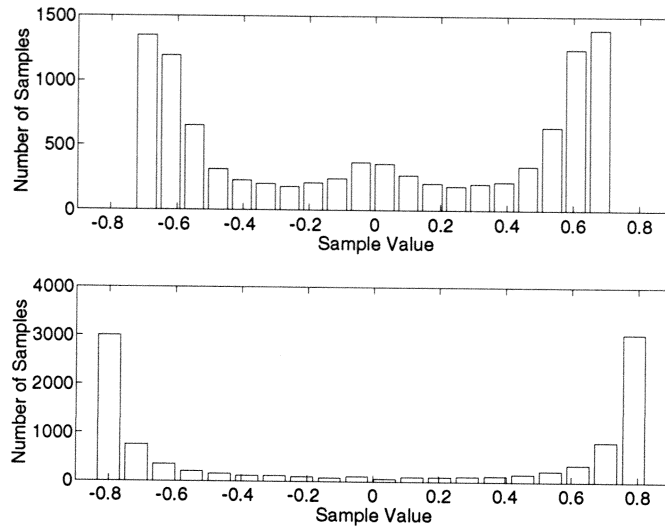


Fig. 4.33. Histograms of the transient (top) and steady-state (bottom) portions of the recorded signal.

Summary

The technique pursued in this project for extracting the linear characteristic of a musical instrument offers a fairly simple method for determining an FIR filter approximation to the behavior of a single air-column discontinuity. The accuracy of this approach, however, is largely dependent on the quality of the equipment used in the experiments. The results obtained in this study were generally valid, but would most likely improve with the acquisition of better measurement/excitation devices.

The approach investigated in this study for nonlinear prediction using musical instrument recordings involves inherent assumptions which hinder its accuracy. As mentioned previously, predicting through transient signals while assuming a constant breath pressure is also theoretically inaccurate, though it might result in some type of “mean” nonlinear characteristic. On the other hand, assuming that an accurate linear characteristic has been obtained, to what should its inverse be properly applied? The synthesized test signals were generated using a digital waveguide implementation based on the theoretical model of Fig. 4.16. Because the nonlinear prediction scheme was itself based on this same model, the nonlinear predictor was able to well identify the model nonlinear characteristic. In real musical instruments, however, any measurement of internal pressure represents the sum of left- and right-going traveling waves. It was hoped that by placing the microphone as close to the reed boundary as possible, the resulting signal would form an approximation to the output of the nonlinearity. In fact, it represents the sum of the output from and the input to this element. Thus, the system of Fig. 4.34 is a better approximation to the experimental instrument and its measured response. Ultimately, the nonlinear prediction approach is valid if a single traveling-wave compo-

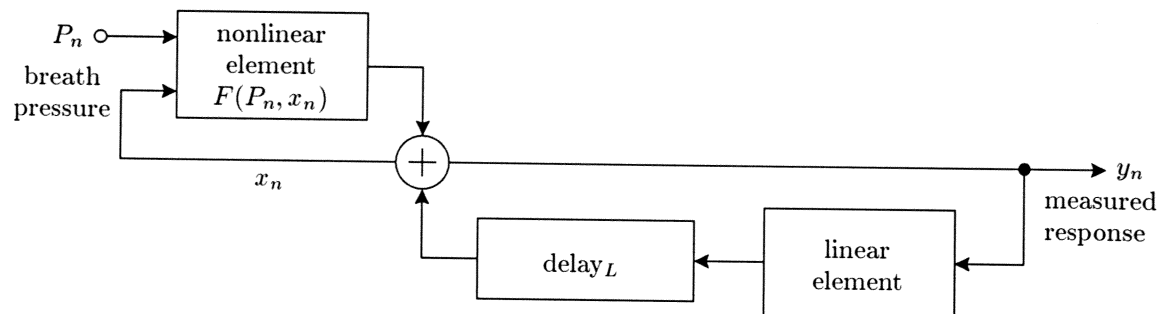


Fig. 4.34. A revised wind instrument model that might better correspond to the experimental instrument.

nent can be measured and/or isolated in steady-state sounds. While this is theoretically possible via measurements with two microphones, it proves extremely difficult in practice.

Chapter 5

Conclusions and Future Research

5.1 Summary and Conclusions

In general, this study provides a comprehensive review of single-reed woodwind instrument acoustic principles and then details a methodology for implementing this theory in the digital waveguide domain. As a result, efficient time-domain simulations of complete instrument systems are possible which incorporate the best available acoustic theory. Of particular importance, the “lumped-section” approach presented in Section 3.3.3 offers an efficient and stable means for implementing conical air column discontinuities that are characterized by growing exponentials and their associated unstable discrete-time filter approximations. Likewise, the two-port scattering junction model of a woodwind tonehole directly integrates the results of Keefe (1981, 1990) for efficient time-domain simulation. The three-port tonehole model offers a one-multiply, one-filter implementation which produces accurate results as well. Closure of the finger hole is best simulated in this form via time-varying control of the open hole resistance and/or acoustic mass parameters.

Further contributions of this study include mouthpiece and register-hole extensions to digital waveguide woodwind models. The tonehole discussion of Section 3.4.3 was directly applicable to the implementation of a woodwind register hole. Further, the series resistance and inertance model of the register hole has direct application to tonehole theory for efficient simulation of hole closure and open-hole radiation. Mouthpiece geometry variations and their associated timbral effects can be explored and implemented in a stable form using the “lumped-section” approach. It is interesting to note from such an implementation that the mouthpiece can potentially impose a “Helmholtz” mode on the overall air column resonance structure. Performance expression is easily implemented in the digital waveguide domain, in part because of the one-to-one correspondence between real instrument and model components.

The discussion of Chapter 2 was primarily motivated by the desire to compare woodwind instrument behavior, as predicted by acoustic theory, with intuition gained from years of professional

performance experience. The contributions of such an analysis are perhaps more relevant to the performance community, though collaborations between acousticians and performers will gain increasing importance in the development and refinement of the science of musical instrument acoustics.

This thesis lays the foundation for the development of complete woodwind instrument computer models based on current acoustic theory for time-domain, discrete-time simulations. The understanding of woodwind acoustic principles is reaching a point where it can aid in the design of real instruments. The computer models described here thus offer a practical means for testing acoustic theory and hold the potential to someday play a role in the computer-aided design of musical instruments.

5.2 Suggestions for Future Research

The “lumped-section” technique discussed in Sections 3.3.3 and 4.1.2 was developed in the late stages of this study. While this approach offers a practical solution for the implementation of conical air column discontinuities which are characterized by growing exponentials and unstable discrete-time filter approximations, further theoretical analysis is needed. In particular, it should be possible to determine a closed-form solution which explicitly demonstrates the stability of the lumped solution despite its unstable internal component. The frequency-domain transmission matrices can be expressed in terms of digital waveguide matrices (van Walstijn and de Bruin, 1995), which can then be cascaded to produce closed-form solutions.

Further aero-acoustic studies of the single-reed excitation mechanism are necessary. Current models are based, in part, on steady-state theory and display undesirable transient behavior. In particular, it appears that analyses of the nonlinear excitation in the presence of *unsteady* flow are warranted.

With the development of more accurate acoustic theory regarding nonlinear excitation mechanisms, digital waveguide models offer a potential means for the study of oral cavity influences on wind instrument acoustic behavior. Cook (1990) developed an articulatory model of the human vocal tract using digital waveguide techniques. It is reasonable to expect that this model can be “attached” to a digital waveguide wind instrument model to explore upstream influences.

Vortex shedding and flow turbulence near the nonlinear excitation mechanism of wind instruments produce noise in the resultant instrument sound. Such effects were not discussed in detail in this study, but are a necessary component of any instrument model. In practice, it is common to add white noise to the breath pressure stream to simulate turbulence within the system. This is clearly inadequate, however, and studies of pulsed and vortex noise (Chafe, 1990, 1995; Cook *et al.*, 1990) should be incorporated in these models.

The three-port tonehole implementation presented in Section 3.4.3 efficiently and accurately modeled the shunt impedance component of the Keefe (1981) tonehole model. Attempts to incorporate

the series impedance in the three-port scheme, however, have thus far been plagued by unstable digital filter scenarios, which result from the negative inductance characterization of Z_a . It may be possible to combine the frequency-dependent negative length correction associated with Z_a with an adjacent delay, in order to recast it as a positive inductance, and thus obtain a stable discrete-time implementation.

Appendix A

The Surface Area of a Spherical Wave Front in a Cone

Throughout this study, reference is made to the surface area of a spherical wave front in a conical frustum. This surface area can be determined in many ways. One method involves projecting an area S given by the surface $z = f(x, y)$ onto a closed region R in the $x - y$ plane, such that (Anton, 1984)

$$S = \iint_R \sqrt{\left(\frac{\partial z}{\partial x}\right)^2 + \left(\frac{\partial z}{\partial y}\right)^2 + 1} dA. \quad (\text{A.1})$$

In rectangular coordinates, a sphere of radius γ is given by $z = \sqrt{\gamma^2 - x^2 - y^2}$, so that the partial derivatives in Eq. (A.1) are given by

$$\frac{\partial z}{\partial x} = \frac{-x}{\sqrt{\gamma^2 - x^2 - y^2}} \quad (\text{A.2a})$$

$$\frac{\partial z}{\partial y} = \frac{-y}{\sqrt{\gamma^2 - x^2 - y^2}}. \quad (\text{A.2b})$$

The surface area S is then found as

$$\begin{aligned} S &= \iint \sqrt{\frac{x^2}{\gamma^2 - x^2 - y^2} + \frac{y^2}{\gamma^2 - x^2 - y^2} + 1} dA \\ &= \iint \frac{\gamma}{\sqrt{\gamma^2 - x^2 - y^2}} dA \\ &= \int_0^{2\pi} \int_0^a \frac{\gamma}{\sqrt{\gamma^2 - r^2}} r dr d\phi \\ &= \int_0^{2\pi} -\gamma \sqrt{\gamma^2 - r^2} \Big|_{r=0}^a d\phi \\ &= \int_0^{2\pi} \left(\gamma^2 - \gamma \sqrt{\gamma^2 - a^2} \right) d\phi = 2\pi \left(\gamma^2 - \gamma \sqrt{\gamma^2 - a^2} \right) \end{aligned}$$

$$\begin{aligned}
&= 2\pi \left(\gamma^2 - \gamma \sqrt{\gamma^2 - \gamma^2 \sin^2 \theta_0} \right) = 2\pi \gamma^2 \left(1 - \sqrt{1 - \sin^2 \theta_0} \right) \\
&= 2\pi \gamma^2 (1 - \cos \theta_0),
\end{aligned} \tag{A.3}$$

where a is the cross-sectional radius at the open end of the cone and ϕ and θ_0 are defined in Fig. A.1.

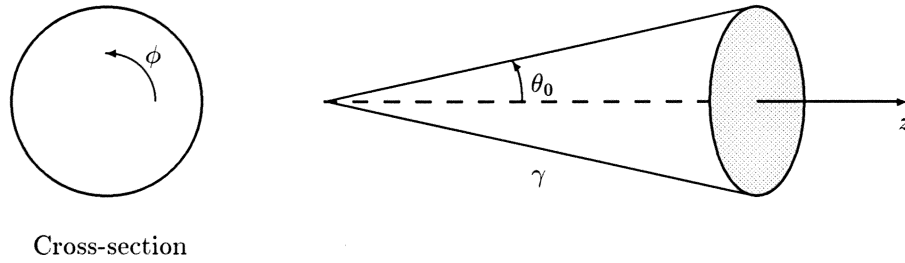


Fig. A.1. A conical section in spherical coordinates.

Benade (1988) provides a different expression for the spherical wave front surface area,

$$S = 2\pi a^2 \frac{1 - \cos \theta_0}{\sin^2 \theta_0}, \tag{A.4}$$

which is equivalent for $a = \gamma \sin \theta_0$.

Appendix B

Saxophone Air Column Measurements

Approximate measurements were taken from a modern Selmer Paris[®] Super Action 80, Series II, alto saxophone (serial number 438024). These values are listed below, together with measurements given by (Nederveen, 1969, p. 106) for comparison.

Estimated Distances (m)	Selmer Alto	Schenkelaars Alto
Reed tip to cone apex	0.12	0.14
Reed tip to $A4\sharp$ – $B4$ hole	0.41	0.40
Reed tip to $C4$ – $D4$ hole	0.79	0.76
β for $A4\sharp$ – $B4$ hole	0.23	0.26
β for $C4$ – $D4$ hole	0.13	0.16

Table B.1. Air column measurements and estimated truncation ratios (β) for Selmer and Schenkelaars alto saxophones.

The estimated distance from reed tip to cone apex was determined by smoothly projecting the neck taper out to its intersection. From the neck end, this distance is approximately equal to 0.18 meters. The mouthpiece provides an additional length of approximately 0.06 meters to the neck, so that the reed tip to apex distance is given by 0.12 meters. Saxophone mouthpieces come in a multitude of shapes and sizes, so that these proportions will vary to great extent. The mouthpiece used in this study was custom built by Ronald L. Caravan, and would be considered to be slightly shorter than an average alto saxophone mouthpiece. The toneholes are given by their *written* note values, and correspond to the pitches produced when those holes are closed–open. That is, when the $C4$ – $D4$ hole is closed, a written $C4$ is produced, while a written $D4$ is sounded when the hole is open. Tonehole measurements were made to the center of the tonehole.

Appendix C

Experimental Equipment

This appendix provides detailed information about most of the equipment used for linear and nonlinear prediction study.

1. **Piezoresistive Pressure Transducer**, Endevco Corporation, Model 8510B-1, Serial #AFE79

The Endevco Model 8510B-1 is a rugged, miniature, high sensitivity piezoresistive pressure transducer. With its high resonance frequency (55000 Hz), wide frequency response (± 0.5 dB to 4000 Hz, ± 5 dB to more than 16000 Hz), high sensitivity, small dimensions, and resistance to moisture, this unit can handle the difficult task of measuring the high sound pressure levels found inside “wind-blown” musical instruments.

2. **Electret Condenser Microphone Cartridge**, Panasonic, Panasonic Part No. WM-063T

The Panasonic WM-063T is a cheap and small (6.0×5.0 mm) electret condenser microphone. Its reported frequency range is 20-20000 Hz with a sensitivity of $-64\text{dB} \pm 3\text{dB}$.

3. **Signal Transmitter**, Radio Shack

This was a cheap “ear plug” style transmitter. The poor frequency response of this unit hindered the accuracy of this study’s results.

4. **Regulated Power Supply**, SRC Division/Moxon Electronics, Model 3564, Serial #13363

5. **Pulse Generator**, Interdesign Inc., Model 1101, Serial #233

6. **Analog to Digital Converter**, Singular Solutions, Model A/D 64x, Serial #AD 01067

Appendix D

MATLAB Code

The following *MATLAB*[®] functions and scripts demonstrate many of the model techniques discussed in this thesis. The function *openpipe* determines a discrete-time reflectance filter approximation to the Levine and Schwinger unflanged open pipe radiation solution. The function *boundary* determines a discrete-time filter approximation to the thermoviscous losses along the walls of a cylindrical pipe. The function *openhole* is used to design two-port scattering junction reflectance and transmittance discrete-time filters for an open tonehole. Similarly, the function *closhole* is used to design two-port scattering junction reflectance and transmittance discrete-time filters for a closed tonehole. The function *branch* is used to design a three-port scattering junction open tonehole branch discrete-time reflectance filter. The script *clarinet* is an example digital waveguide clarinet implementation that demonstrates the use of the above mentioned functions. The nonlinear excitation is modeled using the pressure-dependent reflection coefficient method.

D.1 openpipe.m

```
function [b,a]=openpipe(nb,na,ra,fs,display)
%OPENPIPE Discrete filter least squares fit to Levine & Schwinger
%          unflanged cylindrical bore reflectance.
%
% [B,A] = OPENPIPE(NB,NA,RA,FS,DISPLAY) gives real numerator and
% denominator coefficients B and A of orders NB and NA respectively,
% where RA is the radius of the cylinder (in meters) and FS is the
% desired sampling rate (in Hz). This function calls INVREQZ with
% an omega-2 weighting function for the filter design process. A
% reference temperature of 26.85 degrees celsius (80 F) is assumed.
% If the value of DISPLAY is 1, the continuous-time and
% discrete-time reflectance magnitude and phase responses will be
% plotted.
%
```

```

% By Gary P. Scavone, CCRMA, Stanford University, 12 March 1997.

if nargin~=5,
    error('Number of arguments is incorrect.');
```

return

```
end

% Physical constants and evaluation frequencies

n = 1024;                % Number of evaluation frequencies %
omega = pi/n:pi/n:pi;
c = 347.23;
k = omega*fs/c;

% The Levine & Schwinger results were calculated by numerical
% integrations out to the limit k*a <= 3.8. The following
% sixth-order polynomial approximations were then made to the
% reflectance magnitude and end correction terms. For values
% of k*a > 3.8, the reflectance magnitude and end corrections
% are approximated by smooth extensions.

rPoly = [-0.00121212308521, 0.01893693792170, -0.12135001867818, 0.39739947149894,
          -0.61154450497445, 0.01320529396146, 1.00000000000000];
loaPoly = [-0.00134446448269, 0.01444668268791, -0.06220104767324, 0.136922621132,
            -0.16112693515620, -0.01536258568872, 0.61000296711212];

z = k*ra;
if max(z) <= 3.8,
    r = polyval(rPoly,z);
    loa = polyval(loaPoly,z);
else
    i=1;
    while z(i) <= 3.8,
        i = i + 1;
    end
    z1 = z(1:i-1);
    z2 = z(i:length(z));
    scale = polyval(rPoly,z(i))*z(i)^(3);
    r = [polyval(rPoly,z1),scale./z2.^3];
    loa = polyval(loaPoly,z1);
    scale = polyval(loaPoly,3.8)*0.8^2;
    loa = [loa, scale./(z2 - 3).^2];
end
R = -r.*exp(-2*j*z.*loa);

% Design digital filter using method described in JOS thesis,
% pp. 47-50 & 101-103.

% Weighting to help fit at low frequencies

wt = 1./omega.^2;
```

```

[b,a] = invfreqz(R,omega,nb,na,wt);

% Check filter stability %

ps = roots(a);
if length(ps)>0,
    for j=1:length(ps),
        if abs(ps(j)) >= 1.0,
            disp('Filter is unstable ... change design parameters!');
        end
    end
end

% Plot responses %

if display==1,
    h = freqz(b,a,omega);
    clf
    subplot(2,1,1)
    plot(omega,abs(R),omega,abs(h));
    legend('Continuous-Time Response','Discrete-Time Response');
    title('Open Pipe Reflectance');
    ylabel('Magnitude');
    xlabel('Discrete-Time Radian Frequency')
    grid
    axis([0 pi 0 1.1])
    subplot(2,1,2)
    plot(omega,angle(R),omega,angle(h));
    ylabel('Phase (radians)');
    xlabel('Discrete-Time Radian Frequency')
    grid
    axis([0 pi 0 pi])
    disp('Paused ... hit any key to continue.')
    pause
end

```

D.2 boundary.m

```

function [b,a]=boundary(nb,na,ra,fs,nz,display)
%BOUNDARY Discrete filter least squares fit to the attenuation
%          and phase delay characteristic of viscous and thermal
%          losses along the walls of a rigid cylindrical duct.
%
% [B,A] = BOUNDARY(NB,NA,RA,FS,NZ,DISPLAY) gives real numerator and
% denominator coefficients B and A of order NB and NA respectively,
% where RA is the duct radius (in meters), FS is the system
% sampling rate (in Hz), and NZ is the number of unit sample delays
% for which the boundary losses are modeled. This function calls
% INVREQZ with an omega^(-2) weighting function for the filter

```



```

% design process. A reference temperature of 26.85 degrees celsius
% (80 F) is assumed. If the value of DISPLAY is 1, the continuous-
% time and discrete-time reflectance magnitude and phase responses
% will be plotted.
%
% By Gary P. Scavone, CCRMA, Stanford University, 12 March 1997.

if nargin~=6,
    error('Number of arguments is incorrect.');
```

$$\text{return}$$

```
end

% Physical constants and evaluation frequencies

n = 1024;                % Number of evaluation frequencies %
omega = pi/n:pi/n:pi;
c = 347.23;
rho = 1.1769;
eta = 1.846*10(-5);
k = omega*fs/c;

% Duct characteristic impedance

Ro = rho*c/(pi*ra2);

% Duct Losses (approximations for 300 K)

rv = ra*(rho*fs*omega/eta).(0.5);
alpha = k.*(1.045*rv.(-1) + 1.08*rv.(-2) + 0.75*rv.(-3));
vpinv = (1 + 1.045*rv.(-1))./c;

% Desired Filter Response

H = (exp(-j*omega.*(c.*vpinv - 1) - c*alpha/fs)).nz;

% Design digital filter using method described in JOS thesis,
% pp. 47-50 & 101-103.

% Weighting to help fit at low frequencies

wt = omega.(-2);

[b,a] = invfreqz(H,omega,nb,na,wt);

% Check filter stability %

ps = roots(a);
if length(ps)>0,
    for j=1:length(ps),
        if abs(ps(j)) >= 1.0,
            disp('Filter is unstable ... change design parameters!');
```

```

        end
    end
end

% Plot responses %

if display==1,
    h = freqz(b,a,omega);
    clf
    subplot(2,1,1)
    plot(omega,abs(H),omega,abs(h));
    legend('Continuous-Time Response','Discrete-Time Response');
    title('Boundary-Layer Losses');
    ylabel('Magnitude');
    xlabel('Discrete-Time Radian Frequency')
    grid
    axis([0 pi 0 1.1])
    subplot(2,1,2)
    plot(omega,angle(H),omega,angle(h));
    ylabel('Phase (radians)');
    xlabel('Discrete-Time Radian Frequency')
    grid
    axis([0 pi -pi 0])
    disp('Paused ... hit any key to continue.')
    pause
end

```

D.3 openhole.m

```

function [br,ar,bt,at]=openhole(ra,rb,tw,rc,fs,display)
%OPENHOLE Discrete filter least squares fit to the open tonehole
%         two-port reflectance and transmittance, as derived from
%         Keefe (1990).
%
% [BR,AR,BT,AT] = OPENHOLE(RA,RB,TW,RC,FS,DISPLAY) gives real
% numerator and denominator reflectance coefficients BR and AR
% for a two-zero/one-pole filter, and transmittance coefficients
% BT and AT of order two, where RA is the main bore radius, RB is
% the tonehole radius, TW is the tonehole wall height, RC is the
% tonehole radius of curvature, and FS is the model sampling rate
% (in Hz). All length values should be given in meters. The
% discrete-time transmittance filter is designed using INVREQZ
% with an omega-2 weighting function. The discrete-time
% reflectance filter is designed by Kopec's method, in conjunction
% with INVREQZ. A reference temperature of 26.85 degrees celsius
% (80 F) is assumed. If the value of DISPLAY is 1, the continuous-
% time and discrete-time reflectance magnitude and phase responses
% will be plotted.
%

```

```

% RB can be a vector of tonehole radii, in which case the B's and
% A's are matrices of corresponding filter coefficients. Only the
% first tonehole reflectance responses will be plotted.
%
% By Gary P. Scavone, CCRMA, Stanford University, 12 March 1997.

if nargin~=6,
    error('Number of arguments is incorrect.');
```

$$\text{return}$$

```
end

% Physical constants and evaluation frequencies

n = 1023;                % Number of evaluation frequencies %
omega = pi/n:pi/n:pi;
c = 347.23;
rho = 1.1769;
eta = 1.846*10^(-5);
k = omega*fs/c;
dv = sqrt(2*eta ./ (rho*omega*fs));

% Bore and Tonehole characteristic impedances

Ro = rho*c/(pi*ra^2);
Rho = rho*c/(pi*rb.^2);

% Real part of propagation wavenumber in tonehole %

alpha = (3*10^(-5)./rb)'*sqrt(omega*fs/(2*pi));

% Tonehole geometric height

t = tw + (rb/8).*(rb/ra).*(1 + 0.172*(rb/ra).^2);

% Open tonehole effective length and specific resistance

te = (ones(size(rb'))*(1./k).*tan(t'*k) + ...
      rb'.*(1.4 - 0.58*(rb/ra).^2)*ones(size(k))) ./ ...
      (1 - 0.61*rb'*k.*tan(t'*k));
xie = 0.25*(rb'*k).^2 + (t'*ones(size(k))).*alpha + ...
      (ones(size(rb'))*(0.25*k.*dv)).*((log((2/rc)*rb'))*ones(size(k)));

% Open tonehole series equivalent length

tao = 0.47*rb.*(rb/ra).^4./(tanh(1.84*t./rb) ...
      + 0.62*(rb/ra).^2 + 0.64*(rb/ra));

% Open Tonehole Shunt & Series Impedances %

Zso = Rho' * ones(size(k)).* (j*ones(size(rb'))*k.*te + xie);
Zao = (-j*Rho.*tao).' * k;
```



```

% Open Tonehole Reflectance & Transmittance %

rop = (Zso.*Zao - Ro^2) ./ (Zso.*Zao + 2*Ro*Zso + Ro^2);
top = 2*Ro*Zso ./ (Zso.*Zao + 2*Ro*Zso + Ro^2);

% The Matlab function invfreqz() doesn't do a good job fitting
% zeros for the reflectance. Thus, the filter is designed using
% Kopec's method (JOS thesis, pg. 46-47). A single pole is
% first fit to rop(w) and the resulting response is divided out
% of rop(w) to get D2(w). Two poles are then fit to 1./D2(w).
% These poles become the zeros of the final discrete-time filter.

na = 2;    % poles %
nb = 2;    % zeros %

% Weighting to help fit at low frequencies

wt = 1 ./ omega.^ 2;

br = zeros(length(rb),nb+1);
ar = zeros(length(rb),2);
bt = zeros(length(rb),nb+1);
at = zeros(length(rb),na+1);

for i=1:length(rb),
    [b1,a1] = invfreqz(rop(i,:),omega,0,1,wt);
    temp = freqz(b1,a1,omega);
    [b2,a2] = invfreqz(temp./rop(i,:),omega,0,2,wt);
    br(i,:) = b1*a2/b2;
    ar(i,:) = a1;
    br(i,:) = -abs(rop(i,1))*sum(ar(i,:))*br(i,:)/sum(br(i,:));
    [bt(i,:),at(i,:)] = invfreqz(top(i,:),omega,nb,na,wt);

    % Check filter stability %

    psr = roots(ar(i,:));
    pst = roots(at(i,:));
    if length(psr)>0,
        for j=1:length(psr),
            if abs(psr(j)) >= 1.0,
                disp('Filter is unstable ... change design parameters!');
            end
        end
    end
    if length(pst)>0,
        for j=1:length(pst),
            if abs(pst(j)) >= 1.0,
                disp('Filter is unstable ... change design parameters!');
            end
        end
    end
end

```

```

        end
    end

% Plot responses %

if display==1,
    h = freqz(br(1,:),ar(1,:),omega);
    clf
    subplot(2,1,1)
    plot(omega,abs(rop(1,:)),omega,abs(h));
    legend('Continuous-Time Response','Discrete-Time Response');
    title('Open Tonehole Reflectance');
    ylabel('Magnitude');
    xlabel('Discrete-Time Radian Frequency')
    grid
    axis([0 pi 0 1.1])
    subplot(2,1,2)
    plot(omega,angle(rop(1,:)),omega,angle(h));
    ylabel('Phase (radians)');
    xlabel('Discrete-Time Radian Frequency')
    grid
    axis([0 pi -pi pi])
    disp('Paused ... hit any key to continue.')
    pause
end

```

D.4 closhole.m

```

function [br,ar,bt,at]=closhole(ra,rb,tw,fs,display)
%CLOSHOLE Discrete filter least squares fit to the closed tonehole
%          two-port reflectance and transmittance, as derived from
%          Keefe (1990).
%
% [BR,AR,BT,AT] = CLOSHOLE(RA,RB,TW,FS,DISPLAY) gives real
% numerator and denominator reflectance coefficients BR and AR and
% transmittance coefficients BT and AT of order two, where RA is
% the main bore radius, RB is the tonehole radius, TW is the
% tonehole wall height, and FS is the model sampling rate (in Hz).
% All length values should be given in meters. This function calls
% INVREQZ with a 1/omega^2 weighting function for the filter
% design process. A reference temperature of 26.85 degrees celsius
% (80 F) is assumed. If the value of DISPLAY is 1, the continuous-
% time and discrete-time reflectance magnitude and phase responses
% will be plotted.
%
% RB can be a vector of tonehole radii, in which case the B's and
% A's are matrices of corresponding filter coefficients. Only the
% first tonehole reflectance responses will be plotted.
%

```

```

% By Gary P. Scavone, CCRMA, Stanford University, 12 March 1997.

if nargin~=5,
    error('Number of arguments is incorrect.');
```

$$\text{return}$$

```

end

% Physical constants and evaluation frequencies

n = 1024;                % Number of evaluation frequencies %
omega = pi/n:pi/n:pi;
c = 347.23;
rho = 1.1769;
k = omega*fs/c;

% Bore and Tonehole characteristic impedances

Ro = rho*c/(pi*ra^2);
Rho = rho*c./(pi*rb.^2);

% Tonehole geometric height

t = tw + (rb/8).*(rb/ra).*(1 + 0.172*(rb/ra).^2);

% Closed tonehole series equivalent length

tac = 0.47*rb.*(rb/ra).^4./(coth(1.84*t./rb) + 0.62*(rb/ra).^2 + 0.64*(rb/ra));

% Closed Tonehole Shunt & Series Impedances %

Zsc = -j*Rho.' * ones(size(k)) .* (cot(t'*k) + (t.*(0.25*(rb./t).^2 ...
    + 0.58*(rb/ra).^2 - pi*rb ./ (4*t))))'*k;
Zac = (-j*Rho.*tac).'* k;

% Closed Tonehole Reflectance %

rcl = (Zsc.*Zac - Ro^2) ./ (Zsc.*Zac + 2*Ro*Zsc + Ro^2);
tcl = 2*Ro*Zsc ./ (Zsc.*Zac + 2*Ro*Zsc + Ro^2);

% Design digital filter using method described in JOS thesis,
% pp. 47-50 & 101-103.

na = 2;    % poles %
nb = 2;    % zeros %

% Weighting to help fit at low frequencies

wt = 1 ./ omega.^ 2;

br = zeros(length(rb),nb+1);
ar = zeros(length(rb),na+1);

```



```

bt = zeros(length(rb),nb+1);
at = zeros(length(rb),na+1);

for i=1:length(rb),
    [br(i,:),ar(i,:)] = invfreqz(rcl(i,:),omega,nb,na,wt);
    [bt(i,:),at(i,:)] = invfreqz(tcl(i,:),omega,nb,na,wt);

    % Check filter stability %

    psr = roots(ar(i,:));
    pst = roots(at(i,:));
    if length(psr)>0,
        for j=1:length(psr),
            if abs(psr(j)) >= 1.0,
                disp('Filter is unstable ... change design parameters!');
            end
        end
    end
    if length(pst)>0,
        for j=1:length(pst),
            if abs(pst(j)) >= 1.0,
                disp('Filter is unstable ... change design parameters!');
            end
        end
    end
end

% Plot responses %

if display==1,
    h = freqz(br(1,:),ar(1,:),omega);
    clf
    subplot(2,1,1)
    plot(omega,abs(rcl(1,:)),omega,abs(h));
    legend('Continuous-Time Response','Discrete-Time Response');
    title('Closed Tonehole Reflectance');
    ylabel('Magnitude');
    xlabel('Discrete-Time Radian Frequency')
    grid
    axis([0 pi 0 1.1])
    subplot(2,1,2)
    plot(omega,angle(rcl(1,:)),omega,angle(h));
    ylabel('Phase (radians)');
    xlabel('Discrete-Time Radian Frequency')
    grid
    axis([0 pi -pi pi])
    disp('Paused ... hit any key to continue.')
    pause
end

```

D.5 branch.m

```

function [br,ar]=branch(ra,rb,tw,fs,display)
%BRANCH Discrete filter least squares fit to an open tonehole
%       reflectance for use in a 3-port waveguide model.
%
%       [BR,AR] = BRANCH(RA,RB,TW,FS,DISPLAY) gives real numerator
%       and denominator reflectance coefficients BR and AR of order
%       one, where RA is the main bore radius, RB is the tonehole
%       radius, TW is the tonehole wall height, and FS is the model
%       sampling rate (in Hz). All length values should be given in
%       meters. This function calls INVREQZ with an omega(-2)
%       weighting function for the filter design process. A reference
%       temperature of 26.85 degrees celsius (80 F) is assumed. If
%       the value of DISPLAY is 1, the continuous-time and discrete-time
%       reflectance magnitude and phase responses will be plotted.
%
%       By Gary P. Scavone, CCRMA, Stanford University, 12 March 1997.

if nargin~=5,
    error('Number of arguments is incorrect.');
```

```

    return
end

% Physical constants and evaluation frequencies

n = 1024;                % Number of evaluation frequencies %
omega = pi/n:pi/n:pi;
c = 347.23;
k = omega*fs/c;

% Tonehole geometric height

t = tw + (rb/8).*(rb/ra).*(1 + 0.172*(rb/ra).^2);

% The Levine & Schwinger results were calculated by numerical
% integrations out to the limit k*a <= 3.8. The following
% sixth-order polynomial approximations were then made to the
% reflectance magnitude and end correction terms. For values
% of k*a > 3.8, the reflectance magnitude and end corrections
% are approximated by smooth extensions.

rPoly = [-0.00121212308521, 0.01893693792170, -0.12135001867818, 0.39739947149894,
          -0.61154450497445, 0.01320529396146, 1.00000000000000];
loaPoly = [-0.00134446448269, 0.01444668268791, -0.06220104767324, 0.136922621132,
            -0.16112693515620, -0.01536258568872, 0.61000296711212];

z = k*ra;
if max(z) <= 3.8,
    r = polyval(rPoly,z);

```

```

    loa = polyval(loaPoly,z);
else
    i=1;
    while z(i) <= 3.8,
        i = i + 1;
    end
    z1 = z(1:i-1);
    z2 = z(i:length(z));
    scale = polyval(rPoly,z(i))*z(i)^(3);
    r = [polyval(rPoly,z1),scale./z2.^3];
    loa = polyval(loaPoly,z1);
    scale = polyval(loaPoly,3.8)*0.8^2;
    loa = [loa, scale./(z2 - 3).^2];
end
R = -r.*exp(-2*j*z.*loa);

% Open Tonehole Reflectance %

rop = R.*exp(-2*j*k*t);

% Design digital filter using method described in JOS thesis,
% pp. 47-50 & 101-103.

na = 1;    % poles %
nb = 1;    % zeros %

% Weighting to help fit at low frequencies

wt = 1 ./ omega.^ 2;

br = zeros(1,nb+1);
ar = zeros(1,na+1);

[br,ar] = invfreqz(rop,omega,nb,na,wt);

% Check filter stability %

ps = roots(ar);
if length(ps)>0,
    for j=1:length(ps),
        if abs(ps(j)) >= 1.0,
            disp('Filter is unstable ... change design parameters!');
        end
    end
end

% Plot responses %

if display==1,
    h = freqz(br,ar,omega);
    clf

```



```

subplot(2,1,1)
plot(omega,abs(rop),omega,abs(h));
legend('Continuous-Time Response','Discrete-Time Response');
title('Open Tonehole Reflectance');
ylabel('Magnitude');
xlabel('Discrete-Time Radian Frequency')
grid
axis([0 pi 0 1.1])
subplot(2,1,2)
plot(omega,angle(rop),omega,angle(h));
ylabel('Phase (radians)');
xlabel('Discrete-Time Radian Frequency')
grid
axis([0 pi -pi pi])
disp('Paused ... hit any key to continue.')
pause
end

```

D.6 clarinet.m

```

% clarinet.m
%
% This matlab script implements a digital waveguide clarinet model.
% Two toneholes are implemented with two-port scattering junctions,
% and a third tonehole is implemented with a three-port junction.
% An open-end reflectance filter based on the solution of Levine
% & Schwinger is used, and boundary-layer losses are modeled for the
% longest air column length only. The nonlinear excitation is
% implemented by the pressure-dependent reflection coefficient method.
%
% By Gary P. Scavone, CCRMA, Stanford University, 12 March 1997.

% *** Signal Parameters *** %

fs = 44100;           % sampling rate
N = 15000;           % number of samples to compute

% ***** Air Column Parameters ***** %

c = 347.23;           % speed of sound in air (meters/second)
ra = 0.0189/2;        % radius of bore (meters)
tw = 0.0034;          % shortest tonehole height (meters)
rc = 0.0005;          % tonehole radius of curvature (meters)

% ***** Tonehole Radii (meters) ***** %

rb = [0.00953, 0.00794, 0.00953]/2;

% FINGERING: Fill in the vector below to indicate the tonehole

```

```

%          fingering. Each element in the vector corresponds to
%          the tonehole given by the tonehole radii vector (rb)
%          above. For each element, a "0" indicates an open hole
%          and a "1" indicates a closed hole.

finger = [1 0 0];

% ***** Distances From Excitation To Toneholes & End (m) ***** %

L = [0.6 0.65 0.7 0.8];

% ***** Rounded Distances Between Elements (samples) ***** %

D = round(fs*[L(1) L(2:length(L))-L(1:length(L)-1)]/c);

% ***** Tonehole Filter Coefficient Vectors ***** %
% The first two toneholes are implemented using two-port scattering
% junctions. The last tonehole is implemented using a three-port
% junction.

br_th = zeros(length(rb)-1,3);
ar_th = zeros(length(rb)-1,3);
bt_th = zeros(length(rb)-1,3);
at_th = zeros(length(rb)-1,3);
zrup_th = zeros(length(rb)-1,2);
ztup_th = zeros(length(rb)-1,2);
zrdn_th = zeros(length(rb)-1,2);
ztdn_th = zeros(length(rb)-1,2);

% ***** Closed Tonehole 2-Port Filter Coefficients ***** %

for i=1:2,
    if finger(i)==1,
        [br_th(i,:),ar_th(i,:),bt_th(i,:),at_th(i,:)] = ...
            closhole(ra,rb(i),tw,fs,1);
    end
end

% ***** Open Tonehole 2-Port Filter Coefficients ***** %

for i=1:2,
    if finger(i)==0,
        [br_th(i,:),ar_th(i,1:2),bt_th(i,:),at_th(i,:)] = ...
            openhole(ra,rb(i),tw,rc,fs,1);
    end
end

% ***** Three-Port Junction Scattering Coefficient ***** %

r0 = -rb(3)^2 ./ (rb(3)^2 + 2*ra^2);

```

```

% ***** Three-Port Branch Filter Coefficients ***** %

if finger(3)==0,
    b_branch = [0 1];
    a_branch = [1 0];
else
    [b_branch,a_branch] = branch(ra,rb(3),tw,fs,1);
end
z_branch = [0];

% ***** Open-end Reflectance Filter ***** %

[b_open,a_open] = openpipe(1,2,ra,fs,1);
z_open = [0 0];

% ***** Boundary-Layer Losses ***** %
% The air column lengths between toneholes are short, so that losses
% will be small in these sections. Further, such losses can be
% commuted with fractional-delay filters (which are not incorporated
% here). In this model, boundary-layer losses are only included for
% the first, long cylindrical bore section.

[b_boundary,a_boundary] = boundary(2,2,ra,fs,D(1),1);
z_boundary = zeros(2,2);

% ***** Initialize delay lines ***** %

y = zeros(1,N); % initialize output vector
dl1 = zeros(2,D(1));
dl2 = zeros(2,D(2));
dl3 = zeros(2,D(3));
dl4 = zeros(2,D(4));
ptr = ones(length(rb)+1);
upin2pt = zeros(size(rb-1));
dnin2pt = zeros(size(rb-1));
upin3pt = 0;
dnin3pt = 0;
p_branch = 0; % 3-port tonehole branch pressure
p_oc = 0; % initial oral cavity pressure
pinc = 0.01; % oral cavity pressure increment

% ***** %
% %
% Delay Line %
% |-----| %
% ^ %
% pointer %
% %
% >>--- pointer increments --->> %
% %
% ***** %

```



```

%
% The pointer initially points to each delay line output.
% We can take the output and calculate a new input value
% which is placed where the output was taken from. The
% pointer is then incremented and the process repeated.

% ***** Run Loop Start ***** %

for i = 1:N,

    pbminus = dl1(2,ptr(1));
    upin2pt = [dl1(1,ptr(1)), dl2(1,ptr(2))];
    dnin2pt = [dl2(2,ptr(2)), dl3(2,ptr(3))];
    upin3pt = dl3(1,ptr(3));
    dnin3pt = dl4(2,ptr(4));

% ***** Boundary-Layer Loss Filter Calculations ***** %

    [upin2pt(1),z_boundary(1,:)] = ...
        filter(b_boundary,a_boundary,upin2pt(1),z_boundary(1,:));
    [pbminus,z_boundary(2,:)] = ...
        filter(b_boundary,a_boundary,pbminus,z_boundary(2,:));

% ***** Open-end Filter Calculations ***** %

    [dl4(2,ptr(4)),z_open] = filter(b_open,a_open,dl4(1,ptr(4)),z_open);

% ***** First Tonehole Calculations: Two-Port ***** %

    [temp1,zrup_th(1,:)] = filter(br_th(1,:),ar_th(1,:),upin2pt(1),zrup_th(1,:));
    [temp2,ztdn_th(1,:)] = filter(bt_th(1,:),at_th(1,:),dnin2pt(1),ztdn_th(1,:));
    dl1(2,ptr(1)) = temp1 + temp2;
    [temp1,zrtn_th(1,:)] = filter(br_th(1,:),ar_th(1,:),dnin2pt(1),zrtn_th(1,:));
    [temp2,ztup_th(1,:)] = filter(bt_th(1,:),at_th(1,:),upin2pt(1),ztup_th(1,:));
    dl2(1,ptr(2)) = temp1 + temp2;

% ***** Second Tonehole Calculations: Two-Port ***** %

    [temp1,zrup_th(2,:)] = filter(br_th(2,:),ar_th(2,:),upin2pt(2),zrup_th(2,:));
    [temp2,ztdn_th(2,:)] = filter(bt_th(2,:),at_th(2,:),dnin2pt(2),ztdn_th(2,:));
    dl2(2,ptr(2)) = temp1 + temp2;
    [temp1,zrtn_th(2,:)] = filter(br_th(2,:),ar_th(2,:),dnin2pt(2),zrtn_th(2,:));
    [temp2,ztup_th(2,:)] = filter(bt_th(2,:),at_th(2,:),upin2pt(2),ztup_th(2,:));
    dl3(1,ptr(3)) = temp1 + temp2;

% ***** Third Tonehole Calculations: Three-Port ***** %

    [p_branch,z_branch] = filter(b_branch,a_branch,p_branch,z_branch);
    temp1 = r0*(upin3pt+dnin3pt-2*p_branch);
    dl3(2,ptr(3)) = temp1 + dnin3pt;
    dl4(1,ptr(4)) = temp1 + upin3pt;

```

```

    p_branch = temp1 + dnin3pt + upin3pt - p_branch;

% ***** Excitation Calculations ***** %

    p_delta = 0.5*p_oc - pbminus;

% ***** Pressure-Dependent Reflection Coefficient ***** %

    refl = 0.7 + 0.4*p_delta;
    if refl > 1.0
        refl = 1.0;
    end
    dl1(1,ptr(1)) = 0.5*p_oc - p_delta*refl;

% The system output is determined at the input to the air
% column. The oral cavity is incremented until it reaches
% the desired value.

    y(i) = pbminus + dl1(1,ptr(1));
    if p_oc < 1,
        p_oc = p_oc + pinc;
    end

% ***** Increment Pointers & Check Limits ***** %

    for j=1:4,
        ptr(j) = ptr(j) + 1;
        if ptr(j) > D(j),
            ptr(j) = 1;
        end
    end
end

% Clear Figure Window, Plot, and Play

clf
plot(y)
title('Internal Air-Column Signal')
xlabel('Samples')
ylabel('Signal Level')
sound(y,fs)

```

References

- Agulló, J., Barjau, A., and Martínez, J. (1988). Alternatives to the impulse response $h(t)$ to describe the acoustical behavior of conical ducts. *J. Acoust. Soc. Am.*, 84(5):1606–1612.
- Agulló, J., Barjau, A., and Martínez, J. (1992). On the time-domain description of conical bores. *J. Acoust. Soc. Am.*, 91(2):1099–1105.
- Agulló, J., Cardona, S., and Keefe, D. (1995). Time-domain deconvolution to measure reflection functions for discontinuities in waveguides. *J. Acoust. Soc. Am.*, 97(3):1950–1957.
- Anton, H. (1984). *Calculus, with analytic geometry*. New York: John Wiley and Sons, 2nd edn.
- Ayers, D. R. (1996). Impulse responses for feedback to the driver of a musical wind instrument. *J. Acoust. Soc. Am.*, 100(2):1190–1198.
- Ayers, D. R., Eliason, L. J., and Mahgerefteh, D. (1985). The conical bore in musical acoustics. *Am. J. Phys.*, 53(6):528–537.
- Backus, J. (1961). Vibrations of the reed and air column in the clarinet. *J. Acoust. Soc. Am.*, 33(6):806–809.
- Backus, J. (1963). Small-vibration theory of the clarinet. *J. Acoust. Soc. Am.*, 35(3):305–313.
- Backus, J. (1974). Input impedance curves for the reed woodwind instruments. *J. Acoust. Soc. Am.*, 56(4):1266–1279.
- Backus, J. (1978). Multiphonic tones in the woodwind instrument. *J. Acoust. Soc. Am.*, 63(2):591–599.
- Backus, J. (1985). The effect of the player’s vocal tract on woodwind instrument tone. *J. Acoust. Soc. Am.*, 78(1):17–20.
- Bak, N. and Dømler, P. (1987). The relation between blowing pressure and blowing frequency in clarinet playing. *Acustica*, 63(3):238–241.

- Bartolozzi, B. (1967). *New Sounds for Woodwind*. London: Oxford University Press. Translated and edited by Reginald Smith Brindle.
- Benade, A. H. (1959). On woodwind instrument bores. *J. Acoust. Soc. Am.*, 31(2):137–146.
- Benade, A. H. (1960). On the mathematical theory of woodwind finger holes. *J. Acoust. Soc. Am.*, 32(12):1591–1608.
- Benade, A. H. (1963). Thermal perturbations in woodwind bores. *J. Acoust. Soc. Am.*, 35(11):1901.
- Benade, A. H. (1968). On the propagation of sound waves in a cylindrical conduit. *J. Acoust. Soc. Am.*, 44(2):616–623.
- Benade, A. H. (1976). *Fundamentals of Musical Acoustics*. New York: Oxford University Press.
- Benade, A. H. (1977). On woodwind instrument bores. In E. L. Kent, editor, *Musical Acoustics: Piano and Wind Instruments*, vol. 9 of *Benchmark Papers in Acoustics*, pp. 274–283. Dowden, Hutchinson, and Ross. Reprint of original article with corrections regarding the calculation of input impedance resonance frequencies.
- Benade, A. H. (1985). Air column, reed, and player's windway interaction in musical instruments. In I. R. Titze and R. C. Scherer, editors, *Vocal Fold Physiology, Biomechanics, Acoustics, and Phonatory Control*, chap. 35, pp. 425–452. Denver Center for the Performing Arts.
- Benade, A. H. (1988). Equivalent circuits for conical waveguides. *J. Acoust. Soc. Am.*, 83(5):1764–1769.
- Benade, A. H. and Jansson, E. (1974a). On plane and spherical waves in horns with nonuniform flare: I. Theory of radiation, resonance frequencies, and mode conversion. *Acustica*, 31(2):80–98.
- Benade, A. H. and Jansson, E. (1974b). On plane and spherical waves in horns with nonuniform flare: II. Prediction and measurements of resonance frequencies and radiation losses. *Acustica*, 31(4):185–202.
- Benade, A. H. and Lutgen, S. J. (1988). The saxophone spectrum. *J. Acoust. Soc. Am.*, 83(5):1900–1907.
- Benade, A. H. and Richards, W. B. (1983). Oboe normal mode adjustment via reed and staple proportioning. *J. Acoust. Soc. Am.*, 73(5):1794–1803.
- Berlioz, H. (1842). Musical instruments – Monsieur Adolphe Sax. *Journal des débats politiques et littéraires* (Paris), p. 3. Translated and quoted by Fred L. Hemke in *The Early History of the Saxophone*. Ph.D. thesis, University of Wisconsin, 1975, pp. 20–23.

- Berlioz, H. (1856). *Treatise on Instrumentation*. London: Novello and Co. Ltd. Translated by Mary Cowden Clarke. Revised and edited by Joseph Bennett.
- Berners, D. and Smith, J. O. (1994). On the use of Schrödinger's Equation in the analytic determination of horn reflectance. In ICMC (1994), pp. 419–422.
- Bouasse, H. and Fouchée, M. (1930). *Instruments à vent*, vol. 1. Paris: Librairie Delagrave. New edition: Librairie Scientifique et Technique, A. Blanchard, Paris 1986.
- Brindley, G. (1973). Speed of sound in bent tubes and the design of wind instruments. *Nature*, 246(5434):479–480.
- Caravan, R. L. (1974). *Extensions of Technique for Clarinet and Saxophone*. Ph.D. thesis, Eastman School of Music, The University of Rochester.
- Caravan, R. L. (1979). Utilizing the older curved soprano saxophones. *The Saxophone Symposium*, pp. 16–22.
- Caussé, R., Kergomard, J., and Lurton, X. (1984). Input impedance of brass musical instruments—comparison between experiment and numerical models. *J. Acoust. Soc. Am.*, 75(1):241–254.
- Chafe, C. D. (1990). Pulsed noise in self-sustained oscillations of musical instruments. In *Proc. Int. Conf. Acoustics, Speech, and Signal Processing*, New York. IEEE Press. Available as CCRMA Technical Report STAN-M-65, Department of Music, Stanford University.
- Chafe, C. D. (1995). Adding vortex noise to wind instrument physical models. In ICMC (1995), pp. 57–60.
- Clinch, P. G., Troup, G. J., and Harris, L. (1982). The importance of vocal tract resonance in clarinet and saxophone performance: A preliminary account. *Acustica*, 50:280–284.
- Cohen, P. (1991a). Allen Loomis and the incredible double resonance alto saxophone: Part I. *Saxophone Journal*, pp. 8–10.
- Cohen, P. (1991b). Allen Loomis and the incredible double resonance alto saxophone: Part II. *Saxophone Journal*, pp. 8–11.
- Cohen, P. (1991c). Vents, waves and octave splits: Part I. *Saxophone Journal*, pp. 8–10.
- Cohen, P. (1991d). Vents, waves and octave splits: Part II. *Saxophone Journal*, pp. 8–9.
- Coltman, J. W. (1966). Resonance and sounding frequencies of the flute. *J. Acoust. Soc. Am.*, 40(1):99–107.

- Cook, P. R. (1988). Implementation of single reed instruments with arbitrary bore shapes using digital waveguide filters. Tech. rep., CCRMA, Dept. of Music, Stanford University, Stanford, California, Report no. STAN-M-50.
- Cook, P. R. (1990). *Identification of Control Parameters in an Articulatory Vocal Tract Model, With Applications to the Synthesis of Singing*. Ph.D. thesis, Elec. Eng. Dept., Stanford University.
- Cook, P. R. (1991). Non-linear periodic prediction for on-line identification of oscillator characteristics in woodwind instruments. In ICMC (1991), pp. 157–160.
- Cook, P. R. (1992). A meta-wind-instrument physical model, and a meta-controller for real time performance control. In ICMC (1992), pp. 273–276.
- Cook, P. R. (1995). Integration of physical modeling for synthesis and animation. In ICMC (1995), pp. 525–528.
- Cook, P. R., Chafe, C. D., and Smith, J. O. (1990). Pulsed noise in musical systems: Techniques for extraction, analysis, and visualization. In *Proc. 1990 Int. Computer Music Conf.*, pp. 63–65, Glasgow, Scotland. Computer Music Association.
- Elmore, W. C. and Heald, M. A. (1985). *Physics of Waves*. New York: Dover Publications, Inc.
- Fletcher, N. H. (1979). Excitation mechanisms in woodwind and brass instruments. *Acustica*, 43(1):63–72.
- Fletcher, N. H. and Rossing, T. D. (1991). *The Physics of Musical Instruments*. New York: Springer-Verlag.
- Franken, H., Clement, J., Cauberghs, M., and van de Woestijne, K. P. (1981). Oscillating flow of a viscous compressible fluid through a rigid tube: A theoretical model. *IEEE Trans. Biomed. Eng.*, BME-28:416–420.
- Gilbert, J., Kergomard, J., and Polack, J. D. (1990a). On the reflection functions associated with discontinuities in conical bores. *J. Acoust. Soc. Am.*, 87(4):1773–1780.
- Gilbert, J., Meynial, X., and Kergomard, J. (1990b). The influence of the reed and the reed table on the fundamental frequency of a single-reed system. In *Colloque de Physique*, Supplément au Journal de Physique II, pp. 833–836, Lyon, France. First French Conference on Acoustics.
- Halévy, F., Savart, N., and Boquillon, N. (1848). *Affaire Sax: Rapport d'expertise par messieurs F. Halévy, N. Savart et N. Boquillon*. Paris: Imprimerie Édouard Proux et Cie. Translated and quoted by Fred L. Hemke in *The Early History of the Saxophone*. Ph.D. thesis, University of Wisconsin, 1975, p. 61.

- Helmholtz, H. (1954). *On the Sensations of Tone as a Physiological Basis for the Theory of Music*. New York: Dover Publications, Inc. Translated by Alexander J. Ellis from the 4th German Edition of 1877.
- Hemke, F. L. (1975). *The Early History of the Saxophone*. Ph.D. thesis, University of Wisconsin.
- Hirschman, S. E. (1991). *Digital Waveguide Modeling and Simulation of Reed Woodwind Instruments*. Engineering thesis, Electrical Engineering Dept., Stanford University. Available as CCRMA Technical Report STAN-M-72, Music Dept., Stanford University, July 1991.
- Hirschberg, A., Dane, H. J., Houtsma, A. J. M., Kruijswijk, S. G., van de Laar, R. W. A., Marrou-Maurières, J. P., and Wijnands, P. J. (1990). A quasi-stationary model of air flow in the reed channel of single-reed woodwind instruments. *Acustica*, 70(2):146–154.
- Hirschberg, A., Gilbert, J., Wijnands, A. P. J., and Valkering, A. M. C. (1994). Musical aeroacoustics of the clarinet. In *Journal de Physique IV*, Supplément au Journal de Physique III, n°5, pp. 559–568, Toulouse, France. Third French Conference on Acoustics.
- Hirschberg, A., Kergomard, J., and Weinreich, G., editors (1995). *The Mechanics of Musical Instruments*. No. 355 in CISM Courses and Lectures. New York: Springer-Verlag.
- Hoekje, P. L. (1986). *Intercomponent Energy Exchange and Upstream/Downstream Symmetry in Nonlinear Self-Sustained Oscillations of Reed Instruments*. Ph.D. thesis, Case Western Reserve University.
- Hoekje, P. L. (1995). A brief summary of A.H. Benade's wind instrument adjustment principles. *J. Catgut Soc.*, 2(7):16–24. (Series II).
- Hoersch, V. A. (1925). Non-radial harmonic vibrations within a conical horn. *Physics Review*, 25:218–224.
- ICMC (1991). *Proc. 1991 Int. Computer Music Conf.*, Montreal, Canada. Computer Music Association.
- ICMC (1992). *Proc. 1992 Int. Computer Music Conf.*, San Jose, California. Computer Music Association.
- ICMC (1993). *Proc. 1993 Int. Computer Music Conf.*, Tokyo, Japan. Computer Music Association.
- ICMC (1994). *Proc. 1994 Int. Computer Music Conf.*, Århus, Denmark. Computer Music Association.
- ICMC (1995). *Proc. 1995 Int. Computer Music Conf.*, Banff, Canada. Computer Music Association.
- ICMC (1996). *Proc. 1996 Int. Computer Music Conf.*, Hong Kong. Computer Music Association.

- Jaffe, D. A. and Smith, J. O. (1983). Extensions of the Karplus-Strong plucked string algorithm. *Computer Music J.*, 7(2):56–69. Reprinted in C. Roads (ed.) 1989. *The Music Machine*. Cambridge, Massachusetts, MIT Press, pp. 481–494.
- Jaffe, D. A. and Smith, J. O. (1995). Performance expression in commuted waveguide synthesis of bowed strings. In *ICMC (1995)*, pp. 343–346.
- Kastner, G. (1846). *Méthode complète et raisonnée de saxophone*. Paris: E. Troupenas et Cie. Translated and quoted by Fred L. Hemke in *The Early History of the Saxophone*. Ph.D. thesis, University of Wisconsin, 1975, p. 60.
- Keefe, D., Barjau, A., and Agulló, J. (1993). Theory of wave propagation in axisymmetric horns. In *Proc. Stockholm Musical Acoustics Conf.*, pp. 496–500.
- Keefe, D. H. (1981). *Woodwind Tone-hole Acoustics and the Spectrum Transformation Function*. Ph.D. thesis, Case Western Reserve University.
- Keefe, D. H. (1983). Acoustic streaming, dimensional analysis of nonlinearities, and tone hole mutual interactions in woodwinds. *J. Acoust. Soc. Am.*, 73(5):1804–1820.
- Keefe, D. H. (1984). Acoustical wave propagation in cylindrical ducts: Transmission line parameter approximations for isothermal and nonisothermal boundary conditions. *J. Acoust. Soc. Am.*, 75(1):58–62.
- Keefe, D. H. (1989). Woodwind design algorithms to achieve desired tuning. *J. Catgut Soc.*, 1(3):14–22. (Series II).
- Keefe, D. H. (1990). Woodwind air column models. *J. Acoust. Soc. Am.*, 88(1):35–51.
- Keefe, D. H. (1996). Wind-instrument reflection function measurement in the time domain. *J. Acoust. Soc. Am.*, 99(4):2370–2381. See erratum in *J. Acoust. Soc. Am.*, 100(6):3985.
- Keefe, D. H. (1997). Personal communication.
- Kelly, Jr., J. L. and Lochbaum, C. C. (1962). Speech synthesis. In *Proc. Fourth Int. Congress on Acoustics*, pp. 1–4, Copenhagen, Denmark. Paper G42.
- Kergomard, J. (1989). Tone hole external interactions in woodwind musical instruments. In *Proc. 13th Int. Congress on Acoustics*, Yugoslavia.
- Kool, J. (1987). *Das Saxophon*. England: Egon Publishers Limited. First published in 1931. English translation by Lawrence Gwozdz.
- Laakso, T. I., Välimäki, V., Karjalainen, M., and Laine, U. (1992). Real-time implementation techniques for a continuously variable digital delay in modeling musical instruments. In *ICMC (1992)*, pp. 14–18.

- Laakso, T. I., Välimäki, V., Karjalainen, M., and Laine, U. (1994). Crushing the delay – Tools for fractional delay filter design. Tech. rep., Helsinki University of Technology, Faculty of Electrical Engineering, Laboratory of Acoustics and Audio Signal Processing, Espoo, Finland, Report no. 35.
- Leeson, C. (1960). The modern saxophone mouthpiece. *The Instrumentalist*, 15(2):86–87.
- Levine, H. and Schwinger, J. (1948). On the radiation of sound from an unflanged circular pipe. *Phys. Rev.*, 73(4):383–406.
- Lord Rayleigh, J. W. S. (1896). *The Theory of Sound*. London: The Macmillan Company, 2nd edn. Reprinted 1945, New York: Dover Publications.
- Mapes-Riordan, D. (1993). Horn modeling with conical and cylindrical transmission-line elements. *J. Audio Eng. Soc.*, 41(6):471–484.
- Markel, J. D. and Gray, A. H. (1976). *Linear Prediction of Speech*. New York: Springer-Verlag.
- Martínez, J. and Agulló, J. (1988). Conical bores. Part I: Reflection functions associated with discontinuities. *J. Acoust. Soc. Am.*, 84(5):1613–1619.
- Martínez, J., Agulló, J., and Cardona, S. (1988). Conical bores. Part II: Multiconvolution. *J. Acoust. Soc. Am.*, 84(5):1620–1627.
- McIntyre, M. E., Schumacher, R. T., and Woodhouse, J. (1983). On the oscillations of musical instruments. *J. Acoust. Soc. Am.*, 74(5):1325–1345.
- McIntyre, M. E. and Woodhouse, J. (1979). On the fundamentals of bowed-string dynamics. *Acustica*, 43(2):93–108.
- Morse, P. M. (1981). *Vibration and Sound*. American Institute of Physics, for the Acoustical Society of America. (1st ed. 1936, 2nd ed. 1948).
- Morse, P. M. and Feshbach, H. (1953). *Methods of Mathematical Physics*. New York: McGraw-Hill Book Company, Inc.
- Morse, P. M. and Ingard, K. U. (1968). *Theoretical Acoustics*. Princeton, New Jersey: Princeton University Press.
- Nederveen, C. J. (1969). *Acoustical Aspects of Woodwind Instruments*. Amsterdam, The Netherlands: Frits Knuf.
- Olson, H. F. (1957). *Acoustical Engineering*. Princeton, New Jersey: D. Van Nostrand Company, Inc.
- Oppenheim, A. V. and Schaffer, R. W. (1989). *Discrete-Time Signal Processing*. Englewood Cliffs, New Jersey: Prentice Hall, Inc.

- Plitnik, G. R. and Strong, W. J. (1979). Numerical method for calculating input impedances of the oboe. *J. Acoust. Soc. Am.*, 65(3):816–825.
- Putland, G. R. (1993). Every one-parameter acoustic field obeys Webster’s Horn Equation. *J. Audio Eng. Soc.*, 41(6):435–451.
- Pyle, Jr., R. W. (1975). Effective length of horns. *J. Acoust. Soc. Am.*, 57(6):1309–1317.
- Radiguer, H. (1931). La vie et l’oeuvre d’Adolphe Sax. In Lavignac, editor, *Encyclopédie de la musique et dictionnaire du Conservatoire*, vol. 6, pp. 3732–3747. Paris: Librairie Delagrave. Translated and quoted by Fred L. Hemke in *The Early History of the Saxophone*. Ph.D. thesis, University of Wisconsin, 1975, pp. 62–63.
- Rascher, S. M. (1954). Thoughts about the saxophone mouthpiece. *The Instrumentalist*, 9(2):18–21.
- Rascher, S. M. (1970). The saxophone - A 15-12-4 instrument? *The Instrumentalist*, 24(10):49–51.
- Salmon, V. (1946*a*). Generalized plane wave theory of horns. *J. Acoust. Soc. Am.*, 17:199–211.
- Salmon, V. (1946*b*). A new family of horns. *J. Acoust. Soc. Am.*, 17:212–218.
- Saneyoshi, J., Teramura, H., and Yoshikawa, S. (1987). Feedback oscillations in reed woodwind and brasswind instruments. *Acustica*, 62:194–210.
- Savioja, L., Rinne, T. J., and Takala, T. (1994). Simulation of room acoustics with a 3-D finite difference mesh. In ICMC (1994), pp. 463–466.
- Scavone, G. P. (1995). Digital waveguide modeling of the non-linear excitation of single-reed woodwind instruments. In ICMC (1995), pp. 521–524.
- Scavone, G. P. (1996). Modeling and control of performance expression in digital waveguide models of woodwind instruments. In ICMC (1996), pp. 224–227.
- Scavone, G. P. and Cook, P. R. (1994). Combined linear and non-linear prediction in calibrating models of musical instruments to recordings. In ICMC (1994), pp. 433–434. Send email to gary@ccrma.stanford.edu to request a copy of the full paper.
- Schumacher, R. T. (1981). *Ab Initio* calculations of the oscillations of a clarinet. *Acustica*, 48(2):71–85.
- Shafer, B. (1950). *Through History with J. Wesley Smith*. The Vanguard Press.
- Smith, J. O. (1983). *Techniques for Digital Filter Design and System Identification with Application to the Violin*. Ph.D. thesis, Elec. Eng. Dept., Stanford University.

- Smith, J. O. (1985). A new approach to digital reverberation using closed waveguide networks. In *Proc. 1985 Int. Computer Music Conf.*, pp. 47–53, Vancouver, Canada. Computer Music Association.
- Smith, J. O. (1986). Efficient simulation of the reed-bore and bow-string mechanisms. In *Proc. 1986 Int. Computer Music Conf.*, pp. 275–280, The Hague, Netherlands. Computer Music Association.
- Smith, J. O. (1987). Music applications of digital waveguides. Tech. Rep. STAN-M-39, CCRMA, Music Dept., Stanford University. A compendium containing four related papers and presentation overheads on digital waveguide reverberation, synthesis, and filtering.
- Smith, J. O. (1991). Waveguide simulation of non-cylindrical acoustic tubes. In *ICMC (1991)*, pp. 304–307.
- Smith, J. O. (1996a). Discrete-time modeling of acoustic systems. *CCRMA Technical Report*. Monograph in progress, draft dated Oct. 24, 1996.
- Smith, J. O. (1996b). Discrete-time modeling of acoustic systems with applications to sound synthesis of musical instruments. In *Proc. Nordic Acoustical Meeting, Helsinki*, pp. 21–32. Plenary paper. Available online at <http://www-ccrma.stanford.edu/~jos/>.
- Sommerfeldt, S. D. and Strong, W. J. (1988). Simulation of a player-clarinets system. *J. Acoust. Soc. Am.*, 83(5):1908–1918.
- Stewart, G. W. and Lindsay, R. B. (1930). *Acoustics*. New York: D. Van Nostrand Company, Inc.
- Stewart, S. E. and Strong, W. J. (1980). Functional model of a simplified clarinet. *J. Acoust. Soc. Am.*, 68(1):109–120.
- Thompson, S. C. (1979). The effect of the reed resonance on woodwind tone production. *J. Acoust. Soc. Am.*, 66(5):1299–1307.
- Välimäki, V. (1995). *Discrete-Time Modeling of Acoustic Tubes Using Fractional Delay Filters*. Ph.D. thesis, Helsinki University of Technology, Faculty of Electrical Engineering, Laboratory of Acoustic and Audio Signal Processing, Espoo, Finland, Report no. 37.
- Välimäki, V., Karjalainen, M., and Laakso, T. I. (1993). Modeling of woodwind bores with finger holes. In *ICMC (1993)*, pp. 32–39.
- Välimäki, V., Laakso, T. I., and Mackenzie, J. (1995). Elimination of transients in time-varying allpass fractional delay filters with application to digital waveguide modelling. In *ICMC (1995)*, pp. 327–334.
- Van Duyne, S., Jaffe, D. A., Scandalis, G. P., and Stilson, T. (1996). The signal controlled allpass interpolated delay line. Presented at the CCRMA Affiliates Meeting, 1996.

- Van Duyne, S. and Smith, J. O. I. (1993). Physical modeling with the 2-D digital waveguide mesh. In ICMC (1993), pp. 40–47.
- Van Duyne, S. and Smith, J. O. I. (1996). The 3D tetrahedral digital waveguide mesh with musical applications. In ICMC (1996), pp. 411–418.
- van Walstijn, M. and de Bruin, G. (1995). Conical waveguide filters. In *Proc. Second Int. Conf. Acoustics and Music Research*, pp. 47–54, Ferrara, Italy.
- Weber, W. (1830). Compensation der orgelpfeifen. *Annalen der Physik und Chemie*, 11:397–408.
- Webster, A. (1919). Acoustical impedance and the theory of horns and of the phonograph. *Proc. Nat. Acad. Sci. (US)*, 5:275–282.
- Widrow, B. and Stearns, S. D. (1985). *Adaptive Signal Processing*. Englewood Cliffs, N.J.: Prentice-Hall, Inc.
- Wilson, T. A. and Beavers, G. S. (1974). Operating modes of the clarinet. *J. Acoust. Soc. Am.*, 56(2):653–658.
- Wilson, T. D. (1996). The measured vocal tract impedance for clarinet performance and its role in sound production. *J. Acoust. Soc. Am.*, 99(4):2455–2456.
- Worman, W. E. (1971). *Self-Sustained Nonlinear Oscillations of Medium Amplitude in Clarinet-Like Systems*. Ph.D. thesis, Case Western Reserve University.
- Wyman, F. S. (1972). *An Acoustical Study of Alto Saxophone Mouthpiece Chamber Design*. Ph.D. thesis, Eastman School of Music, The University of Rochester.